frontiers | Research Topics

Green synthesis of nanomaterials: Cytotoxicity and drug delivery, 2nd Edition

Edited by
Mina Sarani, Abolfazl Heydari and Majid Darroudi

Published in
Frontiers in Bioengineering and Biotechnology
Frontiers in Molecular Biosciences

ISSN 1664-8714
ISBN 978-2-8325-3489-2
DOI 10.3389/978-2-8325-3489-2

About Frontiers

Frontiers is more than just an open access publisher of scholarly articles: it is a pioneering approach to the world of academia, radically improving the way scholarly research is managed. The grand vision of Frontiers is a world where all people have an equal opportunity to seek, share and generate knowledge. Frontiers provides immediate and permanent online open access to all its publications, but this alone is not enough to realize our grand goals.

Frontiers journal series

The Frontiers journal series is a multi-tier and interdisciplinary set of open-access, online journals, promising a paradigm shift from the current review, selection and dissemination processes in academic publishing. All Frontiers journals are driven by researchers for researchers; therefore, they constitute a service to the scholarly community. At the same time, the *Frontiers journal series* operates on a revolutionary invention, the tiered publishing system, initially addressing specific communities of scholars, and gradually climbing up to broader public understanding, thus serving the interests of the lay society, too.

Dedication to quality

Each Frontiers article is a landmark of the highest quality, thanks to genuinely collaborative interactions between authors and review editors, who include some of the world's best academicians. Research must be certified by peers before entering a stream of knowledge that may eventually reach the public - and shape society; therefore, Frontiers only applies the most rigorous and unbiased reviews. Frontiers revolutionizes research publishing by freely delivering the most outstanding research, evaluated with no bias from both the academic and social point of view. By applying the most advanced information technologies, Frontiers is catapulting scholarly publishing into a new generation.

What are Frontiers Research Topics?

Frontiers Research Topics are very popular trademarks of the *Frontiers journals series*: they are collections of at least ten articles, all centered on a particular subject. With their unique mix of varied contributions from Original Research to Review Articles, Frontiers Research Topics unify the most influential researchers, the latest key findings and historical advances in a hot research area.

Find out more on how to host your own Frontiers Research Topic or contribute to one as an author by contacting the Frontiers editorial office: frontiersin.org/about/contact

Green synthesis of nanomaterials: Cytotoxicity and drug delivery, 2nd Edition

Topic editors

Mina Sarani — Zabol University of Medical Sciences, Iran

Abolfazl Heydari — Polymer Institute (SAS), Slovakia

Majid Darroudi — Mashhad University of Medical Sciences, Iran

Citation

Sarani, M., Heydari, A., Darroudi, M., eds. (2023). *Green synthesis of nanomaterials: Cytotoxicity and drug delivery, 2nd Edition*. Lausanne: Frontiers Media SA. doi: 10.3389/978-2-8325-3489-2

Publisher's note: This is a 2nd edition due to articles' retraction.

Table of contents

frontiers in Molecular Biosciences

ORIGINAL RESEARCH
published: 02 February 2022
doi: 10.3389/fmolb.2021.832022

Nanoliposome-Encapsulated and Non-Encapsulated Phenolics From *Achillea millefolium* and Their Biological Function in Mice Challenged by *Campylobacter jejuni*: A Comparative Study

Nikta Nateghi[1], *Ehsan Karimi*[1*†] *and Ehsan Oskoueian*[2*†]

[1]Department of Biology, Mashhad Branch, Islamic Azad University, Mashhad, Iran, [2]Department of Research and Development, Arka Industrial Cluster, Mashhad, Iran

OPEN ACCESS

Edited by:
Majid Darroudi,
Mashhad University of Medical Sciences, Iran

Reviewed by:
M. R. Mozafari,
Australasian Nanoscience and Nanotechnology Initiative, Australia
Techn Murthy Chavali Yadav,
Vienna University of Technology, Austria

***Correspondence:**
Ehsan Karimi
ehsankarimi@mshdiau.ac.ir
Ehsan Oskoueian
e.oskoueian@gmail.com

†ORCID:
Ehsan Karimi
https://orcid.org/0000-0002-5011-9611
Ehsan Oskoueian
https://orcid.org/0000-0003-4821-190X

Specialty section:
This article was submitted to Nanobiotechnology, a section of the journal Frontiers in Molecular Biosciences

Received: 09 December 2021
Accepted: 29 December 2021
Published: 02 February 2022

Citation:
Nateghi N, Karimi E and Oskoueian E (2022) Nanoliposome-Encapsulated and Non-Encapsulated Phenolics From Achillea millefolium and Their Biological Function in Mice Challenged by Campylobacter jejuni: A Comparative Study. Front. Mol. Biosci. 8:832022. doi: 10.3389/fmolb.2021.832022

The objective of this research was to develop the nanoliposome-encapsulated phenolic rich fraction from *Achillea millefolium* (*A. millefolium*) and to investigate its antibacterial and health-promoting activities in mice challenged by pathogenic foodborne *Campylobacter jejuni*. The *A. millefolium* was extracted and the ethyl acetate fraction was found to be the phenolic-rich fraction (PRF) containing 14.72 ± 2.39 mg gallic acid equivalent (GAE)/g dry weight (DM). Base on the results, the synthesized nanoliposome-loaded PRF (PRF-NLs) with the size of 187.2 nm exhibited homogeneous dispersion (PDI 0.213) and moderate stability behavior in colloidal dispersions (Zeta potential –37.45). The non-encapsulated PRF and PRF-NLs were gavaged orally in the mice for 28 days, and mice were challenged with *C. jejuni* on day 21. The results indicated that the dietary supplementation of non-encapsulated PRF and PRF-NLs significantly ($p < 0.05$) improved the average daily weight gain, food intake, liver function, antioxidant status, and morphostructural characteristics of the ileum. However, the PRF-NLs appeared to be more potent as compared to non-encapsulated PRF. The higher biological activity of PRF-NLs could be associated with the higher intestinal solubility and absorption of nanoliposome-encapsulated PRF. Thereby, the nanoliposome-encapsulated PRF could be considered as a natural antibiotic alternative called phytobiotic to prevent intestinal infection caused by enteropathogenic *C. jejuni.*

Keywords: phytobiotic, phytogenics, antibiotic alternative, target delivery, gene expression

INTRODUCTION

Campylobacter jejuni (*C. jejuni*), a Gram-negative bacterium that is known as a food-borne pathogen (Chlebicz and Śliżewska 2018). The natural reservoirs of *C. jejuni* are the wild bird's intestine, where is a suitable niche for its dissemination and survival (Abdollahpour et al., 2015). It mediates the N-linked glycosylation of over 30 colonizing, adherence, and invasion proteins (Dasti et al., 2010; Lai et al., 2013). Since this pathogenic bacterium has been more prevalent worldwide and has become increasingly resistant to antibiotics therefore, alternative natural antimicrobials are vital to inhibit or decrease their contamination in food and food-producing animals (Marotta et al., 2019).

The *Achillea millefolium* L. (*A. millefolium*) (known as yarrow) is a well known medicinal plant that belongs to the Asteraceae families and contains more than 100 species (Dias et al., 2013). This

herbal medicine is famous in applied medicine, pharmacological studies, and antibacterial researches due to its important natural bioactive compounds including salicylic and succinic acids, folic acid, caffeic acid, kaempferol, luteolin, apigenin, and other phenolic and flavonoid compounds. *A. millefolium* is wildly distributed in Asia, Africa, Europe, and America and cultivated in various regions all around the world (Dias et al., 2013; Tadić et al., 2017). It also indicated strong cytotoxic and antimicrobial properties according to the high content of phenolic compounds (Taşkın et al., 2016; Abou Baker 2020).

Polyphenols are natural bioactive compounds that attracted a good deal of attention due to scavenging the free radicals through donating hydrogen atoms and interrupting chain oxidation reaction. Several experiments worldwide have evaluated and proven their biological properties including effectiveness against various pathogenic bacteria. There are over 9000 phenolic compounds that have been extracted (Wang et al., 2011) mainly from dietary supplements including apples, tea, red wine, tomatoes, onions and exhibit strong antioxidant and antimicrobial potential (Wang et al., 2018).

However, the widespread use of phenolic compounds has been limited due to their low solubility resulting in poor absorption and biological activities. Previous studies revealed that different carriers like liposomes could improve solubility and enhance the bioactivity of these natural components (Rafiee et al., 2017). Nanoliposomes consist of phospholipid bilayers that are microscopic carriers that can control the release of natural bioactive compounds like polyphenols to the target place and enhance the effectiveness and cellular uptake of the encapsulated natural constitute (Hasan et al., 2014). One of the great benefits of applying nanoliposomes is the acquired features when added to bioactive compounds as their physicochemical potentials including size which enhance their solubility and bioavailability. Meanwhile, they have low toxicity and high biocompatibility to capsulate both hydrophilic and lipophilic active components (Figueroa-Robles et al., 2021). The objective of this research was to develop the nanoliposome-encapsulated phenolic rich fraction from *Achillea millefolium* and to investigate its antibacterial and health-promoting activities in mice challenged by pathogenic foodborne *C. jejuni*.

MATERIALS AND METHODS

Plant Material and Reagents

Herbal medicine markets in Mashhad, Iran, provided fresh aerial parts of *A. millefolium*. Sigma Aldrich (Germany) supplied soybean lecithin with a purity of 99%. As a food-borne pathogen, *C. jejuni* (RTCC 1097) was provided from Razi Vaccine and Serum Research Institute, Karaj, Iran (Gharib Naseri et al., 2012; Ebrahimi et al., 2016). As part of the gene expression analysis, the RNeasy Mini kit from Qiagen (Hilden, Germany), SYBR Green PCR Master Mix from Qiagen (Hilden, Germany), cDNA Quantitect Reverse Transcription Kit (Qiagen, Hilden, Germany), and SYBR Green PCR Master Mix from Qiagen (Hilden, Germany) were utilised. In this study, DNA was extracted using the QIAamp DNA Stool Mini Kit from Qiagen, Hilden, Germany. Besides these, Merck (Germany) provided the rest of the reagents.

Fractionation and Total Phenolic Determination

We cleaned, separated, and freeze dried the freshly cut aerial parts of *A. millefolium* in the first step. Using the reflux method, 900 ml aqueous methanol (80% v/v) and 100 ml of 6 M HCl were added to 100 g of the dried powder for 2 h (Karimi et al., 2019) to do the extraction. An electronic rotary evaporator (Buchi, Flawil, Switzerland) was then used to evaporate the extract (60°C). A separating funnel and different solvents (hexane, ethyl acetate, n-butanol, chloroform, and water) were used to fractionate the dried aqueous-methanolic extract (Oskoueian et al., 2020). A vacuumed rotary evaporator was used to filter and concentrate the supernatant after fractionation. In a test tube covered with aluminum foil, 0.1 ml of the extract was mixed with 2.5 ml of Folin-Ciocalteu reagent (1:10 v/v) and 2 ml of 7.5% sodium carbonate to measure the total phenolic compounds in each fraction. Vortexing of the test tubes and measuring absorbance at 765 nm were done (Oskoueian et al., 2020). These results are reported in milligrams of gallic acid equivalents (GAE) per Gram dry weight. Phenolic rich fractions (PRFs) are defined as fractions containing the most phenolics.

Nanoliposomes Preparation

In 196 g of hot distilled water, 4 g of lecithin were hydrated and agitated for 2 h. To reach the final concentration of 2000 ppm, the PRF after dissolving in ethanol was gradually added to the mixture (2 h) and stirred. The nanoliposome-encapsulated phenolic rich fraction (PRF-NLs) that was obtained after sonication (Cole-Parmer Instrument, United States) for 4–6 min was applied for further characterization.

Characterization of Nanoliposomes

Nanoliposome characteristics such as particle size and zeta potential, were evaluated with Zetasizer Nano ZS-Malvern. The Shape and Nanoliposomes Size Dimensions were also confirmed on the basis of Field Emission Scanning Electron Microscopy (FESEM). According to the fractionation section (Oskoueian et al., 2020), the total phenolic content of nanoliposomes was determined.

Phenolic Profiling of Nanoliposomes

Reversed-Phase High-Performance Liquid Chromatography (RP-HPLC) was used to identify the phenolic compounds present in the nanoliposomes-loaded PRF from *A. millefolium*. In the present experiment, the phenolic standards included catechin, vanillic acid, naringin, gallic acid, syringic acid, salicylic acid, caffeic acid, pyrogallol, cinnamic acid, ellagic acid, chrysin, and ferulic acid. There are two solvents used here, deionized water (solvent A) and acetonitrile (solvent B). After eluting and equilibrating the column with 85 percent solvent A and 15 percent solvent B,

the injection was performed. Following 60 min, the ratio of solvent B was increased to 85%. After 5 min of running the experiment, the ratio of solvent B had decreased to 15 percent. A flow rate of 1 ml/min was used for the next analysis with a ratio of 70 min. The analysis of phenolic at 280 nm was conducted with an analytical column (Intersil ODS-3 5um 4.6 mm × 150 mm Gl Science Inc. United States).

Bacterial Preparation

This experimental challenge was designed to determine the pathogenicity of *C. jejuni*, which was isolated from the cloaca of commercial broiler chicken (Gharib Naseri et al., 2012; Ebrahimi et al., 2016). The *C. jejuni* was propagated in microaerophilic conditions at 42°C using selective culture media (Oxid, United Kingdom). A specific viable concentration of 1×10^9 cfu/ml was obtained by harvesting the bacteria and diluting them in peptone water. Prior to oral gavage, the inoculum was maintained on ice for less than 1 h.

Animal Trial

At the Razi Vaccine and Serum Research Institute in Mashhad, we purchased 40 white male Balb/c mice (20–25 g). To adapt to lab conditions, the mice were kept in individual cages at 58% humidity, 10% humidity, 23 °C, and 1% temperature with 12-h periods of light and darkness for 7 days. During the experiment, 40 mice were divided into four groups of ten and provided with a standard pelleted diet and tap water (Javaneh Khorasan, Mashhad, Iran). There were four experimental groups:

T1: normal diet.
T2: normal diet + infected by *C. jejuni* on day 21.
T3: Normal diet enriched by PRF (10 mg TPC/kg BW/day) + infected by *C. jejuni* on day 21.
T4: Normal diet enriched by nanoliposome-encapsulated PRF (10 mg TPC/kg BW/day) + infected by *C. jejuni* on day 21.

All mice underwent experimental treatment for 4 weeks, and the oral infection (108 cfu of *C. jejuni*) was administered once on day 21 of treatment. General health and food consumption were monitored daily. The mice were sacrificed at the day 28th of the experiment with pentobarbital-HCL (50 mg/kg, i. p.). We collected blood, ileum samples, and liver samples immediately for gene expression analysis, liver enzyme analysis, morphometric evaluation of the ileum, and lipid peroxidation assay. In the experiment, mice were weighed twice, once at the beginning, and once at the end. A code of ethics was adopted by the Islamic Azad University of Mashhad with regards to the animal experiments, IR. IAU.MSHD.REC.1399.013.

Liver Enzymes and Lipid Peroxidation Assay

A blood auto-analyzer (Hitachi 902, Japan) was used to determine serum levels of liver enzymes, such as ALT, AST, and ALP. Peroxidation of lipids in the liver tissue was measured as previously described by Shafaei et al. (2020). Using liver tissue homogenate, 200 µl of lysate was mixed respectively with distilled water (300 µl), BHT (35 µl), sodium dodecyl sulfate (165 µl), and thiobarbituric acid (2 µl). In the following step, the heated solution was cooled for 60 min, then mixed with 2 ml of n-butanol, and centrifuged at 2000 ×g for 5 min. At 532 nm, the absorbance of the n-butanol part of the reaction was measured and the results were expressed as the percentage of malondialdehyde (MDA) variations relative to a control sample.

Histopathology and Morphometric Analyses

At the end of the *in vivo* experiment, the mice were sacrificed and the liver, kidney, and ileum were separated and washed using the physiological serum. They were fixed in buffered formalin (10% formalin in 0.1 M sodium phosphate buffer, pH7), paraffinized, sliced, and stained according to the hematoxylin/eosin protocol (Shafaei et al., 2020). The histopathology slides were observed under a light microscope using a magnification of 20×. The morpho-structural characteristics of ileum including villus height, villus width, crypt depth, and goblet cell count were determined (Navarrete et al., 2015).

Gene Expression Analysis

In order to study how ileum tissue responded to different treatments, we determined the expression of major inflammation markers such as inducible nitric oxide synthase (iNOS), cyclooxygenase 2 (COX2), and antioxidant biomarkers like superoxide dismutase (SOD) and glutathione peroxidase (GPx). RNA was extracted from freshly frozen ileum tissues using an RNeasy Mini kit (Qiagen, Hilden, Germany) after they had been crushed and prepared in accordance with the recommended protocol. Qiagen, Hilden, Germany) reverse transcription kit was used to make the cDNA. **Table 1** shows the characteristics of the primers for the key genes and the housekeeping gene (Beta-actin). In a comparative Real-time PCR (Roche Diagnostics), Qiagen's SYBR Green PCR Master Mix was used (Hilden, Germany). We amplified the target genes using the following protocol: for initial denaturation, 95°C for 5 min (1X), followed by 35 cycles of 95°C for the 30 s, primer annealing at 60 and 58 for 30 s for the inflammatory genes (COX2, iNOS), and antioxidant genes (SOD, GPx), respectively and 30 s of extension in 72°C. In this study, beta-actin was used as a reference gene and the respective gene expressions were normalized to those of the control group (Kathirvel et al., 2010).

Campylobacter jejuni Population Analysis

A real-time PCR (LightCycler 96 instrument, Roche, Basel, Switzerland) was used to determine the relative abundance of the colonized *C. jejuni* population in the ileum digesta. As the ileum is the main site of enteropathogens' fermentation, propagation, and colonization the monogastric, the population of *C. jejuni* in this study was only examined in the ileum section. Initial denaturation was performed at 95°C for 5 min (1X), followed by 35 cycles of 95°C for 30 s, followed by primer annealing at 60, and then 55 for 25 s for *C. jejuni* and total bacteria, respectively, and 20 s extension in 72°C. **Table 2** shows the characteristics of primers. DNA was extracted from ileum digesta using a QIAamp DNA Stool extraction kit

TABLE 1 | The primer sets characteristics used in this study.

Gene	Forward (5′ →3′)	Reverse (5′ →3′)	References
COX2	caagcagtggcaaaggcctcca	ggcacttgcattgatggtggct	Jain et al. (2008)
iNOS	caccttggagttcacccagt	accactcgtacttgggatgc	Kou et al. (2011)
SOD	gagacctgggcaatgtgact	gtttactgcgcaatcccaat	Kathirvel et al. (2010)
GPx	gtccaccgtgtatgccttct	tctgcagatcgttcatctcg	Kathirvel et al. (2010)
β-actin	cctgaaccctaaggccaacc	cagctgtggtggtgaagctg	Shafaei et al. (2020)

TABLE 2 | The list of the primers used for ileum microbial population analysis.

Bacteria	Forward (5′ →3′)	Reverse (5′ →3′)	References
C. jejuni	cgggatagttatagtattgaagtt	gaaggagcataataggatcttg	Razzuoli et al. (2018)
Total bacteria	cggcaacgagcgcaaccc	ccattgtagcacgtgtgtagcc	Denman and McSweeney (2006)

(QIAGEN, Germany). This study used the SYBR GREEN Master Mix (BIO FACT, Korea). A quantitative real-time PCR assay was performed using previously published primers. In this study, we used the ΔΔ Ct method to compare fold changes in the *C. jejuni* bacteria population and expressed the results as fold changes in the amount of *C. jejuni* relative to the overall bacteria population (Si et al., 2007; Feng et al., 2010).

Statistical Analysis

This study used the general linear model (GLM) of SAS (Version 9.1) to analyze the collected data. The significance of the difference among treatments was determined using Duncan's multiple range test. To determine whether there were statistically significant differences among treatments, a p-value of <0.05 was used. The experiments were conducted in triplicate and the results were presented as mean values ±SE of the mean or standard deviation.

RESULTS AND DISCUSSION

Fractionation

The total phenolic content of the fractions are as follow: ethyl acetate fraction 14.72 ± 2.39> n-butanol fraction 12.1 ± 1.19 > chloroform fraction 10.5 ± 0.73 > hexane fraction 8.6 ± 0.49 > water fraction 3.56 ± 0.51 mg GAE/g DM, respectively. Hence, the ethyl acetate fraction was chosen as a phenolic-rich fraction (PRF) and this fraction was used for further evaluations.

Characterization of PRF-NLs

The results of particle size analysis indicated the nanometer size of the nanoliposomes (187.2 nm) and the PDI value of 0.213 lower than 0.3 revealed the homogeneous dispersion (Hasan et al., 2014). The zeta potential is a marker of the stability of colloidal dispersions and the potential value ranged from ±30 to ±40 mV is considered as a colloidal dispersion with moderate stability behavior (**Figure 1**). Thus, the colloidal dispersions of PRF-NLs showed moderate stability behavior. Finally, The microscopic analysis (**Figure 2**) confirmed the spherical shape of nanoliposomes. As well as homogeneous distribution of phenolic compounds.

Phenolic Analysis of PRF-NLs

The total phenolic content of PRF-NLs was 7.04 ± 1.27 mg GAE/g DM. Meanwhile, the HPLC analysis illustrated different natural phenolic compounds such as gallic acid, syringic acid, ferulic acid, caffeic acid, ellagic acid, salicylic acid, and chrysin with the concentration ranging from 132 to 971 μg/g dried nanoliposomes (**Table 3**).

Body Weight and Feed Intake Changes

Based on the results summarized in **Table 4**, the highest and lowest daily weight gain was observed in the mice group supplement with normal diet (T1) and infected group (T2), respectively with the values of 0.21 and 0.13 g/day. These results were consistent with the results obtained for average daily feed intake. Dietary addition of either non-encapsulated PRF or PRF-NLs at a concentration of 10 mg TPC/kg BW/day could improve the average daily and food intake significantly ($p < 0.05$). The improvement in the average daily weight gain and feed intake in the group of mice who received PRF-NLs was significantly ($p < 0.05$) higher than that of mice who received non-encapsulated PRF.

Liver Enzymes and Lipid Peroxidation

The biological markers of liver function and health such as ALT, SGPT, SGOT, and lipid peroxidation are presented in **Table 5**. As known, the increase in these parameters is the important symptoms of liver inflammatory and oxidative stress. Our results demonstrated that infection caused by *C. jejuni* notably ($p < 0.05$) elevated the liver enzymes and lipid peroxidation significantly. While the inclusion of non-encapsulated PRF and PRF-NLs in the dietary regimen of mice alleviated the liver enzymes and lipid peroxidation values significantly ($p < 0.05$). The modulation of liver enzymes and lipid peroxidation were more pronounce ($p < 0.05$) in the group of mice supplemented with PRF-NLs as compared to the mice that received non-encapsulated PRF.

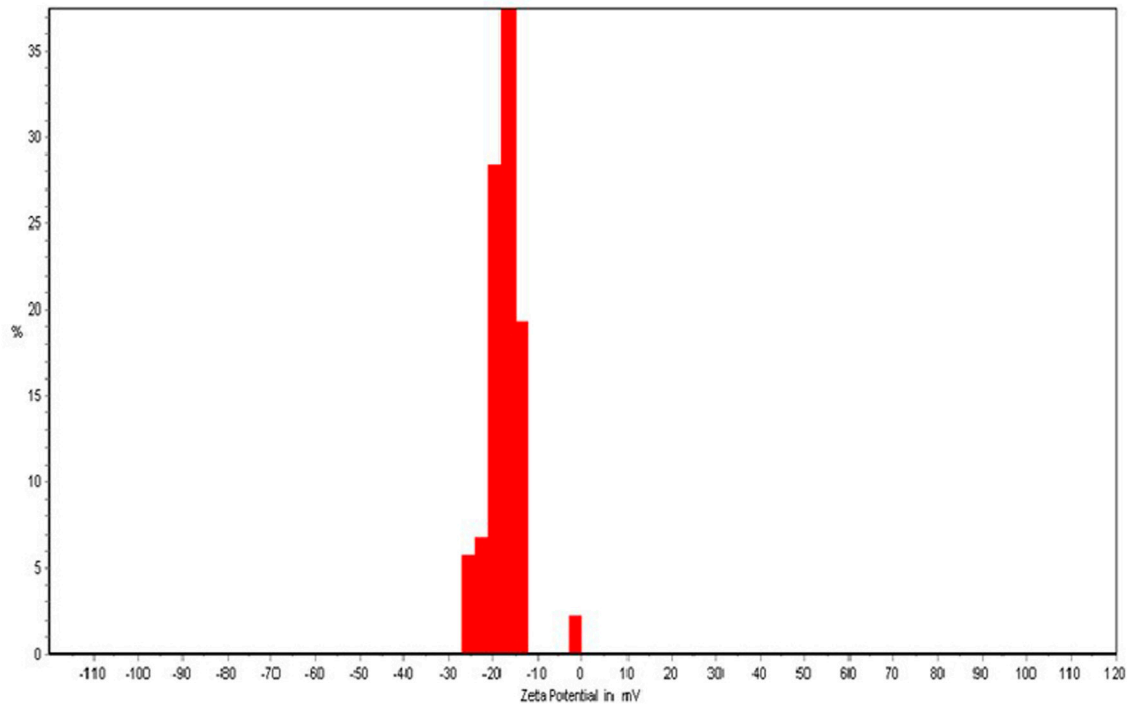

FIGURE 1 | The zeta potential of *Achillea millefolium* phenolics-loaded nanoliposomes.

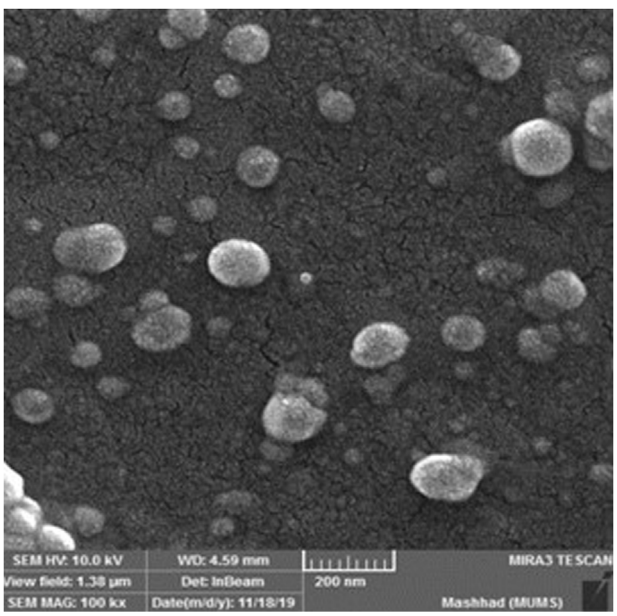

FIGURE 2 | The FESEM analysis of *Achillea millefolium* phenolics-loaded nanoliposomes.

Histopathological Evaluation and Morphometric Analysis

The histopathological examination of liver, kidney, and ileum tissues is presented in **Figure 3**. The normal architecture was observed in the liver, kidney, and ileum tissues in the control group (T1). No prominent histopathological changes in the liver, kidney, and ileum tissues were observed upon infection by *C. jejuni* and supplementation of either non-encapsulated PRF or PRF-NLs. The morphometric analysis of ileum (**Table 6**) revealed that mice challenged by the infection caused by *C. jejuni* (T2) possessed higher crypt depth, villus with lower height, width, and decrease in the goblet cells quantity as compared to the control group (T1). The dietary addition of 10 mg TPC/kg BW/day from non-encapsulated PRF and nanoliposome-encapsulated PRF could significantly ($p < 0.05$) improve the morphostructural characteristics of the ileum. The improvement in the morphostructural characteristics of the intestine resulted in better absorption of nutrients and subsequently enhance the daily weight gain. These observations were consistent with the early study conducted by (Jamroz et al., 2006) who reported the stimulatory effects of plant bioactive compounds on growth and development of villus, increase in the production of mucus on the inner wall of the intestine which prevents enteropathogens colonization.

Gene Expression Analysis

The expression analysis of inflammation- (COX2 and iNOS) and antioxidant-related (SOD and GPx) genes in the ileum tissue are presented in **Table 7**. The intestinal infection caused by *C. jejuni* significantly ($p < 0.05$) up-regulated the inflammation-related genes COX2 and iNOS by 5.1 and 6.8 folds, respectively as compared to the control (T1). In contrast, the *C. jejuni* infection down-regulated the expression of antioxidant-related

TABLE 3 | Phenolic compounds presented in *Achillea millefolium* phenolics-loaded nanoliposomes.

Phenolic compounds (μg/g DW)						
GA	**SY**	**FA**	**CA**	**EA**	**SA**	**CH**
132 ± 3.1	305 ± 4.8	519 ± 4.6	832 ± 2.7	248 ± 3.3	971 ± 1.5	169 ± 3.8

GA, gallic acid; SY, syringic acid; FA, ferulic acid; CA, caffeic acid; EA, ellagic acid; SA, salicylic acid; CH, chrysin.

TABLE 4 | The averages of mice body weight changes and feed intake upon receiving different treatments.

Average	T1	T2	T3	T4	SEM
Average daily weight gain (g)	0.21^{a}	0.13^{d}	0.15^{c}	0.17^{b}	0.05
Average daily feed intake (g)	3.4^{a}	2.7^{c}	3.1^{b}	3.3^{a}	0.11

T1: normal diet; T2: normal diet + infected by C. jejuni *on day 21; T3: Normal diet enriched by PRF (10 mg TPC/kg BW/day) + infected by* C. jejuni *on day 21; T4: Normal diet enriched by nanoliposome-encapsulated PRF (10 mg TPC/kg BW/day) + infected by* C. jejuni *on day 21.*
Values with diferent superscript letters in the same row are signifcantly diferent ($p < 0.05$).

TABLE 5 | The results of liver enzymes and lipid peroxidation.

Liver enzymes	T1	T2	T3	T4	SEM
ALP (IU/L)	204.8^{d}	258.1^{a}	243.0^{b}	228.7^{c}	6.89
SGPT (IU/L)	98.5^{d}	151.3^{a}	139.4^{b}	126.5^{c}	3.57
SGOT (IU/L)	139.5^{d}	173.5^{a}	143.1^{b}	135.6^{c}	4.62
MDA (changes relative to control)	100^{d}	132.5^{a}	121.4^{b}	116.7^{c}	5.12

T1: normal diet; T2: normal diet + infected by C. jejuni *on day 21; T3: Normal diet enriched by PRF (10 mg TPC/kg BW/day) + infected by* C. jejuni *on day 21; T4: Normal diet enriched by nanoliposome-encapsulated PRF (10 mg TPC/kg BW/day) + infected by* C. jejuni *on day 21.*
Values with diferent superscript letters in the same row are signifcantly diferent ($p < 0.05$).

genes (SOD, GPx) by 3.89 and 1.93 folds, respectively, as compared to the control group. The dietary supplementation of 10 mg TPC/kg BW/day from non-encapsulated PRF and nanoliposome-encapsulated PRF significantly ($p < 0.05$) suppressed the expression of inflammation- and increased the expression of antioxidant-related genes significantly ($p < 0.05$).

TABLE 6 | Morphometric analysis of ileum in the mice receiving different treatments.

Parameters	T1	T2	T3	T4	SEM
Villus Height (μm)	423.8^{c}	408.7^{d}	435.4^{b}	452.6^{a}	7.86
Villus Width (μm)	127.4^{c}	101.3^{d}	138.2^{b}	145.1^{a}	9.34
Crypt Depth (μm)	132.5^{b}	152.6^{a}	134.3^{b}	114.7^{c}	7.66
Mean number of Goblet Cells	5.1^{a}	3.5^{b}	3.6^{b}	4.7^{a}	0.86

T1: normal diet; T2: normal diet + infected by C. jejuni *on day 21; T3: Normal diet enriched by PRF (10 mg TPC/kg BW/day) + infected by* C. jejuni *on day 21; T4: Normal diet enriched by nanoliposome-encapsulated PRF (10 mg TPC/kg BW/day) + infected by* C. jejuni *on day 21.*
Values with diferent superscript letters in the same row are signifcantly diferent ($p < 0.05$).

The antioxidant and anti-inflammatory potentials of gallic acid, syringic acid, ferulic acid, caffeic acid, ellagic acid, salicylic acid, and chrysin have been previously documented (Shahidi and Ambigaipalan 2015; Ambriz-Pérez et al., 2016). Hence, the regulation of inflammation- and antioxidant-related genes in the current study might be due to the presence of bioactive phenolics compounds in the non-encapsulated and nanoliposome-encapsulated PRF. Apart from that, the higher intestinal solubility, absorption of nanoliposome-encapsulated PRF resulted in significant ($p < 0.05$) down-regulation in the inflammation- and up-regulation in antioxidant-related genes as compared to the mice received non-encapsulated PRF.

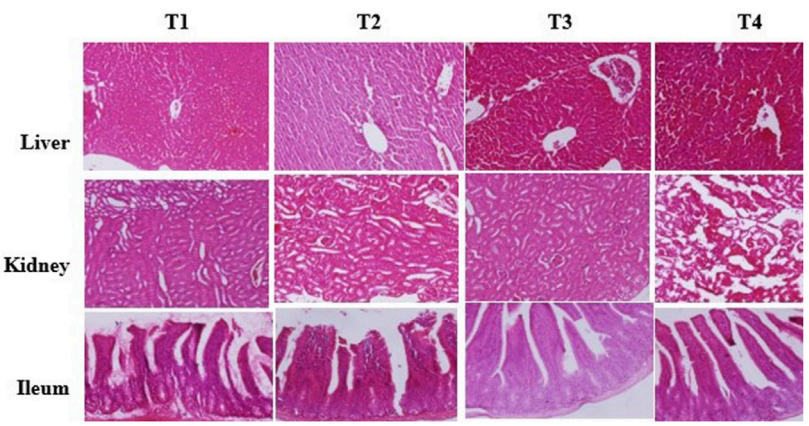

FIGURE 3 | Histopathological analysis of liver, kidney, and ileum of the mice treated with different treatment. T1: normal diet; T2: normal diet + infected by *C. jejuni* on day 21; T3: Normal diet enriched by PRF (10 mg TPC/kg BW/day) + infected by *C. jejuni* on day 21; T4: Normal diet enriched by nanoliposome-encapsulated PRF (10 mg TPC/kg BW/day) + infected by *C. jejuni* on day 21.

TABLE 7 | Gene expression analysis of the mice received different treatments.

	Fold changes				SEM
Genes	**T1**	**T2**	**T3**	**T4**	
COX2	1.0^{d}	$+5.1^{a}$	$+3.3^{b}$	$+2.4^{c}$	0.06
iNOS	1.0^{d}	$+6.8^{a}$	$+4.7^{b}$	$+3.3^{c}$	0.17
SOD	1.0^{c}	-3.89^{d}	$+1.1^{b}$	$+1.8^{a}$	0.09
GPx	1.0^{c}	-1.93^{d}	$+1.8^{b}$	$+2.1^{a}$	0.14

T1: normal diet; T2: normal diet + infected by C. jejuni *on day 21; T3: Normal diet enriched by PRF (10 mg TPC/kg BW/day) + infected by* C. jejuni *on day 21; T4: Normal diet enriched by nanoliposome-encapsulated PRF (10 mg TPC/kg BW/day) + infected by* C. jejuni *on day 21.*
Values with diferent superscript letters in the same row are signifcantly diferent ($p < 0.05$).

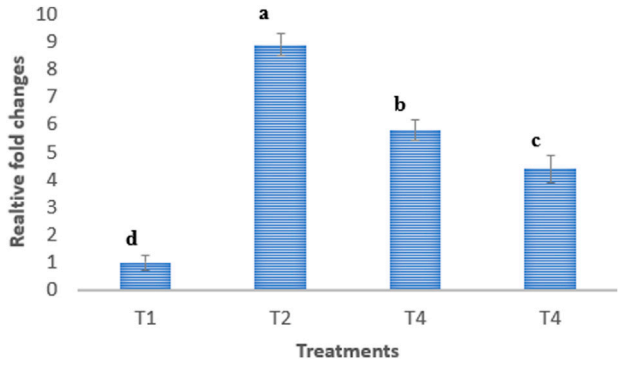

FIGURE 4 | Relative fold changes of *C. jejuni* population in ileum digesta. T1: normal diet; T2: normal diet + infected by *C. jejuni* on day 21; T3: Normal diet enriched by PRF (10 mg TPC/kg BW/day) + infected by *C. jejuni* on day 21; T4: Normal diet enriched by nanoliposome-encapsulated PRF (10 mg TPC/kg BW/day) + infected by *C. jejuni* on day 21.

Relative Quantification of *Campylobacter* jejuni

The relative changes in the ileal population of *C. jejuni* are presented in **Figure 4**. The results illustrated that challenge with *C. jejuni* significantly ($p < 0.05$) increased the population of *C. jejuni* in the ileum digesta by 8.9 folds as compared to the control un-infected group of mice.

The dietary supplementation of non-encapsulated and nanoliposome-encapsulated PRF notably ($p < 0.05$) suppressed the *C. jejuni* population in the ileum digesta by 5.8 and 4.4 folds, respectively. The inhibition of *C. jejuni* in the ileum by nan-encapsulated PRF and nanoliposome-encapsulated PRF is attributed to the presence of antibacterial compounds such as gallic acid, syringic acid, ferulic acid, caffeic acid, ellagic acid, salicylic acid, and chrysin (Bouarab-Chibane et al., 2019) in the PRF.

These results postulated that nanoliposome-encapsulated PRF more effectively modulated the enteropathogenic *C. jejuni* in the ileum as compared to the nonencapsulated PRF. The higher antibacterial activity of nanoliposome-encapsulated PRF as compared to the non-encapsulated PRF could be associated with the higher intestinal solubility and absorption of nanoliposome-encapsulated PRF. Thereby, the nanoliposome-encapsulated PRF could be considered as a natural antibiotic alternative called phytobiotic to prevent intestinal infection caused by *C. jejuni.* Besides, these bioactive phenolics present in the PRF, stimulate the production of intestinal mucus which then create a thick layer of mucus on the inner wall of the ileum and reduces the possible colonization of *C. jejuni* and resulted in the reduced population of *C. jejuni* (Jamroz et al., 2006).

CONCLUSION

The nanoliposome-encapsulated PRF and non-encapsulated PRF at the concentration of 10 mg TPC/kg BW/day could improve the average daily weight gain, food intake, liver function, antioxidant status, and morphostructural characteristics of the ileum and decreased the ileum population of *C. jejuni* in the mice challenged by *C. jejuni* infection, however, the nanoliposome-encapsulated PRF was more functional effective than nonencapsulated PRF in alleviating the side effects of *C. jejuni* infection. Consequently, the nanoliposome-encapsulated PRF could be considered as a promising phytobiotic against *C. jejuni* infection in mice. For the future work we suggest the isolation and encapsulation of phenolics individually and determine the phytobiotic properties against *C. jejuni.*

DATA AVAILABILITY STATEMENT

The raw data supporting the conclusion of this article will be made available by the authors, without undue reservation.

ETHICS STATEMENT

The animal study was reviewed and approved by Islamic Azad University of Mashhad.

AUTHOR CONTRIBUTIONS

NN: Study design, experimental work, formal analysis and writing original draft; EK and EO: project administration, supervision, review, and editing of the original draft; All authors read and approved the final manuscript. All authors contributed equally to this work.

REFERENCES

Abdollahpour, N., Zendehbad, B., Alipour, A., and Khayatzadeh, J. (2015). Wild-bird Feces as a Source of Campylobacter Jejuni Infection in Children's Playgrounds in Iran. *Food Control* 50, 378–381. doi:10.1016/j.foodcont.2014.09.007

Abou Baker, D. H. (2020). *Achillea millefolium* L. Ethyl Acetate Fraction Induces Apoptosis and Cell Cycle Arrest in Human Cervical Cancer (HeLa) Cells. *Ann. Agric. Sci.* 65 (1), 42–48. doi:10.1016/j.aoas.2020.03.003

Ambriz-Pérez, D. L., Leyva-López, N., Gutierrez-Grijalva, E. P., and Heredia, J. B. (2016). Phenolic Compounds: Natural Alternative in Inflammation Treatment. A Review. *Cogent Food Agric.* 2 (1), 1131412. doi:10.1080/23311932.2015.1131412

Bouarab-Chibane, L., Forquet, V., Lantéri, P., Clément, Y., Léonard-Akkari, L., Oulahal, N., et al. (2019). Antibacterial Properties of Polyphenols: Characterization and QSAR (Quantitative Structure-Activity Relationship) Models. *Front. Microbiol.* 10, 829. doi:10.3389/fmicb.2019.00829

Chlebicz, A., and Śliżewska, K. (2018). Campylobacteriosis, Salmonellosis, Yersiniosis, and Listeriosis as Zoonotic Foodborne Diseases: a Review. *Ijerph* 15 (5), 863. doi:10.3390/ijerph15050863

Dasti, J. I., Tareen, A. M., Lugert, R., Zautner, A. E., and Groß, U. (2010). Campylobacter Jejuni: a Brief Overview on Pathogenicity-Associated Factors and Disease-Mediating Mechanisms. *Int. J. Med. Microbiol.* 300 (4), 205–211. doi:10.1016/j.ijmm.2009.07.002

Denman, S. E., and McSweeney, C. S. (2006). Development of a Real-Time PCR Assay for Monitoring Anaerobic Fungal and Cellulolytic Bacterial Populations within the Rumen. *FEMS Microbiol. Ecol.* 58 (3), 572–582. doi:10.1111/j.1574-6941.2006.00190.x

Dias, M. I., Barros, L., Dueñas, M., Pereira, E., Carvalho, A. M., Alves, R. C., et al. (2013). Chemical Composition of Wild and Commercial *Achillea millefolium* L. And Bioactivity of the Methanolic Extract, Infusion and Decoction. *Food Chem.* 141 (4), 4152–4160. doi:10.1016/j.foodchem.2013.07.018

Ebrahimi, H., Rahimi, S., Khaki, P., Grimes, J. L., and Kathariou, S. (2016). The Effects of Probiotics, Organic Acid, and a Medicinal Plant on the Immune Systemand Gastrointestinal Microflora in Broilers Challenged with Campylobacter Jejuni. *Turk J. Vet. Anim. Sci.* 40 (3), 329–336. doi:10.3906/vet-1502-68

Feng, Y., Gong, J., Yu, H., Jin, Y., Zhu, J., and Han, Y. (2010). Identification of Changes in the Composition of Ileal Bacterial Microbiota of Broiler Chickens Infected with Clostridium perfringens. *Vet. Microbiol.* 140 (1-2), 116–121. doi:10.1016/j.vetmic.2009.07.001

Figueroa-Robles, A., Antunes-Ricardo, M., and Guajardo-Flores, D. (2021). Encapsulation of Phenolic Compounds with Liposomal Improvement in the Cosmetic Industry. *Int. J. Pharmaceutics* 593, 120125. doi:10.1016/j.ijpharm.2020.120125

Gharib Naseri, K., Rahimi, S., and Khaki, P. (2012). Comparison of the Effects of Probiotic, Organic Acid and Medicinal Plant on Campylobacter Jejuni Challenged Broiler Chickens. *J. Agric. Sci. Tech.* 14 (7), 1485–1496.

Hasan, M., Belhaj, N., Benachour, H., Barberi-Heyob, M., Kahn, C. J., Jabbari, E., et al. (2014). Liposome Encapsulation of Curcumin: Physico-Chemical Characterizations and Effects on MCF7 Cancer Cell Proliferation. *Int. J. Pharm.* 461 (1-2), 519–528. doi:10.1016/j.ijpharm.2013.12.007

Jain, N. K., Ishikawa, T.-o., Spigelman, I., and Herschman, H. R. (2008). COX-2 Expression and Function in the Hyperalgesic Response to Paw Inflammation in Mice. *Prostaglandins, Leukot. Essent. fatty Acids* 79 (6), 183–190. doi:10.1016/j.plefa.2008.08.001

Jamroz, D., Wertelecki, T., Houszka, M., and Kamel, C. (2006). Influence of Diet Type on the Inclusion of Plant Origin Active Substances on Morphological and Histochemical Characteristics of the Stomach and Jejunum walls in Chicken. *J. Anim. Physiol. Anim. Nutr. (Berl)* 90 (5-6), 255–268. doi:10.1111/j.1439-0396.2005.00603.x

Karimi, E., Mehrabanjoubani, P., Es-Haghi, A., and Chamani, J. (2019). Phenolic Compounds of Endemic Buxus Plants in Caspian Hyrcanian Forest (Buxus Hyrcana Pojark) and Their Biological Activities. *Pharm. Chem. J.* 53 (8), 741–747. doi:10.1007/s11094-019-02072-2

Kathirvel, E., Chen, P., Morgan, K., French, S. W., and Morgan, T. R. (2010). Oxidative Stress and Regulation of Anti-oxidant Enzymes in Cytochrome P4502E1 Transgenic Mouse Model of Non-alcoholic Fatty Liver. *J. Gastroenterol. Hepatol.* 25 (6), 1136–1143. doi:10.1111/j.1440-1746.2009.06196.x

Kou, X., Qi, S., Dai, W., Luo, L., and Yin, Z. (2011). Arctigenin Inhibits Lipopolysaccharide-Induced iNOS Expression in RAW264.7 Cells through Suppressing JAK-STAT Signal Pathway. *Int. Immunopharmacology* 11 (8), 1095–1102. doi:10.1016/j.intimp.2011.03.005

Lai, C.-H., Lai, C.-K., Lin, Y.-J., Hung, C.-L., Chu, C.-H., Feng, C.-L., et al. (2013). Characterization of Putative Cholesterol Recognition/interaction Amino Acid Consensus-like Motif of Campylobacter Jejuni Cytolethal Distending Toxin C. *PloS one* 8 (6), e66202. doi:10.1371/journal.pone.0066202

Marotta, F., Garofolo, G., Di Marcantonio, L., Di Serafino, G., Neri, D., Romantini, R., et al. (2019). Correction: Antimicrobial Resistance Genotypes and Phenotypes of Campylobacter Jejuni Isolated in Italy from Humans, Birds from Wild and Urban Habitats, and Poultry. *Plos one* 14 (11), e0225231. doi:10.1371/journal.pone.0225231

Navarrete, J., Vásquez, B., and Del Sol, M. (2015). Morphoquantitative Analysis of the Ileum of C57BL/6 Mice (Mus musculus) Fed with a High-Fat Diet. *Int. J. Clin. Exp. Pathol.* 8 (11), 14649–14657.

Oskoueian, E., Karimi, E., Noura, R., Ebrahimi, M., Shafaei, N., and Karimi, E. (2020). Nanoliposomes Encapsulation of Enriched Phenolic Fraction from Pistachio Hulls and its Antioxidant, Anti-inflammatory, and Anti-melanogenic Activities. *J. microencapsulation* 37 (1), 1–13. doi:10.1080/02652048.2019.1692941

Rafiee, Z., Barzegar, M., Sahari, M. A., and Maherani, B. (2017). Nanoliposomal Carriers for Improvement the Bioavailability of High - Valued Phenolic Compounds of Pistachio green hull Extract. *Food Chem.* 220, 115–122. doi:10.1016/j.foodchem.2016.09.207

Razzuoli, E., Vencia, W., Fedele, V., Mignone, G., Lazzara, F., Rubini, D., et al. (2018). Evaluation and Validation of an Alternative Method to Detect Campylobacter Spp. In Dairy Products. *Ital. J. Food Saf.* 7 (2), 7180. doi:10.4081/ijfs.2018.7180

Shafaei, N., Barkhordar, S. M. A., Rahmani, F., Nabi, S., Idliki, R. B., Alimirzaei, M., et al. (2020). Protective Effects of Anethum Graveolens Seed's Oil Nanoemulsion against Cadmium-Induced Oxidative Stress in Mice. *Biol. Trace Elem. Res.* 198 (2), 583–591. doi:10.1007/s12011-020-02093-z

Shahidi, F., and Ambigaipalan, P. (2015). Phenolics and Polyphenolics in Foods, Beverages and Spices: Antioxidant Activity and Health Effects - A Review. *J. Funct. Foods* 18, 820–897. doi:10.1016/j.jff.2015.06.018

Si, C., Kun-Lun, H., Wen-Tao, X., Yuan, L., and Yun-Bo, L. (2007). Real-time Quantitative PCR Detection ofEscherichia coliO157:H7. *Chin. J. Agric. Biotechnol.* 4 (1), 15–19. doi:10.1017/s1479236207001349

Tadić, V., Arsić, I., Zvezdanović, J., Zugić, A., Cvetković, D., and Pavkov, S. (2017). The Estimation of the Traditionally Used Yarrow (*Achillea millefolium* L. Asteraceae) Oil Extracts with Anti-inflamatory Potential in Topical Application. *J. Ethnopharmacol* 199, 138–148. doi:10.1016/j.jep.2017.02.002

Taşkın, T., Özakpınar, Ö. B., Gürbüz, B., Uras, F., Gürer, Ü. S., and Bitiş, L. (2016). *Identification of Phenolic Compounds and Evaluation of Antioxidant, Antimicrobial and Cytotoxic Effects of the Endemic Achillea Multifida*.

Wang, T.-Y., Li, Q., and Bi, K.-S. (2018). Bioactive Flavonoids in Medicinal Plants: Structure, Activity and Biological Fate. *Asian J. Pharm. Sci.* 13 (1), 12–23. doi:10.1016/j.ajps.2017.08.004

Wang, Y., Chen, S., and Yu, O. (2011). Metabolic Engineering of Flavonoids in Plants and Microorganisms. *Appl. Microbiol. Biotechnol.* 91 (4), 949–956. doi:10.1007/s00253-011-3449-2

Conflict of Interest: Arka Biotechnology Corporation was affiliated with this study.

The remaining authors declare that the research was conducted in the absence of any commercial or financial relationships that could be construed as a potential conflict of interest.

Publisher's Note: All claims expressed in this article are solely those of the authors and do not necessarily represent those of their affiliated organizations, or those of the publisher, the editors, and the reviewers. Any product that may be evaluated in this article, or claim that may be made by its manufacturer, is not guaranteed or endorsed by the publisher.

frontiers in Bioengineering and Biotechnology

REVIEW
published: 16 February 2022
doi: 10.3389/fbioe.2022.847433

Metallic Nanoparticles for the Modulation of Tumor Microenvironment; A New Horizon

*Siavash Shariatzadeh[1], Negin Moghimi[2], Farima Khalafi[1], Sepehr Shafiee[1], Mohsen Mehrabi[3], Saba Ilkhani[4], Foad Tosan[5], Pooria Nakhaei[6], Ali Alizadeh[7], Rajender S. Varma[8] and Mohammad Taheri[9,10]**

[1]Department of Pharmacology, School of Medicine, Shahid Beheshti University of Medical Sciences, Tehran, Iran, [2]Department of Anatomy, School of Medicine, Shahid Beheshti University of Medical Sciences, Tehran, Iran, [3]Department of Medical Nanotechnology, School of Medicine, Shahroud University of Medical Sciences, Shahroud, Iran, [4]Department of Biology and Anatomical Sciences, School of Medicine, Shahid Beheshti University, Tehran, Iran, [5]Semnan University of Medical Sciences Dental Student Research Committee, Semnan, Iran, [6]School of Medicine, Tehran University of Medical Sciences, Tehran, Iran, [7]Deputy of Research and Technology, Ministry of Health and Medical Education, Tehran, Iran, [8]Regional Centre of Advanced Technologies and Materials, Czech Advanced Technology and Research Institute, Palacký University in Olomouc, Olomouc, Czech Republic, [9]Skull Base Research Center, Loghmna Hakim Hospital, Shahid Beheshti University of Medical Sciences, Tehran, Iran, [10]Institute of Human Genetics, Jena University Hospital, Jena, Germany

OPEN ACCESS

Edited by:
Mina Sarani, Zabol University of Medical Sciences, Iran

Reviewed by:
Rajendra Kumar Singh, Institute of Tissue Regeneration Engineering (ITREN), South Korea
Vijaya Kumar Shanmugam, Institute of Nano Science and Technology (INST), India

***Correspondence:**
Mohammad Taheri
mohammad.taheri@uni-jena.de

Specialty section:
This article was submitted to Nanobiotechnology, a section of the journal Frontiers in Bioengineering and Biotechnology

Received: *02 January 2022*
Accepted: *01 February 2022*
Published: *16 February 2022*

Citation:
Shariatzadeh S, Moghimi N, Khalafi F, Shafiee S, Mehrabi M, Ilkhani S, Tosan F, Nakhaei P, Alizadeh A, Varma RS and Taheri M (2022) Metallic Nanoparticles for the Modulation of Tumor Microenvironment; A New Horizon. Front. Bioeng. Biotechnol. 10:847433. doi: 10.3389/fbioe.2022.847433

Cancer is one of the most critical human challenges which endangers many people's lives every year with enormous direct and indirect costs worldwide. Unfortunately, despite many advanced treatments used in cancer clinics today, the treatments are deficiently encumbered with many side effects often encountered by clinicians while deploying general methods such as chemotherapy, radiotherapy, surgery, or a combination thereof. Due to their low clinical efficacy, numerous side effects, higher economic costs, and relatively poor acceptance by patients, researchers are striving to find better alternatives for treating this life-threatening complication. As a result, Metal nanoparticles (Metal NPs) have been developed for nearly 2 decades due to their important therapeutic properties. Nanoparticles are quite close in size to biological molecules and can easily penetrate into the cell, so one of the goals of nanotechnology is to mount molecules and drugs on nanoparticles and transfer them to the cell. These NPs are effective as multifunctional nanoplatforms for cancer treatment. They have an advantage over routine drugs in delivering anticancer drugs to a specific location. However, targeting cancer sites while performing anti-cancer treatment can be effective in improving the disease and reducing its complications. Among these, the usage of these nanoparticles (NPs) in photodynamic therapy and sonodynamic therapy are notable. Herein, this review is aimed at investigating the effect and appliances of Metal NPs in the modulation tumor microenvironment which bodes well for the utilization of vast and emerging nanomaterial resources.

Keywords: microenvironment, gold nanoparticles, silver nanoparticles, metallic nanoparticles, magnetic nanoparticles, cancer

INTRODUCTION

Cancer is a significant concern in modern societies worldwide. Abnormal cell growth and their transformation into different types of tumors in human organs cause this life-threatening complication (Zaorsky et al., 2017; Shahab et al., 2018; DeSantis et al., 2019). Several pathways and molecular defects are significant in the development and progression of cancer. The leading cause of tumor formation is due to one or a series of gene mutations. Moreover, tumor deterioration, benign or malignant tumor, and metastatic behavior depends on the mutation type and affected genes. The tumor stage is the single most determining parameter to select the therapeutic approaches (Paul and Lal, 2017; Mohd Yusof et al., 2018; Zhao et al., 2020).

Surgery, radiotherapy, chemotherapy, or combination therapy are employed as the therapeutic procedure for most of the cancer types (Temple et al., 2004; Giordano et al., 2005; Verbrugge et al., 2009). Today, blended methods are commonly used in combination with chemotherapeutic agents for most cancers treatment, largely trying to control angiogenic, signaling, DNA replication, and cell cycle process (Urruticoechea et al., 2010; Yuan et al., 2019). Despite mentioned advances, cancer therapy is still complicated and sometimes impossible in most cases, especially in the metastatic stages thus necessitating search for new treatments.

The use of NPs has garnered much attention lately as they can be very effective in medicine due to their unique properties, suitable and tunable features for drug delivery, and their effects on the treatment process. To optimize loading and delivery capacity, NP parameters like as shape, size, and surface chemistry have been carefully designed (Singh et al., 2019). One of the essential properties of NPs is the high surface-to-volume ratio, which elevates their surface energy that can be exploited in various medical applications, especially photodynamictherapy (PDT) (Singh et al., 2020). Daniel and Astrum (Daniel and Astruc, 2004) have summarized the history of the nanoparticles and mentioned the use of metal nanoparticles historically and reported the popularity due to uniform size and sharp size distribution. They have provided various fascinating properties leading to remove barriers in different field of nanotechnology specially in biomedical field because of their unique physiochemical properties (Sintov et al., 2016; Venkatesh et al., 2018). Metal nanoparticles which are traditionally are known with silver and gold, provides unique chrematistics such as SPR (surface plasmon resonance) more effectively that other types of nanoparticles. It has been confirmed that rational design of metal nanoparticles represented well biocompatibility and versatility (Patra et al., 2018). Meanwhile, metal nanoparticles can be engineered as theranostics particles to provide both therapy and imaging simultaneously (Sintov et al., 2016). Theranostics based on nanoparticles (NPs) is a promising paradigm in nanomedicine (Singh et al., 2017). The deployment of nanotechnology in the right situation can overcome many challenges in cancer treatment (Alvarez et al., 2017; Maddela et al., 2021). The proper position in cancer treatment is to identify the vulnerability of cancer cells and destroy them without damaging normal cells and tissues. The tumor microenvironment (TME) in many cancers is now considered a critical target for therapy and has been ascribed to as a crucial involved parameter for promoting tumor growth, proliferation, angiogenesis, invasiveness, and metastasis (Liu et al., 2018a).

Mesenchymal cells, extracellular matrix (ECM), cancer-associated fibroblasts (CAFs), and immune system cells are important components of TME in cancer fate and progression to metastasis (Anton and Glod, 2016; Nadhan et al., 2020a). In the early stages of TME formation, cells and proteins involved in cell death are disrupted through an interaction, and the process of cell proliferation and differentiation is affected (Phan, 2008; Yuan et al., 2016; Murphy and Weaver, 2017a; Farc and Cristea, 2021). Proteins involved in the process of reproduction and programmed death include growth factors and inflammatory factors of the immune system that are involved in tumor angiogenesis (Chang et al., 2002; Phan, 2008; Dumont et al., 2013; Yuan et al., 2016). Out-of-regulation function of immune system cells inhibits their function and reduces suppression of tumorigenesis (Samstein et al., 2012; Lei et al., 2020). By reducing the function of immune cells in addition to reducing the immunogenic function of lymphocytes, increasing inflammatory factors such as cytokines and chemokines cause more tumor metastasis (Talmadge and Gabrilovich, 2013; Wolf et al., 2015; Zhou et al., 2018a).

Due to the prominent effect of TME on the proliferation, migration and metastasis of cancer cells, targeting it can be effective in reducing tumor progression (Labani-Motlagh et al., 2020a; Liu et al., 2020). Due to the fact that the effect of MNPs on TME has been rarely studied, so their study can be effective in further understanding these nanoparticles. In the present study, we first identify TME and its characteristics. Then, nanoparticles and their effects on TME and treatments were investigated.

TUMOR MICROENVIRONMENT

Cancer tissue has a supportive environment in which various components can infiltrate as homeostasis, fighting, or helping elements. TME can involve many cancer processes such as tumor growth, proliferation, angiogenesis, invasiveness, and metastasis via interaction with cancer cells as a dynamic cellular environment. Mesenchymal cells and the extracellular matrix (ECM) as the components of the TME are responsible for secreting various factors which affect cancer fate. Cancer-associated fibroblasts (CAFs) are known to be the main cellular components of TME, which by secreting multiple factors including EGF (endothelial growth factor), VEGF (vascular endothelial growth factor), and HGF (hepatocyte growth factor), can metastasize cancer cells by disrupting and rupturing the ECM via the RTK signal pathway (Anton et al., 2017; Nadhan et al., 2020b). Different cell types are present in TME (**Figure 1**), Such interaction of cells leads to establishing a complex network that can promote or inhibit cancer reliant on tumor condition and cell interaction (Phan, 2008; Murphy and Weaver, 2017b; Farc and Cristea, 2021). Reprograming the surrounding cells, mostly fibroblasts, immune cells, and

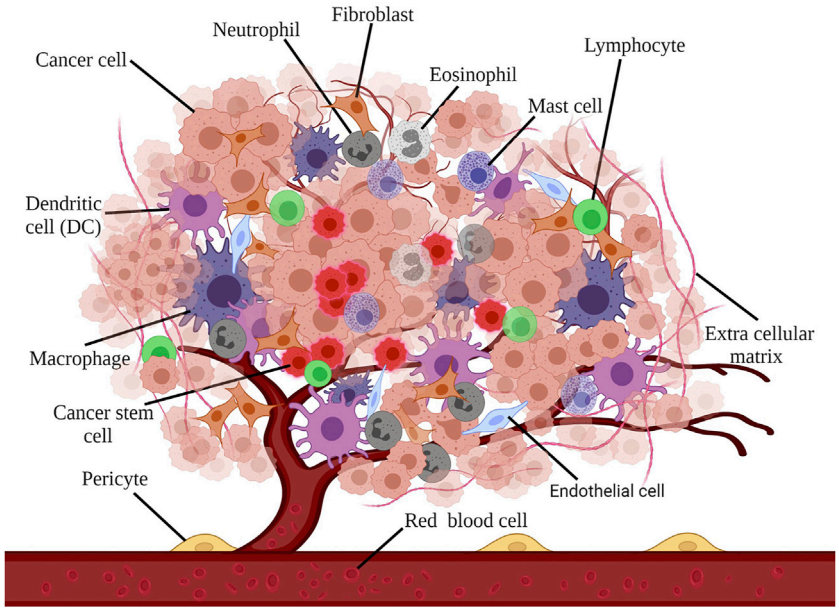

FIGURE 1 | Different cell types are present in TME: macrophages, fibroblasts, endothelial cells, neutrophils, eosinophils, mast cells, lymphocytes, dendritic cells, and dendritic cells, each representing a diverse impact on cancer tissue.

vascular cells by tumor cells, is the first step for TME formation (Yuan et al., 2016).

Fibroblasts constitute the main component of the tumor stroma which can be recognized through distinctive markers such as vimentin, smooth muscle actin-α (SMAα), fibroblast activation protein (FAP) (Chang et al., 2002; Phan, 2008). To create CAFs, tumor cells induce fibroblasts and blood vessels by different factors such as PDGF (platelet-derived growth factor) or FGF (fibroblast growth factor) and hypoxia through activating PDGF, IL1, stromal cell-derived factor (SDF), TGFβ, and reactive oxygen species (ROS). Thus, CAFs formed the overall shape of TME through ECM secretion and cytokines and growth factors activating such as TGFβ, HGF, SDF, and MMPs, and inducing angiogenesis by VEGF and PDGF (Dumont et al., 2013).

Immune-related cells are the other most dominant cells in TME. It has been reported that both tumor-antagonizing and tumor-promoting cells are present in TME. Macrophages, neutrophils, natural killer cells, T cells, and dendritic cells are the essential tumor-antagonizing cells of the immune system, while myeloid-derived suppressor cells (MDSCs) and regulatory T cells (Tregs) are among the most significant tumor-promoting immune cells (Lei et al., 2020). Foxp3 is the distinctive marker of Tregs, which is essential for their function (Samstein et al., 2012). Besides the suppressive role, Tregs represent a regulatory function on effector T cells which is significant in some severe conditions, including autoimmune disease that suppresses the over-reactive immune response. Therefore, cancer suppression by cytotoxic T cells possibly can be inhibited due to the presence of Tregs in TME (Wolf et al., 2015). On the other hand, MDSCs use a different mechanism for tumor promotion; they are seemingly induced in TME followed by cytokines and chemokines secretions. Thus, MDSCs exert their impact through cancer cell migration, promote metastasis and angiogenesis (Talmadge and Gabrilovich, 2013; Zhou et al., 2018b).

TME MODULATION

TME has a substantial effect on metastasis and cancer resistance, so that it is introduced as the primary barrier against the clinical use of immunotherapy. Furthermore, in view of its prominent effect in proliferation, migration, and metastasis, it can be considered an extraordinary target in the treatment of cancer (Liu et al., 2020; Labani-Motlagh et al., 2020b). Given the challenges and limitations of current therapies, TME modulation can be regarded as an alternative approach, which can significantly enhance the effectiveness of existing treatments. In addition, TME represents some unique features, including hypoxia, low pH, and immunosuppressive environment that can be recruited as the target for TME modulation (**Figure 2**) (Chen et al., 2015; Janoniene et al., 2017; Mpekris et al., 2017).

TME and Hypoxia

One of the essential elements for energy metabolism is oxygen. Hypoxia causes intratumorally oxygen gradients and increase the hypoxia-inducible factor 1α (HIF-1α), a key marker in hypoxia mechanisms and the central mediator of hypoxia-induced signaling. On the other hand, hypoxic TME leads to tumor development and drug resistance through uncharacteristic angiogenesis, desmoplasia, and inflammation (Mayer et al., 2008; Jain, 2014; Whatcott et al., 2015). HIF-1α has been reported to be overexpressed in various cancer types and has accounted for tumor survival through drug resistance (Sun et al., 2007; Mayer et al., 2008; Simiantonaki et al., 2008). The effect of

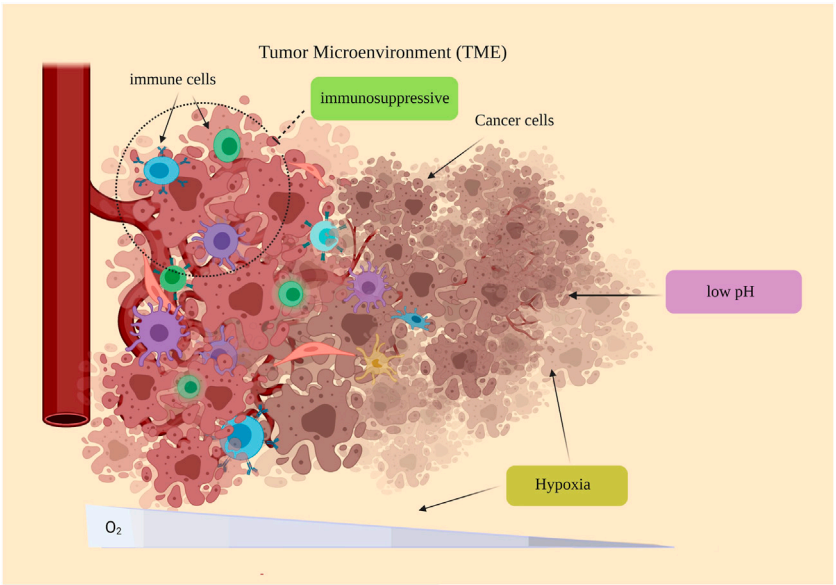

FIGURE 2 | Some special features of the TME: hypoxia, low pH, and immunosuppressive environment. The immunosuppressive environment of TME has been observed in many cancers. Because of rapid proliferation and the imbalance between oxygen supply and consumption, the TME oxygen level tends to be reduced, which is ascribed as hypoxic regions observed in most tumors. PH reduction is another feature of TME.

HIF has been proven in cancer stem cell (Emami Nejad et al., 2021). Besides, hypoxic TME is apparently involved in p53 and mitochondrial regulation and modulation in cancer cells (Jing et al., 2019).

TME, Low pH and Immunosuppressive Environment

Nevertheless, a low pH environment can be induced by hypoxia in TME, leading to multidrug resistance. Multiple mechanisms have been attributed to this cause, such as genetic alteration, ion trapping, or multidrug transporter p-glycoprotein (P-gp) overactivity. Due to the semi-permeable properties of the cellular membrane, unlike the charged particles, small uncharged molecules can diffuse into the cells (Zub et al., 2015). Considering the pH-depending property of several chemotherapeutic agents, intracellular pH alteration leads to low diffusion of chemotherapies into the cell membrane, resulting in drug resistance. On the other hand, as mentioned P-gp is an essential drug-resistant mechanism in low pH TME (Triner and Shah, 2016).

Considering mentioned properties, treatments based on targeting acidic conditions and hypoxia TME can be very effective. As an example, one approach could target hypoxia by inhibiting VEGEF or PI3K/AKT/HIF-1α pathway (Jing et al., 2019). In general, accurate targeting of one of the main features of TME and its disruption, including hypoxic conditions that subsequently cause high acidity of this structure, can be considered a critical therapeutic approach. However, one of the main problems in this area is the accurate delivery and targeting, which possibly can be overcome with nanotechnology.

EFFECT OF NPS ON TME MODULATION

TME modulation, as described in the previous section, can be exploited as one of the main treatments for various types of solid cancers. In this section, the effects of nanotechnology and NPs on TME modulation are highlighted.

NPs are generally referred to as particles with dimensions of about 1–100 nm and possess various attributes and different properties than their bulk sample. Such difference creates very distinctive properties that are generally ascribed to their high surface-to-volume ratio (Maddela et al., 2021). The antibacterial properties of silver NPs have long been recognized (Mozafari et al., 2021). However, in the last few decades, due to the availability of new technologies, it has become possible to make a wide range of NPs, from quantum dot nanoparticles to nanofibers.

The use of NPs for targeted drug delivery has been studied in many diseases, and excellent clinical results have been observed (Tietze et al., 2013; Mu et al., 2020). Due to the NPs's size and high surface-to-volume ratio, it is possible to load the drug in different parts of NPs, including the surface of the NPs, inside the capsule-like structures and connecting to internal components such as those seen in dendrimers. Therefore, they can provide effective TME modulation (Dadwal et al., 2018; Hu et al., 2019). One of the critical drug accumulators in cancer is the enhanced permeability and retention (EPR) effect. It has been well understood that NPs (20–200 nm) can effectively get accumulated in cancer cells due to their adoptable size to the vascular endothelial pores and permeability (Huai et al., 2019).

Despite the unique opportunities that EPR plays in NPs accumulation in cancer cells, studies have shown that due to the high heterogeneity of cancer cells and the abnormality of

vasculature in cancer tissue, NPs did not reach the cancer tissue more effectively. Therefore, researchers have resorted to active-targeted drug delivery approaches because the EPR effect in drug delivery systems is considered passive. In this regard, NPs are designed to target specific cancer markers. Due to the extremely high cancer antigenicity, one of the factors that are mainly considered in the active targeting of cancer cells is the VEGF receptor. Consequently, the design of NPs based on this factor and the simultaneous use of the EPR effect can increase the drug accumulation in TME to an adequate level. Among other cancer-targeting agents, anginex and RGD peptides can be mentioned for targeting galectin-1 and integrin αvβ3, respectively (Byrne et al., 2008; Zhu et al., 2017; Liu et al., 2018b; Fu et al., 2019).

Moreover, metal NPs can be considered as a therapeutic agent in addition to being drug delivery entities. In this regard, plasmon resonance and photoluminescence properties of metal NPs can be mentioned (Hu et al., 2019). Furthermore, NPs have been used in various studies for TME modulation as follows: for modulation of the acidic TME, modulation of tumor ECM structure, immunosuppressive TME modulation, and also for the reduction of tumor hypoxia by oxygen delivery, oxygenation, and alleviate oxygen consumption (Liu et al., 2018a).

METAL NANOPARTICLES FOR TME MODULATION

One of the most attractive NPs in the field of biomedicine and especially drug delivery are metal NPs. These NPs, which are generally between 1 and 100 nm in size, have extraordinary properties that distinguish them from other NPs. These unique properties include magnetic, optical, and catalytic properties. Metal NPs have various capabilities depending on the type, material, shape, composition, and size. With the precise engineering of these NPs, one can expect to receive multiple responses under the same conditions. Also, with the accurate design of Metal NPs in terms of composition and size, the bioavailability, biological activity, and toxicity, as one of the central Metal NPs limitations, can be controlled (Sharma et al., 2018).

Due to the unique properties, Metal NPs are widely studied in cancer therapy through various approaches, including drug delivery, PDT, and antioxidants. However, one of the essential properties of Metal NPs, especially gold, silver, and copper nanoparticles, is the presence of surface plasmon resonance (SPR); SPR refers to the oscillation resonance of surface electrons in particles that are excited by light. Because nanoparticles have a larger surface-to-volume ratio compared to their bulk particles, SPR will be much more pronounced in them. Therefore, the SPR property has been widely used in photodynamic therapy through nanoparticles. Specifically, individual nanoparticles can be designed to be responsive to near-infrared absorbance to acquire photothermal agents to treat the tumor (Bhattacharyya et al., 2011). Furthermore, gold-based nanostructures, rhodium, and CuS nanoparticles have been proposed to provide photothermal responses, which can be recruited as biosensors despite the therapy approach. Considering all these properties and simultaneous use as a drug delivery system, Metal NPs appear to be an ideal option for TME modulation (**Figure 3**).

Metal NP -based sensors can lead to significant signal amplification, higher sensitivity, and great improvements in the detection and quantification of biomolecules and different ions. Nanoparticles with antioxidant properties increase cell damage by increasing cellular ROS (Sharma et al., 2018; Fu et al., 2019). ROS are group of materials including H_2O_2 and hydroxyl radicals (·OH) generated in eukaryotic cells. Despite previous thought that considered ROS as the byproduct of cells, it has been confirmed that ROSs are involved in several signaling pathways. ROS are produced in mitochondria through reduction of oxygen molecules form superoxide anions, peroxisomes and the endoplasmic reticulum. ROS are essential for multiple cellular functions at the normal level, such as gene expression (Chakraborty et al., 2021; Grebinyk et al., 2021). However, excess ROS production have been documented in various tumor cells due to increased metabolic rate, gene mutation and relative hypoxia (Wilson et al., 2018). The overload ROS can damage the normal cell causing various pathological conditions (Xiao et al., 2012a; Shanmugam et al., 2014a). Hence, the ROS modulation can be an appropriate approach regarding cancer treatment. cerium dioxide nanoparticles (CeNPs) is an almost new emerging nanoparticle regarding cancer treatment via ROS modulation (Shanmugam et al., 2014b). CeNPs have presented a powerful redox property through witching the oxidation state of Ce3+ and Ce4+ (Wang et al., 2009; Tsai et al., 2013). According to previous studies CeNPs can modulate ROS state through catalase- and superoxide dismutase (SOD)-like activity (Choi et al., 2007; Xiong et al., 2020). Filippi et al. have reported that CeNPs exert high ·OH scavenging activity in both phosphate buffered saline and surrogate lung fluid (Shanmugam et al., 2014b). In drug delivery, they cause programmed death by entering cancer cells (Bhattacharyya et al., 2011).

Metal NPs for Modulation TME Hypoxia

Hypoxia, low oxygen, and oxygen overconsumption is a significant feature of TME. Therefore, modulation of TME hypoxia appears to be a practical approach for tumor treatment. One system to modulate TME is related to oxygenation which is most often used during photodynamic therapy. Oxygen molecules can produce highly stable peroxides that bind to the broken ends of DNA, which dramatically enhances photodynamic therapy. It can be acknowledged that the oxygen molecule has a dual behavior in the treatment of cancer.

On the one hand, by increasing the amount of oxygen in the TME, ionizing radiation produces free radicals that can destroy DNA beyond repair. On the other hand, with the lack of oxygen, the effect of ionizing radiation on photodynamic therapy on the breakdown of DNA dual strands seems to be seriously reduced (Yoshimura et al., 2013). In this context, Metal NPs can function well as photosynthesizers and significantly increase the effect of radiation on TME modulation.

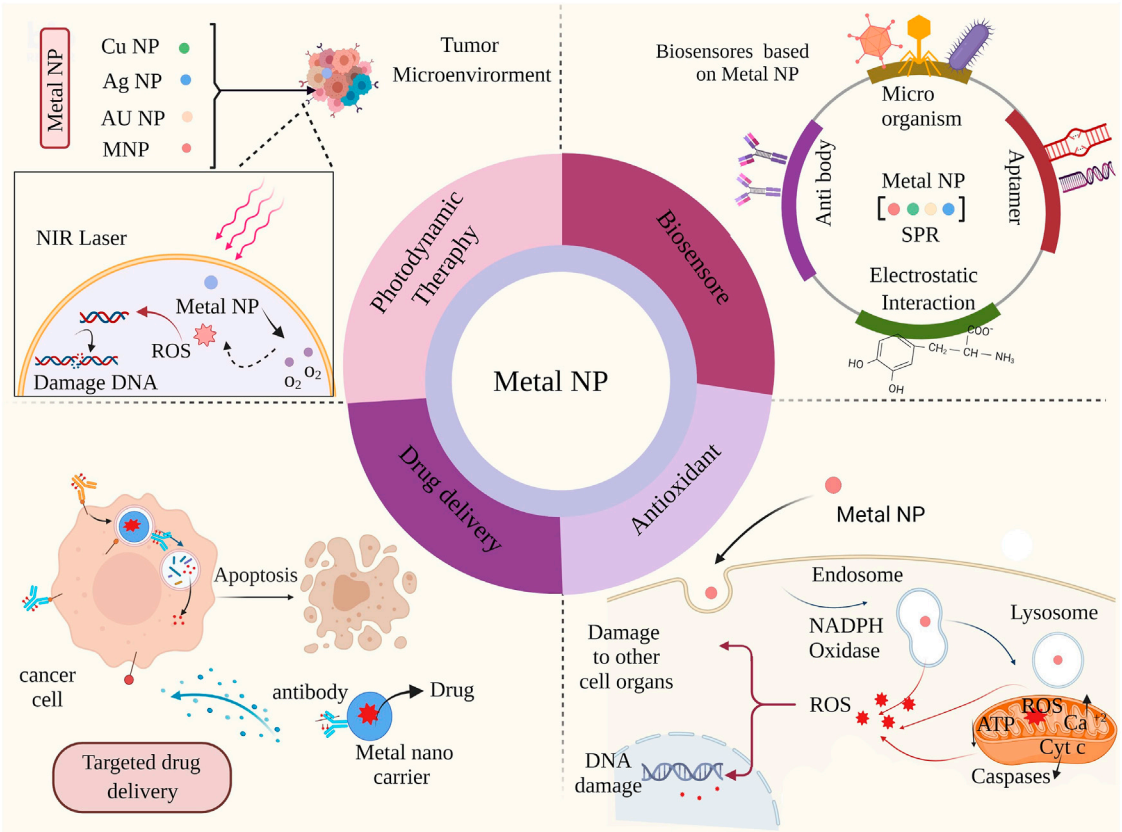

FIGURE 3 | Miscellaneous biomedical applications of metal nanoparticles: Metal nanoparticles cause further damage to cancer cells and cell death through photodynamic treatment with TME irradiation. Metal nanoparticles can also be used as biosensors.

One of the most exciting nanoparticles in photodynamic therapy as photosynthesizers due to their catalytic properties, is gold nanoparticles. The effect of gold nanoparticles is due to their high energy transfer in the excited state to molecules such as oxygen. In this regard, it causes highly toxic ROS species that modulate TME and eventually kill the cancer cell mass. Due to this mechanism, the presence of molecules such as O_2 can significantly increase the ability of nanoparticles to produce ROS, including $^1O_2$; it also prevents the PDT from being endangered due to the hypoxic state of TME (Dhakshinamoorthy et al., 2020; Yang et al., 2021).

Liang et al. have used gold nanocages@manganese dioxide to impede tumor metastasis through PDT and oxygenation. First, they fabricated core-shell anocage@manganese dioxide (AuNC@MnO_2, AM) nanoparticles using the template method. Next, a laser instrument has been recruited to induce PDT of this nanoparticle. The mechanism underlying oxygen generation was due to the degradation MnO_2 part in the low pH microenvironment of cancer, which leads to a large amount of production of O_2, which finally significantly enhanced the PDT effect on breast cancer cell line (Liang et al., 2018). In another study, wang et al. have reported the benefit of a rhodium-gold metals-based porous core-shell nanoparticle-elevated oxygenation to promote PDT for cancer therapy (Wang et al., 2020a).

As mentioned earlier, TME hypoxia itself is a barrier to successful PDT. However, developing hypoxia in TME using other systems is a treatment procedure. For example, sonosensitizers is a substance that reacts with ultrasound waves to produce ROS in cancer cells (Liang et al., 2018; Wang et al., 2020b). However, one of the problems with organic sonosensitizers is their stability and low solubility in aqueous media. For this reason, much attention has recently been paid to develop inorganic sonosensitizers, comprising Metal NPs (**Figure 4**).

Titanium dioxide nanoparticles, for example, can serve as a sonosensitizer on their own (Pan et al., 2018; Yang et al., 2020a). Zhong et al. developed a type of sonosensitizer using copper metal where copper divalent ions cause GSH depletion through the redox reaction, which ultimately increases the hypoxia of cancer cells. This group used the Pt and Cu elements to fabricate $PtCu_3$ $PtCu_3$ nanocage sonosensitizer via solvothermal method. Furthermore, they pegylated the nanocage that induced peroxidase activity wherein pegylated PtCu3 nanocages could act as glutathione peroxidase, accelerating the process of GSH depletion in the presence of oxidase molecules. Additionally, their anticancer effect was examined both, *in vitro* and *in vitro* in

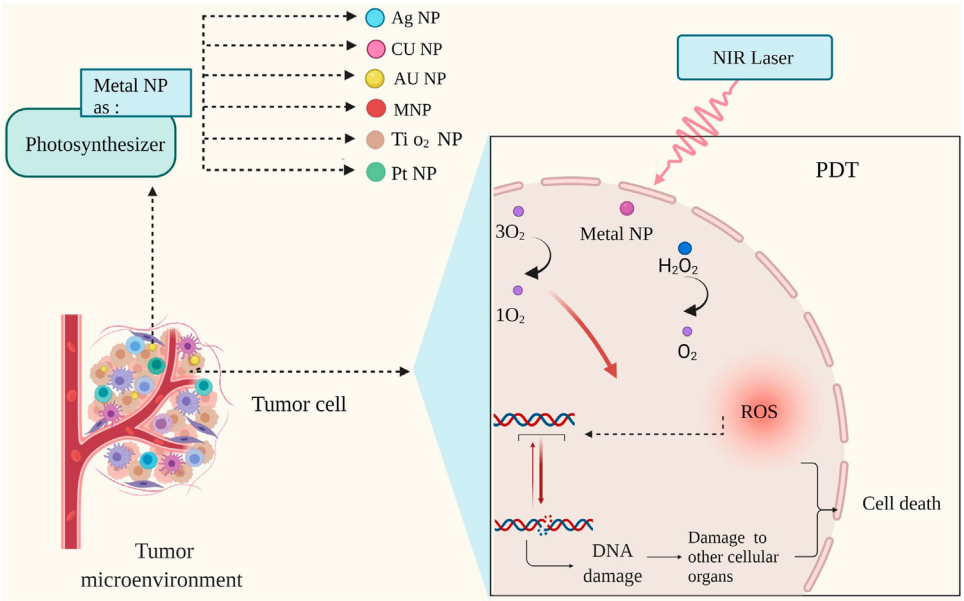

FIGURE 4 | Mechanism of photodynamic therapy (PDT) with metal nanoparticles. During photodynamic therapy, nanoparticles increase oxygen production; This increase in cell oxygen production is associated with damage to nucleic acid, and the cascade created by the nanoparticles leads tumor cells to planned death (Liang et al., 2018; Yang et al., 2020b).

cancer mice models. The results showed that these metal nanosonosensitizer with ultrasound had the excellent effect on killing cancer cells (Zhong et al., 2020).

Metal Nanoparticles for TME Modulation Using Low pH

Another exciting feature of TME is its high pH compared to normal cells due to the increased metabolism of cancer cells. This feature has been used in many cancer treatment approaches (Barar and Omidi, 2013; Justus et al., 2013). Zhang et al. have proposed a pH-responsive loaded-doxorubicin (DOX) metal-organic framework (MOF, ZIF-8) gold nanocluster (AuNCs@MOF-DOX) for modulation of the breast cancer TME as a PDT/chemotherapy combination therapy; both, the AuNCs and DOX are released through ZIF-8 collapse due to the low pH condition in TME. Next, AuNCs and DOX serve as the PDT and chemotherapy agents, representing significant cancer cell killing compared to a single action (Zhang et al., 2020).

One effective nanoparticle subdivision for TME modulation is attributed to the ferromagnetic nanoparticles (γ-Fe_2O_3 or Fe_3O_4 NPs). In normal cells, they transform the toxic H_2O_2 into H_2O and O_2, while in the low pH condition of TME, ferromagnetic can catalytically produce highly toxic ROS such as hydroxyl radicals (·OH) from H_2O_2 (Huai et al., 2019). In addition, Fu et al. have investigated the effect of the different structures of Fe_3O_4 on cancer therapy. The intrinsic peroxidase-like activity of Fe_3O_4 has been well established as various designs, including nanoclusters, nanoflowers, and nanodiamonds, were used to analyze the peroxidase activity of Fe_3O_4 in the low pH of the cancer microenvironment. According to their *in vitro* evaluation, the nanoclusters form had the most critical effect on the peroxidase-like activity of Fe_3O_4 NPs. They also reported that the cancer cell death followed by Fe_3O_4 could be attributed to the ROS generation just after the endocytose and concluded that cancer cell-killing performance of Fe_3O_4 NPs is a function of cell endocytosis and enzyme-like activity (Fu et al., 2017).

Metal NPs for Modulation TME ECM

Like any other tissue in the human body, the tumor has its own ECM, which serves as a supportive structure for tumor growth, migration, and metastasis. Collagens, elastin, fibronectins, laminins, glycoproteins, and proteoglycan are the common tumor ECM components. Therefore, ECM alteration is of great importance for TME modulation. The ECM modulation of tumors can be performed in various ways, including ECM disruption that mimics the tumor ECM to obstruct tumor progression, and intrusion in native ECM construction. Multiple methods are used for ECM elimination, including physical processes such as photothermal, hyperthermia, ultrasound, biochemical enzymes, and chemical agents (Chen et al., 2018). For example, Kolosnjaj-Tabi et al. have proposed a silica-coated iron oxide nanochain as an efficient, super magnetic NPs for ECM degradation of cancer tissue through PDT. The effect of fabricated metal-based nanochain was evaluated in the cancer model through near-infrared irradiation. According to the *in vitro* investigation, the cancer cells were eliminated, wherein the potency of this nanochain to melt the collagen matrix has been proposed (Kolosnjaj-Tabi et al., 2019).

Nevertheless, ECM degradation is an essential step in the metastasis process, where cancer cells need more space to be overproliferated, and ECM represents a substantial obstacle.

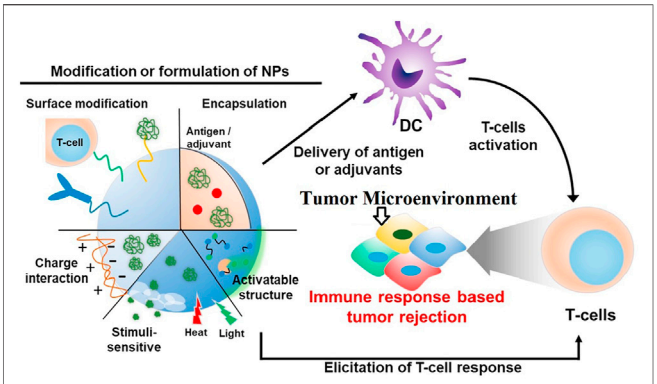

FIGURE 5 | tumor antigen-specific T-lymphocytes for cancer immunotherapy. During cancer immunotherapy, after preparation and presentation of antigen by different molecular methods on dendritic cells, T cells are activated. Immune cells are one of the most important components. Activation of T cells is associated with the development of a specific immune response and destroys the tumor (Yoon et al., 2018).

Consequently, maintaining the tumor ECM or rebuilding it appears to be a logical procedure to overcome tumor cells in such a situation. Hu et al. proposed a transformable formulation as an artificial ECM for preventing the tumor metastasis. The primary mechanism of their proposed procedure depended on the NPs transformation into nanofibers. An RGD ligand-integrin receptor performed this transformation structure. The RGD binding process to integrins is significantly dependent on the RGD interactions metal ions such as Ca^{2+}, Mg^{2+} at "metal ion-dependent adhesion site" (MIDAS) (Hu et al., 2017).

STRATEGIES FOR METAL NPS TO MODULATE IMMUNE RESPONSES

Instead of killing cancer cells directly, Metal NPs mainly modulate immune organs or immune cells to eradicate cancer cells. By injecting into the tumor medium, Metal NPs activate APCs to improve antigen delivery and T cell immune responses. They also increase antitumor efficacy by stimulating the immune system *in situ* and regulating T cell viability. Cytokines engineered into NPs can be transported to TME to increase antitumor activity (Liu et al., 2014).

Lymph node dendritic cells (DCs) are vital cells for processing and delivering antigens. The results showed that by attaching the nanoparticles to these cells, the nanoparticles could be directed to the specified TME. Because these immune cells are constantly delivering antigens to the tumor environment, transfecting them into tumor tissue can increase T lymphocytes and lead to more cancer cell death (Liu et al., 2014; Wilson et al., 2019).

The findings show that the binding of metal nanoparticles to immune cells can increase the effectiveness of cancer treatment and be used as anti-cancer vaccines in the future. Cancer vaccines use immune system mechanisms to identify tumor cells. In this way, cancer cells are detected by the immune system after antigenic changes and the progression of cancerous tissue is prevented (Li et al., 2018). However, after preparation and presentation of antigen by DCs, activation and proliferation of T cells is very important for cancer immunotherapy (Xin Yu et al., 2019; Li and Burgess, 2020; Zhu et al., 2020) (**Figure 5**).

The results show that different nanomaterials can be used as immune stimulants to activate T cells in TME (Stephan et al., 2010; Park et al., 2012; Schmid et al., 2017). Poly (lactic-co-glycolic acid) (PLGA) is a nanomaterial that binds to drug nanoparticles and targets T cells in TME to activate these cells and eradicate tumor cells. In most cases, nanomaterials are attached to nanoparticles by encapsulation (Zheng et al., 2013; Tang et al., 2018; Wang et al., 2018).

Various molecular mechanisms have been proposed to increase the effectiveness of this method, and in short, all of these strategies are based on increasing the death of tumor cells by the immune system. In fact, by this mechanism, it detects and destroys the specific immunity of cancer cells, thus reducing the inflammatory response in TME (Francis and Thomas, 2017; Meir et al., 2017; Smith et al., 2017).

METALLIC NANOPARTICLES AND CLINICAL EFFECTS OF CANCER

Various studies have shown the role of different nanoparticles on cancer inhibition (**Table 1**). In one study, the anti-cancer effect of an organic metal nanoparticle was investigated. These findings showed the stability of nanoparticles and its effect on reducing tumor growth was significant. This was the first report to use MOF-derived nanoparticles in targeted nuclear PDT (Zeng et al., 2020). In another study, MOF-derived nanoparticles were used to alter cellular redox homeostasis. The findings show the high potency of these nanoparticles in improving the anti-cancer performance of PDT and suggest a new way to increase the therapeutic power based on ROS (Cheng et al., 2019).

Other studies have shown the effect of PLGA encapsulation in docorbiocin on immune stimulation (Wohlfart et al., 2011; Malinovskaya et al., 2017). The findings of this study confirm the innovation in immunotherapy methods with the help of metal nanoparticles and suggest different methods to increase the efficiency and cost-effectiveness of treatment (Abu-Serie and Eltarahony, 2021; Grebinyk et al., 2021). Findings on the effect of CSNP nanoparticles on inhibiting the growth of uterine cancer cells showed the effectiveness of this nanoparticle. The researchers stated that future research could examine the CSNP-modulating immune mechanism as potential treatment strategies aimed at escaping immunity as an important feature of cancer (Chakraborty et al., 2021). Another study showed that PBAE nanoparticles in the nanoparticle-mediated cytosolic delivery method for STING agonists synergize with cell cycle inhibitors, and this synergy has a strong potential to enhance cancer immunotherapy (Wilson et al., 2018).

TABLE 1 | Metallic nanoparticles for the modulation of tumor microenvironment.

Result	Sample	Type of nanoparticle	Type of study	Running title	Author/Year
Au nanorods (NRs), Au nanoshells, other Au-related nanomaterials, graphene oxide, upconversion nanoparticles, and other related materials [including materials such as CuS, Fe_3O_4-related systems, and carbon nanotubes (CNTs)] proposed as good NIR nanomaterials	Cell lines	Near-infrared light-responsive (NIR) nanomaterials	review	Near-infrared light-responsive nanomaterials in cancer therapeutics	Shanmugam et al. (2014a)
The *in vitro* and *in vivo* results demonstrate that this platform selectively delivers anti-cancer drugs to target cells, releases them upon NIR irradiation, and effectively inhibits tumor growth through thermo-chemothera	Tumor growth in a mouse model	near-infrared (NIR): complementary DNA strands, the gold NR (50 nm × 10 nm), and a polyethylene glycol (PEG) layer	Animal	DNA Self-Assembly of Targeted Near-Infrared-Responsive Gold Nanoparticles for Cancer Thermo-Chemotherapy†	Xiao et al. (2012b)
This targeting vehicle provided remote-controlled delivery of this high toxic cargo cocktail at the tumor site, ensuring extra specificity that can avoid acute toxicity, where release of Dox and Pt (IV) was achieved upon NIR 808 nm diode laser irradiation	Tumor growth in a mouse model	Au nanorods (NRs)	Animal	Oligonucleotides—Assembled Au Nanorod-Assisted Cancer Photothermal Ablation and Combination Chemotherapy with Targeted Dual-Drug Delivery of Doxorubicin and Cisplatin Prodrug	Shanmugam et al. (2014b)
Rod-in-shell structure was a promising hyperthermia agent for the *in vivo* photothermal ablation of solid tumors when activated using a continuous-wave 808 m (first NIR window) or a 1,064 nm (second NIR window) diode laser	Tumor growth in a mouse model	Au nanorod (NR)	Animal	Au Nanorod Design as Light-Absorber in the First and Second Biological Near-Infrared Windows for *in Vivo* Photothermal Therapy	Tsai et al. (2013)
Multifunctional nanoparticle composed of a single, amine-modified gold nanorod, decorated with multiple "pearls" of Fe3O4 nanoparticles capped with carboxy groups showed simultaneous targeting, dual-mode imaging, and photothermal ablation of breast cancer cells is demonstrated	Breast cancer cells	Gold Nanorod/Fe3O4 Nanoparticle	*In vitro*		Wang et al. (2009)
The multifunctional APS/AuNR/PLGA-PEG nanoparticles can serve as an excellent synergistic agent for Focused ultrasound (FUS) therapy, facilitating real-time imaging, promoting thermal ablation effects, and boosting FUS-induced immune effects	Tumor growth in a mouse model	EGylated PLGA nanoparticles encapsulating astragalus polysaccharides (APS) and gold nanorods (AuNRs)	*In vitro* and *in vivo*	Multifunctional Nanoparticles Encapsulating Astragalus Polysaccharide and Gold Nanorods in Combination with Focused Ultrasound for the Treatment of Breast Cancer	Xiong et al. (2020)
The efficient phagocytosis of Au nanoshells by both monocytes and macrophages, photoinduced ablation of Au-nanoshellladen monocytes/macrophage, tumor recruitment, and photoinduced cell death of macrophages in the hypoxic microenvironment of a human breast tumor spheroid have all been successfully demonstrated	Human breast tumor spheroids	Au nanoshells	*In vitro*	A Cellular Trojan Horse for Delivery of Therapeutic Nanoparticles into Tumors	Choi et al. (2007)

(Continued on following page)

TABLE 1 | (*Continued*) Metallic nanoparticles for the modulation of tumor microenvironment.

Result	Sample	Type of nanoparticle	Type of study	Running title	Author/Year
Cancer cells targeted with the MagGNS AbHER2/neu *in vitro* were detectable by a commercial clinical MRI system, and were rapidly destroyed upon short exposure to femtosecond laser pulses with an NIR wave-length and a low power	SKBR3 cells	Magnetic gold nanoshells (Mag-GNS)	*In vitro*	Designed Fabrication of Multifunctional Magnetic Gold Nanoshells and Their Application to Magnetic Resonance Imaging and Photothermal Therapy	Kim et al. (2006)
HeLa cells incubated with GNS-MCs *in vitro* can be killed photothermally by exposure to NIR light	HeLa cells	Novel multifunctional theranostic agent based on gold-nanoshelled microcapsules (GNS-MCs)	*In vitro*	Gold-Nanoshelled Microcapsules: A Theranostic Agent for Ultrasound Contrast Imaging and Photothermal Therapy	Ke et al. (2011)
The Aptamer AS1411 show excellent stability. Significantly, the Mn3O4-PEG @ C & A inhibited tumor growth in a high-performance mouse model without any biotoxicity	Tumor growth in a mouse model	A new nanoenzyme (Mn3O4-PEG @ C & A) with the inherent activity of catalase	Animal Clinical	nanoenzyme for enhancing nucleus-targeted photodynamic therapy	Zeng et al. (2020)
Inside tumor cells can effectively block the Rx removal pathway mediated PDT and TrxR inhibition causes a profound increase in cellular ROS levels	Liver tumor cells	A porous metal-organic (MOF) framework as a photodynamic therapy agent (PDT) and a transporter for the alkaloid transporter piperlongumin (PL)	Animal Clinical	Nanotherapeutics interfere for highly photodynamic therapy	Cheng et al. (2019)
Within 1 h, doxorubicin could reach its destination, DNA, in the nucleus without degradation, while PLGA nanoparticles, were still in the chamber and lysosomes were observed	Brain tumor cells	doxorubicin-loaded PLGA nanoparticles	Human clinical	Delivery of nanoparticles into glioblastoma cells	Malinovskaya et al. (2017)
Significant antitumor effect of doxorubicin nanoparticles was observed. PLGA-coated poloxamer nanoparticles with doxorubicin transport through are effective in the treatment of glioblastoma	Tumor cells in mice	Poly (lactic-co-glycolic acid) (PLGA) nanoparticles	Animal clinical	Efficient Chemotherapy Using Nanoparticles with Different Stabilizers	Wohlfart et al. (2011)
This nanoparticle is able to improve the therapeutic index. The strong anti-cancer activity of this nanomedicine is promising. The strong anti-cancer activity of this nanomedicine is promising	lung cancer cell line, liver cancer cell line and Breast cancer cell line	Copper oxide nanoparticles (CuO NPs)	Human clinical	copper oxide nanoparticles for augmenting anticancer activity	Abu-Serie and Eltarahony (2021)
Combining the natural alkaloid Ber with C60 could be a new treatment strategy for lung cancer	LLC cells in mice	Berberine (Ber) combined with C60	Human clinical	Antitumor efficiency of the alkaloid complexed with C60 fullerene in Lewis lung carcinoma	Grebinyk et al. (2021)
Unlike Nanoparticles, showed an inhibitory effect on the expression of genes encoding the NLRP3 inflammatory complex, but also reduced activation of the NLRP3 inflammatory complex. The combination of gallic acid with CSNP suppressed the immune system in cervical cancer	Cervical cancer cell lines	Nanoparticles (CSNP) and gallic acid conjugated gallic acid (gCSNP)		Nanoparticles modulates NLRP3 inflammasome complex activation in cervical cancer	Chakraborty et al. (2021)
Gold nanorods have been specifically mentioned as a new agent for simultaneous bioimaging and cancer treatment	Tumor cell lines in breast cancer	Gold Nanorods (GNRs)	review	Synthesis of gold nanorods and photothermal therapy	Khan et al. (2021)

(Continued on following page)

TABLE 1 | (*Continued*) Metallic nanoparticles for the modulation of tumor microenvironment.

Result	Sample	Type of nanoparticle	Type of study	Running title	Author/Year
Strong immune responses at extracellular CDN concentrations are less than 100-fold *in vitro*. The formulation of CDBA PBAE nanoparticles improves potency in the treatment of melanoma	Melanoma tumors B16	Polybeta amino ester (PBAE) nanoparticles to deliver CDN to the cytosol	Clinical	nanoparticles for enhanced cancer immunotherapy	Wilson et al. (2018)

CONCLUSION

The distinctive features of TME provide the opportunity to exploit its use as a new approach to cancer treatment. The high metabolism of cancer cells and the excessive craving for proliferation prevents the development of new vascular tissues and vessels, and this in itself can be used in the successful delivery of therapeutic agents to these cells, which today are known as the EPR effect. Furthermore, due to the high metabolism of these cells, the tumor environment has high hypoxia conditions which can be utilized extensively in sonodynamic therapy. The use of metal nanoparticles as sonosensitizers addresses the problem of natural sonosensitizers, which have low solubility and viscosity, and as a result, ensuing ROS can destroy tumor tissue. Besides, the fantastic optical properties of metal nanoparticles, including gold nanoparticles, have received much attention in photodynamic therapy. By producing oxygen in cancerous tissues and using suitable radiation, photosynthesizers such as metal nanoparticles can create highly toxic ROS. The effect of acidic environment on TME has been discussed, and it was shown that systems designed with metal nanoparticles could use this low pH condition to release their drug and provide a high-impact combination therapy. At low pH, ferromagnetic nanoparticles kill cancer tissue by converting H_2O_2 to toxic singlet O_2 species. Overall, we see special consideration to metal nanoparticles. Given the tremendous potential metal nanoparticles have resemblance in TME modulation, there looks to be a promising future for cancer therapy. The most critical challenges to be considered in future research are targeting and toxicity, which should be carefully considered. In addition to the above, it is important to consider new therapeutic strategies for the use of metal nanoparticles in immunotherapy. Because despite the progress, many efforts are still needed to apply cancer treatment with minimal side effects. Barriers to biological research must be removed. Then, the necessary conditions for clinical research will be provided so that in the future, like conventional treatments, nanoparticles can be taken as an effective step to reduce the problems of cancer patients.

AUTHOR CONTRIBUTIONS

All authors contributed to the conception and the main idea of the work. SiS, NM, AA, RV, MM, FK, SeS, SI, FT, and PN drafted the main text, figures, and tables. MT supervised the work and provided the comments and additional scientific information. MT and SiS also reviewed and revised the text. All authors read and approved the final version of the work to be published.

REFERENCES

Abu-Serie, M. M., and Eltarahony, M. (2021). Novel Nanoformulation of Disulfiram with Bacterially Synthesized Copper Oxide Nanoparticles for Augmenting Anticancer Activity: an *In Vitro* Study. *Cancer Nanotechnology* 12 (1), 1–17. doi:10.1186/s12645-021-00097-5

Alvarez, M. M., Aizenberg, J., Analoui, M., Andrews, A. M., Bisker, G., Boyden, E. S., et al. (2017). Emerging Trends in Micro- and Nanoscale Technologies in Medicine: From Basic Discoveries to Translation. *ACS nano* 11 (6), 5195–5214. doi:10.1021/acsnano.7b01493

Anton, K., and Glod, J. (2016). Tumor-Secreted Factors that Induce Mesenchymal Stromal Cell Chemotaxis. *Mesenchymal Stromal Cells as Tumor Stromal Modulators*, 193–214. doi:10.20892/j.issn.2095-3941.2016.0033

Anton, K., and Glod, J. (2017). "Tumor-Secreted Factors that Induce Mesenchymal Stromal Cell Chemotaxis," in *Mesenchymal Stromal Cells as Tumor Stromal Modulators*. Editors M. F. Bolontrade and M. G. García (Boston: Academic Press), 193–214. doi:10.1016/b978-0-12-803102-5.00008-2

Barar, J., and Omidi, Y. (2013). Dysregulated pH in Tumor Microenvironment Checkmates Cancer Therapy. *Bioimpacts* 3 (4), 149–162. doi:10.5681/bi.2013.036

Bhattacharyya, S., Kudgus, R. A., Bhattacharya, R., and Mukherjee, P. (2011). Inorganic Nanoparticles in Cancer Therapy. *Pharm. Res.* 28 (2), 237–259. doi:10.1007/s11095-010-0318-0

Byrne, J. D., Betancourt, T., and Brannon-Peppas, L. (2008). Active Targeting Schemes for Nanoparticle Systems in Cancer Therapeutics. *Adv. Drug Deliv. Rev.* 60 (15), 1615–1626. doi:10.1016/j.addr.2008.08.005

Chakraborty, R., Bose, U., Pawaskar, G., Bola Sadashiva, S. R., and Raval, R. (2021). Nanoparticles Derived from Insect Exoskeleton Modulates NLRP3 Inflammasome Complex Activation in Cervical Cancer Cell Line Model. *Cancer Nanotechnology* 12 (1), 1–12. doi:10.1186/s12645-021-00090-y

Chang, H. Y., Chi, J.-T., Dudoit, S., Bondre, C., van de Rijn, M., Botstein, D., et al. (2002). Diversity, Topographic Differentiation, and Positional Memory in Human Fibroblasts. *Proc. Natl. Acad. Sci.* 99 (20), 12877–12882. doi:10.1073/pnas.162488599

Chen, H., Tian, J., He, W., and Guo, Z. (2015). H2O2-activatable and O2-Evolving Nanoparticles for Highly Efficient and Selective Photodynamic Therapy against Hypoxic Tumor Cells. *J. Am. Chem. Soc.* 137 (4), 1539–1547. doi:10.1021/ja511420n

Chen, Q., Liu, G., Liu, S., Su, H., Wang, Y., Li, J., et al. (2018). Remodeling the Tumor Microenvironment with Emerging Nanotherapeutics. *Trends Pharmacological Sciences* 39 (1), 59–74. doi:10.1016/j.tips.2017.10.009

Cheng, Q., Yu, W., Ye, J., Liu, M., Liu, W., Zhang, C., et al. (2019). Nanotherapeutics Interfere with Cellular Redox Homeostasis for Highly Improved Photodynamic Therapy. *Biomaterials* 224, 119500. doi:10.1016/j.biomaterials.2019.119500

Choi, M.-R., Stanton-Maxey, K. J., Stanley, J. K., Levin, C. S., Bardhan, R., Akin, D., et al. (2007). A Cellular Trojan Horse for Delivery of Therapeutic Nanoparticles into Tumors. *Nano Lett.* 7 (12), 3759–3765. doi:10.1021/nl072209h

Dadwal, A., Baldi, A., and Kumar Narang, R. (2018). Nanoparticles as Carriers for Drug Delivery in Cancer. *Artif. Cell nanomedicine, Biotechnol.* 46 (Suppl. 2), 295–305. doi:10.1080/21691401.2018.1457039

Daniel, M.-C., and Astruc, D. (2004). Gold Nanoparticles: Assembly, Supramolecular Chemistry, Quantum-Size-Related Properties, and Applications toward Biology, Catalysis, and Nanotechnology. *Chem. Rev.* 104 (1), 293–346. doi:10.1021/cr030698+

DeSantis, C. E., Miller, K. D., Dale, W., Mohile, S. G., Cohen, H. J., Leach, C. R., et al. (2019). Cancer Statistics for Adults Aged 85 Years and Older, 2019. *CA A. Cancer J. Clin.* 69 (6), 452–467. doi:10.3322/caac.21577

Dhakshinamoorthy, A., Navalón, S., Asiri, A. M., and Garcia, H. (2020). Gold-Nanoparticle-Decorated Metal-Organic Frameworks for Anticancer Therapy. *ChemMedChem* 15 (23), 2236–2256. doi:10.1002/cmdc.202000562

Dumont, N., Liu, B., Defilippis, R. A., Chang, H., Rabban, J. T., Karnezis, A. N., et al. (2013). Breast Fibroblasts Modulate Early Dissemination, Tumorigenesis, and Metastasis through Alteration of Extracellular Matrix Characteristics. *Neoplasia* 15 (3), 249–IN7. doi:10.1593/neo.121950

Emami Nejad, A., Najafgholian, S., Rostami, A., Sistani, A., Shojaeifar, S., Esparvarinha, M., et al. (2021). The Role of Hypoxia in the Tumor Microenvironment and Development of Cancer Stem Cell: a Novel Approach to Developing Treatment. *Cancer Cel Int* 21 (1), 62. doi:10.1186/s12935-020-01719-5

Farc, O., and Cristea, V. (2021). An Overview of the Tumor Microenvironment, from Cells to Complex Networks (Review). *Exp. Ther. Med.* 21 (1), 96. doi:10.3892/etm.2020.9528

Francis, D. M., and Thomas, S. N. (2017). Progress and Opportunities for Enhancing the Delivery and Efficacy of Checkpoint Inhibitors for Cancer Immunotherapy. *Adv. Drug Deliv. Rev.* 114, 33–42. doi:10.1016/j.addr.2017.04.011

Fu, Q., Zhao, Y., Yang, Z., Yue, Q., Xiao, W., Chen, Y., et al. (2019). Liposomes Actively Recognizing the Glucose Transporter GLUT1and Integrin αvβ3for Dual-Targeting of Glioma. *Arch. Pharm. Chem. Life Sci.* 352 (2), 1800219. doi:10.1002/ardp.201800219

Fu, S., Wang, S., Zhang, X., Qi, A., Liu, Z., Yu, X., et al. (2017). Structural Effect of Fe3O4 Nanoparticles on Peroxidase-like Activity for Cancer Therapy. *Colloids Surf. B: Biointerfaces.* 154, 239–245. doi:10.1016/j.colsurfb.2017.03.038

Giordano, S. H., Hortobagyi, G. N., Kau, S.-W. C., Theriault, R. L., and Bondy, M. L. (2005). Breast Cancer Treatment Guidelines in Older Women. *Jco* 23 (4), 783–791. doi:10.1200/jco.2005.04.175

Grebinyk, A., Prylutska, S., Grebinyk, S., Evstigneev, M., Krysiuk, I., Skaterna, T., et al. (2021). Antitumor Efficiency of the Natural Alkaloid Berberine Complexed with C60 Fullerene in Lewis Lung Carcinoma *In Vitro* and *In Vivo*. *Cancer Nanotechnology* 12 (1), 1–18. doi:10.1186/s12645-021-00096-6

Hu, S., Ren, Y., Wang, Y., Li, J., Qu, J., Liu, L., et al. (2019). Surface Plasmon Resonance Enhancement of Photoluminescence Intensity and Bioimaging Application of Gold nanorod@CdSe/ZnS Quantum Dots. *Beilstein J. Nanotechnol.* 10 (1), 22–31. doi:10.3762/bjnano.10.3

Hu, X.-X., He, P.-P., Qi, G.-B., Gao, Y.-J., Lin, Y.-X., Yang, C., et al. (2017). Transformable Nanomaterials as an Artificial Extracellular Matrix for Inhibiting Tumor Invasion and Metastasis. *ACS nano* 11 (4), 4086–4096. doi:10.1021/acsnano.7b00781

Huai, Y., Hossen, M. N., Wilhelm, S., Bhattacharya, R., and Mukherjee, P. (2019). Nanoparticle Interactions with the Tumor Microenvironment. *Bioconjug. Chem.* 30 (9), 2247–2263. doi:10.1021/acs.bioconjchem.9b00448

J. Zhou, Y. Nefedova, A. Lei, and D. Gabrilovich (Editors) (2018). "Neutrophils and PMN-MDSC: Their Biological Role and Interaction with Stromal Cells," *Seminars in Immunology* (Elsevier).

Jain, R. K. (2014). Antiangiogenesis Strategies Revisited: from Starving Tumors to Alleviating Hypoxia. *Cancer cell* 26 (5), 605–622. doi:10.1016/j.ccell.2014.10.006

Janoniene, A., Liu, Z., Baranauskiene, L., Mäkilä, E., Ma, M., Salonen, J., et al. (2017). A Versatile Carbonic Anhydrase IX Targeting Ligand-Functionalized Porous Silicon Nanoplatform for Dual Hypoxia Cancer Therapy and Imaging. *ACS Appl. Mater. Inter.* 9 (16), 13976–13987. doi:10.1021/acsami.7b04038

Jing, X., Yang, F., Shao, C., Wei, K., Xie, M., Shen, H., et al. (2019). Role of Hypoxia in Cancer Therapy by Regulating the Tumor Microenvironment. *Mol. Cancer* 18 (1), 157. doi:10.1186/s12943-019-1089-9

Justus, C. R., Dong, L., and Yang, L. V. (2013). Acidic Tumor Microenvironment and pH-Sensing G Protein-Coupled Receptors. *Front. Physiol.* 4, 354. doi:10.3389/fphys.2013.00354

Ke, H., Wang, J., Dai, Z., Jin, Y., Qu, E., Xing, Z., et al. (2011). Gold-Nanoshelled Microcapsules: A Theranostic Agent for Ultrasound Contrast Imaging and Photothermal Therapy. *Angew. Chem. Int. Ed.* 50 (13), 3017–3021. doi:10.1002/anie.201008286

Khan, N. U., Lin, J., Younas, M. R., Liu, X., and Shen, L. (2021). Synthesis of Gold Nanorods and Their Performance in the Field of Cancer Cell Imaging and Photothermal Therapy. *Cancer Nanotechnology* 12 (1), 1–33. doi:10.1186/s12645-021-00092-w

Kim, J., Park, S., Lee, J. E., Jin, S. M., Lee, J. H., Lee, I. S., et al. (2006). Designed Fabrication of Multifunctional Magnetic Gold Nanoshells and Their Application to Magnetic Resonance Imaging and Photothermal Therapy. *Angew. Chem. Int. Ed.* 45 (46), 7754–7758. doi:10.1002/anie.200602471

Kolosnjaj-Tabi, J., Kralj, S., Griseti, E., Nemec, S., Wilhelm, C., Plan Sangnier, A., et al. (2019). Magnetic Silica-Coated Iron Oxide Nanochains as Photothermal Agents, Disrupting the Extracellular Matrix, and Eradicating Cancer Cells. *Cancers* 11 (12), 2040. doi:10.3390/cancers11122040

Labani-Motlagh, A., Ashja-Mahdavi, M., and Loskog, A. (2020). The Tumor Microenvironment: A Milieu Hindering and Obstructing Antitumor Immune Responses. *Front. Immunol.* 11 (940), 940. doi:10.3389/fimmu.2020.00940

Labani-Motlagh, A., Ashja-Mahdavi, M., and Loskog, A. (2020). The Tumor Microenvironment: A Milieu Hindering and Obstructing Antitumor Immune Responses. *Front. Immunol.* 11, 940. doi:10.3389/fimmu.2020.00940

Lei, X., Lei, Y., Li, J.-K., Du, W.-X., Li, R.-G., Yang, J., et al. (2020). Immune Cells within the Tumor Microenvironment: Biological Functions and Roles in Cancer Immunotherapy. *Cancer Lett.* 470, 126–133. doi:10.1016/j.canlet.2019.11.009

Li, A. W., Sobral, M. C., Badrinath, S., Choi, Y., Graveline, A., Stafford, A. G., et al. (2018). A Facile Approach to Enhance Antigen Response for Personalized Cancer Vaccination. *Nat. Mater* 17 (6), 528–534. doi:10.1038/s41563-018-0028-2

Li, J., and Burgess, D. J. (2020). Nanomedicine-based Drug Delivery towards Tumor Biological and Immunological Microenvironment. *Acta pharmaceutica Sinica B* 10 (11), 2110–2124. doi:10.1016/j.apsb.2020.05.008

Liang, R., Liu, L., He, H., Chen, Z., Han, Z., Luo, Z., et al. (2018). Oxygen-boosted Immunogenic Photodynamic Therapy with Gold Nanocages@manganese Dioxide to Inhibit Tumor Growth and Metastases. *Biomaterials* 177, 149–160. doi:10.1016/j.biomaterials.2018.05.051

Liu, H., Moynihan, K. D., Zheng, Y., Szeto, G. L., Li, A. V., Huang, B., et al. (2014). Structure-based Programming of Lymph-Node Targeting in Molecular Vaccines. *Nature* 507 (7493), 519–522. doi:10.1038/nature12978

Liu, J., Chen, Q., Feng, L., and Liu, Z. (2018). Nanomedicine for Tumor Microenvironment Modulation and Cancer Treatment Enhancement. *Nano Today* 21, 55–73. doi:10.1016/j.nantod.2018.06.008

Liu, Q., Sacco, P., Marsich, E., Furlani, F., Arib, C., Djaker, N., et al. (2018). Lactose-Modified Chitosan Gold(III)-PEGylated Complex-Bioconjugates: From Synthesis to Interaction with Targeted Galectin-1 Protein. *Bioconjug. Chem.* 29 (10), 3352–3361. doi:10.1021/acs.bioconjchem.8b00520

Liu, Y., Guo, J., and Huang, L. (2020). Modulation of Tumor Microenvironment for Immunotherapy: Focus on Nanomaterial-Based Strategies. *Theranostics* 10 (7), 3099–3117. doi:10.7150/thno.42998

Maddela, N. R., Chakraborty, S., and Prasad, R. (2021). *Nanotechnology for Advances in Medical Microbiology*. Springer Nature.

Malinovskaya, Y., Melnikov, P., Baklaushev, V., Gabashvili, A., Osipova, N., Mantrov, S., et al. (2017). Delivery of Doxorubicin-Loaded PLGA Nanoparticles into U87 Human Glioblastoma Cells. *Int. J. Pharm.* 524 (1-2), 77–90. doi:10.1016/j.ijpharm.2017.03.049

Mayer, A., Höckel, M., Wree, A., Leo, C., Horn, L.-C., and Vaupel, P. (2008). Lack of Hypoxic Response in Uterine Leiomyomas Despite Severe Tissue Hypoxia. *Cancer Res.* 68 (12), 4719–4726. doi:10.1158/0008-5472.can-07-6339

Meir, R., Shamalov, K., Sadan, T., Motiei, M., Yaari, G., Cohen, C. J., et al. (2017). Fast Image-Guided Stratification Using Anti-programmed Death Ligand 1 Gold Nanoparticles for Cancer Immunotherapy. *ACS nano* 11 (11), 11127–11134. doi:10.1021/acsnano.7b05299

Mohd Yusof, H., Ab-Rahim, S., Ab-Rahim, S., Suddin, L. S., Ahmad Saman, M. S., and Mazlan, M. (2018). Metabolomics Profiling on Different Stages of

Colorectal Cancer: A Systematic Review. *Mjms* 25 (5), 16–34. doi:10.21315/mjms2018.25.5.3

Mozafari, M. R., Torkaman, S., Karamouzian, F. M., Rasti, B., and Baral, B. (2021). Antimicrobial Applications of Nanoliposome Encapsulated Silver Nanoparticles: A Potential Strategy to Overcome Bacterial Resistance. *Cnano* 17, 26–40. doi:10.2174/1573413716999200712184148

Mpekris, F., Baish, J. W., Stylianopoulos, T., and Jain, R. K. (2017). Role of Vascular Normalization in Benefit from Metronomic Chemotherapy. *Proc. Natl. Acad. Sci. USA* 114 (8), 1994–1999. doi:10.1073/pnas.1700340114

Mu, W., Chu, Q., Liu, Y., and Zhang, N. (2020). A Review on Nano-Based Drug Delivery System for Cancer Chemoimmunotherapy. *Nano-micro Lett.* 12 (1), 142. doi:10.1007/s40820-020-00482-6

Murphy, K., and Weaver, C. (2017). *Integrated Dynamics of Innate and Adaptive immunityJaneway's Immunobiology*. 9th ed. New York: Garland Science, 458–459.

Murphy, K., and Weaver, C. (2017). *Integrated Dynamics of Innate and Adaptive immunityJaneway's Immunobiology*. 9th Edition. New York and London: Garland Science, 445–488.

Nadhan, R., Srinivas, P., and Pillai, M. R. (2020). RTKs in Pathobiology of Head and Neck Cancers. *Adv. Cancer Res.* 147, 319–373. doi:10.1016/bs.acr.2020.04.008

Nadhan, R., Srinivas, P., and Pillai, M. R. (2020). "RTKs in Pathobiology of Head and Neck Cancers," in *Advances in Cancer Research*. Editors R Kumar, and P. B. Fisher (Academic Press), 147, 319–373. doi:10.1016/bs.acr.2020.04.008

Pan, X., Bai, L., Wang, H., Wu, Q., Wang, H., Liu, S., et al. (2018). Metal-Organic-Framework-Derived Carbon Nanostructure Augmented Sonodynamic Cancer Therapy. *Adv. Mater.* 30 (23), 1800180. doi:10.1002/adma.201800180

Park, J., Wrzesinski, S. H., Stern, E., Look, M., Criscione, J., Ragheb, R., et al. (2012). Combination Delivery of TGF-β Inhibitor and IL-2 by Nanoscale Liposomal Polymeric Gels Enhances Tumour Immunotherapy. *Nat. Mater* 11 (10), 895–905. doi:10.1038/nmat3355

Patra, J. K., Das, G., Fraceto, L. F., Campos, E. V. R., Rodriguez-Torres, M. d. P., Acosta-Torres, L. S., et al. (2018). Nano Based Drug Delivery Systems: Recent Developments and Future Prospects. *J. Nanobiotechnol* 16 (1), 71. doi:10.1186/s12951-018-0392-8

Paul, S., and Lal, G. (2017). The Molecular Mechanism of Natural Killer Cells Function and its Importance in Cancer Immunotherapy. *Front. Immunol.* 8, 1124. doi:10.3389/fimmu.2017.01124

Phan, S. H. (2008). Biology of Fibroblasts and Myofibroblasts. *Proc. Am. Thorac. Soc.* 5 (3), 334–337. doi:10.1513/pats.200708-146dr

Samstein, R. M., Arvey, A., Josefowicz, S. Z., Peng, X., Reynolds, A., Sandstrom, R., et al. (2012). Foxp3 Exploits a Pre-existent Enhancer Landscape for Regulatory T Cell Lineage Specification. *Cell* 151 (1), 153–166. doi:10.1016/j.cell.2012.06.053

Schmid, D., Park, C. G., Hartl, C. A., Subedi, N., Cartwright, A. N., Puerto, R. B., et al. (2017). T Cell-Targeting Nanoparticles Focus Delivery of Immunotherapy to Improve Antitumor Immunity. *Nat. Commun.* 8 (1), 1747. doi:10.1038/s41467-017-01830-8

Shahab, L., McGowan, J. A., Waller, J., and Smith, S. G. (2018). Prevalence of Beliefs about Actual and Mythical Causes of Cancer and Their Association with Socio-Demographic and Health-Related Characteristics: Findings from a Cross-Sectional Survey in England. *Eur. J. Cancer* 103, 308–316.

Shanmugam, V., Chien, Y.-H., Cheng, Y.-S., Liu, T.-Y., Huang, C.-C., Su, C.-H., et al. (2014). Oligonucleotides-Assembled Au Nanorod-Assisted Cancer Photothermal Ablation and Combination Chemotherapy with Targeted Dual-Drug Delivery of Doxorubicin and Cisplatin Prodrug. *ACS Appl. Mater. Inter.* 6 (6), 4382–4393. doi:10.1021/am5000905

Shanmugam, V., Selvakumar, S., and Yeh, C.-S. (2014). Near-infrared Light-Responsive Nanomaterials in Cancer Therapeutics. *Chem. Soc. Rev.* 43 (17), 6254–6287. doi:10.1039/c4cs00011k

Sharma, A., Goyal, A. K., and Rath, G. (2018). Recent Advances in Metal Nanoparticles in Cancer Therapy. *J. Drug Target.* 26 (8), 617–632. doi:10.1080/1061186x.2017.1400553

Simiantonaki, N., Taxeidis, M., Jayasinghe, C., Kurzik-Dumke, U., and Kirkpatrick, C. J. (2008). Hypoxia-inducible Factor 1 Alpha Expression Increases during Colorectal Carcinogenesis and Tumor Progression. *BMC cancer* 8 (1), 320–413. doi:10.1186/1471-2407-8-320

Singh, R. K., Knowles, J. C., and Kim, H. W. (2019). Advances in Nanoparticle Development for Improved Therapeutics Delivery: Nanoscale Topographical Aspect. *J. Tissue Eng.* 10, 2041731419877528. doi:10.1177/2041731419877528

Singh, R. K., Kurian, A. G., Patel, K. D., Mandakhbayar, N., Lee, N.-H., Knowles, J. C., et al. (2020). Label-free Fluorescent Mesoporous Bioglass for Drug Delivery, Optical Triple-Mode Imaging, and Photothermal/photodynamic Synergistic Cancer Therapy. *ACS Appl. Bio Mater.* 3 (4), 2218–2229. doi:10.1021/acsabm.0c00050

Singh, R. K., Patel, K. D., Leong, K. W., and Kim, H.-W. (2017). Progress in Nanotheranostics Based on Mesoporous Silica Nanomaterial Platforms. *ACS Appl. Mater. Inter.* 9 (12), 10309–10337. doi:10.1021/acsami.6b16505

Sintov, A. C., Velasco-Aguirre, C., Gallardo-Toledo, E., Araya, E., and Kogan, M. J. (2016). "Metal Nanoparticles as Targeted Carriers Circumventing the Blood-Brain Barrier," in *International Review of Neurobiology*. Editor K. T Al-Jamal (Academic Press), 130, 199–227. doi:10.1016/bs.irn.2016.06.007

Smith, T. T., Stephan, S. B., Moffett, H. F., McKnight, L. E., Ji, W., Reiman, D., et al. (2017). *In Situ* programming of Leukaemia-specific T Cells Using Synthetic DNA Nanocarriers. *Nat. Nanotech* 12 (8), 813–820. doi:10.1038/nnano.2017.57

Stephan, M. T., Moon, J. J., Um, S. H., Bershteyn, A., and Irvine, D. J. (2010). Therapeutic Cell Engineering with Surface-Conjugated Synthetic Nanoparticles. *Nat. Med.* 16 (9), 1035–1041. doi:10.1038/nm.2198

Sun, H.-C., Qiu, Z.-J., Liu, J., Sun, J., Jiang, T., Huang, K.-J., et al. (2007). Expression of Hypoxia-Inducible Factor-1 Alpha and Associated Proteins in Pancreatic Ductal Adenocarcinoma and Their Impact on Prognosis. *Int. J. Oncol.* 30 (6), 1359–1367. doi:10.3892/ijo.30.6.1359

Talmadge, J. E., and Gabrilovich, D. I. (2013). History of Myeloid-Derived Suppressor Cells. *Nat. Rev. Cancer* 13 (10), 739–752. doi:10.1038/nrc3581

Tang, L., Zheng, Y., Melo, M. B., Mabardi, L., Castaño, A. P., Xie, Y.-Q., et al. (2018). Enhancing T Cell Therapy through TCR-Signaling-Responsive Nanoparticle Drug Delivery. *Nat. Biotechnol.* 36 (8), 707–716. doi:10.1038/nbt.4181

Temple, L. K. F., Hsieh, L., Wong, W. D., Saltz, L., and Schrag, D. (2004). Use of Surgery Among Elderly Patients with Stage IV Colorectal Cancer. *Jco* 22 (17), 3475–3484. doi:10.1200/jco.2004.10.218

Tietze, R., Lyer, S., Dürr, S., Struffert, T., Engelhorn, T., Schwarz, M., et al. (2013). Efficient Drug-Delivery Using Magnetic Nanoparticles - Biodistribution and Therapeutic Effects in Tumour Bearing Rabbits. *Nanomedicine: Nanotechnology, Biol. Med.* 9 (7), 961–971. doi:10.1016/j.nano.2013.05.001

Triner, D., and Shah, Y. M. (2016). Hypoxia-inducible Factors: a central Link between Inflammation and Cancer. *J. Clin. Invest.* 126 (10), 3689–3698. doi:10.1172/jci84430

Tsai, M.-F., Chang, S.-H. G., Cheng, F.-Y., Shanmugam, V., Cheng, Y.-S., Su, C.-H., et al. (2013). Au Nanorod Design as Light-Absorber in the First and Second Biological Near-Infrared Windows for *In Vivo* Photothermal Therapy. *ACS nano* 7 (6), 5330–5342. doi:10.1021/nn401187c

Urruticoechea, A., Alemany, R., Balart, J., Villanueva, A., Viñals, F., and Capellá, G. (2010). Recent Advances in Cancer Therapy: an Overview. *Cpd* 16 (1), 3–10. doi:10.2174/138161210789941847

Venkatesh, N., Bhowmik, H., and AJBJoS, K. (2018). Metallic Nanoparticle: a Review. *Biomed. J. Scientific Tech. Res.* 4 (2), 3765–3775. doi:10.26717/bjstr.2018.04.0001011

Verbrugge, I., Wissink, E. H. J., Rooswinkel, R. W., Jongsma, J., Beltraminelli, N., Dupuis, M., et al. (2009). Combining Radiotherapy with APO010 in Cancer Treatment. *Clin. Cancer Res.* 15 (6), 2031–2038. doi:10.1158/1078-0432.ccr-08-2125

Wang, C., Wang, J., Zhang, X., Yu, S., Wen, D., Hu, Q., et al. (2018). *In Situ* formed Reactive Oxygen Species-Responsive Scaffold with Gemcitabine and Checkpoint Inhibitor for Combination Therapy. *Sci. Transl Med.* 10 (429). doi:10.1126/scitranslmed.aan3682

Wang, C., Chen, J., Talavage, T., and Irudayaraj, J. (2009). Gold Nanorod/Fe3O4Nanoparticle "Nano-Pearl-Necklaces" for Simultaneous Targeting, Dual-Mode Imaging, and Photothermal Ablation of Cancer Cells. *Angew. Chem.* 121 (15), 2797–2801. doi:10.1002/ange.200805282

Wang, J., Sun, J., Hu, W., Wang, Y., Chou, T., Zhang, B., et al. (2020). A Porous Au@Rh Bimetallic Core-Shell Nanostructure as an H2 O2 -Driven Oxygenerator to Alleviate Tumor Hypoxia for Simultaneous Bimodal Imaging and Enhanced Photodynamic Therapy. *Adv. Mater.* 32 (22), e2001862. doi:10.1002/adma.202001862

Wang, J., Sun, J., Hu, W., Wang, Y., Chou, T., Zhang, B., et al. (2020). A Porous Au@Rh Bimetallic Core-Shell Nanostructure as an H 2 O 2 -Driven Oxygenerator to Alleviate Tumor Hypoxia for Simultaneous Bimodal Imaging and Enhanced Photodynamic Therapy. *Adv. Mater.* 32 (22), 2001862. doi:10.1002/adma.202001862

Whatcott, C. J., Han, H., and Von Hoff, D. D. (2015). Orchestrating the Tumor Microenvironment to Improve Survival for Patients with Pancreatic Cancer. *Cancer J. (Sudbury, Mass)* 21 (4), 299–306. doi:10.1097/ppo.0000000000000140

Wilson, D. R., Sen, R., Sunshine, J. C., Pardoll, D. M., Green, J. J., and Kim, Y. J. (2018). Biodegradable STING Agonist Nanoparticles for Enhanced Cancer Immunotherapy. *Nanomedicine: Nanotechnology, Biol. Med.* 14 (2), 237–246. doi:10.1016/j.nano.2017.10.013

Wilson, D. S., Hirosue, S., Raczy, M. M., Bonilla-Ramirez, L., Jeanbart, L., Wang, R., et al. (2019). Antigens Reversibly Conjugated to a Polymeric Glyco-Adjuvant Induce Protective Humoral and Cellular Immunity. *Nat. Mater* 18 (2), 175–185. doi:10.1038/s41563-018-0256-5

Wohlfart, S., Khalansky, A. S., Gelperina, S., Maksimenko, O., Bernreuther, C., Glatzel, M., et al. (2011). Efficient Chemotherapy of Rat Glioblastoma Using Doxorubicin-Loaded PLGA Nanoparticles with Different Stabilizers. *PLoS One* 6 (5), e19121. doi:10.1371/journal.pone.0019121

Wolf, D., Sopper, S., Pircher, A., Gastl, G., and Wolf, A. M. (2015). Treg(s) in Cancer: Friends or Foe. *J. Cel. Physiol.* 230 (11), 2598–2605. doi:10.1002/jcp.25016

Xiao, Z., Ji, C., Shi, J., Pridgen, E. M., Frieder, J., Wu, J., et al. (2012). DNA Self-Assembly of Targeted Near-Infrared-Responsive Gold Nanoparticles for Cancer Thermo-Chemotherapy. *Angew. Chem.* 124 (47), 12023–12027. doi:10.1002/ange.201204018

Xiao, Z., Ji, C., Shi, J., Pridgen, E. M., Frieder, J., Wu, J., et al. (2012). DNA Self-Assembly of Targeted Near-Infrared-Responsive Gold Nanoparticles for Cancer Thermo-Chemotherapy. *Angew. Chem. Int. Ed.* 51 (47), 11853–11857. doi:10.1002/anie.201204018

Xin Yu, J., Hubbard-Lucey, V. M., and Tang, J. (2019). Immuno-oncology Drug Development Goes Global. *Nat. Rev. Drug Discov.* 18 (12), 899–900. doi:10.1038/d41573-019-00167-9

Xiong, J., Jiang, B., Luo, Y., Zou, J., Gao, X., Xu, D., et al. (2020). Multifunctional Nanoparticles Encapsulating astragalus Polysaccharide and Gold Nanorods in Combination with Focused Ultrasound for the Treatment of Breast Cancer. *Ijn* Vol. 15, 4151–4169. doi:10.2147/ijn.s246447

Yang, C.-C., Wang, C.-X., Kuan, C.-Y., Chi, C.-Y., Chen, C.-Y., Lin, Y.-Y., et al. (2020). Using C-Doped TiO2 Nanoparticles as a Novel Sonosensitizer for Cancer Treatment. *Antioxidants* 9 (9), 880. doi:10.3390/antiox9090880

Yang, C. C., Wang, C. X., Kuan, C. Y., Chi, C. Y., Chen, C. Y., Lin, Y. Y., et al. (2020). Using C-Doped TiO2 Nanoparticles as a Novel Sonosensitizer for Cancer Treatment. *Antioxidants (Basel)* 9 (9). doi:10.3390/antiox9090880

Yang, H., Liu, R., Xu, Y., Qian, L., and Dai, Z. (2021). Photosensitizer Nanoparticles Boost Photodynamic Therapy for Pancreatic Cancer Treatment. *Nano-micro Lett.* 13 (1), 35. doi:10.1007/s40820-020-00561-8

Yoon, H. Y., Selvan, S. T., Yang, Y., Kim, M. J., Yi, D. K., Kwon, I. C., et al. (2018). Engineering Nanoparticle Strategies for Effective Cancer Immunotherapy. *Biomaterials* 178, 597–607. doi:10.1016/j.biomaterials.2018.03.036

Yoshimura, M., Itasaka, S., Harada, H., and Hiraoka, M. (2013). Microenvironment and Radiation Therapy. *Biomed. Res. Int.* 2013, 685308. doi:10.1155/2013/685308

Yuan, X., Larsson, C., and Xu, D. (2019). Mechanisms Underlying the Activation of TERT Transcription and Telomerase Activity in Human Cancer: Old Actors and New Players. *Oncogene* 38 (34), 6172–6183. doi:10.1038/s41388-019-0872-9

Yuan, Y., Jiang, Y.-C., Sun, C.-K., and Chen, Q.-M. (2016). Role of the Tumor Microenvironment in Tumor Progression and the Clinical Applications (Review). *Oncol. Rep.* 35 (5), 2499–2515. doi:10.3892/or.2016.4660

Zaorsky, N. G., Churilla, T. M., Egleston, B. L., Fisher, S. G., Ridge, J. A., Horwitz, E. M., et al. (2017). Causes of Death Among Cancer Patients. *Ann. Oncol.* 28 (2), 400–407. doi:10.1093/annonc/mdw604

Zeng, X., Yan, S., Chen, P., Du, W., and Liu, B.-F. (2020). Modulation of Tumor Microenvironment by Metal-Organic-Framework-Derived Nanoenzyme for Enhancing Nucleus-Targeted Photodynamic Therapy. *Nano Res.* 13 (6), 1527–1535. doi:10.1007/s12274-020-2746-4

Zhang, L., Gao, Y., Sun, S., Li, Z., Wu, A., and Zeng, L. (2020). pH-Responsive Metal-Organic Framework Encapsulated Gold Nanoclusters with Modulated Release to Enhance Photodynamic Therapy/chemotherapy in Breast Cancer. *J. Mater. Chem. B* 8 (8), 1739–1747. doi:10.1039/c9tb02621e

Zhao, Z., Bai, H., Duan, J. C., and Wang, J. (2020). Individualized Treatment Recommendations for Lung Cancer Patients at Different Stages of Treatment during the Outbreak of 2019 Novel Coronavirus Disease. *Zhonghua Zhong Liu Za Zhi* 42 (4), 301–304. doi:10.3760/cma.j.cn112152-20200228-00146

Zheng, Y., Stephan, M. T., Gai, S. A., Abraham, W., Shearer, A., and Irvine, D. J. (2013). *In Vivo* targeting of Adoptively Transferred T-Cells with Antibody- and Cytokine-Conjugated Liposomes. *J. Controlled Release* 172 (2), 426–435. doi:10.1016/j.jconrel.2013.05.037

Zhong, X., Wang, X., Cheng, L., Tang, Y. a., Zhan, G., Gong, F., et al. (2020). GSH-Depleted PtCu 3 Nanocages for Chemodynamic- Enhanced Sonodynamic Cancer Therapy. *Adv. Funct. Mater.* 30 (4), 1907954. doi:10.1002/adfm.201907954

Zhou, J., Nefedova, Y., Lei, A., Gabrilovich, D., and Pmn-Mdsc (2018). Neutrophils and PMN-MDSC: Their Biological Role and Interaction with Stromal Cells. *Semin. Immunol.* 35, 19–28. doi:10.1016/j.smim.2017.12.004

Zhu, R., Wang, Z., Liang, P., He, X., Zhuang, X., Huang, R., et al. (2017). Efficient VEGF Targeting Delivery of DOX Using Bevacizumab Conjugated SiO2@LDH for Anti-neuroblastoma Therapy. *Acta Biomater.* 63, 163–180. doi:10.1016/j.actbio.2017.09.009

Zhu, Y., Yu, X., Thamphiwatana, S. D., Zheng, Y., and Pang, Z. (2020). Nanomedicines Modulating Tumor Immunosuppressive Cells to Enhance Cancer Immunotherapy. *Acta pharmaceutica Sinica B* 10 (11), 2054–2074. doi:10.1016/j.apsb.2020.08.010

Zub, K. A., Sousa, M. M. L. d., Sarno, A., Sharma, A., Demirovic, A., Rao, S., et al. (2015). Modulation of Cell Metabolic Pathways and Oxidative Stress Signaling Contribute to Acquired Melphalan Resistance in Multiple Myeloma Cells. *PloS one* 10 (3), e0119857. doi:10.1371/journal.pone.0119857

Conflict of Interest: The authors declare that the research was conducted in the absence of any commercial or financial relationships that could be construed as a potential conflict of interest.

Publisher's Note: All claims expressed in this article are solely those of the authors and do not necessarily represent those of their affiliated organizations, or those of the publisher, the editors and the reviewers. Any product that may be evaluated in this article, or claim that may be made by its manufacturer, is not guaranteed or endorsed by the publisher.

frontiers in Bioengineering and Biotechnology

ORIGINAL RESEARCH
published: 28 February 2022
doi: 10.3389/fbioe.2022.821256

VHPKQHR Peptide Modified Ultrasmall Paramagnetic Iron Oxide Nanoparticles Targeting Rheumatoid Arthritis for T_1-Weighted Magnetic Resonance Imaging

Chunyu Zhang[1,2,3], Wentao Huang[1,2,3], Chen Huang[4], Chengqian Zhou[5], Yukuan Tang[4], Wei Wei[6], Yongsheng Li[6], Yukuan Tang[4], Yu Luo[7]*, Quan Zhou[8]* and Wenli Chen[1,2,3]**

[1]MOE Key Laboratory of Laser Life Science, Institute of Laser Life Science, College of Biophotonics, South China Normal University, Guangzhou, China, [2]Guangdong Provincial Key Laboratory of Laser Life Science, College of Biophotonics, South China Normal University, Guangzhou, China, [3]Guangzhou Key Laboratory of Spectral Analysis and Functional Probes, College of Biophotonics, South China Normal University, Guangzhou, China, [4]Department of Minimally Invasive Interventional Radiology, Guangzhou Panyu Central Hospital, Guangzhou, China, [5]Neuroscience Laboratory, Hugo Moser Research Institute at Kennedy Krieger, Baltimore, MD, United States, [6]Institution of GuangDong Cord Blood Bank, Guangzhou, China, [7]Shanghai Engineering Technology Research Center for Pharmaceutical Intelligent Equipment, Shanghai Frontiers Science Research Center for Druggability of Cardiovascular Noncoding RNA, Institute for Frontier Medical Technology, College of Chemistry and Chemical Engineering, Shanghai University of Engineering Science, Shanghai, China, [8]Department of Radiology, The Third Affiliated Hospital of Southern Medical University, Guangzhou, China

OPEN ACCESS

Edited by:
Yen San Chan,
Curtin University Sarawak, Malaysia

Reviewed by:
Xiao-Feng Li,
Anhui Medical University, China
Ganesan Ramamoorthi,
Moffitt Cancer Center, United States

***Correspondence:**
Yukuan Tang
tyk20126@126.com
Yu Luo
yuluo@sues.edu.cn
Quan Zhou
zhouquan3777@smu.edu.cn
Wenli Chen
chenwl@scnu.edu.cn

Specialty section:
This article was submitted to Nanobiotechnology, a section of the journal Frontiers in Bioengineering and Biotechnology

Received: 24 November 2021
Accepted: 14 January 2022
Published: 28 February 2022

Citation:
Zhang C, Huang W, Huang C, Zhou C, Tang Y, Wei W, Li Y, Tang Y, Luo Y, Zhou Q and Chen W (2022) VHPKQHR Peptide Modified Ultrasmall Paramagnetic Iron Oxide Nanoparticles Targeting Rheumatoid Arthritis for T_1-Weighted Magnetic Resonance Imaging. Front. Bioeng. Biotechnol. 10:821256. doi: 10.3389/fbioe.2022.821256

Magnetic resonance imaging (MRI) could be the ideal diagnostic modality for early rheumatoid arthritis (RA). Vascular cell adhesion molecule-1 (VCAM-1) is highly expressed in synovial locations in patients with RA, which could be a potential target protein for RA diagnosis. The peptide VHPKQHR (VHP) has a high affinity to VCAM-1. To make the contrast agent to target RA at an early stage, we used VHP and ultrasmall paramagnetic iron oxide (USPIO) to synthesize UVHP (U stands for USPIO) through a chemical reaction with 1-(3-dimethylaminopropyl)-3-ethylcarbodiimide hydrochloride and N-hydroxysuccinimide. The size of UVHP was 6.7 nm; the potential was –27.7 mV, and the r_2/r_1 value was 1.73. Cytotoxicity assay exhibited that the cell survival rate was higher than 80% at even high concentrations of UVHP (Fe concentration 200 μg/mL), which showed the UVHP has low toxicity. Compared with no TNF-α stimulation, VCAM-1 expression was increased nearly 3-fold when mouse aortic endothelial cells (MAECs) were stimulated with 50 ng/mL TNF-α; cellular Fe uptake was increased very significantly with increasing UVHP concentration under TNF-α treatment; cellular Fe content was 17 times higher under UVHP with Fe concentration 200 μg/mL treating MAECs. These results indicate that UVHP can target overexpression of VCAM-1 at the cellular level. RA mice models were constructed with adjuvant-induced arthritis. *In vivo* MRI and biodistribution results show that the signal intensity of knee joints was increased significantly and Fe accumulation in RA model mice compared with normal wild-type mice after injecting UVHP 24 h. These results suggest that we have synthesized a simple, low-cost, and less toxic contrast agent UVHP, which targeted VCAM-1 for early-stage RA diagnosis and generates high contrast in T_1-weighted MRI.

Keywords: rheumatoid arthritis, magnetic resonance imaging, USPIO, VCAM-1, UVHP

1 INTRODUCTION

Rheumatoid arthritis (RA), a chronic systemic immune disease (Firestein, 2003), has a global prevalence of 0.5% to 1% (Abdel-Nasser et al., 1997; Kvien, 2004). Early diagnosis and correct treatment can effectively alleviate the incidence of RA patients (Luo et al., 2018). Conventional radiography, computed tomography, ultrasonography, and magnetic resonance imaging (MRI) are common imaging methods for RA (Østergaard et al., 2008). Because of the high resolution of the tissue, MRI may be one of the most ideal methods used clinically for the early diagnosis of RA (Østergaard et al., 2008; Hou et al., 2020).

MRI contrast agents are divided into longitudinal relaxation contrast agents (T_1-weighted contrast agents) and transverse relaxation contrast agents (T_2-weighted contrast agents) according to their principle of action (Zhao et al., 2021). T_1-weighted contrast agent shortens the longitudinal relaxation time of the tissue and enhances the signal; T_2-weighted contrast agent shortens the transverse relaxation time of the tissue and weakens the signal. As the T_2 signal is dark, and T_1 is a bright signal, and the high magnetic moment of the T_2 contrast agent may cause magnetic-susceptibility artifacts (Na et al., 2009; Zhou et al., 2020), and human vision prefers bright signals; T_1 contrast agent is more prevalently used than T_2 in a clinical setting.

Commonly used clinical T_1 contrast agents include Gd-DTPA (gadopentetate meglumine) (Carr et al., 1984), Gd-DOTA (Dotarem) (Meyer et al., 1988), and other Gd-type contrast agents, and Mn-DPDP (mangafodipir) (Jynge et al., 2020), $MnCl_2$, and other Mn contrast agents. However, these contrast agents are not selective, and Gd-based contrast agents may be nephrotoxic (Prince et al., 2008). Because contrast agents can improve the sensitivity of MRI (Caravan, 2006), it is necessary to find a contrast agent for early targeted diagnosis of RA.

Superparamagnetic iron oxide nanoparticles (SPIO) and ultrasmall SPIO (USPIO) are T_2 contrast agents that have been used in the clinic (Zhao et al., 2021). USPIO exhibits a decrease in magnetization due to the spin tilt effect as the particle size decreases, which effectively shortens the T_1 relaxation time of water protons. So, the USPIO can be used to improve T_1-weighted MRI signals (Chen et al., 2020). USPIO with a particle size of less than 5 nm has received more and more attention from researchers as MRI T_1 contrast agents (Zhou et al., 2020).

Simon et al. compared the imaging performance of 3.0 nm USPIO coated with carboxyl glucose and GD-DTPA for arthritis. The study shows that USPIO has a higher blood half-life and a more significant T_1 contrast (Simon et al., 2006). Li et al. designed a T_1/T_2-weighted contrast agent light-addressable ultrasmall Fe_3O_4 nanoparticles, which targeted macrophages in arthritis by folic acid. After 405-nm laser irradiation, the nanoparticle forms nanoclusters leading to T_1-weighted MRI change into T_2-weighted MRI (Li et al., 2019).

The specific mechanism of RA is currently unknown, but many clinical phenotypes of RA have been reported, including inflammatory factors (such as tumor necrosis factor-α [TNF-α] and interleukin-8) in the joint environment of RA patients; these inflammatory factors lead to the vascular cell adhesion molecule-1 (VCAM-1) overexpression in the synovium around the joint. Overexpression VCAM-1 was observed in fibroblast-like synoviocytes and endothelial cells (Elices et al., 1992; Dolati et al., 2016). VHPKQHR (VHP) is a peptide targeted to VCAM-1 identified by phage display technology and has been applied to target atherosclerotic plaque (Nahrendorf et al., 2006; Xu et al., 2019), but the use of VHP combined with USPIO for RA targeted imaging has not been reported yet.

This study synthesized a T_1-weighted MRI contrast agent UVHP (USPIO combined with VHP) that can target RA. Because of its low cost, simple method, and low toxicity, UVHP has the potential for clinical application.

2 MATERIALS AND METHODS

2.1 Synthesis and Characterization of USPIO and UVHP

2.1.1 Synthesis of USPIO

Synthesis of USPIO by the method provided in the published research article (Luo et al., 2015) was performed as follows: sodium citrate (final concentration 45.60 mM) was added to 80 mL of homogeneous $FeCl_3$ solution (dissolved in the final concentration of diethylene glycol 81.77 mM) in a water bath at 80°C until a clarified solution was formed. Subsequently, sodium acetate (final concentration 299.06 mM) was added to the above mixture and dissolved, and then the mixture was transferred to a 100-mL Teflon-lined stainless-steel autoclave reactor and sealed. The autoclave was placed in an oven at 200°C for 4 h. After cooling to room temperature, the black precipitate was collected by centrifugation (13,200*g*, 15 min). Precipitation was washed three times with ethanol to remove excess reactants and by-products then were dissolved in 10 mL ddH_2O and lyophilized to obtain 460 mg powder for the next step.

2.1.2 Synthesis of UVHP

USPIO (100 mg) was dissolved in 18 mL of ddH_2O at room temperature. 1-(3-Dimethylaminopropyl)-3-ethylcarbodiimide (molecular weight [MW] = 192; Shanghai Yuanye Bio-Technology Co., Ltd.) in 1 mL ddH_2O (final concentration 0.047 M) and N-hydroxysuccinimide (MW = 115.8; Shanghai Yuanye Bio-Technology Co., Ltd.) in 1 mL H_2O (final concentration 0.03 M) were added to the reaction solution and activated by vigorous stirring under ice bath conditions for 6 h. The peptide (VHPKQHR, Sangon Biotech [Shanghai] Co., Ltd.) 20 mg (MW = 1,081) was added and reacted for 6 h under an ice bath. The reaction was carried out with a dialysis membrane (MW cutoff = 1,500) in phosphate-buffered saline (PBS, three times, 2 L) and ddH_2O (six times, 2 L) to dialyze the mixture for 3 days under an ice bath to remove unreacted excess reactants. After freeze-drying, 83.4 mg UVHP was obtained (U stands for USPIO, VHP stands for VHPKQHR).

2.1.3 Characterization of Nanoparticles

Fourier transform infrared (FTIR) spectra were measured on a Bio-Rad FTS 6000 spectrometer (Bio-Rad Company, Hercules,

CA, USA) at 25°C (Li et al., 2020). Thermogravimetry (TGA) curves were carried out using a NETZSCH thermal analyzer (DSC 204F1) at a heating rate of 10°C/min in a nitrogen atmosphere (Yu et al., 2015). Zeta potential and dynamic light scattering (DLS) measurements were conducted using a Malvern Zetasizer Nano ZS (Malvern Instruments) (Li et al., 2020). The morphology and size of USPIO and UVHP were characterized by a field emission 2100F transmission electron microscope (TEM; JEOL, Japan) under 200-kV acceleration voltage (Yang et al., 2021). One-tesla MRI scanner (NM42-040H-I, Niumag, China) was used to measure the r_1 and r_2 values of USPIO and UVHP. The Fe contents of USPIO and UVHP were detected by ICP-OES (inductively coupled plasma optical emission spectrometer; Thermo E. IRIS Duo) (Tao et al., 2019). For example, we weighed 2,000 μg UVHP, and after measuring with ICP-OES, the Fe content was 262 μg. According to this result, we can weigh the corresponding UVHP amount according to the Fe content required by our experiments (Supplemental data). T_1 relaxometry and T_2 relaxometry were performed by a 0.5-T NMR analyzer (MINIPQ001; Shanghai Niumag Co., China).

2.2 Material, Cell Cultivation, and Sample Processing

2.2.1 Cell Material and Culture

Mouse aortic endothelial cells (MAECs) were purchased from CHI Scientific, Inc. Raw 264.7 cell line was obtained from ATCC (American Type Culture Collection). Human fibroblast-like synoviocyte RA (HFLS-RA) cell line was purchased from Guangzhou Jennio-bio Co., Ltd. (Guangzhou, China). MAECs, HFLS-RA cells, and raw 264.7 cells were grown in Dulbecco modified eagle medium (DMEM) medium containing 10% fetal bovine serum and 1% penicillin–streptomycin at 37°C in a humidified atmosphere with 5% CO_2.

2.2.2 Animal Model and Culture

Two-month-old female C57BL/6 mice were purchased from Animal Experimental Center, Southern Medical University. The mice had free access to food and water under a 12-h light/12-h dark cycle. All animal experiments were approved by the Institutional Animal Ethics Committee of South China Normal University and were carried out following the National Institutes of Health Guidelines for the Care and Use of Laboratory Animals of South China Normal University.

C57BL/6 mice were used to construct RA model mice. Complete Freund's adjuvant was mixed with 2% methylated bovine serum albumin (mBSA) in equal volume and injected into the axillae of 2-month-old female C57BL/6 mice at 0.1 mL per side. Three weeks later, 2% mBSA solution (dissolved in sterile water) was injected into the joint cavity of mice at 10 μL per side (Jones et al., 2018). Two months later, RA model (antigen-induced arthritis) mice were molded. In animal experiments, C57BL/6 mice of the same sex and age were used as wild-type (WT) mice. RA model mice identification: RA model mice (n = 3) were euthanized, and the knee joints were fixed with formalin and were sent to Servicebio (Wuhan, China) for hematoxylin and eosin (H&E) staining, with C57BL/6 mice (n = 3) as controls. Safranin O/fast green (safranin/O) staining was carried out with the modified Safranin O-Fast Green FCF Cartilage Stain Kit (Solarbio, Beijing, China). The histological scoring of the sections was performed by three unwitting researchers using the Mankin scoring system. According to the classification of Mankin and his colleagues, the score is divided into four stages: near normal (0–2), early (2–6), middle (6–10), and late (10–14) (Iannitti et al., 2013; Nishitani et al., 2014).

2.2.3 Hemolytic Assay

Fresh blood from 8-week-old C57BL/6 mice is added to a tube containing sodium heparin. The erythrocyte was collected by centrifugation at 650*g* for 10 min. Then, erythrocyte was diluted to 0.25% with PBS (pH 7.4) and incubated with different concentrations of UVHP (Fe concentration 12.5, 25, 50, 100, 200 μg/mL) at 37°C for 12 h. Erythrocyte diluted with deionized water was used as a negative control, and erythrocyte diluted with PBS was used as a positive control. After 12 h of treatment, each group was centrifuged at 10,000*g* for 5 min, and 200 μL of supernatant was placed in a 96-well plate. The absorbance at 542 nm was measured using a microplate reader (INFINITE M200, Tecan, Switzerland). Each group was repeated three times.

2.2.4 Cytotoxicity Assay

The cytotoxicity of UVHP on RAW264.7 and HFLS-RA cells was investigated by the Cell Counting Kit-8 (CCK-8; Dojindo Laboratories, Kumamoto, Japan) method. The cells were inoculated at a cell density of 1×10^4 per well in 96-well plates and were cultured for 12 h or 24 h with a fresh medium containing different concentrations of UVHP (Fe concentration 0, 5, 10, 25, 50, 100, 150, 200 μg/mL) instead of nutrient-depleted medium, followed by 2 h with fresh serum-free medium containing 10% CCK-8. The absorbance at 450 nm in each well was measured using a microplate reader (INFINITE M200, Tecan, Switzerland); cell viability was calculated according to the instructions. All experiments were performed three times in parallel.

2.2.5 Toxicity Evaluation

The UVHP (Fe content 150 μg, dissolved in 100 μL PBS) was injected into RA mice (n = 3) through the tail vein. After 14 days, organs (heart, liver, spleen, lungs, kidneys) were collected from the mice. Sections and H&E staining were obtained from Servicebio (Wuhan, China) after 24 h of fixation with formalin. The RA mice (n = 3) injected with saline served as controls.

2.2.6 Western Blot

We treated MAECs with TNF-α (Abbkine Scientific Co., Ltd.) at concentrations of 10 and 50 ng/mL for 24 h (Fan et al., 2019); the cell culture medium was removed and washed three times with PBS. The cells were lysed by adding cell lysate on ice for 30 min and then quickly scraped with a clean cell scraper. Cell debris and lysate were centrifuged at 13,200*g* for 20 min, and then the supernatant was collected. Protein samples were denatured and separated on sodium dodecyl sulfate–polyacrylamide gels

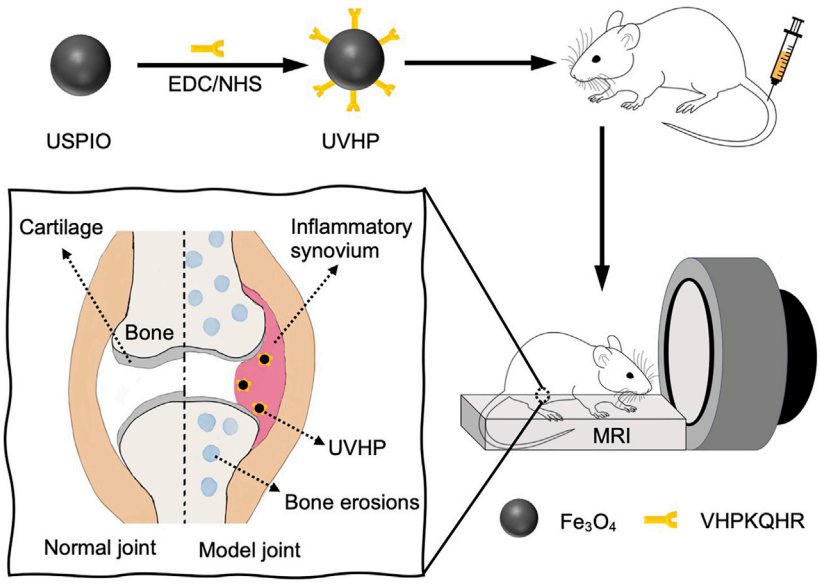

FIGURE 1 | Schematic illustration of the preparation and targeting rheumatoid arthritis of UVHP.

and then transferred to polyvinylidene difluoride membranes (cat. no.: IPVH00010 PORE SIZE: 0.45 μm; Merck Millipore Ltd.). The membranes were blocked with TBST solution (150 mM NaCl, 10 mM Tris–HCl, pH 7.4, 0.1% Tween 20) containing 5% skim milk for 2 h, followed by incubation with specific primary antibody (anti–VCAM-1 polyclonal antibody, Servicebio; anti-GAPDH [GAPDH was used as loading control], Absin, Shanghai, China) and secondary antibody (goat anti-rabbit immunoglobulin G [IgG, corresponding to VCAM-1]; MultiSciences, Hangzhou, China; goat anti-mouse IgG [corresponding to GAPDH], Dingguo, Beijing, China). Signals were detected using an image analyzer (Tanon-5200, Shanghai, China). The experiment was repeated three times, and results were analyzed using ImageJ software.

2.2.7 The *In Vivo* Biodistribution of UVHP

The mice after scanning with MRI were euthanized, and the organs heart, liver, spleen, lungs, kidneys, and knee joints were extracted and weighed, respectively. They were cut into small pieces of 1 to 2 mm and digested with aqua regia solution for 24 h, and then ICP-OES was used to detect the Fe content of different organs (Hou et al., 2020).

2.2.8 Cell Targeting MRI Experiment of UVHP

Cells (MAECS or HFLS-RA cells) were seeded at 1×10^5 cells per well in six-well plates with DMEM, and TNF-α (50 ng/mL for MAECs and 10 ng/mL for HFLS-RA [Croft et al., 1999]) or the same volume of PBS (as a control) was added, respectively. After 24 h of incubation, DMEM containing USPIO, UVHP (both Fe 50 μg/mL), or DMEM (as a control) replaced the original cell culture medium, treatment for 24 h. Raw 264.7 cells were also seeded at 1×10^5 cells per well in six-well plates with DMEM. After 24 h, DMEM containing USPIO, UVHP (both Fe 50 μg/mL), or DMEM (as a control) was used to replace the original cell culture medium for 24 h of treatment. The cells were washed three times with PBS to remove USPIO/UVHP that were not phagocytosed by the cells and then collected by trypsin and dispersed in 0.5 mL agarose (1%). MRI scan was obtained with a Philips 3.0 T Achieva MRI system (Healthcare, Best, the Netherlands), with the following scan parameters: FOV (field of view) = 60 × 60 mm, matrix = 256 × 256, slice thickness = 2 mm, TR (time of repetition) = 1,200 ms, and TE (time of echo) = 17 ms.

2.2.9 Cell Targeting Quantitative Determination Experiment of UVHP

Cells (MAECS or HFLS-RA cells) were seeded in six-well plates at a density of 1×10^5 and treated with TNF-α (50 ng/mL) for 24 h. The culture medium was replaced by a fresh culture medium containing UVHP (Fe concentration 25, 50, 100, and 200 μg/mL) and incubated for 24 h. The cells were washed three times with 1 mL PBS to remove the UVHP that were not taken up by the cells and then trypsinized and collected by centrifugation. The cells were resuspended with 1 mL PBS; the number of cells per well was counted, and then the cells were digested with aqua regia (Luo et al., 2015). ICP-OES was used to detect the Fe content of MAECs. For comparison, the same experiments were performed with cells (MAECS or HFLS-RA cells) treated with PBS (instead of TNF-α) for 24 h, and the subsequent UVHP treatment of cells and other operations are the same.

2.2.10 *In Vivo* MRI of UVHP Targeting RA

The knee joints of RA mice (n = 3) and C57BL/6 mice (n = 3) were scanned with a 7-T MRI (Bruker Biospec 7 T), with the following scan parameters: TR = 900, TE = 9 ms,

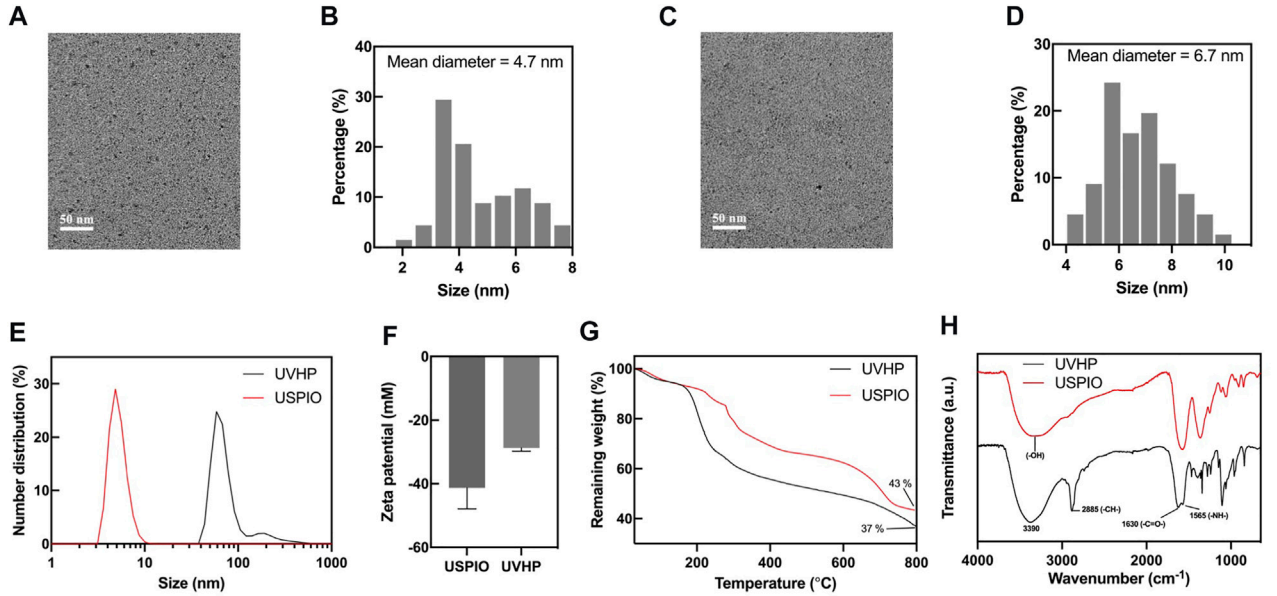

FIGURE 2 | Characterizations of USPIO and UVHP. **(A)** TEM image of USPIO; **(B)** size distribution histogram of USPIO; **(C)** TEM image of UVHP; **(D)** size distribution histogram of UVHP; **(E)** hydrodynamic sizes of USPIO and UVHP; **(F)** zeta potentials of USPIO, UVHP; **(G)** TGA curves of USPIO, UVHP; **(H)** FTIR spectra of USPIO, UVHP.

FOV = 80 × 80 mm, matrix = 256 × 256, ST (slice thickness) = 1 mm.

Two groups of RA mice (n = 3) were selected and injected with USPIO, UVHP (both Fe content 150 μg, dissolved in 100 μL PBS) in the tail vein, respectively. Two groups of C57BL/6 mice (n = 3) were selected and treated with the same conditions as controls. The mice were scanned after injecting UVHP for 24 h. T_1-weighted imaging was performed with a 7-T MRI scanner (Bruker Biospec 7 T). Scan parameters were as follows: TR = 1,000, TE = 8.5 ms, FOV = 80 × 80 mm, matrix = 256 × 160, ST = 1 mm. For image analysis, all images were analyzed via MRI viewing station (Paravision 5.1; Bruker, Karlsruhe, Germany).

2.2.11 Statistical Analysis

The significant difference of the experimental data was performed by one-way analysis-of-variance statistical analysis. When $p < 0.05$, the values were considered to be statistically significantly different. $p < 0.05$ is represented by (*), $p < 0.01$ is represented by (**), and $p < 0.001$ is represented by (***).

3 RESULTS

3.1 Synthesis and Characterization of USPIO and UVHP

We synthesized surface carboxylated USPIO according to the articles by Chen et al. (2020) and Luo et al. (2015) (for more details, see *Materials and Methods*). After that, we linked peptides VHP and USPIO together with an amide bond to form UVHP (**Figure 1**) (for more details, see *Materials and Methods*). TEM was used to characterize the size and morphology of USPIO and UVHP (**Figures 2A**,C). The size distribution histogram showed that the mean diameter of the USPIO was 4.7 ± 2.76 nm (**Figure 2B**); the zeta potential was −40 mV. Compared with USPIO, the particle size of the UVHP increased to 6.69 ± 2.78 nm (**Figure 2D**), and the zeta potential changed to −27.7 mV (**Figure 2F**), which should be attributed to the VHP connecting to the USPIO surface. DLS analysis showed that the hydrodynamic sizes of USPIO and UVHP were approximately 4 and 60 nm, respectively (**Figure 2E**). The increase in the hydrodynamic size of UVHP may be due to the decrease in the surface potential of the particles after the VHP was connected, which reduced the repulsion between the particles (Liu et al., 2013).

The combination of peptide VHP with USPIO was further confirmed by Fourier FTIR. As shown in **Figure 2H**, the absorption peaks in FTIR spectra at 3,390 cm^{-1}, 2,885 cm^{-1}, 1,630 cm^{-1}, and 1,565 cm^{-1} represent the O–H, C–H, and N–H stretching of UVHP, which could be attributed to the successful connection VHP with USPIO. The VHP conjugated to the surface of USPIO was quantitatively characterized by TGA (**Figure 2G**). The USPIO had a weight loss of 57% (**Figure 2G**), which should be attributed to the citrate on the particle surface. The weight loss of UVHP was 63% after modification with the peptide VHP. The above results indicate that we successfully synthesized UVHP.

3.2 T_1 and T_2 Relaxometry and MRI of USPIO and UVHP

To test the potential of UVHP in MRI application, we monitor the MRI signal intensity of T_1-weighted MRI and T_2-weighted MRI of USPIO and UVHP using a 3.0-T clinical MRI system. The MRI

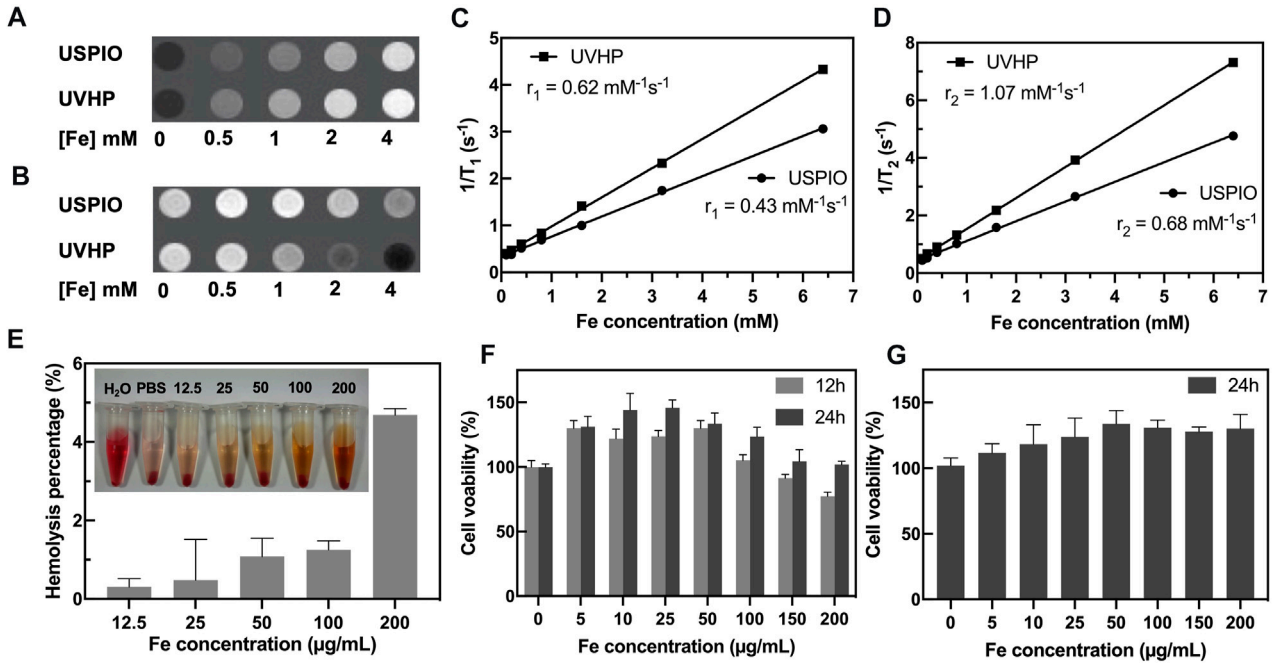

FIGURE 3 | MRI scans and cytotoxicity assay of UVHP. T_1-weighted **(A)** and T_2-weighted **(B)** images of UVHP aqueous solution at different Fe concentrations (0, 0.5, 1, 2, and 4 mM) taken by a 3.0-T clinical MRI system under the following parameters: FOV = 100 mm; matrix = 168 × 168; section thickness = 2 mm; TR = 2,000 ms; TE = 60 ms. USPIO was used as control. **(C,D)** Plot of $1/T_1$ and $1/T_2$ over Fe concentration of UVHP, the slope indicates the specific relaxivity (r_1 and r_2). USPIO was used as control. **(E)** The hemolysis assay of UVHP (Fe concentration 12.5, 25, 50, 100, 200 μg/mL). PBS and water were used as negative and positive controls. **(F)** The viability of RAW 264.7 cells after coculture with UVHP at different Fe concentrations for 12 or 24 h was measured by the CCK8 assay. RAW 264.7 cells treated with PBS were used as control, respectively. **(G)** The viability of HFLS-RA cells after coculture with UVHP at different Fe concentrations for 24 h was measured by the CCK8 assay. HFLS-RA cells treated with PBS were used as control, respectively.

results (**Figure 3A**) showed that as the Fe concentration increased, the T_1-weighted MRI scan became brighter, and UVHP would be slightly brighter than USPIO under the same Fe concentration. The T_2-weighted MRI (**Figure 3B**) showed that the image became darker as the Fe concentration increased; UVHP would be slightly darker compared with USPIO under the same Fe concentration (**Figure 3B**). Furthermore, when picking relaxation rate ($1/T_1$ or $1/T_2$) as the ordinate and Fe concentration as the abscissa, Fe concentration is linearly proportional to the value of $1/T_1$ or $1/T_2$ (Luo et al., 2015), and their slope was the longitudinal relaxation rate r_1 and transverse relaxation rate r_2 values of USPIO and UVHP, respectively (**Figures 3C**, D). The r_1 and r_2 values of USPIO were 0.43 and 0.68 $mM^{-1}s^{-1}$, respectively; the r_2/r_1 ratio was 1.58. As for UVHP, the r_1 and r_2 values were 0.62 and 1.07 $mM^{-1}s^{-1}$, respectively; the r_2/r_1 ratio was 1.73. T_1 contrast agent should have a high r_1 relaxation rate and low r_2/r_1 value, and theoretically, r_2/r_1 value in the range of 1 to 2 should be suitable for T1-weighted MRI (Tromsdorf et al., 2009). Combining T_1-weighted MRI and the value of r_2/r_1, USPIO and UVHP could be used as a potential T_1-weighted imaging contrast agent in the future.

3.3 Hemolysis and Cytotoxicity Assay of UVHP

Hemolytic assay was used to investigate the hemocompatibility of the UVHP. As shown in **Figure 3E**, there was no significant hemolysis phenomenon observed for blood cells treated with UVHP with Fe concentrations of 12.5, 25, 50, 100, and 200 μg/mL. Further quantitative analysis showed that the hemolytic percentages of UVHP (Fe concentrations 0–200 μg/mL) were all lower than 5% (a threshold value) (Hu et al., 2015).

The cytotoxicity of UVHP was evaluated by CCK-8 before *in vivo* biomedical applications (**Figure 3F**). After incubation with the UVHP at Fe concentrations of 0, 5, 10, 25, 50, 100, 150, and 200 μg/mL for 12 h, the cell viability of RAW264.7 was approximately 80% at 200 μg/mL Fe concentration. Most investigators chose 80% as the threshold for cytotoxicity (Chen et al., 2020). Next, we extended the treatment time to 24 h; as **Figure 3F** shows, the cell survival rate was still greater than 80% when Fe concentration was 200 μg/mL. In order to further investigate the cytotoxicity of UVHP in RA, we incubated HFLS-RA cells with UVHP for 24 h, and the result of cell viability (**Figure 3G**) was similar to that of RAW264.7 cells. These results indicate that UVHP had low toxicity and hemocompatibility in Fe concentration of 0 to 200 μg/mL.

3.4 UVHP Targeting Cells (MAECs or HFLS-RA Cells) of TNF-α Stimulation

It has been previously reported that TNF-α is highly expressed in RA lesions (Choy and Panayi, 2001; da Costa Moura, 2013), and VCAM-1 overexpression was observed in MAECs under stimulation with TNF-α (Fan et al., 2019). So, we chose

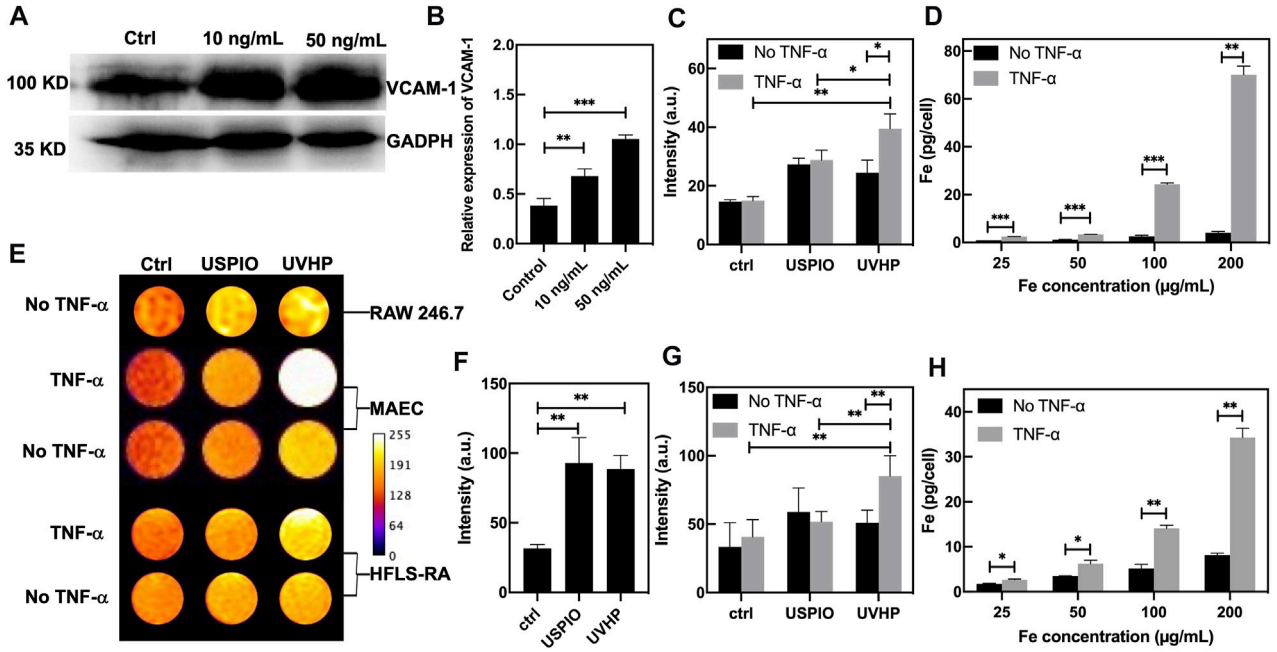

FIGURE 4 | TNF-α–stimulated MAEC high expression of VCAM-1 and cell targeting assay. **(A)** Western blot of MAECs treated with TNF-α (10 ng/mL, 50 ng/mL). MAECs treated with PBS were used as control. **(B)** Quantitative Western blot analysis of VCAM-1. **(C)** T_1-weighted MRI signal values of non–TNF-α–stimulated MAECs and TNF-α–stimulated MAECs treated with the USPIO and UVHP (both Fe concentration 50 μg/mL). **(D)** The TNF-α–stimulated MAEC uptake of the UVHP with different concentrations (Fe concentration 25, 50, 100, and 200 μg/mL) for 24 h. No TNF-α–stimulated MAECs were used as control. **(E)** T_1-weighted MR pseudocolor images of cells. Raw 264.7 cells treated with USPIO or UVHP (both Fe concentration 50 μg/mL) for 24 h. MAECs treated with USPIO or UVHP (both Fe concentration 50 μg/mL) for 24 h in the presence or absence of TNF-α (50 ng/mL). HFLS-RA cells treated with USPIO or UVHP (both Fe concentration 50 μg/mL) for 24 h in the presence or absence of TNF-α (10 ng/mL). All cells treated with PBS as controls. **(F)** T_1-weighted MRI signal values of non–TNF-α–stimulated raw 264.7 cells treated with the USPIO and UVHP (both Fe concentration 50 μg/mL). **(G)** T_1-weighted MRI signal values of non–TNF-α–stimulated HFLS-RA cells and TNF-α–stimulated HFLS-RA cells treated with the USPIO and UVHP (both Fe concentration 50 μg/mL). **(H)** The TNF-α–stimulated HFLS-RA cell uptake of the UVHP with different concentrations (Fe concentration 25, 50, 100, and 200 μg/mL) for 24 h. Non–TNF-α–stimulated HFLS-RA cells were used as control.

MAECs with TNF-α treatment to mimic the microenvironment at the site of arthritis. As shown in **Figure 4A**, compared with the MAECs treated with PBS (as control), the expression of VCAM-1 was increased after MAECs treated with TNF-α for 24 h. The Western blot analysis demonstrated that VCAM-1 expression in MAECs was increased two and three times after 10 and 50 ng/mL TNF-α stimulation, respectively, comparing with the control (**Figure 4B**). These results confirm that TNF-α could increase the VCAM-1 expression in MAECs.

First, we used MRI to explore the effect of UVHP on RAW264.7 cells. After 24 h of UVHP or USPIO treatment, RAW264.7 cells were examined under T_1-weighted MRI, and the signal intensity was counted (**Figure 4E**, first row). The results (**Figure 4F**) showed that there was no significant difference in the signal intensity between cells treated with UVHP and that, after USPIO treatment, both were higher than those of PBS-treated cells.

In order to explore the ability of UVHP to target VCAM-1, we used UVHP to treat MAECs and HFLS-RA cells, respectively. As shown in **Figure 4E**, we set up a PBS experimental group and a TNF-α experimental group for each cell type, which treated them with PBS or TNF-α for 24 h, respectively. Each group contained three different cell treatment subgroups: PBS, UVHP, or USPIO (both Fe concentration 50 ng/mL); for 24 h, the T_1-weighted MRI signal intensity was counted (**Figure 4E**, second to fifth row). The signal of the statistical results is shown in **Figure 4C** and **Figure 4G**. In the PBS group (no TNF-α treatment), there was no significant difference in the signals after UVHP and USPIO treated MAECs and HFLS-RA cells, and both were higher than those treated with PBS. These results show that both USPIO and UVHP enhanced the T1-weighted signal strength, which are similar to the results of the RAW264.7 cells experiment above. In the TNF-α treatment group, the T_1-weighted MRI signal after UVHP treatment was significantly higher than that of the USPIO group, and both were significantly higher than those treated with PBS. Because TNF-α stimulates cells (MAECs or HFLS-RA cells; Croft et al., 1999) to express VCAM-1, we can conclude from the results that UVHP can target cells with VCAM-1 overexpression.

We further evaluated the targeting capability of UVHP to VCAM-1 with ICP-OES. The above MRI and statistical results have shown that UVHP can indeed target cells that are highly expressing VCAM-1. Cells (MAECs or HFLS-RA cells) were treated with TNF-α for 24 h and then incubated with different concentrations of UVHP (Fe concentration 25, 50, 100, 200 μg/mL). We found that the iron content in both cells was limitedly increased with the increase in UVHP concentration (**Figure 4D** and **Figure 4H**). At the same time, compared with the TNF-α treatment groups, the uptake of Fe was also significantly increased

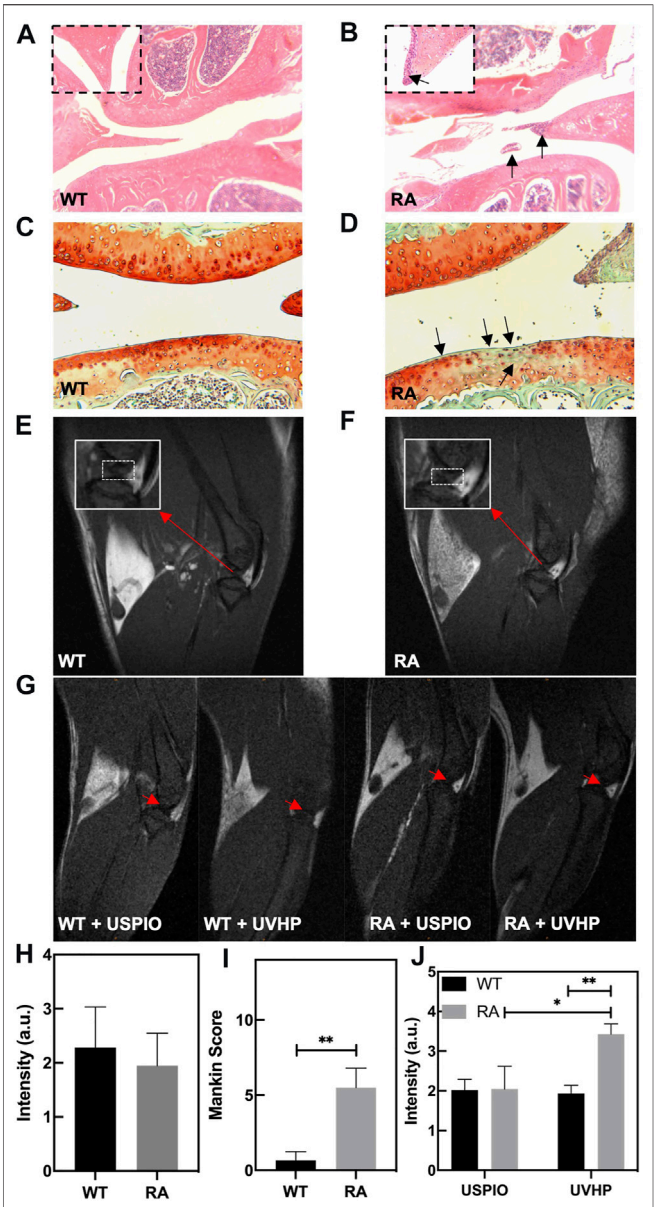

FIGURE 5 | Photomicrographs of representative hematoxylin and eosin (H&E)–stained sections of knee joint from WT mice **(A)** and RA mice **(B)**. The arrow shows the infiltration of inflammatory cells. **(C,D)** Safranin O/fast green staining sections of knee joint from WT mice **(C)** and RA mice **(D)**. The arrow shows the cartilage layer lesion area. **(E,F)** T_1-weighted MRI of the knee joint in WT and RA mice; red arrows indicate the site of interest. **(G)** T_1-weighted MRI of the knee joint in WT and RA mice injected with UVHP through the tail vein, at the same time WT and RA mice injected with USPIO in the tail vein as controls; red arrows indicate the site of interest. **(H)** MRI signal value of T_1-weighted MRI of the knee joint in WT and RA mice. **(I)** Mankin score of knee joints in WT and RA mice. **(J)** Signal value of T1-weighted MRI of the knee joint in WT and RA mice injected with USPIO and UVHP, respectively.

under PBS treatment with increasing UVHP concentration, but overall significantly lower than in the TNF-α treatment group with the same UVHP concentration (**Figure 4D** and **Figure 4H**). These results further confirmed that UVHP had a targeted function at the cellular level.

3.5 RA Model Mice Construction and UVHP Targeting Joint MRI

RA model mice construction details are listed in *Materials and Methods*. The knee joint sections of the model mice were taken for H&E staining and safranin O/fast green staining.

Compared with normal mice (**Figure 5A**), there are inflammatory cells immersed in the knee joint and the synovium observed in the RA model mice (**Figure 5B**). The safranin O/fast green staining showed that the cartilage structure of the RA model mice (**Figure 5D**) was destroyed. The cartilage surface was rough, and the cartilage cells were decolorized. The Mankin score (**Figure 5I**) of the RA model mice was significantly higher than that of WT mice, and it was in the early stage (Ehrlich et al., 1978). These results indicate that we established the RA model mice successfully.

To confirm the targeting joint MRI effect of UVHP on RA mice, first, we performed T_1-weighted MRI on normal WT and RA mice, respectively. As shown in **Figures 5E, F**, the area framed by the dashed line is the synovial fluid region between the joints. Our statistics for this part of the area showed that there was no significant difference between normal WT and RA mice (**Figure 5H**).

Next, we injected USPIO and UVHP to normal WT mice and RA mice via the tail vein, respectively; 24 h later, we performed a T_1-weighted MRI of the joint area (**Figure 5G**). The signal values of the synovial region between the joints were counted, and the results are shown in **Figure 5J**. There was no significant difference in signal values between WT and RA mice after USPIO injection, but the signal values of RA mice were significantly higher than those of WT mice after UVHP injection (**Figure 5J**). This indicates that more UVHPs were enriched at the joint region of RA mice, whereas USPIO was not enriched at that region. These results proved that UVHP could be targeted to joints of RA mice. To further confirm that UVHP could target the RA region, the changes of Fe content in the knee joint were tested by ICP-OES. The results show that there was no significant difference in Fe content in the knee joints of the WT and RA mice injected with USPIO, but the RA mice injected with UVHP showed a significant increase in Fe content in the knee joints of RA mice (**Figure 6A**), which was consistent with our MRI results (**Figure 5J**). This indicates that UVHP could target the joints of the RA model mice.

3.6 Biodistribution of UVHP *in vivo*

After injection of USPIO and UVHP via the tail vein to the RA mice 24 h later, these mice were euthanized. The Fe content of the heart, liver, spleen, lung, and kidney was quantified by ICP-OES. The results show that comparing with the order of the Fe distribution in RA mice: the spleen, heart, lung, liver, and kidney (from high to low) (**Figure 6B**), after injection of USPIO or UVHP to RA mice, the order of the Fe distribution in RA mice was spleen, liver, heart, lung, and kidney. The Fe contents in the spleen and liver of RA mice injected with USPOI or UVHP were significantly higher than those injected with PBS, indicating that most of the USPIO and UVHP were absorbed in the spleen and liver. Reports show more phagocytosis of nanoparticles by macrophages in the liver and spleen (Maldiney et al., 2014), suggesting that RA mice may mainly metabolize UVHP through the liver and spleen.

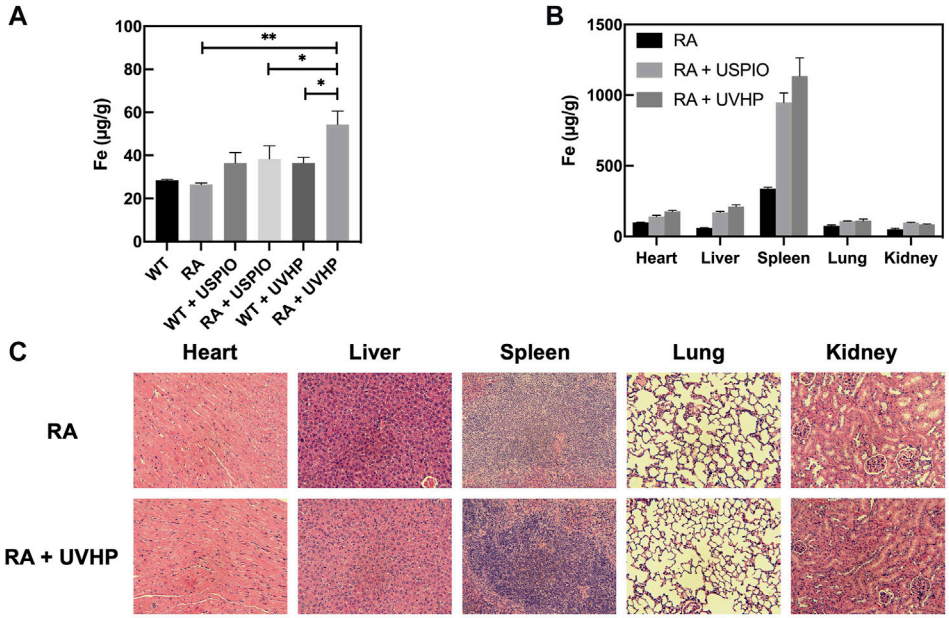

FIGURE 6 | Fe content in different tissues. **(A)** Elemental Fe content in the knee joint 24 h after tail vein injection of USPIO, UVHP to RA mice, WT mice, and PBS-injected RA mice, with WT mice as control. Each group (n = 3 per group) was injected with an equal Fe concentration (250 μg Fe, in 0.1 mL PBS). **(B)** Biodistribution of Fe in the major organs (heart, liver, spleen, lung, kidney) in RA mice (n = 3) at 24 h after intravenous administration of the USPIO, UVHP (250 μg Fe, in 0.1 mL PBS). The Fe content of each organ was measured by ICP-OES. RA mice (n = 3) injected with PBS served as controls. **(C)** Sections of each organ (heart, liver, spleen, lung, kidney). The tail vein of RA mice (n = 3) was injected with UVHP (Fe contains 250 μg in 0.1 mL PBS), and H&E staining of each organ (heart, liver, spleen, lung, kidney) was performed after 14 days. RA mice (n = 3) injected with saline served as control.

3.7 Safety Evaluation of UVHP

Section pictures of organs stained by H&E were used to investigate the biosafety of UVHP. The morphological analysis (**Figure 6C**) showed that compared with RA mice injected with PBS, the morphology of major organs (the heart, lung, liver, spleen, and kidney) still showed no significant change after injecting UVHP to RA mice for 14 days, which indicates UVHP had no significant influence on RA mice.

4 DISCUSSION

Magnetic iron oxide nanoparticles (>50 nm) are commonly used as T_2 contrast agents; but when their size is reduced to small diameters (usually <5 nm), the particle surface area increases dramatically, causing relaxation changes of iron nearby water protons (Zhou et al., 2015). Although a large number of studies have explored the potential of USPIO as a T_1 contrast agent, Shen et al. synthesized a series of USPIO (sizes from 1.9 to 4.9 nm) to explore the optimal size for making T_1-weighted MRI contrast agents, and the results show that 3.6 nm was the optimal size (Shen et al., 2017). Multiple factors affect T_1-weighted MRI of USPIO, including size, shape, composition, surface coating, hydrophobicity, and degree of aggregation of USPIO (Jeon et al., 2021). The average size of our synthesized USPIO was 4.7 nm, and the UVHP potential was −27.7 mV with good dispersion, and our results confirm that UVHP targeted not only the cells with high VCAM-1 expression but also the RA mice joint sites, which indicates the potential of UVHP as a T_1 contrast agent. In the process of USPIO and UVHP being engulfed by cells or entering living tissues, USPIO and UVHP aggregation may occur and lead to enhancement of T_2-weighted MRI (Roch et al., 2005); thus, we speculate that our synthesized USPIO and UVHP may be suitable for both T_1- and T_2-weighted MRI.

Because of the central role of macrophages in the pathogenesis of RA (Mulherin et al., 1996; Kinne et al., 2007), current contrast agents targeting RA imaging are focused on macrophages. Folic acid (Dai et al., 2014) or other molecules were utilized to target inflammatory macrophages in RA area (Hou et al., 2020). Based on the mechanism of inflammatory factors in the synovial fluid of RA patients leading to high VCAM-1 expression in synovial tissue (Carter and Wicks, 2001), we used UVHP targeting VCAM-1 of MAECs in RA. ICP-OES test results proved that UVHPs were enriched in arthritis and may provide a new targeting RA contrast agent for medical MRI.

Most T_1-weighted contrast agents targeting RA are based on Gd reagents. For example, Hou. et al. synthesized the RA contrast agent CB86-DTPA-Gd targeting translocator protein based on Ga chelates (Hou et al., 2020). The risk of Gd long-term toxicity may trigger nephrogenic systemic fibrosis, as well as Gd deposition in the brain (Todd et al., 2007; Wei et al., 2017). Many studies have demonstrated the biosafety of USPIO, including at the cellular level, such as in hepatocytes (He et al., 2018) and stem cells (Ledda et al., 2020), and at the biological level, such as in mice (Ledda et al., 2020) and rats (Garcia-Fernandez et al., 2020). Through CCK-8 assays, hemolysis assays, and organ H&E staining section assays, we demonstrated that UVHP has good biosafety at the cell and tissue levels.

In vitro experiments with cultured human monocytes have shown that various iron oxides have different abilities to be phagocytosed, with SPIO being more readily taken up by human monocytes than USPIO (Metz et al., 2004). *In vivo*, the larger particles (SPIO) are mainly taken up by macrophage cells in the liver, whereas the smaller particles (USPIO) are mainly taken up by macrophages in the bone marrow, lymph nodes, and spleen (Weissleder et al., 1990). Our results show that ultimately only a smaller amount of UVHP is concentrated in the RA lesion area. Analysis on the distribution of UVHP in the organism should also note that UVHP was less concentrated in the RA lesion region in contrast to the liver, spleen, heart, lung, and kidney. Based on the above results, we speculate that USPIO and UVHP may have the function of T_1-weighted MRI similar to Gd. We look forward to further in-depth research later.

5 CONCLUSION

In summary, we synthesized a simple, low-cost, and less toxic contrast agent UVHP, which targets VCAM-1 and may be useful for early-stage RA diagnosis and generate high contrast in T_1-weighted MRI.

DATA AVAILABILITY STATEMENT

The original contributions presented in the study are included in the article/**Supplementary Material**, further inquiries can be directed to the corresponding authors.

ETHICS STATEMENT

The animal study was reviewed and approved by the Institutional Animal Ethics Committee of South China Normal University.

AUTHOR CONTRIBUTIONS

CuZ, YL, and WH: conceptualization and compilation of data. CuZ and WC: writing part and proofreading. CuZ, QZ, and CH: designing of figure. CuZ, CeZ, YT, WW, YL, and YT: language polishing. All authors contributed to the article and approved the submitted version.

FUNDING

This work was supported by the National Natural Science Foundation of China (No. 81471659), Guangzhou Science and Technology Planning Project (202103000002), Guangdong Medical Science and Technology Research Foundation (B2021376) and Panyu Major Science and Technology Planning Project (2020-Z04-002).

SUPPLEMENTARY MATERIAL

The Supplementary Material for this article can be found online at: https://www.frontiersin.org/articles/10.3389/fbioe.2022.821256/full#supplementary-material

REFERENCES

Abdel-Nasser, A. M., Rasker, J. J., and Vaikenburg, H. A. (1997). Epidemiological and Clinical Aspects Relating to the Variability of Rheumatoid Arthritis. *Semin. Arthritis Rheum.* 27, 123–140. doi:10.1016/S0049-0172(97)80012-1

Caravan, P. (2006). Strategies for Increasing the Sensitivity of Gadolinium Based MRI Contrast Agents. *Chem. Soc. Rev.* 35, 512–523. doi:10.1039/B510982P

Carr, D., Brown, J., Bydder, G., Steiner, R., Weinmann, H., Speck, U., et al. (1984). Gadolinium-DTPA as a Contrast Agent in MRI: Initial Clinical Experience in 20 Patients. *Am. J. Roentgenol.* 143, 215–224. doi:10.2214/ajr.143.2.215

Carter, R. A., and Wicks, I. P. (2001). Vascular Cell Adhesion Molecule 1 (CD106): a Multifaceted Regulator of Joint Inflammation. *Arthritis Rheum.* 44, 9852–9994. doi:10.1002/1529-0131(200105)44:5<985:aid-anr176>3.0.co;2-p

Chen, S., Zhang, Q., Sun, H., Zheng, Y., Chen, Q., Luo, Y., et al. (2020). A Cation Exchange Strategy to Construct a Targeting Nanoprobe for Enhanced T1-Weighted MR Imaging of Tumors. *J. Mater. Chem. B* 8, 8519–8526. doi:10.1039/d0tb01632b

Choy, E. H. S., and Panayi, G. S. (2001). Cytokine Pathways and Joint Inflammation in Rheumatoid Arthritis. *N. Engl. J. Med.* 344, 907–916. doi:10.1056/NEJM200103223441207

Croft, D., McIntyre, P., Wibulswas, A., and Kramer, I. (1999). Sustained Elevated Levels of VCAM-1 in Cultured Fibroblast-like Synoviocytes Can Be Achieved by TNF-α in Combination with Either IL-4 or IL-13 through Increased mRNA Stability. *Am. J. Pathol.* 154 (4), 1149–1158. doi:10.1016/S0002-9440(10)65367-9

Dai, F., Du, M., Liu, Y., Liu, G., Liu, Q., and Zhang, X. (2014). Folic Acid-Conjugated Glucose and Dextran Coated Iron Oxide Nanoparticles as MRI Contrast Agents for Diagnosis and Treatment Response of Rheumatoid Arthritis. *J. Mater Chem. B* 2 (16), 2240–2247. doi:10.1039/c3tb21732a

da Costa Moura, C. (2013). *Development of Multifunctional Nanoparticles for Targeted Therapy and Imaging of Rheumatoid Arthritis*: Faculty of Engineering University of Porto.

Dolati, S., Sadreddini, S., Rostamzadeh, D., Ahmadi, M., Jadidi-Niaragh, F., and Yousefi, M. (2016). Utilization of Nanoparticle Technology in Rheumatoid Arthritis Treatment. *Biomed. Pharmacother.* 80, 30–41. doi:10.1016/j.biopha.2016.03.004

Ehrlich, M. G., Houle, P. A., Vigliani, G., and Mankin, H. J. (1978). Correlation between Articular Cartilage Collagenase Activity and Osteoarthritis. *Arthritis Rheum.* 21 (7), 761–766. doi:10.1002/art.1780210704

Elices, M.-D. J. W. E., Mj, A.-G. J., Zvaifler, N., et al. (1992). a4ßl Integrin (VLAA) Ligands in Arthritis: Vascular Cell Adhesion Molecule Expression in Synovium and on Fibroblast-like Synoviocytes. *J. Immunol.* 149, 1424. PMID: 1380043.

Fan, X., Chen, X., Feng, Q., Peng, K., Wu, Q., Passerini, A. G., et al. (2019). Downregulation of GATA6 in mTOR-Inhibited Human Aortic Endothelial Cells: Effects on TNF-α-Induced VCAM-1 Expression and Monocytic Cell Adhesion. *Am. J. Physiol.-Heart Circ. Physiol.* 316, H408–H420. doi:10.1152/ajpheart.00411.2018

Firestein, G. S. (2003). Evolving Concepts of Rheumatoid Arthritis. *Nature* 423, 356–361. doi:10.1038/nature01661

Garcia-Fernandez, J., Turiel, D., Bettmer, J., Jakubowski, N., Panne, U., Rivas García, L., et al. (2020). *In Vitro* and *In Situ* Experiments to Evaluate the Biodistribution and Cellular Toxicity of Ultrasmall Iron Oxide Nanoparticles Potentially Used as Oral Iron Supplements. *Nanotoxicology* 14, 388–403. doi:10.1080/17435390.2019.1710613

He, C., Jiang, S., Yao, H., Zhang, L., Yang, C., Zhan, D., et al. (2018). Endoplasmic Reticulum Stress Mediates Inflammatory Response Triggered by Ultra-small Superparamagnetic Iron Oxide Nanoparticles in Hepatocytes. *Nanotoxicology* 12, 1198–1214. doi:10.1080/17435390.2018.1530388

Hou, Z., Wang, Q., Guo, Z., Wang, T., Wu, H., Ma, C., et al. (2020). Gadolinium-conjugated CB86: a Novel TSPO-Targeting MRI Contrast Agent for Imaging of Rheumatoid Arthritis. *J. Drug Target.* 28, 398–407. doi:10.1080/1061186X.2019.1669040

Hu, Y., Li, J., Yang, J., Wei, P., Luo, Y., Ding, L., et al. (2015). Facile Synthesis of RGD Peptide-Modified Iron Oxide Nanoparticles with Ultrahigh Relaxivity for Targeted MR Imaging of Tumors. *Biomater. Sci.* 3, 721–732. doi:10.1039/C5BM00037H

Iannitti, T., Elhensheri, M., Bingöl, A. Ö., and Palmieri, B. (2013). Preliminary Histopathological Study of Intra-articular Injection of a Novel Highly Cross-Linked Hyaluronic Acid in a Rabbit Model of Knee Osteoarthritis. *J. Mol. Hist.* 44 (2), 191–201. doi:10.1007/s10735-012-9457-4

Jeon, M., Halbert, M. V., Stephen, Z. R., and Zhang, M. (2021). Iron Oxide Nanoparticles as T 1 Contrast Agents for Magnetic Resonance Imaging: Fundamentals, Challenges, Applications, and Prospectives. *Adv. Mater.* 33, 1906539. doi:10.1002/adma.201906539

Jones, G. W., Hill, D. G., Sime, K., and Williams, A. S. (2018). *In Vivo* Models for Inflammatory Arthritis. *Methods Mol. Biol.* 1725, 101–118. doi:10.1007/978-1-4939-7568-6_9

Jynge, P., Skjold, A. M., Falkmer, U., Andersson, R. G. G., Seland, J. G., Bruvold, M., et al. (2020). MnDPDP: Contrast Agent for Imaging and Protection of Viable Tissue. *Contrast Media Mol. Imaging* 2020, 1–17. doi:10.1155/2020/3262835

Kinne, R. W., Stuhlmüller, B., and Burmester, G.-R. (2007). Cells of the Synovium in Rheumatoid Arthritis. Macrophages. *Arthritis Res. Ther.* 9, 224–240. doi:10.1186/ar2333

Kvien, T. K. (2004). Epidemiology and burden of Illness of Rheumatoid Arthritis. *Pharmacoeconomic* 22, 1–12. doi:10.2165/00019053-200422001-00002

Ledda, M., Fioretti, D., Lolli, M. G., Papi, M., Di Gioia, C., Carletti, R., et al. (2020). Biocompatibility Assessment of Sub-5 Nm Silica-Coated Superparamagnetic Iron Oxide Nanoparticles in Human Stem Cells and in Mice for Potential Application in Nanomedicine. *Nanoscale* 12 (3), 1759–1778. doi:10.1039/C9NR09683C

Li, X., Lu, S., Xiong, Z., Hu, Y., Ma, D., Lou, W., et al. (2019). Light-Addressable Nanoclusters of Ultrasmall Iron Oxide Nanoparticles for Enhanced and Dynamic Magnetic Resonance Imaging of Arthritis. *Adv. Sci.* 6, 1901800. doi:10.1002/advs.201901800

Li, H., Han, J., and Liang, G. (2020). Phase Transfer of Hydrophobic Nanoparticles Using a Zwitterionic Sulfobetaine Siloxane Generates Highly Biocompatible and Compact Surfaces. *ACS Appl. Nano Mater.* 3, 1489–1496. doi:10.1021/acsanm.9b02306

Liu, H., Xu, Y., Wen, S., Zhu, J., Zheng, L., Shen, M., et al. (2013). Facile Hydrothermal Synthesis of Low Generation Dendrimer-Stabilized Gold Nanoparticles for *In Vivo* Computed Tomography Imaging Applications. *Polym. Chem.* 4, 1788. doi:10.1039/c2py20993d

Luo, Y., Yang, J., Yan, Y., Li, J., Shen, M., Zhang, G., et al. (2015). RGD-functionalized Ultrasmall Iron Oxide Nanoparticles for Targeted T1-Weighted MR Imaging of Gliomas. *Nanoscale* 7, 14538–14546. doi:10.1039/c5nr04003e

Luo, Q., Zhang, L., Li, X., Fu, B., Deng, Z., Qing, C., et al. (2018). Identification of Circular RNAs Hsa_circ_0044235 in Peripheral Blood as Novel Biomarkers for Rheumatoid Arthritis. *Clin. Exp. Immunol.* 194, 118–124. doi:10.1111/cei.13181

Maldiney, T., Bessière, A., Seguin, J., Teston, E., Sharma, S. K., Viana, B., et al. (2014). The *In Vivo* Activation of Persistent Nanophosphors for Optical Imaging of Vascularization, Tumours and Grafted Cells. *Nat. Mater* 13, 418–426. doi:10.1038/nmat3908

Metz, S., Bonaterra, G., Rudelius, M., Settles, M., Rummeny, E., and Daldrup-Link, H. (2004). Capacity of Human Monocytes to Phagocytose Approved Iron Oxide MR Contrast Agents *In Vitro*. *Eur. Radiol.* 14, 1851–1858. doi:10.1007/s00330-004-2405-2

Meyer, D., Schaefer, M., and Bonnemain, B. (1988). Gd-DOTA, A Potential MRI Contrast Agent Current Status of Physicochemical Knowledge. *Invest. Radiol.* 23 (Suppl. 1), S232–S235. doi:10.1097/00004424-198809001-00048

Mulherin, D., Fitzgerald, O., and Bresnihan, B. (1996). Synovial Tissue Macrophage Populations and Articular Damage in Rheumatoid Arthritis. *Arthritis Rheum.* 39, 115–124. doi:10.1002/art.1780390116

Na, H. B., Song, I. C., and Hyeon, T. (2009). Inorganic Nanoparticles for MRI Contrast Agents. *Adv. Mater.* 21, 2133–2148. doi:10.1002/adma.200802366

Nahrendorf, M., Jaffer, F. A., Kelly, K. A., Sosnovik, D. E., Aikawa, E., Libby, P., et al. (2006). Noninvasive Vascular Cell Adhesion Molecule-1 Imaging Identifies Inflammatory Activation of Cells in Atherosclerosis. *Circulation* 114, 1504–1511. doi:10.1161/CIRCULATIONAHA.106.646380

Nishitani, K., Kobayashi, M., Kuroki, H., Mori, K., Shirai, T., Satake, T., et al. (2014). Ultrasound Can Detect Macroscopically Undetectable Changes in Osteoarthritis Reflecting the Superficial Histological and Biochemical Degeneration: *Ex Vivo* Study of Rabbit and Human Cartilage. *PLOS ONE* 9 (2), e89484. doi:10.1371/journal.pone.0089484

Østergaard, M., Pedersen, S. J., and Døhn, U. M. (2008). Imaging in Rheumatoid Arthritis - Status and Recent Advances for Magnetic Resonance Imaging, Ultrasonography, Computed Tomography and Conventional Radiography. *Best Pract. Res. Clin. Rheumatol.* 22, 1019–1044. doi:10.1016/j.berh.2008.09.014

Prince, M. R., Zhang, H., Morris, M., MacGregor, J. L., Grossman, M. E., Silberzweig, J., et al. (2008). Incidence of Nephrogenic Systemic Fibrosis at Two Large Medical Centers. *Radiology* 248, 807–816. doi:10.1148/radiol.2483071863

Roch, A., Gossuin, Y., Muller, R. N., and Gillis, P. (2005). Superparamagnetic Colloid Suspensions: Water Magnetic Relaxation and Clustering. *J. Magnetism Magn. Mater.* 293, 532–539. doi:10.1016/j.jmmm.2005.01.070

Shen, Z., Chen, T., Ma, X., Ren, W., Zhou, Z., Zhu, G., et al. (2017). Multifunctional Theranostic Nanoparticles Based on Exceedingly Small Magnetic Iron Oxide Nanoparticles for T_1-Weighted Magnetic Resonance Imaging and Chemotherapy. *ACS Nano* 11, 10992–11004. doi:10.1021/acsnano.7b04924

Simon, G. H., von Vopelius-Feldt, J., Wendland, M. F., Fu, Y., Piontek, G., Schlegel, J., et al. (2006). MRI of Arthritis: Comparison of Ultrasmall Superparamagnetic Iron Oxide vs. Gd-DTPA. *J. Magn. Reson. Imaging* 23, 720–727. doi:10.1002/jmri.20556

Tao, C., Zheng, Q., An, L., He, M., Lin, J., Tian, Q., et al. (2019). T1-Weight Magnetic Resonance Imaging Performances of Iron Oxide Nanoparticles Modified with a Natural Protein Macromolecule and an Artificial Macromolecule. *Nanomaterials* 9, 170. doi:10.3390/nano9020170

Todd, D. J., Kagan, A., Chibnik, L. B., and Kay, J. (2007). Cutaneous Changes of Nephrogenic Systemic Fibrosis: Predictor of Early Mortality and Association with Gadolinium Exposure. *Arthritis Rheum.* 56, 3433–3441. doi:10.1002/art.22925

Tromsdorf, U. I., Bruns, O. T., Salmen, S. C., Beisiegel, U., and Weller, H. (2009). A Highly Effective, Nontoxic T1 MR Contrast Agent Based on Ultrasmall PEGylated Iron Oxide Nanoparticles. *Nano Lett.* 9, 4434–4440. doi:10.1021/nl902715v

Wei, H., Bruns, O. T., Kaul, M. G., Hansen, E. C., Barch, M., Wiśniowska, A., et al. (2017). Exceedingly Small Iron Oxide Nanoparticles as Positive MRI Contrast Agents. *Proc. Natl. Acad. Sci. USA* 114, 2325–2330. doi:10.1073/pnas.1620145114

Weissleder, R., Elizondo, G., Wittenberg, J., Rabito, C. A., Bengele, H. H., and Josephson, L. (1990). Ultrasmall Superparamagnetic Iron Oxide: Characterization of a New Class of Contrast Agents for MR Imaging. *Radiology* 175, 489–493. doi:10.1148/radiology.175.2.2326474

Xu, W., Zhang, S., Zhou, Q., and Chen, W. (2019). VHPKQHR Peptide Modified Magnetic Mesoporous Nanoparticles for MRI Detection of Atherosclerosis Lesions. *Artif. Cell Nanomed. Biotechnol.* 47, 2440–2448. doi:10.1080/21691401.2019.1626411

Yang, Y., Zhang, T., and Xing, D. (2021). Single 808 Nm Near-Infrared-Triggered Multifunctional Upconverting Phototheranostic Nanocomposite for Imaging-Guided High-Efficiency Treatment of Tumors. *J. Biophotonics* 14, e202100134. doi:10.1002/jbio.202100134

Yu, Z., Peng, C., Luo, Y., Zhu, J., Chen, C., Shen, M., et al. (2015). Poly(γ-glutamic Acid)-Stabilized Iron Oxide Nanoparticles: Synthesis, Characterization and Applications for MR Imaging of Tumors. *RSC Adv.* 5, 76700–76707. doi:10.1039/c5ra15814a

Zhao, J., Chen, X., Ho, K.-H., Cai, C., Li, C.-W., Yang, M., et al. (2021). Nanotechnology for Diagnosis and Therapy of Rheumatoid Arthritis: Evolution towards Theranostic Approaches. *Chin. Chem. Lett.* 32, 66–86. doi:10.1016/j.cclet.2020.11.048

Zhou, Z., Wu, C., Liu, H., Zhu, X., Zhao, Z., Wang, L., et al. (2015). Surface and Interfacial Engineering of Iron Oxide Nanoplates for Highly Efficient Magnetic Resonance Angiography. *ACS Nano* 9, 3012–3022. doi:10.1021/nn507193f

Zhou, H., Qiu, X., and Shen, Z. (2020). T_1-weighted Magnetic Resonance Imaging Contrast Agents and Their Theranostic Nanoprobes. *Nan fang Yi ke da Xue Xue Bao = J. South. Med. Univ.* 40, 427–444. doi:10.12122/j.issn.1673-4254.2020.03.24

Conflict of Interest: The authors declare that the research was conducted in the absence of any commercial or financial relationships that could be construed as a potential conflict of interest.

Publisher's Note: All claims expressed in this article are solely those of the authors and do not necessarily represent those of their affiliated organizations, or those of the publisher, the editors and the reviewers. Any product that may be evaluated in this article, or claim that may be made by its manufacturer, is not guaranteed or endorsed by the publisher.

frontiers in Bioengineering and Biotechnology

ORIGINAL RESEARCH
published: 07 March 2022
doi: 10.3389/fbioe.2022.855136

Investigation of Antimicrobial and Cytotoxic Properties and Specification of Silver Nanoparticles (AgNPs) Derived From *Cicer arietinum* L. Green Leaf Extract

Ayşe Baran[1], Mehmet Fırat Baran[2,3], Cumali Keskin[2,3], Abdulkerim Hatipoğlu[4], Ömer Yavuz[5,6], Sevgi İrtegün Kandemir[7], Mehmet Tevfik Adican[8,9], Rovshan Khalilov[9,10,11], Afat Mammadova[12], Elham Ahmadian[13], Gvozden Rosić[14]*, Dragica Selakovic[14]* and Aziz Eftekhari[15,16]**

[1]Department of Biology, Mardin Artuklu University Graduate Education Institute, Mardin, Turkey, [2]Department of Medical Services and Techniques, Vocational School of Health Services, Mardin Artuklu University, Mardin, Turkey, [3]Joint Ukrainian-Azerbaijan International Research and Education Center of Nanobiotechnology and Functional Nanosystems, Drohobych, Ukraine, [4]Department of Nutrition and Dietetics, Faculty of Health Sciences, Mardin Artuklu University, Mardin, Turkey, [5]Department of Chemistry, Faculty of Science, Dicle University, Diyarbakir, Turkey, [6]Dicle University Central Research Laboratory, , Diyarbakir, Turkey, [7]Department of Medical Biology, Dicle University Central Research Laboratory, Faculty of Medicine, Dicle University, Diyarbakir, Turkey, [8]Electricity and Energy Department, Vocational School, Mardin Artuklu University, Mardin, Turkey, [9]Department of Biophysics and Biochemistry, Baku State University, Baku, Azerbaijan, [10]Institute of Radiation Problems, National Academy of Sciences of Azerbaijan, Baku, Azerbaijan, [11]Russian Institute for Advanced Study, Moscow State Pedagogical University, Moscow, Russia, [12]Department of Botany and Plant Physiology, Baku State University, Baku, Azerbaijan, [13]Kidney Research Center, Tabriz University of Medical Sciences, Tabriz, Iran, [14]Department of Physiology, Faculty of Medical Sciences, University of Kragujevac, Kragujevac, Serbia, [15]Health Innovation & Accelerations Center, Tabriz University of Medical Sciences, Tabriz, Iran, [16]Stem Cell Research Center, Tabriz University of Medical Sciences, Tabriz, Iran*

OPEN ACCESS

Edited by:
Abolfazl Heydari, Polymer Institute (SAS), Slovakia

Reviewed by:
Siamak Javanbakht, University of Tabriz, Iran
Fatma Nur Parın, Bursa Technical University, Turkey

***Correspondence:**
Cumali Keskin
ckeskinoo@gmail.com
Gvozden Rosić
grosic@medf.kg.ac.rs
Dragica Selakovic
dragica984@gmail.com
Aziz Eftekhari
Eftekharia@tbzmed.ac.ir

Specialty section:
This article was submitted to Nanobiotechnology, a section of the journal Frontiers in Bioengineering and Biotechnology

Received: *14 January 2022*
Accepted: *07 February 2022*
Published: *07 March 2022*

Citation:
Baran A, Fırat Baran M, Keskin C, Hatipoğlu A, Yavuz Ö, İrtegün Kandemir S, Adican MT, Khalilov R, Mammadova A, Ahmadian E, Rosić G, Selakovic D and Eftekhari A (2022) Investigation of Antimicrobial and Cytotoxic Properties and Specification of Silver Nanoparticles (AgNPs) Derived From Cicer arietinum L. Green Leaf Extract. Front. Bioeng. Biotechnol. 10:855136. doi: 10.3389/fbioe.2022.855136

Using biological materials to synthesize metallic nanoparticles has become a frequently preferred method by researchers. This synthesis method is both fast and inexpensive. In this study, an aqueous extract obtained from chickpea (*Cicer arietinum* L.) (CA) leaves was used in order to synthesize silver nanoparticles (AgNPs). For specification of the synthesized AgNPs, UV-vis spectrophotometer, Fourier transform infrared spectroscopy (FT-IR), X-ray diffraction analysis (XRD), transmission electron microscopy (TEM), scanning electron microscopy (SEM), electron dispersive X-ray (EDX), and zeta potential (ZP) analyses data were used. Biologically synthesized AgNPs demonstrated a maximum surface plasmon resonance of 417.47 nm after 3 h. With the powder XRD model, the mean crystallite dimension of nanoparticles was determined as 12.17 mm with a cubic structure. According to the TEM results, the dimensions of the obtained silver nanoparticles were found to be 6.11–9.66 nm. The ZP of the electric charge on the surface of AgNPs was measured as −19.6 mV. The inhibition effect of AgNPs on food pathogen strains and yeast was determined with the minimum inhibition concentration (MIC) method. AgNPs demonstrated highly effective inhibition at low concentrations especially against the growth of *B. subtilis* (0.0625) and *S. aureus* (0.125) strains. The cytotoxic effects of silver nanoparticles on cancerous cell lines (CaCo-2, U118, Sk-ov-3) and healthy cell lines (HDF) were revealed. Despite the increase

of AgNPs used against cancerous and healthy cell lines, no significant decrease in the percentage of viability was detected.

Keywords: cytotoxic activity, green synthesis, nanomaterials, food pathogens, nanomedicine, SEM-EDX

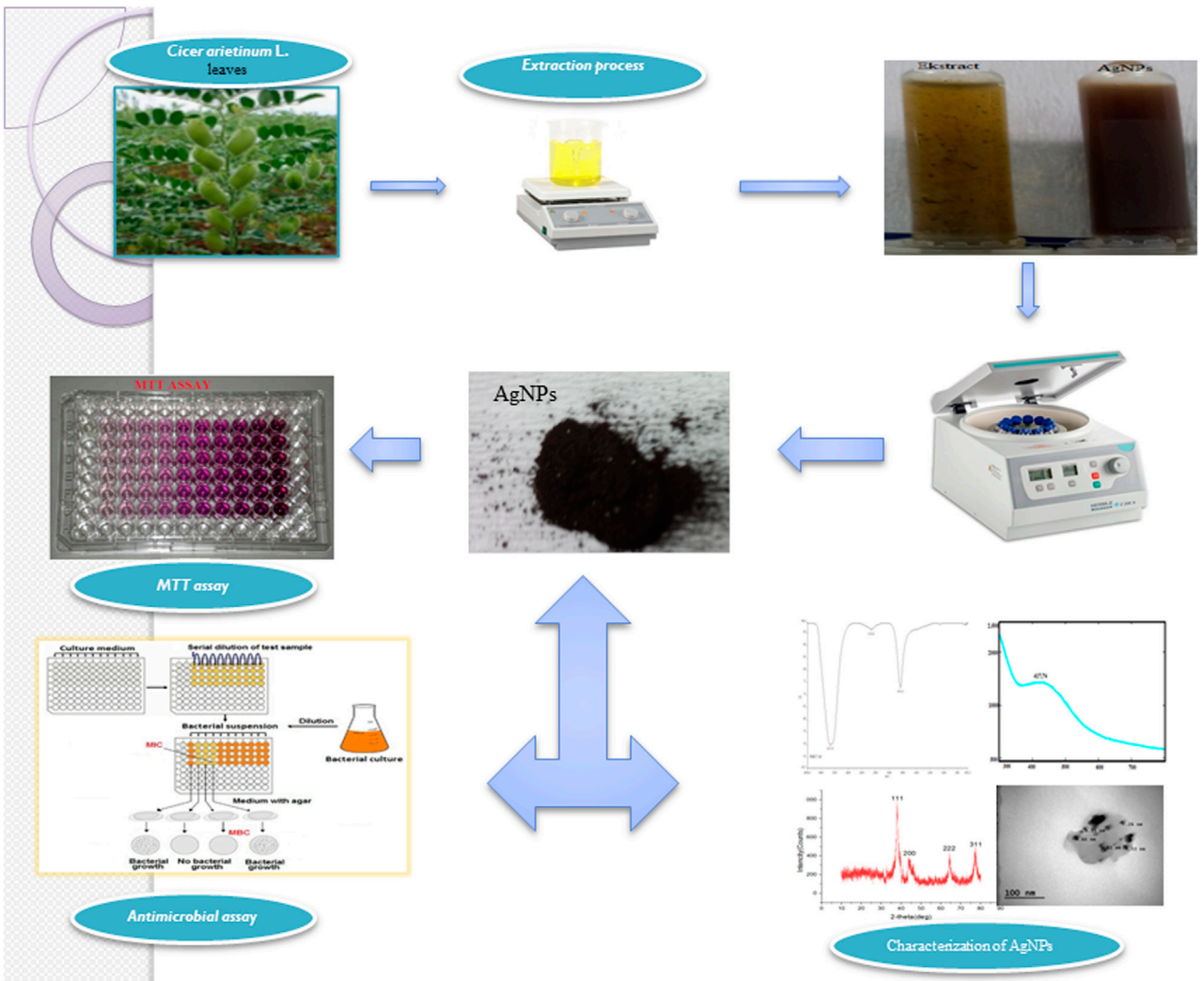

FIGURE 1 | Graphical illustration of the study.

TABLE 1 | Instrument conditions.

Instrument	Condition
SEM-EDX (EVO 40 LEQ)	Mag: 500–60.00 K X; EHT: 20.00 kV; WD: 11–12 mm; Signal A: SE1
TEM (Quanta)	1–100 nm
XRD (Rad B-DMAX II)	Dedector: SC-70; Solid phase; 2-theta (deg): 37.96; FWHM (deg): 1.17; Count (deg): 184; X-Ray: 40 kV, 15 mA
Zeta-sizer (Malvern Ins.Ltd.)	Zeta Deviation (mV): 5.81; Viscosity (cP): 0.8872; Conductivity (mS/cm): 0.00843; Dispersant Dielectric Constant: 78.5; Temperature (°C): 25; Count Rate (kcps): 93.3
FT-IR ATR (Perkine Elmer ONE)	Strong Ratio Spectrum Magnitude Universal Atr Double

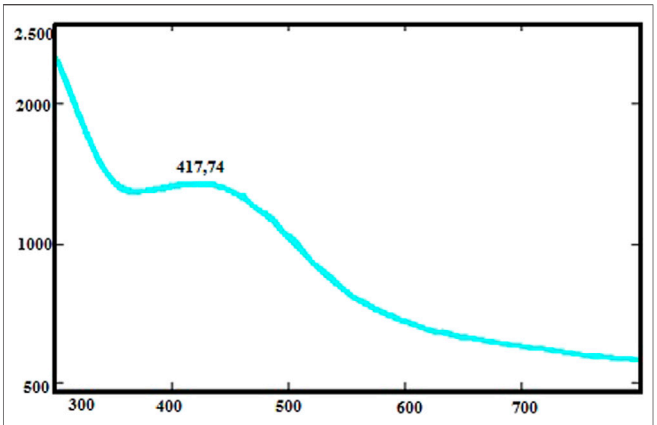

FIGURE 2 | UV-vis absorption spectra of CA-AgNPs.

INTRODUCTION

Nanotechnology is revealing new perspectives for the diagnosis and cure of numerous deadly autoimmune and chronic disorders like cancer (Kafshdooz et al., 2018; Yadi et al., 2018). Nanoparticles have become the main subject of scientific works in the last few decades because of their diverse properties, like different catalytic behaviors, chemical stability, and electric conductivity (Patra and Baek, 2016). Nanoparticles have become an indispensable source of biological research due to their structural and dimensional similarities to biological molecules. Nanoparticles are considered antimicrobial agents because they show good antibacterial properties resulting from their extensive surface area and volume that provides desired contact with the bacterial cell (Kumar et al., 2016). These properties allow nanoparticles to be used in diagnostic, cell labeling, biomarker, drug delivery, cancer therapy, and water purification applications (Mousavi et al., 2018; Kumari et al., 2019; Kowsalya et al., 2021).

In recent years to examine the morphological properties of nanoparticles, laser CVD, physical adsorption, and emulsion polymerization techniques are commonly being used. However, these technologies require the usage of stabilizing/reducing harmful chemicals or non-biologically degradable agents (Jayaprakash et al., 2017). For this reason, it is preferred to produce nanoparticles with fast, low-cost "green synthesis" procedures that do not use toxic solvents or pollute the environment, instead of current traditional methods (Hussain et al., 2016; Jayaprakash et al., 2017; Bandeira et al., 2020). Living organisms in nature can convert metal salts into nanoparticles by reducing them. In this context, scientific studies have focused on synthesizing these nanomaterials from non-artificial sources like plants (Aktepe and Baran, 2021), bacteria (Javaid et al., 2018), fungi (Molnár et al., 2018), algae (Parial et al., 2012), seaweeds (Chellapandian et al., 2019), and viruses (Mohmed et al., 2017).

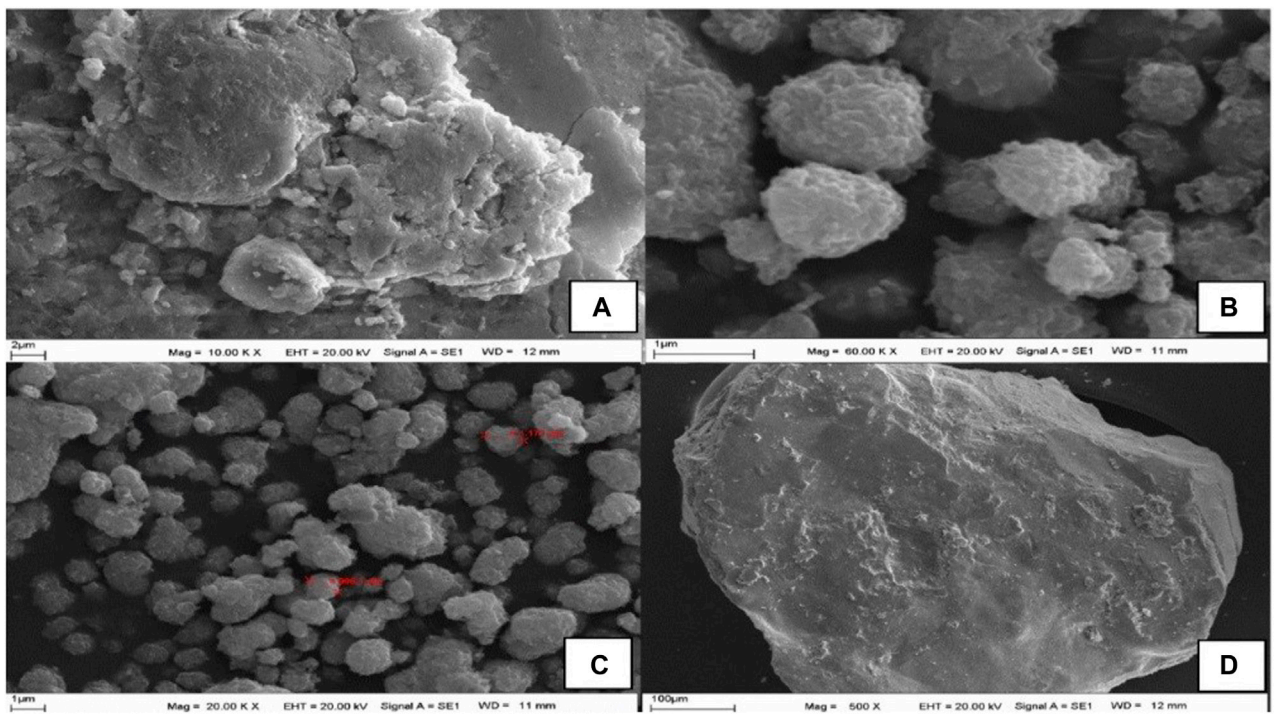

FIGURE 3 | (A–D) SEM images of CA-AgNPs in different scanning areas.

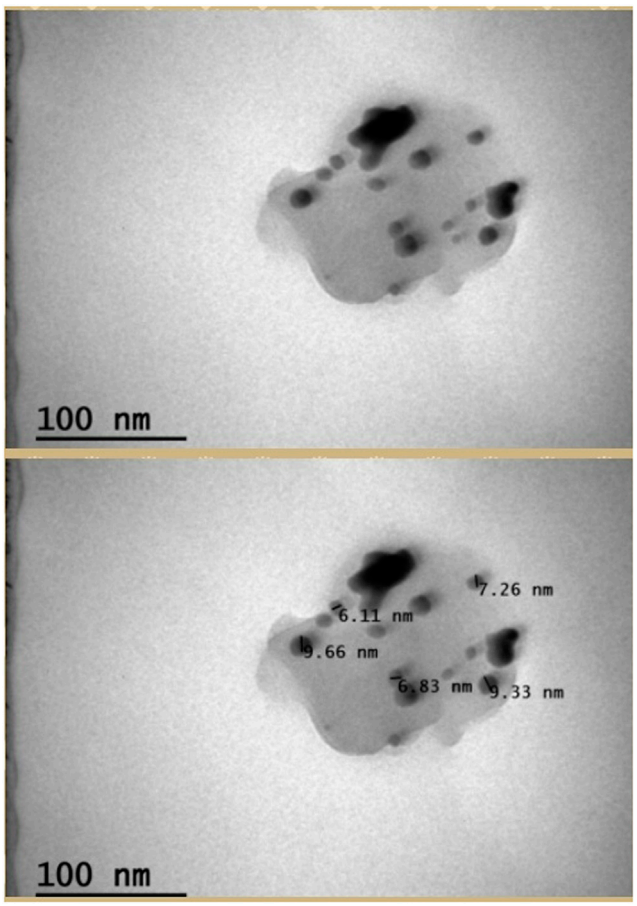

FIGURE 4 | TEM results of CA-AgNPs.

In many nanoparticle studies, gold (Au) (Hatipoğlu, 2021), silver (Ag) (Baran, 2019; Umaz et al., 2019; Baran et al., 2021b), zinc (Zn) (Jayappa et al., 2020), nickel (Ni) (Din et al., 2018), iron (Fe) (Devatha et al., 2016), platinum (Pt) (Ramkumar et al., 2017b), selenium (Se) (Abu-Elghait et al., 2021), titanium (Ti), and palladium (Pd) (Gioria et al., 2020) are frequently used metals. Especially silver (Ag) is known to be an important metal suppressing the growth of bacteria. The Ag ion can prevent cell division and DNA replication (Ramya and Subapriya, 2012). Owing to their small dimensions, silver nanoparticles (AgNPs) bind to cell membrane proteins and catalyze the formation of reactive oxygen species (ROS) in bacterial cells. Thus, they cause cell death due to oxidative stress (Hoseinnejad et al., 2018; Alkhalaf et al., 2020; Hasanzadeh et al., 2021).

The most important advantage of choosing plants as a resource in the biological synthesis of nanoparticles (NPs) is that they contain many naturally occurring reducing agents such as flavonoids, reductases, phenolic acids, and dehydrogenases, which have a key role in the synthesis of magnetic nanoparticles (MNPs) (Shumail et al., 2021).

In this study considering the properties of plants, the synthesis and stabilization of silver nanoparticles were achieved by reducing Ag metal salt by using chickpea (*Cicer arietinum* L.) (CA) leaf extract. Plant-based synthesized AgNPs were investigated for their effectiveness against pathogens, microorganisms, and cancerous and healthy cell lines (**Figure 1**).

MATERIALS AND METHODS

Materials

In the study, CA leaves obtained from Büyük Çelikli Village of Sur County of Diyarbakır were used. AgNO3 (99.8% purity), colistin, vancomycin, and fluconazole were commercially purchased from Sigma Aldrich. E. coli ATCC 25922, *P. aeruginosa* ATCC27853, *B. subtilis* ATCC 11774, *S. aureus* ATCC 29213, and C. albicans were used to test the antimicrobial activities of AgNPs. Cytotoxicity tests (MTT) related to cell lines (CaCo-2/human colon epidermal adenocarcinoma; U118 MG/human brain glioma cells; SK-OV-3/human ovarian cancer cell line; HDF/human dermal fibroblasts) were performed in the Dicle University Central Research Laboratory.

Herbal Extraction Process

Green leaves of CA were washed with deionized distilled water to remove residues and dehydrated at 25 ± 2°C. A total of 250 g of ground plant material was mixed with deionized pure water (500 ml) and boiled in a flask. After boiling, the cooled extract was filtered with a membrane filter (0.45 μm).

Plant-Based Synthesis of Silver Nanoparticles

Firstly, an aqueous solution of 5 mM $AgNO_3$ with solid $AgNO_3$ was prepared. The CA extracts (500 ml) and 100 ml of AgNO3 were allowed to react in a glass vessel (1:5 ratio) at room temperature. Maximum absorbance of biologically synthesized AgNPs was determined by wavelength scanning (UV-vis spectroscopy) at various time periods (15, 30, 45, 60, 120, and 180 min) depending on the color change. At the end of the synthesis, the solution, which became a dark color depending on time, was subjected to centrifugation (6000 rpm, 20 min). The purpose of this process is to separate the synthesized nanoparticles from plant residues. The solid fraction obtained at the end of centrifugation was washed several times with distilled water and the resulting residue (AgNPs) was dried in an oven at 60°C for 72 h.

Instrumentation

The maximum absorbance of synthesized AgNPs was measured at the 300–800 nm wavelength range with a spectrophotometer (Agilent CARY 60). Size, morphology, crystal structure, surface distribution, and zeta potential (ZP) values of AgNPs were revealed by scanning electron microscopy (SEM) (EVO 40 LEQ), transmission electron microscopy (TEM) (Quanta), field emission scanning electron microscopy (FE-SEM) (Quanta FEG240), electron dispersive X-ray (EDX) (Quanta FEG 240), X-ray diffraction analysis (XRD) (Rad B-DMAX II), and

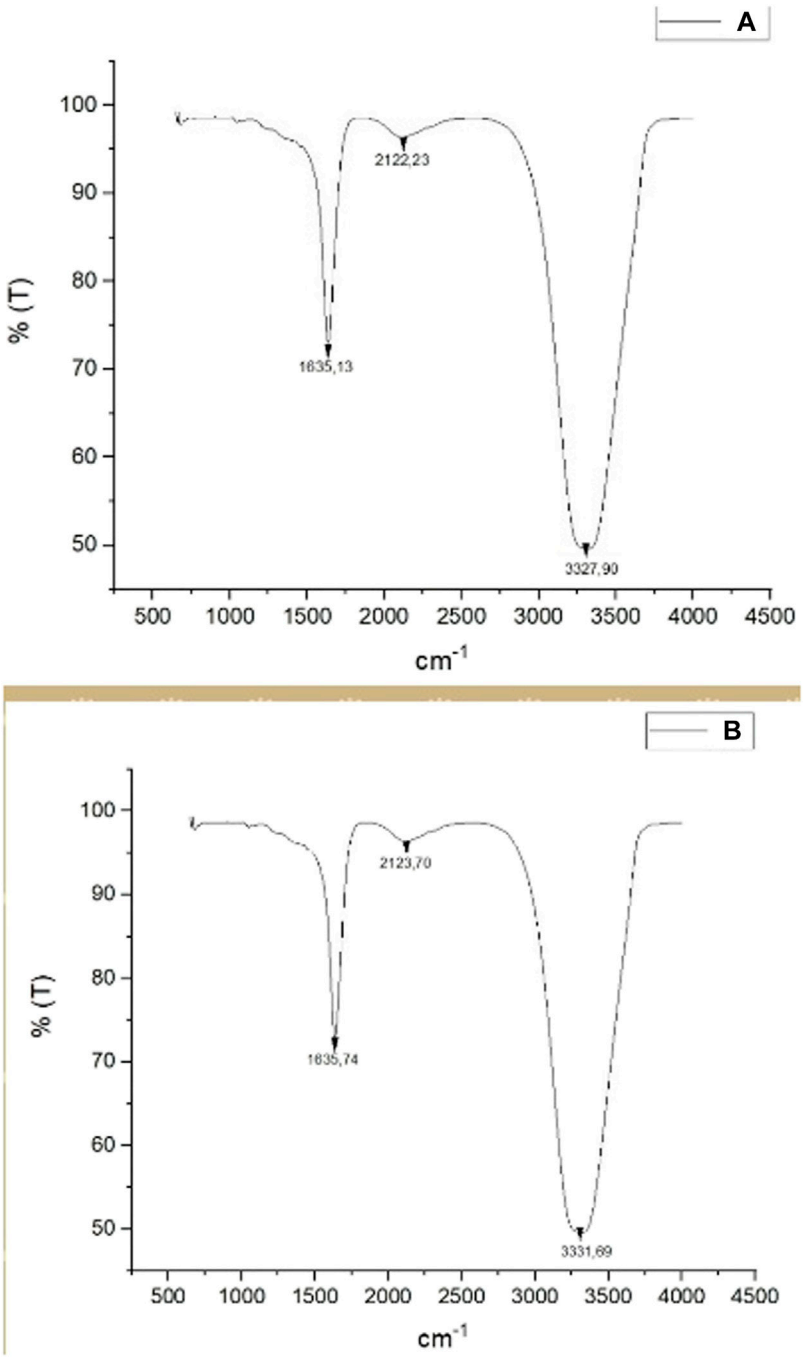

FIGURE 5 | (A) FT-IR spectra data of CA leaf extract. **(B)** FT-IR spectra data of synthesized CA-AgNPs.

Zetasizer (Malvern Ins. Ltd.). The crystal dimension of AgNPs was calculated according to the $D = K\lambda/(\beta \cos\theta)$ equation (Asadi et al., 2018; Baran et al., 2018). In addition, Fourier transform infrared spectroscopy attenuated total reflectance (FT-IR ATR) was used to identify the functional groups present in the CA extract, and the functional groups responsible for the reduction at the end of the reaction test analysis conditions of used instruments are given in **Table 1**.

Antimicrobial Activities of Silver Nanoparticles

Growth inhibition of plant-based AgNPs on Gram-positive (*B. subtilis*; *S. aureus*) and Gram-negative (*E. coli*; *P. aeruginosa*) strains and yeast (*C. albicans*) was determined using a 96-well microplate with minimum inhibition concentration (MIC) method. Mueller Hinton broth and cell culture growth medium (Roswell Park Memorial Institute medium/ RPMI)

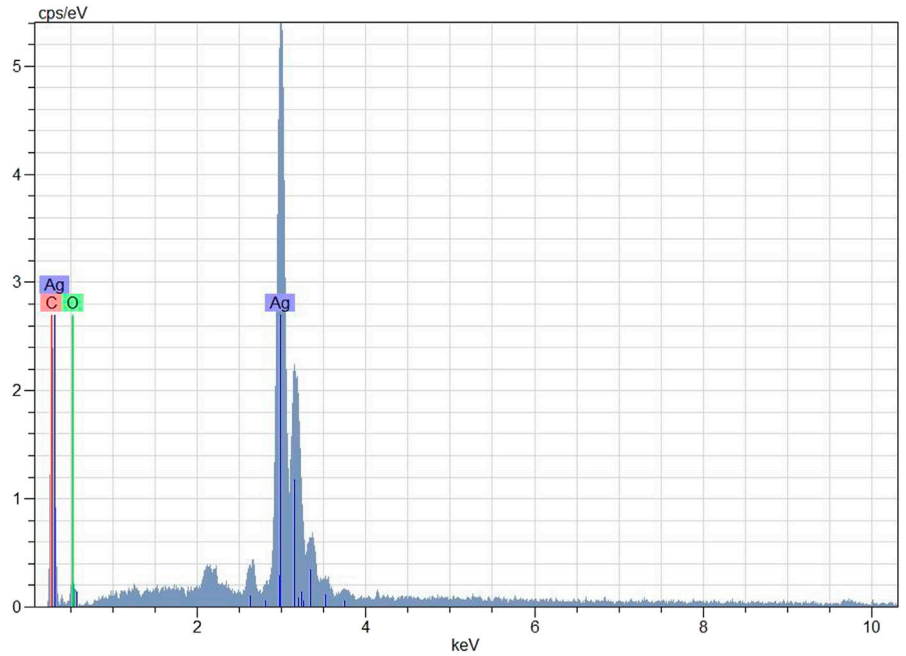

FIGURE 6 | Elemental composition of AgNPs with EDX analysis.

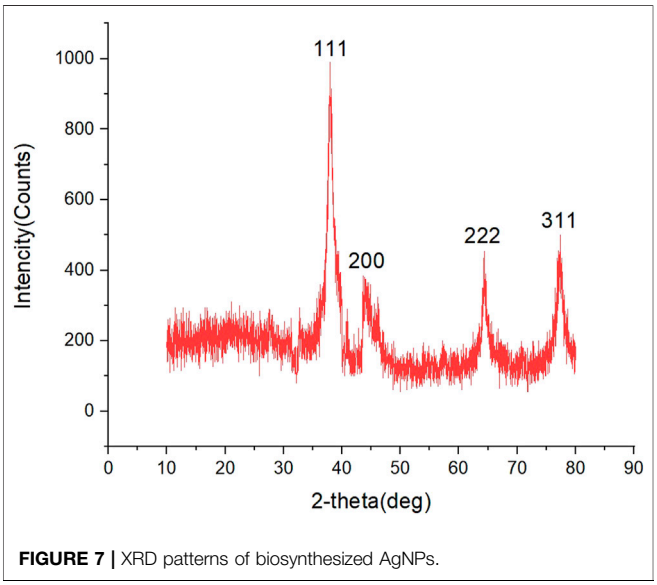

FIGURE 7 | XRD patterns of biosynthesized AgNPs.

were added to the wells for the growth of bacteria and yeast. The AgNP solution was added to the wells with the culture medium and microorganisms to determine the MIC value. Firstly, 100 µL of mixed culture medium was taken from the wells each time and transferred to the next well. Then the microorganism solutions adjusted according to the 0.5 McFarland standard were added to the microplates and incubated at 37°C/24 h. The minimum concentration without growth after incubation was determined as the MIC value (Baran et al., 2020). Commercially purchased standard antibiotics (colistin, vancomycin, and fluconazole) and 1 mM $AgNO_3$ solution were used to compare the growth inhibitory activities of AgNPs on pathogen microorganisms.

Evaluation of Viability Suppressor Activities of AgNPs by the MTT Method on Cell Line Seeding in a 96-Well Plate

The MTT method was performed to determine the plant-based AgNP ratio of cytotoxicity (viability suppressor) on cancerous and healthy cell cultures. T-75 T-flasks were used to prepare the culture medium. CaCo-2, HDF, and U118 cell lines were cultivated in DMEM solution. The human ovarian cancer cell line (SK-OV-3) was incubated in RPMI solution. Prepared cultures were incubated at 5% CO2, 37°C, and 95% air and humidity conditions. When the cells reached about 80% confluency in the hemocytometer measurement, cell cultures were suspended at different concentrations and transferred to microplates (96-well) for incubation (overnight). At the end of the period, the cultured cell lines were treated with nanoparticles at different concentrations (25, 50, 100, and 200 µg/ml) and incubated for 2 days. In the next step, the MTT solution was transferred to the microplate wells and incubated for 3 h, and then DMSO was added and kept at room temperature for 0.25 h. The absorbance (540 nm) of the microplates was measured with MultiScan Go (Thermo).

By using the below formula, the percentage viability of the cell lines was calculated.

% viability = U/C*100 (Vickers, 2017).

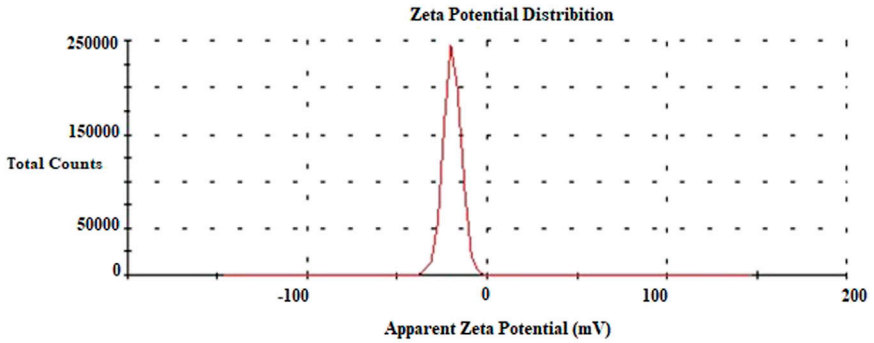

FIGURE 8 | Zeta potential data of AgNPs.

TABLE 2 | MIC results of AgNPs, $AgNO_3$, and standard antibiotics (μg/ml).

Microorganisms	AgNPs	$AgNO_3$	Antibiotics[a]
B. subtilis (Gram-positive)	0.0625	1.32	1
S. aureus (Gram-positive)	0.125	2.65	2
P. aeruginosa (Gram-negative)	1.0	1.32	4
E. coli (Gram-negative)	1.0	0.66	2
C. albicans (yeast)	0.5	0.66	2

[a]*Colistin: Gram-negative bacteria; Vancomycin: Gram-positive bacteria; Fluconazole:* Candida albicans.

TABLE 3 | The percentage viability rates of the cell lines suppressed with AgNPs.

Cell line	Concentration μg/mL			
	25	50	100	200
U118	84.53117	72.77605	72.73556	73.18908
CaCo-2	99.74733	44.98866	38.54875	36.04794
Sk-ov-3	102.5666	91.0701	80.9948	70.88769
HDF	79.70489	77.31011	73.07289	61.86905

U: Absorbance of cells treated with AgNPs.
C: The absorbance values of control cells.

RESULTS AND DISCUSSION

UV-Visible Spectroscopic *Analysis*

The color change was observed after the CA leaf extracts with AgNO3 solution were left to react in a container. The UV-vis spectrum of AgNPs appeared to change from light green to purple (**Figure 2**). Because of the surface plasmon resonance, AgNPs gave a peak at a specific absorbance value of about 417.47 nm. Similarly, some researchers reported that the absorption spectrum of AgNPs is between 425–461 nm (Udayasoorian et al., 2011).

Evaluation of SEM and TEM Data

SEM, FE-SEM, and TEM images of synthesized AgNPs are given in **Figures 3**, **4**. According to these results, it was seen that the nanomaterial was mostly spherical, nano-sized, and in clusters that were not in direct contact with each other. This indicates the stabilization of the AgNPs. It was reported that AgNPs have a spherical morphology and nano-dimensions in similar studies (Ramkumar et al., 2017a; Pallela et al., 2018). The biosynthesized nanoparticles are expected to have stronger antimicrobial activity, on account of their relatively small size. In the particle measurement done with TEM, it was seen that the sizes of AgNPs were approximately between 6.11–9.66 nm and the average size was approximately 7.83 nm (**Figure 4**). In some studies, using different materials, the sizes of AgNPs were reported to be between 2–95 nm (Nguyen et al., 2018; Behravan et al., 2019).

Evaluation of FT-IR Analysis Data

The FT-IR spectroscopy analysis determined the functional groups involved in the plant-derived reduction. The frequency of all stretch in the range of 4500–500 cm^{-1} was recorded with four scans at 1 cm^{-1} resolution. **Figure 4** shows a comparison of FT-IR spectra for the aqueous CA extract (**Figure 5A**) and synthesized AgNPs (**Figure 5B**). When the biomolecules involved in reduction during the formation of AgNPs were examined (**Figures 5A,B**), the absorption peak at 1635 cm^{-1} corresponded to the C=O stretching vibration, indicating the presence of amide. Because of the phenolic compounds in the CA leaf extract, it can be concluded that the absorption peak at 2122 cm^{-1} belongs to alkyne (C≡C) groups while the absorption peak at 3331 cm-1 belongs to O-H and N-H stretching (Atalar et al., 2021). Presumably, these determined functional groups are responsible for the reduction of metal ions (Mandal et al., 2015).

Evaluation of EDX Analysis Data

According to the EDX profile (**Figure 6**), it was confirmed that the biosynthesized nanoparticles had silver in their composition. It was also seen that the elemental composition of silver was high (**Figure 6**). AgNPs showed a typical optical absorption peak at about 3 KeV owing to the surface plasmon resonance (SPR). It can be said that the other emerging peaks are because of phytochemicals attached to the surface of AgNPs in the CA leaf pulp (Punuri et al., 2012). Khamhaengpol and Siri (2017) and Dada et al. (2019) also revealed the EDX silver peaks in their work.

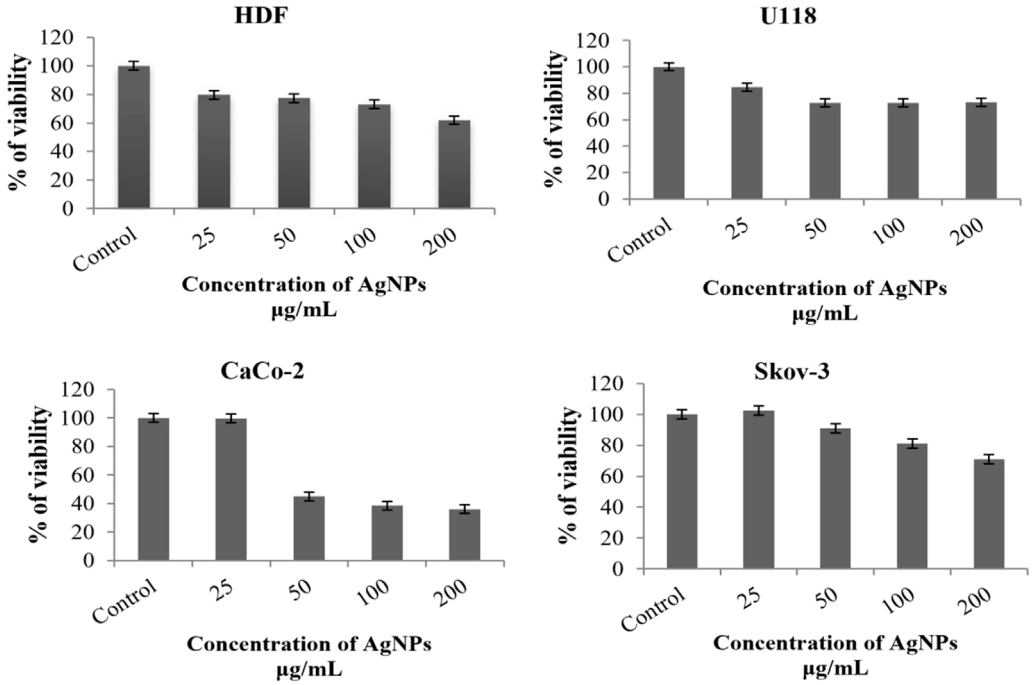

FIGURE 9 | Evaluation of the percentage viability rates as a result of the cytotoxic effect of AgNPs 2 days after combining them with CaCo-2, U118, HDF, and Sk-ov-3 cell lines.

XRD Analysis

The XRD spectrum model for the synthesized AgNPs is shown in **Figure 7**. In XRD analysis results, peaks of 111°, 200°, 220°, and 311°, which coincide with 37.96, 44.29, 64.32, and 77.33, respectively at 2θ, were sharp peaks representing the spherical crystal structure of silver. The peaks indicated that the AgNPs were cubic in structure. It has been reported in many studies that these peaks belong to silver (Huang et al., 2019; Keskin et al., 2021). The highest peak, 37.96, was taken as the peak angle. The size of the nanomaterials was calculated as approximately 12.17 nm according to the below equation ((Baran et al., 2021a).

$$D = K\lambda / (\beta \cos\theta)$$

In the equation, D = the size of the particle, K = the constant value (0.89), λ = the wavelength value of XRD (1.5418 Å), β = the FWHM value of the high peak, and cosθ = the Braggθ angle of the high peak.

Evaluation of Zeta Potential Analysis Data

The zeta potential analysis gives the electric charge on the surface of the surrounded material. The high negative value of the zeta potential prevents the particles from sticking together or clumping together. This indicates the stability of the AgNP colloid. On the other hand, nanoparticles with a significantly lower negative charge can enter the cell more easily (58–60). The zeta potential of the biosynthesized AgNPs was found to be −19.6 mV (**Figure 8**). This value indicated that the AgNPs were stable and uniformly distributed. The different zeta potential values of AgNPs synthesized from various materials have been reported previously (Ferreyra Maillard et al., 2018; Amer et al., 2020).

Evaluation of Antimicrobial Properties of AgNPs

The antimicrobial effects of AgNPs have become more important due to microorganisms that cause disease in humans developing resistance to conventional antibiotics. *S. aureus*, *B. subtillis*, *E. coli*, and *P. aeruginosa* strains and *C. albicans* yeast are pathogenic microorganisms frequently encountered in food-borne diseases (Yang et al., 2017; Mostafa et al., 2018). It was determined that the biosynthesized AgNPs significantly inhibited the growth of these microorganisms even at low concentrations (**Table 2**). It was observed that AgNPs strongly inhibited the growth of *S. aureus* and *B. subtilis* when compared to other microorganisms. Since silver has a strong tendency to interact with phosphorus and sulfur atoms in the bacterial cell wall, it interacts with the thiol and phosphorus groups in the bacterial cell membrane, thereby disrupting the bacterial respiration process. This causes the death of bacteria (Hamouda and Baker Jr, 2000). On the other hand, since the cell wall of Gram-positive bacteria has a hard polysaccharide layer, the transition to the Gram-positive bacterial wall is more difficult when compared to Gram-negative bacteria. Therefore, the inhibitory activity of AgNPs in Gram-positive bacteria is stronger than in Gram-negative bacteria (Tamboli and Lee, 2013). Thuc et al. (2016) reported that Gram-positive *S.*

aureus has approximately 2–3 times higher resistance to AgNPs than Gram-negative *E. coli* and *P. aeruginosa* (Thuc et al., 2016). These effective inhibitory activities of AgNPs on different bacteria strains and yeasts were also reported by many researchers (Niknejad et al., 2015; Aygün et al., 2020).

Evaluation of Cytotoxic Activities of AgNPs

AgNPs obtained by biosynthesis of chickpea leaf extract were applied to healthy cells (HDF) and three different cancer cell lines (CaCo-2, U118, and Sk-ov 3), and the results obtained after 48 h are shown in **Table 3** and **Figure 9**. According to these results, it was seen that there was no toxic effect in HDF with a survival rate of 79.70% at a 25 μg/ml concentration. It was determined that the most suppressed concentration of viability was on CaCo-2 cells at 200 mg/ml (**Table 3**). Despite the increase in the concentration of AgNPs in other cancer cell lines, the increase in the percentage of viability can be explained by the proliferative properties of AgNPs for these cells (Morais et al., 2020).

It is known that AgNPs show strong oxidative properties (Wongpreecha et al., 2018). AgNPs tend to settle in biomolecules such as cell membranes and nuclei. They exert a toxic effect by stimulating apoptosis with an increase in ROS after localization (Gliga et al., 2014; Morais et al., 2020). The concentration, exposure time, shape, size, charge, degree of deposition, and chemistry of the surface composition can have a significant impact on the toxicity of AgNPs (Swamy et al., 2015). In studies conducted to examine the toxic effects of AgNPs on CaCo-2 cells, it was reported that concentrations above 3.75–5.5 μg/ml showed toxic effects (Zein et al., 2020). Inhibitory concentrations in Sk-ov-3 cells were reported to be 9.4 μg/ml (Fahrenholtz et al., 2017) and 29.36 μg/ml (Noor et al., 2021). Zhang et al. (2010) reported that the 100 μg/ml concentration of silver nanoparticles was toxic on cell viability on HDF cell lines (Zhang et al., 2010).

CONCLUSION

In this study, green synthesis of silver nanoparticles (AgNPs) was carried out using *Cicer arietinum* leaf extract in a low-cost, environmentally friendly, simple, and fast method. No toxic or hazardous substances were used in the biosynthesis. The rapid and green synthesis of CA-AgNPs was successfully completed using the available phytochemicals in *Cicer arietinum* leaf extract as reducing agents. SEM and TEM images showed that spherically symmetrical plant-based AgNPs were formed due to their high stability. UV-vis absorption, XRD, and EDX analyses confirmed the synthesis of silver nanoparticles. Various microscopic analyses indicated that AgNPs had mostly spherical morphology with an average size of about 7.83 nm. The obtained analysis data showed that the smaller the size of the nanoparticles, the greater their antimicrobial activity, and the obtained AgNPs had strong antibacterial and anticandidal activity even at very low concentrations. The cytotoxic activities of CA-AgNPs were evaluated by the MTT method. A 25 μg/ml concentration of CA-AgNPs suppressed healthy cells by 20% and suppressed the viability of cancer cell lines by 1–15%. As the concentration increased, the suppression rate in cell lines other than U118 also increased. It was determined that silver nanoparticles synthesized using plant material had a high suppressive effect on the viability of CaCo-2 cells in parallel with the increase in concentration. It is known that NPs can be used in many commercial products for biological and medical applications. According to the results obtained, it is thought that CA-AgNPs can be used effectively as antimicrobial and anticancer agents in the food industry and medical applications.

DATA AVAILABILITY STATEMENT

The original contributions presented in the study are included in the article/Supplementary Material, further inquiries can be directed to the corresponding authors.

AUTHOR CONTRIBUTIONS

All authors contributed to the conception and the main idea of the work. AB, MF, CK, AH, OY, SI, MA, and MF drafted the main text, figures, and tables. CK, AE, GR, and DS supervised the work and provided the comments and additional scientific information. RK, EA, and AM also reviewed and revised the text. All authors read and approved the final version of the work to be published.

FUNDING

This work was funded by the Mardin Artuklu University Scientific Research Projects Coordinatorship (Project no: MAU.BAP.21. SHMYO.020).

ACKNOWLEDGMENTS

We are also thankful to the Tabriz University of Medical Sciences, University of Kragujevac, and Baku State University for moral support.

REFERENCES

Abu-Elghait, M., Hasanin, M., Hashem, A. H., and Salem, S. S. (2021). Ecofriendly Novel Synthesis of Tertiary Composite Based on Cellulose and Myco-Synthesized Selenium Nanoparticles: Characterization, Antibiofilm and Biocompatibility. *Int. J. Biol. Macromolecules* 175, 294–303. doi:10.1016/j.ijbiomac.2021.02.040

Aktepe, N., and Baran, A. (2021). Fast and Low Cost Biosynthesis of AgNPs with almond Leaves: Medical Applications with Biocompatible Structures. *Progr Nutr.* 23, e2021271. doi:10.23751/pn.v23i3.11996

Alkhalaf, M. I., Hussein, R. H., and Hamza, A. (2020). Green Synthesis of Silver Nanoparticles by Nigella Sativa Extract Alleviates Diabetic Neuropathy through Anti-inflammatory and Antioxidant Effects. *Saudi J. Biol. Sci.* 27, 2410–2419. doi:10.1016/j.sjbs.2020.05.005

Amer, M. I., Moustafa, S. H., and El-Hagary, M. (2020). Enhanced Band Structure, Optoelectronic and Magnetic Properties of spray Pyrolysis Ni-Doped SnO2 Nanostructured Films. *Mater. Chem. Phys.* 248, 122892. doi:10.1016/j.matchemphys.2020.122892

Asadi, N., Annabi, N., Mostafavi, E., Anzabi, M., Khalilov, R., Saghfi, S., et al. (2018). Synthesis, Characterization and *In Vitro* Evaluation of Magnetic Nanoparticles Modified with PCL-PEG-PCL for Controlled Delivery of 5FU. *Artif. Cell Nanomedicine, Biotechnol.* 46, 938–945. doi:10.1080/21691401.2018.1439839

Atalar, M. N., Baran, A., Baran, M. F., Keskin, C., Aktepe, N., Yavuz, Ö., et al. (2021). Economic Fast Synthesis of Olive Leaf Extract and Silver Nanoparticles and Biomedical Applications. *Particulate Sci. Tech.* 1977443, 1–9. doi:10.1080/02726351.2021.1977443

Aygün, A., Özdemir, S., Gülcan, M., Cellat, K., and Şen, F. (2020). Synthesis and Characterization of Reishi Mushroom-Mediated green Synthesis of Silver Nanoparticles for the Biochemical Applications. *J. Pharm. Biomed. Anal.* 178, 112970. doi:10.1016/j.jpba.2019.112970

Bandeira, M., Giovanela, M., Roesch-Ely, M., and Devine, J. (2020). Green Synthesis of Zinc Oxide Nanoparticles: A Review of the Synthesis Methodology and Mechanism of Formation. *Sust. Chem. Pharm.* 15, 100223. doi:10.1016/j.scp.2020.100223

Baran, M. F., and Applied Ecology and Environmental Research (2019). Synthesis, Characterization and Investigation of Antimicrobial Activity of Silver Nanoparticles from Cydonia Oblonga Leaf. *Appl. Ecol. Env. Res.* 17, 2583–2592. doi:10.15666/aeer/1702_25832592

Baran, M., Koç, A., and Uzan, S. J. (2018). Synthesis, Characterization and Antimicrobial Applications of Silver Nanoparticles (AgNPs) with Kenger (Gundelia Tournefortii) Leaf. *EJONS Int. J Math, Eng Nat. Sci* 5, 44–52.

Baran, M. F., Keskin, C., and Keskin, C. (2020). Determination of Antimicrobial and Toxic Metal Removal Activities of Plant-Based Synthesized (Capsicum Annuum L. Leaves), Ecofriendly, Gold Nanomaterials. *Glob. Challenges* 4, 1900104. doi:10.1002/gch2.201900104

Baran, A., Baran, M. F., Keskin, C., Kandemir, S. I., Valiyeva, M., Mehraliyeva, S., et al. (2021a). Ecofriendly/Rapid Synthesis of Silver Nanoparticles Using Extract of Waste Parts of Artichoke (Cynara Scolymus L.) and Evaluation of Their Cytotoxic and Antibacterial Activities. *J. Nanomater.* 2021, 1–10. doi:10.1155/2021/2270472

Baran, A., Keskin, C., Baran, M. F., Huseynova, I., Khalilov, R., Eftekhari, A., et al. (2021b). Ecofriendly Synthesis of Silver Nanoparticles Using Ananas Comosus Fruit Peels: Anticancer and Antimicrobial Activities. *Bioinorganic Chem. Appl.* 2021, 1–8. doi:10.1155/2021/2058149

Behravan, M., Panahi, A. H., Hossein Panahi, A., Ziaee, M., Mahdavi, R., and Mirzapour, A. (2019). Facile green Synthesis of Silver Nanoparticles Using Berberis Vulgaris Leaf and Root Aqueous Extract and its Antibacterial Activity. *Int. J. Biol. Macromolecules* 124, 148–154. doi:10.1016/j.ijbiomac.2018.11.101

Chellapandian, C., Ramkumar, B., Puja, P., Shanmuganathan, R., Pugazhendhi, A., and Kumar, P. (2019). Gold Nanoparticles Using Red Seaweed Gracilaria Verrucosa: Green Synthesis, Characterization and Biocompatibility Studies. *Process Biochem.* 80, 58–63. doi:10.1016/j.procbio.2019.02.009

Dada, A. O., Adekola, F. A., Dada, F. E., Adelani-Akande, A. T., Bello, M. O., and Okonkwo, C. R. (2019). Silver Nanoparticle Synthesis by *Acalypha wilkesiana* Extract: Phytochemical Screening, Characterization, Influence of Operational Parameters, and Preliminary Antibacterial Testing. *Heliyon.* 5 (10), e02517. doi:10.1016/j.heliyon.2019.e02517

Devatha, C. P., Thalla, A. K., and Katte, S. Y. (2016). Green Synthesis of Iron Nanoparticles Using Different Leaf Extracts for Treatment of Domestic Waste Water. *J. Clean. Prod.* 139, 1425–1435. doi:10.1016/j.jclepro.2016.09.019

Din, M. I., Rani, A., Mukhtar, M., Aihetasham, A., Mukhtar, M. J. E. N., Monitoring, et al. (2018). Single Step green Synthesis of Stable Nickel and Nickel Oxide Nanoparticles from Calotropis Gigantea : Catalytic and Antimicrobial Potentials. *Environ. Nanotechnology, Monit. Manag.* 9, 29–36. doi:10.1016/j.enmm.2017.11.005

Fahrenholtz, C. D., Swanner, J., Ramirez-Perez, M., and Singh, R. (2017). Heterogeneous Responses of Ovarian Cancer Cells to Silver Nanoparticles as a Single Agent and in Combination with Cisplatin. *J. Nanomater.* 2017, 5107485. doi:10.1155/2017/5107485

Ferreyra Maillard, A. P. V., López de Mishima, B. A., Hollmann, A., Hollmann, A. J. C., and Biointerfaces, S. (2018). Interaction of green Silver Nanoparticles with Model Membranes: Possible Role in the Antibacterial Activity. *Colloids Surf. B: Biointerfaces* 171, 320–326. doi:10.1016/j.colsurfb.2018.07.044

Gioria, E., Signorini, C., Wisniewski, F., and Gutierrez, L. (2020). Green Synthesis of Time-Stable Palladium Nanoparticles Using Microfluidic Devices. *J. Environ. Chem. Eng.* 8, 104096. doi:10.1016/j.jece.2020.104096

Gliga, A. R., Skoglund, S., Wallinder, I. O., Fadeel, B., Karlsson, H. L. J. P., and Toxicology, F. (2014). Size-dependent Cytotoxicity of Silver Nanoparticles in Human Lung Cells: the Role of Cellular Uptake, Agglomeration and Ag Release. *Part. Fibre Toxicol.* 11, 1–17. doi:10.1186/1743-8977-11-11

Hamouda, T., and Baker, J. R. (2000). Antimicrobial Mechanism of Action of Surfactant Lipid Preparations in Enteric Gram-Negative Bacilli. *Antimicrob. mechanism Action. surfactant lipid preparations enteric Gram-negative bacilli* 89, 397–403. doi:10.1046/j.1365-2672.2000.01127.x

Hasanzadeh, A., Gholipour, B., Rostamnia, S., Eftekhari, A., Tanomand, A., Valizadeh. K, A., et al. (2021). Biosynthesis of AgNPs onto the Urea-Based Periodic Mesoporous Organosilica (AgxNPs/Ur-PMO) for Antibacterial and Cell Viability Assay. *J. Colloid Interf. Sci.* 585, 676–683. doi:10.1016/j.jcis.2020.10.047

Hatipoğlu, A. (2021). Green Synthesis of Gold Nanoparticles from Prunus Cerasifera Pissardii Nigra Leaf and Their Antimicrobial Activities on Some Food Pathogens. *Prog. Nutr.* 23, e2021241. doi:10.23751/pn.v23i3.11947

Hoseinnejad, M., Jafari, S. M., and Katouzian, I. (2018). Inorganic and Metal Nanoparticles and Their Antimicrobial Activity in Food Packaging Applications. *Crit. Rev. Microbiol.* 44, 161–181. doi:10.1080/1040841x.2017.1332001

Huang, X., Wang, R., Jiao, T., Zou, G., Zhan, F., Yin, J., et al. (2019). Facile Preparation of Hierarchical AgNP-Loaded MXene/Fe3O4/Polymer Nanocomposites by Electrospinning with Enhanced Catalytic Performance for Wastewater Treatment. *ACS Omega* 4, 1897–1906. doi:10.1021/acsomega.8b03615

Hussain, I., Singh, N. B., Singh, A., Singh, H., and Singh, S. C. (2016). Green Synthesis of Nanoparticles and its Potential Application. *Biotechnol. Lett.* 38, 545–560. doi:10.1007/s10529-015-2026-7

Javaid, A., Oloketuyi, S. F., Oloketuyi, M. M., and Khan, F. (2018). Diversity of Bacterial Synthesis of Silver Nanoparticles. *BioNanoSci.* 8, 43–59. doi:10.1007/s12668-017-0496-x

Jayappa, M. D., Kumar, M. A. P., Prabhu, A., Sheikh, S., Prabhu, A., Devasya, R. P., et al. (2020). Green Synthesis of Zinc Oxide Nanoparticles from the Leaf, Stem and *In Vitro* Grown Callus of Mussaenda Frondosa L.: Characterization and Their Applications. *Appl. Nanosci* 10, 3057–3074. doi:10.1007/s13204-020-01382-2

Jayaprakash, N., Vijaya, J. J., Vijaya, K., Kombaiah, K., Kennedy, L. J., Kennedy, R. J., et al. (2017). Green Synthesis of Ag Nanoparticles Using Tamarind Fruit Extract for the Antibacterial Studies. *J. Photochem. Photobiol. B: Biol.* 169, 178–185. doi:10.1016/j.jphotobiol.2017.03.013

Kafshdooz, L., Pourfathi, H., Akbarzadeh, A., Kafshdooz, T., Razban, Z., Sheervalilou, R., et al. (2018). The Role of microRNAs and Nanoparticles in Ovarian Cancer: a Review. *Artif. Cell Nanomedicine, Biotechnol.* 46, 241–247. doi:10.1080/21691401.2018.1454931

Keskin, C., Atalar, M. N., Firat Baran, M., and Baran, A. J. (2021). Environmentally Friendly Rapid Synthesis of Gold Nanoparticles from Artemisia Absinthium Plant Extract and Application of Antimicrobial Activities. *J. Inst. Sci. Tech.* 11, 365–375. doi:10.21597/jist.779169

Khamhaengpol, A., and Siri, S. (2017). Green Synthesis of Silver Nanoparticles Using Tissue Extract of Weaver Ant Larvae. *Mater. Lett.* 192, 72–75. doi:10.1016/j.matlet.2017.01.076

Kowsalya, E., Mosachristas, K., Balashanmugam, P., Manivasagan, V., Devasena, T., and Jaquline, C. (2021). Sustainable Use of Biowaste for Synthesis of Silver Nanoparticles and its Incorporation into Gelatin-Based Nanocomposite Films for Antimicrobial Food Packaging Applications. *J. Food Process Eng.* 44, e13641. doi:10.1111/jfpe.13641

Kumar, N., Biswas, K., and Gupta, R. K. (2016). Green Synthesis of Ag Nanoparticles in Large Quantity by Cryomilling. *RSC Adv.* 6, 111380–111388. doi:10.1039/c6ra23120a

Kumari, P., Alam, M., and Siddiqi, W. A. (2019). Usage of Nanoparticles as Adsorbents for Waste Water Treatment: An Emerging Trend. *Sust. Mater. Tech.* 22, e00128. doi:10.1016/j.susmat.2019.e00128

Mandal, A., Sekar, S., Chandrasekaran, N., Mukherjee, A., and Sastry, T. P. (2015). Vibrational Spectroscopic Investigation on Interaction of Sago Starch Capped

Silver Nanoparticles with Collagen: a Comparative Physicochemical Study Using FT-IR and FT-Raman Techniques. *RSC Adv.* 5, 15763–15771. doi:10.1039/c4ra09694k

Mohmed, A. A., Saad, E., Fouda, A., Elgamal, M. S., and Salem, S. (2017). Extracellular Biosynthesis of Silver Nanoparticles Using Aspergillus Sp. And Evaluation of Their Antibacterial and Cytotoxicity. *J. Appl. Life Sci. Int.* 11, 1–12. doi:10.9734/jalsi/2017/33491

Molnár, Z., Bódai, V., Szakacs, G., Erdélyi, B., Fogarassy, Z., Sáfrán, G., et al. (2018). Green Synthesis of Gold Nanoparticles by Thermophilic Filamentous Fungi. *Scientific Rep.* 8, 1–12. doi:10.1038/s41598-018-22112-3

Morais, M., Teixeira, A. L., Teixeira, F., Machado, V., Medeiros, R., and Prior, J. A. V. (2020). Cytotoxic Effect of Silver Nanoparticles Synthesized by Green Methods in Cancer. *J. Med. Chem.* 63, 14308–14335. doi:10.1021/acs.jmedchem.0c01055

Mostafa, A. A., Almaary, K. S., Sholkamy, E. N., Bakri, M. M., Sholkamy, E. N., and Bakri, M. (2018). Antimicrobial Activity of Some Plant Extracts against Bacterial Strains Causing Food Poisoning Diseases. *Saudi J. Biol. Sci.* 25, 361–366. doi:10.1016/j.sjbs.2017.02.004

Mousavi, S. M., Ghasemi, Y., Amani, A. M., Savar Dashtaki, A., Amani, A. M., Arjmand, O., et al. (2018). Green Synthesis of Silver Nanoparticles toward Bio and Medical Applications: Review Study. *Artif. Cell Nanomedicine, Biotechnol.* 46, S855–S872. doi:10.1080/21691401.2018.1517769

Nguyen, T.-D., Dang, C.-H., and Mai, D.-T. (2018). Biosynthesized AgNP Capped on Novel Nanocomposite 2-Hydroxypropyl-β-Cyclodextrin/alginate as a Catalyst for Degradation of Pollutants. *Carbohydr. Polym.* 197, 29–37. doi:10.1016/j.carbpol.2018.05.077

Niknejad, F., Nabili, M., Daie Ghazvini, R., and Moazeni, M. (2015). Green Synthesis of Silver Nanoparticles: Another Honor for the Yeast Model *Saccharomyces cerevisiae*. *mazu-cmm* 1, 17–24. doi:10.18869/acadpub.cmm.1.3.17

Noor, F., Noor, A., Ishaq, A. R., Farzeen, I., Saleem, M. H., Ghaffar, K., et al. (2021). Recent Advances in Diagnostic and Therapeutic Approaches for Breast Cancer: A Comprehensive Review. *Curr. Pharm. Des.* 27, 2344–2365. doi:10.2174/1381612827666210303141416

Pallela, P. N. V. K., Ruddaraju, L. K., Ruddaraju, L. K., Yoon, S.-G., and Yoon, S.-G. (2018). Ultra Small, Mono Dispersed green Synthesized Silver Nanoparticles Using Aqueous Extract of Sida Cordifolia Plant and Investigation of Antibacterial Activity. *Microb. Pathogenesis* 124, 63–69. doi:10.1016/j.micpath.2018.08.026

Parial, D., Patra, H. K., Patra, A. K., and Pal, R. (2012). Screening of Different Algae for green Synthesis of Gold Nanoparticles. *Eur. J. Phycology* 47, 22–29. doi:10.1080/09670262.2011.653406

Patra, J. K., and Baek, K.-H. (2016). Green Synthesis of Silver Chloride Nanoparticles Using Prunus Persica L. Outer Peel Extract and Investigation of Antibacterial, Anticandidal, Antioxidant Potential. *Green. Chem. Lett. Rev.* 9, 132–142. doi:10.1080/17518253.2016.1192692

Punuri, J. B., Sharma, P., Sibyala, S., Tamuli, R., and Bora, U. (2012). Piper Betle-Mediated green Synthesis of Biocompatible Gold Nanoparticles. *Int. Nano Lett.* 2, 1–9. doi:10.1186/2228-5326-2-18

Ramkumar, V. S., Gopalakrishnan, K., Sivagurunathan, P., Saratale, G. D., Saratale, G. D., Kannapiran, E., et al. (2017a). Biofabrication and Characterization of Silver Nanoparticles Using Aqueous Extract of Seaweed Enteromorpha Compressa and its Biomedical Properties. *Biotechnol. Rep.* 14, 1–7. doi:10.1016/j.btre.2017.02.001

Ramkumar, V. S., Prakash, S., Ahila, N. K., Vinoj, G., Selvam, S., Kumar, G., et al. (2017b). Synthesis of Platinum Nanoparticles Using Seaweed Padina Gymnospora and Their Catalytic Activity as PVP/PtNPs Nanocomposite towards Biological Applications. *Biomed. Pharmacother.* 92, 479–490. doi:10.1016/j.biopha.2017.05.076

Ramya, M., and Subapriya, M. (2012). *Green Synthesis of Silver Nanoparticles*, 1, 54–61.

Shumail, H., Khalid, S., Ahmad, I., Khan, H., Amin, S., and Ullah, B. (2021). Review on Green Synthesis of Silver Nanoparticles through Plants. *Endocr. Metab. Immune Disord. Drug Targets* 21 (6), 994–1007. doi:10.2174/1871530320666200729153714

Swamy, M. K., Mohanty, S. K., Sinniah, U. R., and Spectroscopy, B. (2015). Synthesis and Characterization of Silver Nanoparticles Using Fruit Extract of Momordica Cymbalaria and Assessment of Their *In Vitro* Antimicrobial, Antioxidant and Cytotoxicity Activities. *Spectrochimica Acta A: Mol. Biomol. Spectrosc.* 151, 939–944. doi:10.1016/j.saa.2015.07.009

Tamboli, D. P., and Lee, D. S. (2013). Mechanistic Antimicrobial Approach of Extracellularly Synthesized Silver Nanoparticles against Gram Positive and Gram Negative Bacteria. *J. Hazard. Mater.* 260, 878–884. doi:10.1016/j.jhazmat.2013.06.003

Thuc, D. T., Huy, T. Q., Hoang, L. H., Tien, B. C., Van Chung, P., Thuy, N. T., et al. (2016). Green Synthesis of Colloidal Silver Nanoparticles through Electrochemical Method and Their Antibacterial Activity. *Mater. Lett.* 181, 173–177. doi:10.1016/j.matlet.2016.06.008

Udayasoorian, C., Kumar, K. V., and Jayabalakrishnan, M. (2011). Extracellular Synthesis of Silver Nanoparticles Using Leaf Extract of Cassia Auriculata. *Dig. J. Nanomater. Biostructures* 6, 279–283.

Umaz, A., Koç, A., Baran, M. F., Atalar, M. J., and Keskïn, M. N. (2019). Investigation of Antimicrobial Activity and Characterization, Synthesis of Silver Nanoparticles from Hypericum Triquetrifolium Turra Plant. *J. Inst. Sci. Tech.* 9, 1467–1475. doi:10.21597/jist.533115

Vickers, N. J. (2017). Animal Communication: When I'm Calling You, Will You Answer Too? *Curr. Biol.* 27, R713–R715. doi:10.1016/j.cub.2017.05.064

Wongpreecha, J., Polpanich, D., Suteewong, T., Kaewsaneha, C., and Tangboriboonrat, P. (2018). One-pot, Large-Scale green Synthesis of Silver Nanoparticles-Chitosan with Enhanced Antibacterial Activity and Low Cytotoxicity. *Carbohydr. Polym.* 199, 641–648. doi:10.1016/j.carbpol.2018.07.039

Yadi, M., Mostafavi, E., Saleh, B., Davaran, S., Aliyeva, I., Khalilov, R., et al. (2018). Current Developments in green Synthesis of Metallic Nanoparticles Using Plant Extracts: a Review. *Artif. Cell Nanomedicine, Biotechnol.* 46, S336–S343. doi:10.1080/21691401.2018.1492931

Yang, S.-C., Lin, C.-H., Aljuffali, I. A., and Aljuffali, J.-Y. (2017). Current Pathogenic *Escherichia coli* Foodborne Outbreak Cases and Therapy Development. *Arch. Microbiol.* 199, 811–825. doi:10.1007/s00203-017-1393-y

Zein, R., Alghoraibi, I., Soukkarieh, C., Salman, A., and Alahmad, A. (2020). *In-vitro* Anticancer Activity against Caco-2 Cell Line of Colloidal Nano Silver Synthesized Using Aqueous Extract of Eucalyptus Camaldulensis Leaves. *Heliyon* 6, e04594.

Zhang, Y., Yang, D., Kong, Y., Wang, X., Pandoli, O., and Gao, G. (2010). Synergetic Antibacterial Effects of Silver Nanoparticles@ Aloe Vera Prepared via a green Method. *Nano Biomed. Eng.* 2, 252–257. doi:10.5101/nbe.v2i4.p252-257

Conflict of Interest: The authors declare that the research was conducted in the absence of any commercial or financial relationships that could be construed as a potential conflict of interest.

Publisher's Note: All claims expressed in this article are solely those of the authors and do not necessarily represent those of their affiliated organizations, or those of the publisher, the editors and the reviewers. Any product that may be evaluated in this article, or claim that may be made by its manufacturer, is not guaranteed or endorsed by the publisher.

frontiers | Frontiers in Bioengineering and Biotechnology

ORIGINAL RESEARCH
published: 05 April 2022
doi: 10.3389/fbioe.2022.849464

Reduced Genotoxicity of Gold Nanoparticles With Protein Corona in *Allium cepa*

Sagar S. Arya[1,2], *James E. Rookes*[2], *David M. Cahill*[2] *and Sangram K. Lenka*[1]*

[1]*The Energy and Resources Institute, TERI-Deakin Nanobiotechnology Centre, Gurugram, India,* [2]*School of Life and Environmental Sciences, Deakin University, Waurn Ponds Campus, Geelong, VIC, Australia*

Increased usage of gold nanoparticles (AuNPs) in biomedicine, biosensing, diagnostics and cosmetics has undoubtedly facilitated accidental and unintentional release of AuNPs into specific microenvironments. This is raising serious questions concerning adverse effects of AuNPs on off-target cells, tissues and/or organisms. Applications utilizing AuNPs will typically expose the nanoparticles to biological fluids such as cell serum and/or culture media, resulting in the formation of protein corona (PC) on the AuNPs. Evidence for PC altering the toxicological signatures of AuNPs is well studied in animal systems. In this report, we observed significant genotoxicity in *Allium cepa* root meristematic cells (an off-target bioindicator) treated with high concentrations (≥100 µg/ml) of green-synthesized vanillin capped gold nanoparticles (VAuNPs). In contrast, protein-coated VAuNPs (PC-VAuNPs) of similar concentrations had negligible genotoxic effects. This could be attributed to the change in physicochemical characteristics due to surface functionalization of proteins on VAuNPs and/or differential bioaccumulation of gold ions in root cells. High elemental gold accumulation was evident from µ-XRF mapping in VAuNPs-treated roots compared to treatment with PC-VAuNPs. These data infer that the toxicological signatures of AuNPs are influenced by the biological route that they follow to reach off-target organisms such as plants. Hence, the current findings highlight the genotoxic risk associated with AuNPs, which, due to the enhanced utility, are emerging as new pollutants. As conflicting observations on the toxicity of green-synthesized AuNPs are increasingly reported, we recommend that detailed studies are required to investigate the changes in the toxicological signatures of AuNPs, particularly before and after their interaction with biological media and systems.

Keywords: vanillin capped gold nanoparticles, protein corona, plant, genotoxicity, chromosomal aberrations

OPEN ACCESS

Edited by:
Ravi Shukla,
RMIT University, Australia

Reviewed by:
Arpita Poddar,
RMIT University, Australia
Hemant Kumar Daima,
Amity University Jaipur, India

***Correspondence:**
Sangram K. Lenka
keshari2u@gmail.com

Specialty section:
This article was submitted to Nanobiotechnology, a section of the journal Frontiers in Bioengineering and Biotechnology

Received: *11 January 2022*
Accepted: *15 March 2022*
Published: *05 April 2022*

Citation:
Arya SS, Rookes JE, Cahill DM and Lenka SK (2022) Reduced Genotoxicity of Gold Nanoparticles With Protein Corona in Allium cepa. Front. Bioeng. Biotechnol. 10:849464. doi: 10.3389/fbioe.2022.849464

INTRODUCTION

The global market of gold nanoparticles (AuNPs) is estimated to reach 6.33 billion USD by 2025 due to their increasing usage in biomedicine, biosensing, diagnostics and cosmetics (Grandviewresearch, 2019). AuNPs have gained wide application because of their chemical inertness, perceived low intrinsic cytotoxicity, customizable nanoscale morphology, prospects for surface functionalization and their plasmonic properties that are capable of inducing biological responses (Mosquera et al., 2020; Umapathi et al., 2020; Kumawat et al., 2022). However, this rapid increase in the use of AuNPs has enhanced the likelihood of their release into a specific microenvironment (Gomez et al., 2014)

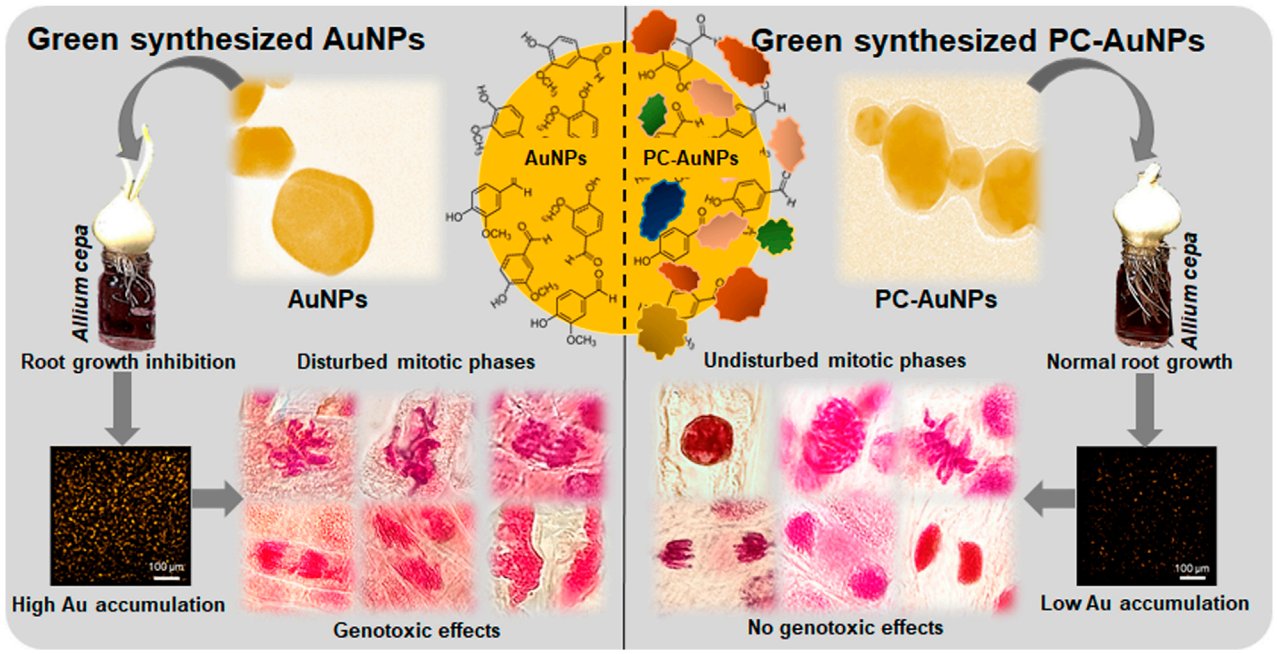

GRAPHICAL ABSTRACT |

through their use such as that for functionalized/capped AuNPs that have been examined for cancer diagnosis/therapy (Sztandera et al., 2018), wound healing (Naraginti et al., 2016), drug delivery (Katsnelson et al., 2013; Kyriazi et al., 2018; Lopez-Chaves et al., 2018; Ansari et al., 2019), as cosmetic components (Cao et al., 2016), for chemical sensing (Qin et al., 2018) and antibacterial applications (Zong et al., 2017; Govindaraju et al., 2018). During such biological applications, AuNPs are exposed to biological fluids or cell culture media, which can result in the adsorption of proteins onto their surface, forming a so-called "protein corona" (PC) (Mosquera et al., 2020). This aggregated cloud of proteins has been attributed to altering or masking the functional signatures of green-synthesized AuNPs (Mosquera et al., 2020). With increasing reports of green-synthesized AuNPs being tested in animal cell cultures/models (Naraginti et al., 2016; Mukherjee et al., 2017; Ovais et al., 2018), and with promotion of AuNPs-supplemented cosmetics (Cao et al., 2016; Fytianos et al., 2020), it is important to evaluate and compare the toxicity of such engineered AuNPs with and without PC on off-target organisms. Previous toxicity studies have focused predominantly on animal cell cultures (Wheeler et al., 2021), suggesting that the relevance of PC formed on AuNPs, and the collective effect of such PC-AuNPs on off-target organisms is yet to be determined.

Since the 1980s, *A. cepa* has been extensively used to investigate the possible genotoxic effects of chemicals on off-target species (WHO, 1985). The United Nations Environment Programme and International Programme on Chemical Safety certify *A. cepa* as a standard bioindicator to analyze genotoxicity of environmental pollutants (Grant, 1982; WHO, 1985; Adair and Cobb, 1999). *Allium cepa* is also one of the best-suited models for *in vivo* cytogenotoxicity analysis of emerging environmental pollutants and is often used to predict and/or correlate the toxicity data with animal cell cultures/models (Maity et al., 2020). The prime advantages in using *A. cepa* as an *in vivo* model include easy monitoring of root growth in direct contact with the target chemical/material, since this species exhibits distinct phenotypic and genotypic responses to genotoxic materials (Bonciu et al., 2018). Further, the cytogenetic abnormalities of mitotic phases can be easily observed using optical microscopy as well as rapid and cost-effective assays that can be developed using root culture (Tedesco and Laughinghouse IV, 2012). Therefore, numerous studies have used *A. cepa*-based assays to test the genotoxicity of nanoparticles (Kumari et al., 2011; Pesnya, 2013; Saha and Gupta, 2017; Scherer et al., 2019; Liman et al., 2021). Collectively, these previous investigations indicate that spontaneous reactive oxygen species (ROS) generation occurs following cellular internalization of various types of nanoparticles, resulting in lipid peroxidation that leads to a decrease in the mitotic index and the triggering of chromosomal abnormalities. The system *A. cepa* was chosen based on the ease of availability and visualization of chromosomal aberrations in real time compared to other model plants, such as *Vicia* spp. and *Nicotiana tabacum*, respectively. Although *Nicotiana* spp. are used to assess nanotoxicity based on comet assay, root growth and biochemical parameters (Lovecká et al., 2021), are secondary observations.

While numerous studies have highlighted the genotoxic effects of silver and other metal nanoparticles on *A. cepa*, only a few reports describe the influence of AuNPs, which is surprising given

the enormous research focus and potential industrial applications of AuNPs. There are some reports, which provide evidence for the genotoxic signatures of functionalized/capped AuNPs on *A. cepa* (Gopinath et al., 2013; Rajeshwari et al., 2016a; Rajeshwari et al., 2016b; Debnath et al., 2018). For instance, it was observed that the mitotic index of *A. cepa* meristematic cells treated with citrate-capped AuNPs was directly proportional to the concentration and inversely related to the size of AuNPs (Rajeshwari et al., 2016b). In the case of CTAB-capped Au nanorods, cyto-genotoxicity increased in a dose-dependent manner, whereas for PEG-capped gold nanorods the toxicity remained insignificant irrespective of the tested concentration range, which was 0.1–10 μg/ml (Rajeshwari et al., 2016a). Contrary to the above findings, AuNPs synthesized using *Sphaeranthus indicus* extract (1–10%) promoted mitotic cell division in *A. cepa* root tips depending on the concentration of extract used, with 10% of extract synthesized AuNPs showing the highest mitotic index (Balalakshmi et al., 2017). Similarly, studies performed on *Oryza sativa* (Ndeh et al., 2017), *Vigna radiata* (Das et al., 2017), and several other species (Venzhik et al., 2021), showed that AuNPs have the potential to enhance germination rate, growth and photosynthesis at higher concentrations, i.e., 10–1,000 μg/ml. Such contradictory observations towards AuNPs suggest that, AuNPs, irrespective of their origin and application, should be tested for the presence of off-target effects at high concentrations.

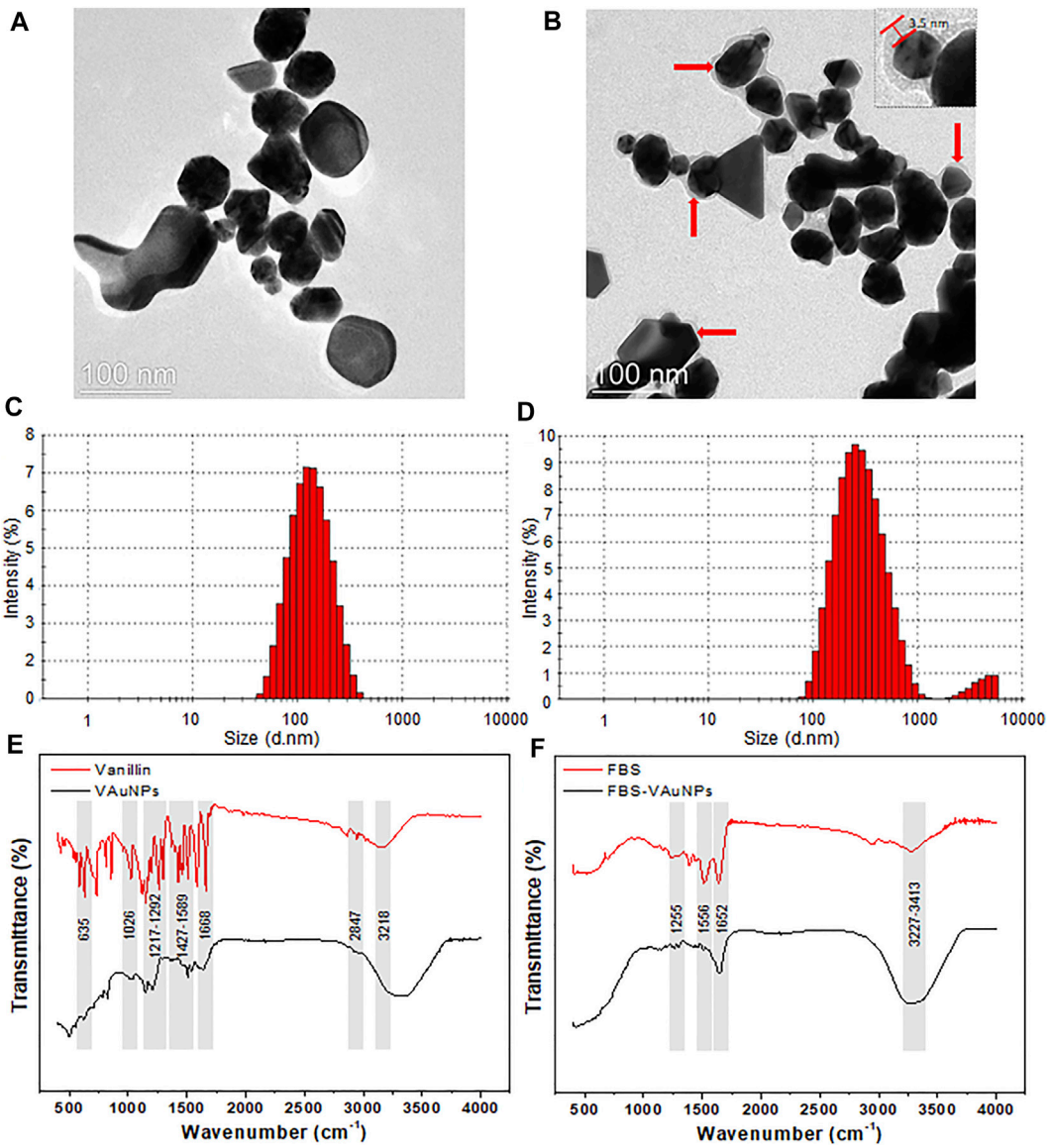

FIGURE 1 | TEM, hydrodynamic size distribution and FTIR of bare VAuNPs **(A,C,E)**, and PC-VAuNPs **(B,D,F)**, respectively. Solid red arrows **(B)** show the build-up of protein coating with average thickness of 3.5 ± 1.73 nm, which appears as a grey shadow around dark VAuNPs.

Presently, given the conflicting results in the literature describing the bioactivity and biocompatibility of engineered AuNPs in plants, there is no clear consensus towards the toxicological signature of AuNPs (Sani et al., 2021). Furthermore, none of the available data details how the PC can influence the toxicological signatures of AuNPs, specifically on an off-target plant model. In this regard, we investigated the genotoxic effects of green-synthesized vanillin capped gold nanoparticles (VAuNPs) (Arya et al., 2019), and protein-coated VAuNPs (PC-VAuNPs) on *A. cepa* (PC in the present study refers to the coating of proteins after treating VAuNPs with Fetal bovine serum). Vanillin (vanilla flavour) was used as a capping agent owing to its popularity as a flavouring molecule (Arya et al., 2022), as well as its widely reported bioactive potential (Arya et al., 2021a; Arya et al., 2021b). Moreover, we have earlier reported that vanillin and its gold nanoparticle formulations can be used as antibiotic resistance reversal agents. Organic capping agents like curcumin or citric acid are extensively explored for toxicity studies. Additionally, the outcome of the toxicity studies of vanillin capped AuNP can be correlated with curcumin capped AuNPs as well.

Due to the growing interest in green-synthesized AuNPs compared with those that are chemically synthesized, we used biomolecule capped AuNPs for our genotoxicity analysis. This report details the differences in the genotoxicity between bare and protein-coated AuNPs on the off-target model plant *A. cepa*. The outcomes provide important new information on the role of PC in defining the toxicological signatures of green-synthesized AuNPs.

MATERIALS AND METHODS

Synthesis and Characterization of VAuNPs With and Without Protein Corona

VAuNPs were synthesized according to the previously described method (Arya et al., 2019). Briefly, 2 mM gold chloride ($HAuCl_4$) was reduced with 1 mM vanillin (Sigma Aldrich, St. Louis, United States) for 3 h at room temperature. The synthesized VAuNPs were centrifuged (13,000 rpm, 20 min; Eppendorf™ Cooled Centrifuge 5424 R, Germany) and washed thrice with sterile deionized water.

To mimic the laboratory cell culture condition, the procedure to form PC around VAuNPs was performed as described earlier with slight modifications (Cheng et al., 2015; Mosquera et al., 2020). Briefly, the VAuNPs were incubated in fetal bovine serum [FBS, 10% in phosphate buffer saline (PBS)] at 37 ± 2°C for 24 h to form FBS-VAuNPs, i.e., PC-VAuNPs. After incubation, the VAuNPs suspension was centrifuged (13,000 rpm, 20 min; Eppendorf™ Cooled Centrifuge 5424 R, Germany) and the pellet formed was rinsed thrice with PBS to remove unbound proteins from VAuNPs. The synthesis of bare VAuNPs and PC-VAuNPs was confirmed by their characterization using UV-visible spectrophotometry (UV-2450, Spectrophotometer, Shimadzu, Kyoto, Japan), dynamic light scattering (Malvern Zetasizer Nano ZS, United States), transmission electron microscopy (TEM) (FEI Tecnai F20 TEM, Philips, Netherlands) and Fourier transform infrared spectrophotometry (FTIR) (Nicolet 6,700, Thermo Scientific, United States).

Allium cepa Genotoxicity and Microscopic Analysis

The genotoxicity studies were performed in *A. cepa* with the synthesized VAuNPs as described earlier (Rajeshwari et al., 2016b). Equal-sized (25–30 mm) and healthy *A. cepa* bulbs, weighing 30–35 g obtained from a local vegetable market (Gurugram, India) were grown under dark conditions in an enclosed chamber. A temperature of 25 ± 2°C was maintained, and renewed water supply was provided for every 24 h. Roots of 2–3 cm were excised from the bulb and treated with various concentrations (0, 12.5, 25, 50, 100 and 200 μg/ml) of the VAuNPs. A treatment group exposed to 100 μM $AgNO_3$ (16.98 μg/ml) was used as the positive control due to its proven genotoxicity and root growth inhibitory effects (Cvjetko et al., 2017). Ultrapure ion-free "MilliQ" water was used as a negative control. The aqueous colloidal solutions of VAuNPs and $AgNO_3$ were prepared by resuspending and dissolving, respectively, in ultrapure ion-free MilliQ water. Three replicates were made for each concentration.

After 4 h of exposure, the root tips were removed and rinsed with sterile deionized water. Then, the root tips were immersed in 1 M HCl for 20 min and dipped in acetocarmine stain for 5 min (Rajeshwari et al., 2016b). The root tips were then rinsed to remove excess stain and approximately 1–2 mm sections were cut, using a scalpel, from each root tip. The sections were placed onto a glass slide and covered with a coverslip. The coverslips were gently pressed using light thumb pressure to prepare a uniformly thick section squash. The slides were examined under an optical microscope (Axiostar, Zeiss, Germany) and the genotoxic effect of VAuNPs and $AgNO_3$ on the root tip cells were determined by scoring 10^3 cells with three replicates per test concentration. The mitotic index, phase index, and the total number of cellular abnormalities observed in mitotic cells were calculated using the following formulas (Saha and Gupta, 2017).

$$Mitotic\ index\ (MI)\% = \left(\frac{TDC}{TC}\right)*100$$

$$Phase\ index\ (PI)\% = \left(\frac{TCP}{TDC}\right)*100$$

$$Chromosonal\ Aberrations\ (CA)\% = \left(\frac{TCA}{TC}\right)*100$$

Where, TDC was the total number of dividing cells, TC was the total number of cells counted, TCP the total number of cells in a particular mitotic phase and TCA the total number of cells that showed chromosomal aberrations.

Similarly, the protein coated VAuNPs (100 and 200 μg/ml) were analyzed for any genotoxic effects using the above protocol. Vanillin (1 mM) and Fetal Bovine Serum (10% FBS in sterile deionized water) were used as controls, based on their use in capping and coating, respectively.

Allium cepa Root Growth Assay

A growth inhibition test was performed according to the protocol of Cvjetko et al. (2017). *A. cepa* bulbs were scraped and peeled to remove dried roots and outer shells, respectively to expose the root primordial apices. Bulbs were then placed on the top of flat bottom glass tubes (Borosil, India) (one bulb per tube) filled with different concentrations of VAuNPs (0, 12.5, 25, 50, 100, and 200 μg/ml), and kept in dark conditions at 25 ± 2°C for 96 h. The $AgNO_3$ treatment of 100 μM (16.98 μg/ml) was used as a positive control. To determine the root length and EC_{50} value, the length of the five longest roots (30 roots from 3 bulbs) was measured from each control and treated onion bulb.

Similarly, the PC-VAuNPs (100 and 200 μg/ml) were analyzed for any root growth inhibition effects using the above-mentioned protocol. Vanillin (1 mM) and FBS (10% FBS in sterile deionized water) were used as controls.

Estimation of Catalase Activity

Catalase (CAT) activity in the root tips cells was evaluated as previously described (Rajeshwari et al., 2015; Souza et al., 2020), with slight modification. Approximately 200 mg of root tips (e.g., a minimum of 10 roots) from each treatment of VAuNPs (0—200 μg/ml), $AgNO_3$ (100 μM), vanillin (1 mM), FBS (10%) and PC-VAuNPs (100 and 200 μg/ml) were taken after 4 h of incubation and were homogenized manually in a chilled mortar and pestle at 4°C in 1.5 ml potassium phosphate buffer (100 mM, pH 7) containing 0.1 mM EDTA. The homogenate was centrifuged for 30 min at 10,000 rpm and 4°C (Eppendorf™ Cooled Centrifuge 5424 R, Germany), and then the enzyme-containing supernatant was separated and used to estimate CAT activity. The 3 ml reaction mixture consisted of 2.96 ml of potassium phosphate buffer (100 mM, pH 7) and 20 μl of enzyme extract. The reaction was started by adding 2.5 μl of 30% of hydrogen peroxide (H_2O_2). The activity was quantified based on the consumption of exogenous H_2O_2 by CAT, generating water and oxygen with a decrease in spectrophotometric absorbance at 280 nm.

Histochemical Staining and Determination of Superoxide Radical

The production of a superoxide radical (O_2^-) was visually examined in *A. cepa* roots with histochemical staining using nitro blue tetrazolium to determine the level of oxidative stress. The presence of O_2^- was detected as per the method of Mangalampalli et al. (2018). The roots were treated with VAuNPs (0—200 μg/ml), $AgNO_3$ (100 μM), vanillin (1 mM), FBS (10%) and PC-VAuNPs (100 and 200 μg/ml) along with control for 4 h and then stained with 2 mM nitro blue tetrazolium (NBT; Sigma-Aldrich, United States) in 20 mM PBS (pH 6.8) for 10 min and subsequently washed with deionized water. Superoxide anions were observed as a deposit of dark blue insoluble formazan compounds (Soltys et al., 2011), and images were acquired with a digital camera (Olympus E-520 camera, OLYMPUS, Tokyo, Japan).

To estimate O_2^- generation, the onion root tips were treated with VAuNPs (0—200 μg/ml), $AgNO_3$ (100 μM), vanillin (1 mM), FBS (10%) and PC-VAuNPs (100 and 200 μg/ml) along with control for a sampling period of 4 h. After treatment, 100 mg of root tips were homogenized in 0.5 ml of freshly prepared 0.1% trichloro acetic acid using a precooled (4°C) mortar and pestle. The homogenate was incubated with 0.3 ml of reaction mixture containing Tris-HCl buffer (50 mM; pH 6.5), NBT (0.2 mM), nicotinamide adenine dinucleotide (0.2 mM), and sucrose (250 mM) for 30 min at 28 ± 2°C in the dark. The blue mono-formazan formed was measured at 530 nm and its concentration was calculated using an extinction coefficient of 12.8 L/(mol*cm), which provided an indirect measurement of the concentration of O_2^- radical generated and was expressed as μmol NBT reduced in 0.1 g fresh weight of roots.

Micro-XRF Mapping of Au in *Allium cepa* Roots

μ-XRF was performed to study the Au uptake in *A. cepa* roots as described by Tefera et al. (2020). Onion bulbs with roots that were 1 week old were transferred to VAuNPs and PC-VAuNPs colloidal solutions of 200 μg/ml for 24 h. After 24 h, the distal 1 cm of the roots were excised and gently rinsed with MilliQ water. The roots were then immediately frozen in liquid nitrogen and stored at–20°C prior to use for Au mapping.

Au mapping was performed using μ-XRF (XGT9000, Horiba Scientific, Kyoto, Japan). The electron voltage was maintained at 50 kV with a beam intensity of 1,000 μA. The fluorescence yield was detected using a silicon drift detector. The Au distribution was collected using a map size of 0.5 mm width and height. The elemental composition of *A. cepa* roots was determined for the meristematic and elongation zones.

Statistical Analysis

All experiments were performed in triplicate. Means of pooled data with standard deviation were statistically compared to the control using One-way ANOVA followed by Duncan's multiple range test. Data were analysed using a commercial statistics package (IBM SPSS Statistics 27.0) and means were considered statistically significant when $p < 0.05$.

RESULTS AND DISCUSSION

Synthesis and Characterization of VAuNPs With and Without Protein Corona

The characterization of synthesized VAuNPs with and without PC revealed certain physiochemical differences. The UV-visible spectra originating from the optoelectronic surface plasmon resonance property confirmed the synthesis of VAuNPs, whereas the difference in the surface plasmon resonance of PC-VAuNPs and VAuNPs indicated aggregation of the PC-VAuNPs due to PC formation (**Supplementary Figure S1**). TEM analysis showed that the VAuNPs were mainly hexagonal, spherical, irregular and occasionally triangular in

shape (**Figure 1A**). TEM images also revealed the formation of PC around VAuNPs when treated with 10% FBS, i.e., formation of PC-VauNPs (**Figure 1B**). The thickness of the PC around VAuNPs varied, but was on average 3.5 nm (**Figure 1B**). This observation is in accordance with the literature, which suggests that protein abundance of PC is variable and depends on the type and amount of proteins in the biological fluid (Liu et al., 2020), and in this case the presence of FBS. Dynamic light scattering showed an increase in the hydrodynamic size and zeta potential measurements of bare VAuNPs, compared to PC-VAuNPs (**Figures 1C,D**), and were recorded as 99.94 ± 3.41 and 226.14 ± 5.12, and -31.9 mV and +9.21 mV, respectively. Similarly to the increase in the nanoparticle size and surface charge reversal observed in our study, Li et al. (2021) reported that humic acid adsorption on AuNPs increases their effective size and reverses nanoparticle surface charge. Further, Boldeiu et al. (2019) reported that citrate- and honey-capped AuNPs suspended in culture media supplemented with 10% FBS resulted in the formation of PC around AuNPs, which promoted agglomeration and clustering of the AuNPs. Moreover, it has been observed that the kinetics of PC formation and the characteristics of PC are based on the particle size as well as their shape (Piella et al., 2017). For instance, the thickness of PC on AuNPs influences the hydrodynamic size of nanoparticles (Cheng et al., 2015). In addition, it is observed that smaller nanoparticles show more increase in their size after corona formation compared to larger ones. It is reported that, smaller particles are more stable and have higher surface area than the larger particles, which results in the faster dispersion of smaller particles due to increased Brownian motion and subsequent enhancement in the coating of available proteins (Piella et al., 2017). Thus, the size of PC on smaller VAuNPs is high compared to larger VAuNPs.

The FTIR spectra of VAuNPs revealed the presence of different functional groups of vanillin molecules capped on the surface of VAuNPs (**Figure 1E**). FTIR peaks observed at 635 cm^{-1} and 1,668 cm^{-1}, 1,026 cm^{-1}, 1,217–1,292 cm^{-1} and 3,218 cm^{-1}, 1,427–1,589 cm^{-1}, and 2,847 cm^{-1} correspond to stretching and bending vibrations of the aldehyde group (C=O), stretching vibrations of O-CH_3, stretching (a broad band) and bending (a medium band) vibrations of the hydroxy group (-OH), stretching vibrations of C=C-C, and stretching vibrations of -C-H with weak band absorption, respectively (Aarabi et al., 2017; Fatoni et al., 2018; Arya et al., 2019). Similarly, the FTIR spectra of VAuNPs treated with FBS revealed the coating of proteins on the surface of VAuNPs (**Figure 1F**). The FTIR peaks observed at 1,255 cm^{-1}, 1,556 cm^{-1}, 1,652 cm^{-1} and 3,227–3,414 cm^{-1} corresponds to C-O deformation vibrations in the carboxylic group, -NH bending vibrations of amide II and C-N stretching in -CO-NH- in proteins, stretching vibrations of C=O of amide I in proteins, stretching vibrations of -OH and -NH in hydroxy and amine groups, respectively (Song et al., 2016). The FTIR of FBS treated VAuNPs suggests that several functional groups of vanillin present on VAuNPs are masked by proteins from FBS to form a PC on VAuNPs (**Figures 1E,F**). The stretching vibrations arising from -OH group on VAuNPs (**Figure 1E**) are severely contracted, as well as the intensity of the absorption bands in PC-VAuNPs (**Figure 1F**). Increase in the FTIR peak intensity in the range 3,227–3,414 cm^{-1} of PC-VAuNPs (**Figure 1F**) compared to bare VAuNPs (**Figure 1E**) suggests the successful coating of hydroxy group-containing amino acids such as serine, threonine and tyrosine. Another plausible explanation to the observed reduction of vibrational modes is that protein conjugation may have resulted in the exchange of vanillin from the surface of VAuNPs.

Allium cepa Genotoxicity Assessment for VAuNPs With and Without Protein Corona

AuNPs are certainly among the most preferred metal nanoparticles for biomedical and biosensing applications owing to their tuneable plasmonic properties and chemically inert nature. However, such increase in their use poses considerable risk of intentional/unintentional release and accumulation of AuNPs into the target environment, often presenting a threat towards off-target organisms such as plants. For instance, reports of an animal model (male wistar rats) administered with AuNPs suggested that AuNPs were excreted through faeces and urine (Katsnelson et al., 2013; Lopez-Chaves et al., 2018; Ansari et al., 2019). Additionally, the AuNPs used in cosmetics (Cao et al., 2016), which interact with biological fluids secreted by the dermal layer are washed-off and released into sewage water. These studies clearly indicate that AuNPs would eventually enter the environment if they are used as a part of nanomedicines/cosmetics. However, AuNPs from such sources will be coated with biomolecular corona which may alter the functional signatures of AuNPs. Similarly, inappropriate handling of nanoparticles can lead to their spread in the form of aerosols (Gomez et al., 2014). Therefore, it is important to assess and compare the toxicological signatures of such biomedically relevant AuNPs with and without biomolecular corona (here PC) on off-target organisms. To address this, the effect of some chemically and green synthesized AuNPs have been tested in root cells in the off-target model organism *A. cepa*, although only at relatively low concentrations (0.1–10 μg/ml) (Rajeshwari et al., 2016a; Rajeshwari et al., 2016b; Debnath et al., 2018). These studies suggested that AuNPs induce genotoxicity by generating oxidative stress in the root cells in a dose dependent manner. Interestingly, several studies have shown that at much higher concentrations (400–1,000 μg/ml), AuNPs can promote growth and germination in rice (*Oryza sativa*) (Ndeh et al., 2017), Mung Bean (*Vigna radiata*) (Das et al., 2017), and other plant species (Venzhik et al., 2021). However, there is no report that evaluates and compares, on plants, the effect of AuNPs with and without PC.

Therefore, in the present study we considered and tested a range of concentrations, i.e., 12.5–200 μg/ml of VAuNPs [assuming that vanillin capping would increase the biocompatibility of AuNPs, as mentioned for phytomolecules by Cao et al. (2017)] to assess their genotoxicity in *A. cepa* root tip cells. Based on the outcome of VAuNPs treatments, we tested PC-VAuNPs at 100 and 200 μg/ml concentrations. **Table 1** shows the percentage of mitotic index, phase index and chromosomal

TABLE 1 | Phase index (PI), mitotic index (MI) and chromosomal aberrations (CA) of *A. cepa* root meristematic cells treated with VAuNPs (0—200 µg/ml), $AgNO_3$ (100 µM), Vanillin (1 mM), FBS (10%) and PC-VAuNPs (100 and 200 µg/ml).

Treatment	Conc	PI (% ± SD)				MI (% ± SD)	CA (% ± SD)
		Prophase	Metaphase	Anaphase	Telophase		
VAuNPs (µg/ml)	0 (water control)	96.71 ± 2.64^{ab}	1.89 ± 0.05^{f}	0.72 ± 0.12^{def}	0.43 ± 0.19^{cd}	45.70 ± 1.67^{a}	0.06 ± 0.04^{e}
	12.5	95.49 ± 0.84^{c}	2.51 ± 0.22^{cde}	0.91 ± 0.18^{def}	0.68 ± 0.18^{bcd}	43.70 ± 0.71^{ab}	0.66 ± 0.12^{de}
	25	94.98 ± 1.82^{d}	2.82 ± 0.07^{cde}	0.88 ± 0.12^{def}	0.64 ± 0.10^{cd}	41.23 ± 0.82^{c}	0.83 ± 0.16^{de}
	50	92.16 ± 1.83^{e}	3.25 ± 0.16^{bc}	1.33 ± 0.30^{cd}	1.25 ± 0.39^{b}	40.00 ± 0.49^{c}	1.06 ± 0.18^{d}
	100	89.86 ± 3.34^{f}	4.48 ± 0.37^{b}	2.13 ± 0.16^{bc}	2.88 ± 0.31^{a}	31.23 ± 0.78^{d}	2.83 ± 0.33^{c}
	200	86.15 ± 0.45^{h}	6.20 ± 0.28^{a}	3.10 ± 0.50^{ab}	3.88 ± 0.28^{a}	25.76 ± 1.06^{e}	4.53 ± 0.49^{b}
$AgNO_3$ (µM)	100	89.92 ± 7.50^{g}	3.56 ± 0.51^{bc}	3.31 ± 0.20^{a}	1.35 ± 0.37^{bc}	27.13 ± 1.93^{e}	15.90 ± 1.12^{a}
Vanillin (mM)	1	96.55 ± 2.25^{bc}	1.98 ± 0.31^{f}	0.68 ± 0.19^{ef}	0.30 ± 0.10^{d}	43.60 ± 0.66^{ab}	0.13 ± 0.04^{e}
FBS (%)	10	96.91 ± 1.32^{a}	2.27 ± 0.27^{def}	0.44 ± 0.17^{f}	0.22 ± 0.18^{d}	45.36 ± 0.77^{a}	0.10 ± 0.08^{e}
PC-VAuNPs (µg/ml)	100	95.27 ± 2.30^{c}	2.55 ± 0.33^{cde}	0.97 ± 0.19^{de}	1.12 ± 0.18^{b}	44.43 ± 0.89^{a}	0.53 ± 0.12^{de}
	200	93.34 ± 3.08^{d}	2.88 ± 0.17^{bcd}	1.28 ± 0.31^{cd}	1.92 ± 0.17^{a}	41.45 ± 0.38^{bc}	0.83 ± 0.16^{de}

Data represented as mean ± SD, alphabets indicate significant difference from the control according to Duncan's multiple range test.

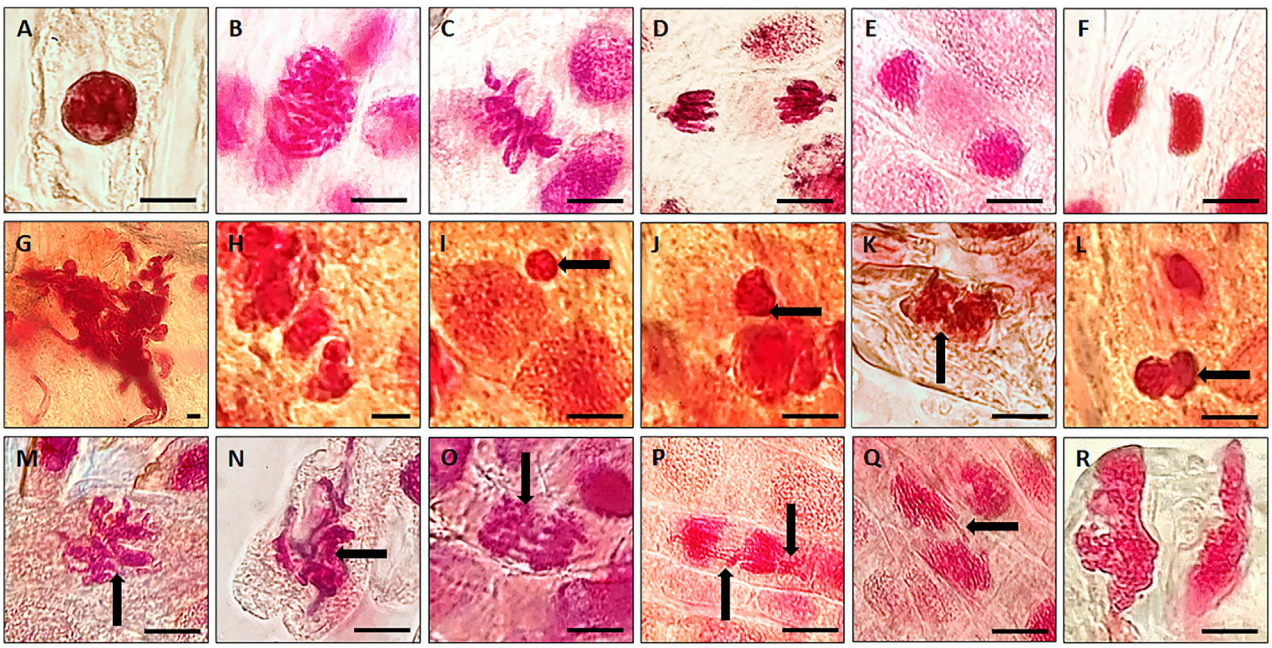

FIGURE 2 | Representative photographs of individual phases of mitosis observed in untreated (control) *A. cepa* root tip cells; **(A)** Interphase; **(B)** Prophase; **(C)** Metaphase; **(D)** Anaphase; **(E)** Telophase; **(F)** Cytokinesis. Representative images of chromosomal and nuclear anomalies more frequently observed following either exposure to higher concentrations of VAuNPs (100 and 200 µg/ml) or 100 µM $AgNO_3$ in dividing cells of *A. cepa* roots; **(G)** nuclear clumping and lesions, **(H,I)** micronuclei, (Black arrow shows the feature) **(J–L)** binucleate, **(M)** sticky chromosomes at metaphase, **(N,O)** disturbed metaphase, **(P,Q)** anaphase bridge and laggard chromosome, **(R)** disturbed telophase. (Scale 10 µm). Here, both VAuNPs and $AgNO_3$ treatments produced similar chromosomal/nuclear anomalies. Representative images of $n \geq 10^3$ cells for each treatment.

aberrations observed when *A. cepa* root tips were incubated with different concentrations of VAuNPs, where $AgNO_3$ and ultrapure ion free MilliQ water is used as positive and negative controls, respectively. The MI values of positive and negative control samples were 27.13 ± 1.93 and 45.70 ± 1.67, respectively. In comparison to the negative control, a significant reduction in the frequency of different dividing stages was observed at higher concentrations of treatment groups such as 100 µg/ml and 200 µg/ml. Similarly, significant increases in chromosomal and nuclear abnormalities were observed at these concentrations, which corresponded with that for the positive control. A concentration-dependent decrease in the MI values was recorded with an increasing concentration of VAuNPs (**Table 1**). The MI value (25.76 ± 1.06) of 200 µg/ml VAuNPs, which is below that for the $AgNO_3$ treatment (27.13 ± 1.93) clearly highlights the genotoxic effects of VAuNPs at higher

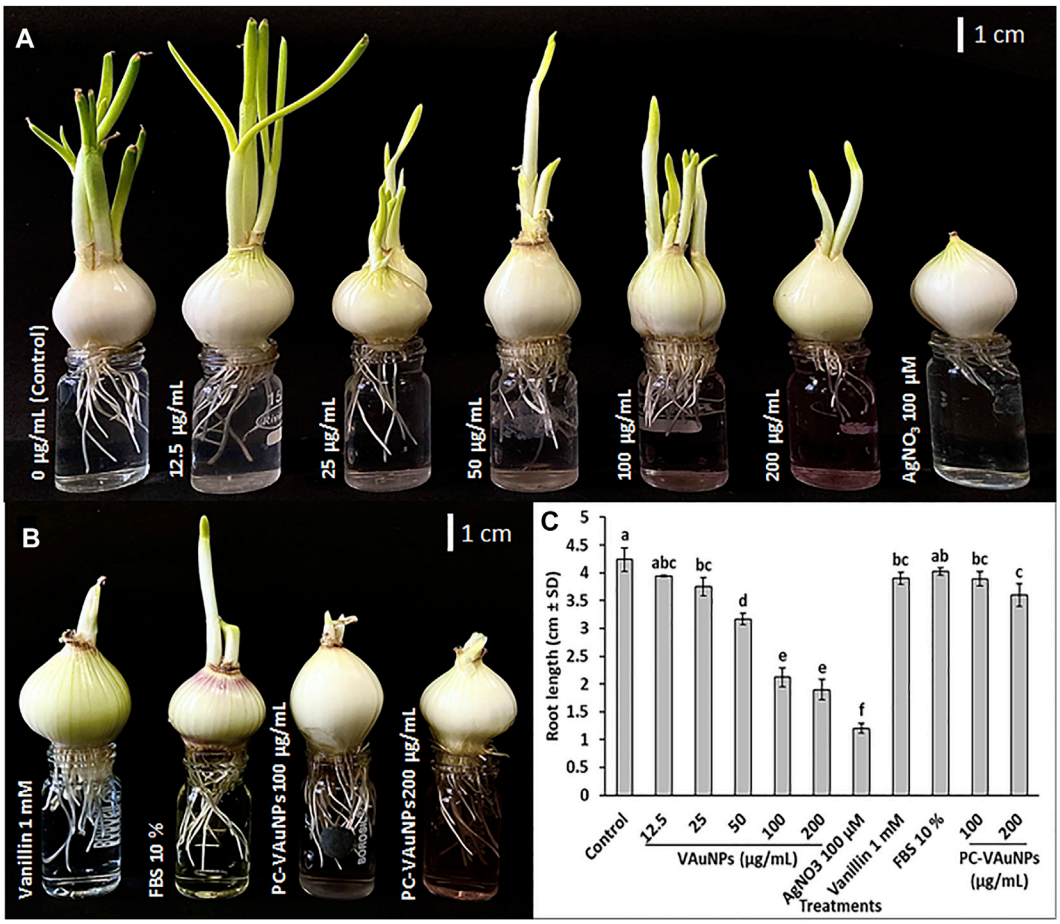

FIGURE 3 | Allium cepa root growth assay **(A)** *A. cepa* root growth inhibition observed at different VAuNPs concentrations (12.5—200 µg/ml) after 96 h, $AgNO_3$ was used as positive control; **(B)** *A. cepa* root growth inhibition assay of protein coated VAuNps (PC-VAuNPs, 100 and 200 µg/ml), after 96 h; **(C)** Effect of VAuNPs (0—200 µg/ml), $AgNO_3$ (100 µM), Vanillin (1 mM), FBS (10%) and PC-VAuNPs (100—200 µg/ml) on root growth of *A. cepa*. Data represented as mean ± SD, bars with different letters are significantly different from the control according to Duncan's multiple range test.

concentrations. Mitotic cells of the untreated negative control cells showed the expected phases of cell division such as prophase, metaphase, anaphase and telophase (**Figure 2**).

With the reduction in MI values, the frequency of chromosomal and nuclear aberrations increased in all the treatment groups. It is reported by Saha and Gupta (2017) that similar to mutagenic agents, toxic chemicals or nanoparticles can decrease the mitotic activity of the treated cells by inhibiting the cells from entering prophase and restricting them to interphase or G_2 phase. The reduction in MI is also attributed to blockage at the G1 stage that leads to the suppression of DNA synthesis. In addition, the pole shift by the depolymerization of spindle fibers led to the occurrence of different chromosomal aberrations in metaphase and anaphase (Rajeshwari et al., 2016b). The disturbance in spindle fibers followed by improper chromosome folding attributed to the formation of sticky chromosomes and chromosomal bridges, which cause the fragmentation of the chromosomes, leading to chromosomal anomalies. Thus the occurrence of chromosomal aberrations of root meristem cells indicates genotoxicity of the tested compounds (Smaka-Kincl et al., 1996). Chromosomal and nuclear abnormalities observed in the various treatments included nuclear clumping and lesions (**Figure 2G**), micronuclei (**Figures 2H,I**), binucleate cells (**Figures 2J–L**), sticky chromosomes at metaphase (**Figure 2M**), disturbed metaphase (**Figures 2N,O**), anaphase bridge and laggard chromosome (**Figures 2P,Q**), and disturbed telophase (**Figure 2R**).

A study performed with *Nicotiana xanthi* suggested that AuNPs (3.5 and 18 nm) were internalized by this species in a size-dependent manner and caused phytotoxicity after entering plant cells and subcellular organelles (Sabo-Attwood et al., 2012). Thus, AuNPs have the potential to induce changes in stress response genes, which can impede major cellular processes even following short-term AuNP exposure (Rajeshwari et al., 2016b). Debnath *et al.* (2018) reported that green-synthesized AuNPs between 50 and 100 nm reduced the MI in *A. cepa* cells in a concentration-dependent manner. Contrastingly, Gopinath et al. (2013) found that AuNPs prepared using a *Terminalia arjuna* leaf extract

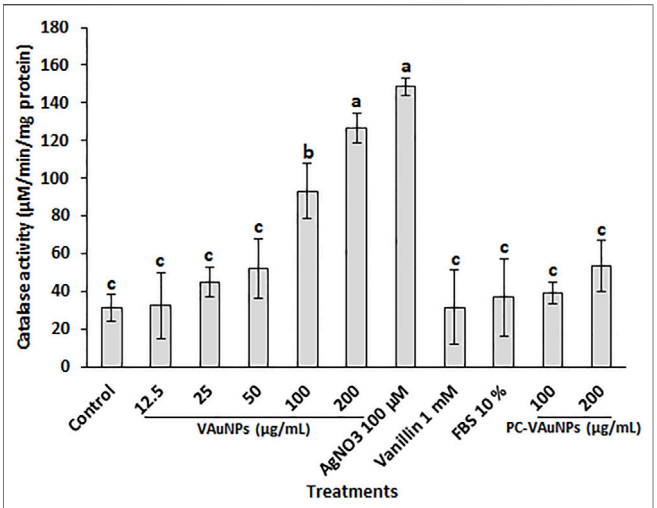

FIGURE 4 | Catalase activity in *A. cepa* root tips following interaction with VAuNPs (0—200 µg/ml), $AgNO_3$ (100 µM), vanillin (1 mM), FBS (10%) and PC-VAuNPs (100 and 200 µg/ml) for 4 h. Data represented as mean ± SD, bars with different letters are significantly different from the control according to Duncan's multiple range test.

showed an increase in the MI and PI in a concentration-dependent manner (10–1,000 µM). However, in both these studies, any potential genotoxic effect of the plant extract alone was not evaluated, therefore making it difficult to determine whether the changes in the genotoxic signatures were due to AuNPs, phytochemicals or a combination of both. In a related study, Rajeshwari et al. (2016b) studied the effect of both AuNPs and citrate, which was used to synthesize the AuNPs. They observed that the capping agent, citrate, had no impact on the MI and PI, suggesting that genotoxicity was a function of the AuNPs. Using a similar approach, we observed that the capping agent, vanillin, and FBS, did not exhibit any genotoxicity effects when tested individually (**Table 1**).

Apart from AuNPs, some studies have been carried out with other metallic nanoparticles. For example, zinc oxide nanoparticles (ZnONPs) used at similar concentrations and size as used here induced chromosomal aberrations in *A. cepa* root tip cells (Kumari et al., 2011). Analysis of *A. cepa* root cells in that study by SEM and TEM showed ZnONP-like deposits inside the cell-matrix of 100 nm in size and also confirmed the internalization of ZnONPs and their agglomeration. It was also reported in this study that post-internalization, the nanoparticles were transported through plasmodesmata, during which the nanoparticles may aggregate, resulting in an increase in their size. For MgONPs of 50 nm in size, a concentration-dependent decrease in MI values was observed when treated with 12.5 µg/ml to 100 µg/ml MgONPs (Mangalampalli et al., 2018). Similarly, many other nanoparticles such as AgNPs (<60 nm) (Saha and Gupta, 2017), Al_2O_3NPs (<50 nm) (Rajeshwari et al., 2015), Cr_2O_3NPs (hydrodynamic size: 0—500 nm) (Kumar et al., 2015), TiO_2NPs (<25 nm) (Fadoju et al., 2020), and BONPs (Bismuth III oxide nanoparticles) (90—210 nm) (Liman, 2013) were reported to be genotoxic at lower or similar concentrations.

To evaluate the genotoxic effects, the *A. cepa* assay was examined using higher concentrations of PC-coated VAuNPs (PC-VAuNPs) (100 µg/ml and 200 µg/ml). The PC-VAuNPs when used at these higher concentrations did not show any genotoxicity in cells, which was also confirmed from the deduced MI and PI values of the treated root meristem cells (**Table 1**). FBS (10%) and Vanillin (1 mM) treatments were used as controls for PC-VAuNPs. The MI of root meristems for 100 µg/ml and 200 µg/ml PC-VAuNPs treatments were 44.43 ± 0.89 and 41.56 ± 0.38, respectively, which were significantly less than that for the bare VAuNPs treatments at the higher concentrations (**Table 1**). Similarly, a significant reduction was observed in the number and frequency of chromosomal aberrations in PC-VAuNPs treatments at both 100 µg/ml and 200 µg/ml concentrations compared to VAuNPs (**Table 1**). The possible explanation for the differences in the genotoxicity between bare VAuNPs and PC-VAuNPs is related to their physicochemical properties, most importantly the hydrodynamic size and zeta potential. It has been reported that increased hydrodynamic size and agglomeration occurs when the zeta potential of nanoparticles skews towards neutral, which retards the electrostatic repulsion between the nanoparticles, thereby resulting in enhanced aggregation, and reduced bioavailability and toxicity. In general, low zeta potential values between–20 mV and +20 mV favours aggregation of nanoparticles (Ye et al., 2018). Similar to this observation, addition of the positively charged amino acid, Lysine, to suspended AuNPs (−34.8 mV) accelerated the agglomeration of AuNPs and significantly reduced their zeta potential to 7.2 mV (Ye et al., 2018). Also, it has been reported that translocation efficiency from root to shoot of AuNPs that have a negative zeta potential is greater than AuNPs with positive or neutral zeta potential values (Zhu et al., 2012). This signifies that AuNPs with negative zeta potentials are more likely to be rapidly internalized by the root and translocated to the shoot, whereas AuNPs with either a positive or neutral zeta potential adhere to and remain at the root surface.

A recent report (Janani et al., 2021), has detailed the influence of PC on the toxicity of ZnONPs in *A. cepa*. The ZnONPs with PC exhibited less cytotoxicity, chromosomal aberrations and micronuclei formation compared to ZnONPs without PC. Further, though not in plants, Li et al. (2021) demonstrated that humic acid adsorption onto AuNPs increases their size and hydrophobicity and reverses the surface charge, which sterically hinders the binding of AuNPs to bacterial cell membrane. Thus, the toxicity of nanoparticles is mitigated by a decrease in the chance of AuNPs association with bacteria, and AuNPs-induced membrane damage. Such findings provide compelling evidences for how modified surfaces change their toxicological signatures.

Nevertheless, to date, most studies targeted to evaluate the effect of PC on the toxicity of metal nanoparticles (particularly

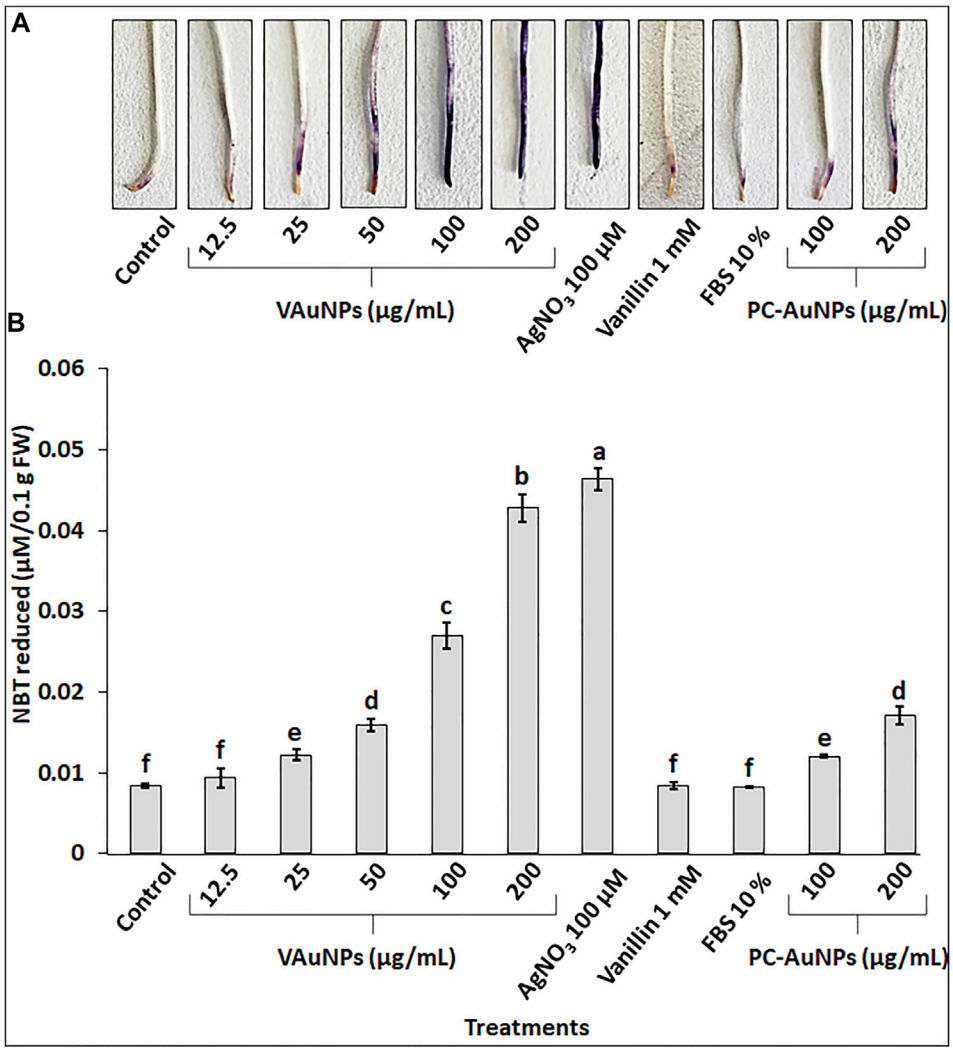

FIGURE 5 | Visualization **(A)** and quantitation **(B)** of super oxide radical by NBT staining in roots of *A. cepa* treated with VAuNPs (0—200 µg/ml), $AgNO_3$ (100 µM), vanillin (1 mM), FBS (10%) and PC-VAuNPs (100 and 200 µg/ml) along with control. Data represented as mean ± SD, alphabets indicate significant difference from the control according to Duncan's multiple range test.

AuNPs) have been performed on animal cells or systems. Moreover, they were targeted to compare the mechanism of internalization of bare and PC-coated nanoparticles as well as to evaluate their toxicity. Collectively, the animal cell studies have concluded that the surface modification of nanoparticles by protein adsorption leads to reduced toxicity (Falahati et al., 2019). Further, the toxic effects are often attributed to the interaction of nanoparticles with the cell membrane, whereas Cheng et al. (2015) suggest that the modification of the nanoparticles with a corona protein coat eliminates such direct contact and decreases their toxicity. Additionally, the PC influences cellular uptake of AuNPs by phagocytic and nonphagocytic cells in a size-dependent manner (Cheng et al., 2015). It was also reported that the association of anionic nanoparticles with serum proteins reduces the likelihood of their interaction with animal cells (Charbgoo et al., 2018). Clathrin- and Cavelin-mediated endocytosis are reported to be one of the major mechanisms for internalization of PC coated AuNPs of 20–50 nm in size (Charbgoo et al., 2018). Contrary to animal cells, a clathrin-independent pathway is likely involved in AuNPs uptake in plant cells, and has been reported for cysteine functionalized AuNPs of −31.9 mV zeta potential (Li et al., 2016). In that study, the uptake of AuNPs in rice and tomato was blocked by specific inhibitors such as ikarugamycin and wortmannin (inhibitors of clathrin-mediated and clathrin-independent endocytosis, respectively). These results with inhibitors suggested that the uptake of AuNPs involved a combination of both clathrin-dependent and -independent mechanisms. In this regard, it would be of interest to investigate and compare the uptake mechanisms into plant cells that AuNPs with and without PC follow.

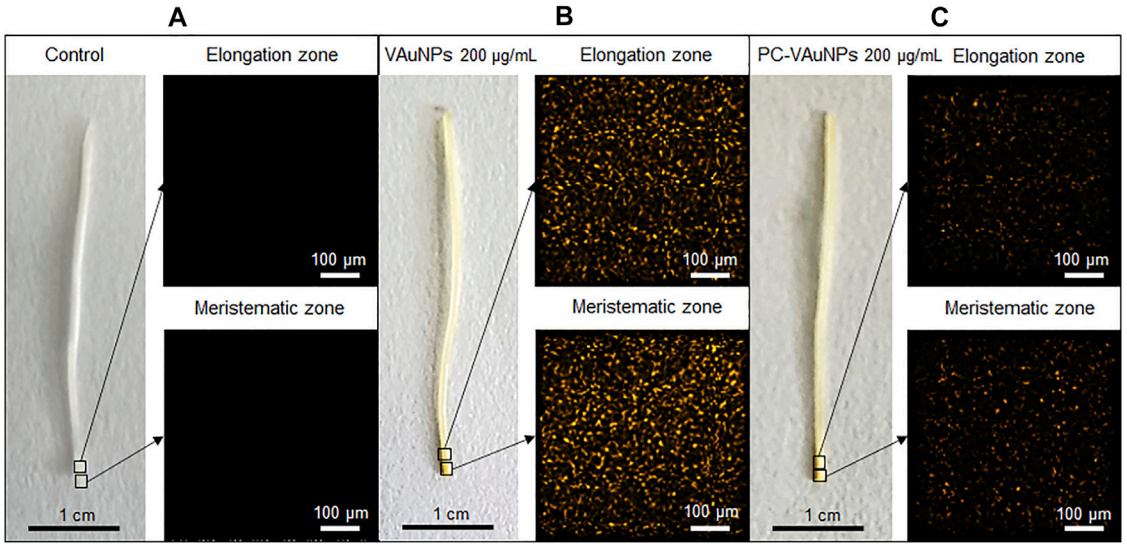

FIGURE 6 | Micro-XRF mapping of elemental gold in elongation and meristematic zone of *Allium cepa* roots treated with; **(A)** Water control, **(B)** VAuNPs (200 µg/ml) and **(C)** PC-VAuNPs (200 µg/ml).

Allium cepa Root Growth Assay for VAuNPs With and Without Protein Corona

The *A. cepa* root growth assay revealed that VAuNPs significantly inhibited root growth in a concentration-dependent-manner (**Figures 3A–C**), which is consistent with the previous findings of a decrease in the MI values with increasing concentration of VAuNPs. The effective concentration (EC_{50}) value, which retards 50% of root growth compared to the negative control, was found to be 100 µg/ml. The development and growth of *A. cepa* roots in 100 µg/ml and 200 µg/ml treatments were severely inhibited, with average root length of <2 cm after 96 h following exposure. It was observed that AuNPs of size 10, 14 and 18 nm inhibited the elongation of the primary root and lateral root formation in *Arabidopsis thaliana* at a concentration of 100 µg/ml (Siegel et al., 2018). Similarly, root growth inhibition was observed in Hordeum vulgare plants when exposed to citrate-stabilized AuNPs, at a concentration range of 3—10 µg/ml, whereas a lower concentration of AuNPs (1 µg/ml) promoted root growth (Charbgoo et al., 2018). Similar to VAuNPs, Deng et al. (2016) reported that CuONPs of 40 nm inhibited the growth of *A. cepa* roots in a concentration-dependent manner.

Unlike bare VAuNPs, high concentrations of PC-VAuNPs showed no negative impact on the growth of *A. cepa* roots (**Figures 3A–C**). The reason for the reduced genotoxicity of PC-VAuNPs is most likely related to their increased hydrodynamic size and their agglomeration due to reduced zeta potential. Similarly, Ding et al. (2019) reported that humic acid adsorption onto AgNPs significantly reduced the damage caused to the plant's (*Lemna minor*) morphology and ultrastructure in comparison to bare AgNPs. Further, Ekvall et al. (2021) demonstrated that preexposure of Cobalt nanoparticles to biomolecules, which are always present in natural ecosystems reduced their toxic potency to *Daphnia magna*.

Determination of Catalase Activity in *Allium cepa* Root Tips

It has been reported that the generation of ROS such as superoxide (O_2^-), hydroxyl (OH^-), and hydrogen peroxide (H_2O_2) may be the primary cause of root growth inhibition in *A. cepa* when exposed to AuNPs (Rajeshwari et al., 2016b). The analyses performed in the previous study revealed that oxidative stress was an important mechanism linked to induction of cellular toxicity. Toxicity was likely promoted by factors such as oxidative groups functionalized on the surface of the nanoparticles followed by active redox cycling and interaction of nanoparticles with cellular components.

CAT is one of the major enzymatic ROS scavengers, which functions as efficient machinery for the detoxification of ROS such as H_2O_2. Gechev et al. (2006), reported that catalase was active only at relatively high H_2O_2 concentrations in plant systems. The CAT assay used here confirmed that VAuNPs generated oxidative stress in the *A. cepa* root tip cells in a concentration-dependent manner (**Figure 4**). In comparison, treatment of root tips with PC-VAuNPs generated significantly lower amounts of CAT activity compared to the bare VAuNPs at the same concentrations (100 and 200 µg/ml) and the positive control (100 µM $AgNO_3$). More than a two-fold decrease in the catalase activity was observed in 200 µg/ml PC-VAuNPs treatment compared to bare VAuNPs of similar concentration.

It is reported that post internalization into plant cells, AuNPs are transported from 1 cell to another *via* plasmodesmata along with accumulation occurring inside the plant cell wall (Zhang et al., 2022). However, as evidenced from the characterization studies, the

PC formed on VAuNPs and the resultant increased hydrodynamic size is likely to be responsible for the reduced toxicity and rate of internalization, respectively. Thus, the outcome of the present study corresponds to the previous findings of reduced genotoxicity and increased root growth in PC-VAuNPs compared to bare VAuNPs.

Histochemical Staining and Determination of Superoxide Radical

The production of O_2^- was examined in *A. cepa* roots with histochemical staining using NBT for qualitative determination of the level of oxidative stress when roots were treated with VAuNPs (0—200 μg/ml), $AgNO_3$ (100 μM), vanillin (1 mM), FBS (10%) and PC-VAuNPs (100 and 200 μg/ml) along with the water control (**Figure 5A**). The intensity of dark blue insoluble formazan (blue) staining increased based on O_2^- production in a concentration-dependent manner in the VAuNPs treatments. Whereas, the level of O_2^- produced in the PC-VAuNPs (100 and 200 μg/ml) treatments was much lower compared with similar concentrations of VAuNPs, and 100 μM $AgNO_3$. A similar concentration-dependent effect on O_2^- generation was observed in *A. cepa* roots treated with magnesium oxide nanoparticles (0—100 μg/ml) (Mangalampalli et al., 2018).

Quantitative analysis of O_2^- in *A. cepa* roots confirmed the generation of oxidative stress in all the treatments (**Figure 5B**). The O_2^- generation in VAuNPs treatments was enhanced in a concentration dependent manner. Further, as visualized in histochemical staining (**Figure 5A**), a significant difference was observed in the level of O_2^- in VAuNPs and PC-VAuNPs treatments at the higher concentrations (100 and 200 μg/ml).

Micro-XRF Mapping of Gold in *Allium cepa* Roots

The bio-uptake of gold ions along a longitudinal section of *A. cepa* roots treated with VAuNPs and PC-AuNPs 200 μg/ml was determined using μ-XRF. Pixel intensity (**Figure 6**) indicated the level of gold fluorescence in treated and control roots. As compared to the water control treatment (**Figure 6A**), μ-XRF maps obtained from the fluorescence intensity of elements clearly indicated gold ion uptake within 24 h in VAuNPs and PC-VAuNPs (**Figures 6B,C**) treated samples. However, the difference in the intensities between VAuNPs and PC-VAuNPs is indicative of low-toxicity of PC-VAuNPs even when used at the highest concentration tested of 200 μg/ml. **Supplementary Table S1** (provided at the bottom of the MS) details the presence of predominant elements in treated and control roots. Notably, a high intensity of elemental gold was obtained in the VAuNPs treatment which may be due to the uptake of both VAuNPs and ionic gold. For instance, it has been reported, that metallic nanoparticles may release a substantial fraction of metal ions in aqueous solution, and for such nanoparticles impacts on the test organism may be partly due to metal-ion-related toxicity (He et al., 2015). A similar study on *A. thaliana* roots exposed to gold ionic stress (200 μM) increased the H_2O_2 level in root tip tissues (Li et al., 2018), which may indicate, in the present study, that enhanced catalase activity is related to cellular toxicity of gold ions in the higher concentration of VAuNPs treatments. Taylor et al. (2014) reported that gold is taken up by the plants (*Arabidopsis thaliana* L.) predominantly in the ionic form when compared with AuNPs, and that plants respond to gold by upregulating the stress related genes and downregulating specific metal transporters to reduce the gold uptake. In the present study, PC formation on VAuNPs may have reduced the rate of gold ionization at the interface of VAuNPs and water, and an increase in hydrodynamic size likely hampered the internalization of the nanoparticles, which eliminated the toxicity arising from both ionic gold and VAuNPs. Similar to the present study, Ding et al. (2019) demonstrated that humic acid adsorption inhibited the absorption and accumulation of Ag in *Lemna minor* roots and leaves, which also reduced the toxicity associated with AgNPs.

CONCLUSION AND PROSPECTS

The genotoxic effects of VAuNPs and PC-VAuNPs were assessed in the off-target model organism *A. cepa*. A dose-dependent decrease in MI values and an increase in chromosomal aberrations were observed in root meristems when treated with VAuNPs. Different types of chromosomal and nuclear anomalies observed here suggest that VAuNPs had adverse effects on root tip cells. The genotoxic effect was quite profound at higher concentrations of VAuNPs, whereas, treatment with PC-VAuNPs demonstrated a remarkable reduction in the frequency of chromosomal aberrations, and they had no impact on the MI and PI compared to bare VAuNPs. A higher accumulation of gold in roots, recorded by μ-XRF mapping, in VAuNPs treated roots compared to that found for PC-VAuNPs treated roots may underlie the genotoxicity found in the root tip cells. The outcomes of our studies show that the formation of PC can significantly reduce the genotoxicity of VAuNPs. As there are conflicting reports on the status of green-synthesized AuNPs, we recommend that more studies are required that focus on characterization of the nanoparticles and changes in their physicochemical properties before and after their exposure to biological media and systems. Understanding of the potential toxicity and mutagenicity of AuNPs on off-target organisms is required due to the current focus of research on biomedical/antibacterial applications and their use in cosmeceutical formulations. Therefore, attention needs to be drawn to the development of regulatory tools that may limit, during their utilization, AuNP release into the environment. Considering our current findings and those of previous studies, it is clear that AuNPs may impose cyto-genotoxicity irrespective of their method of synthesis. The research presented here supports a growing scientific consensus that our current knowledge of engineered AuNPs is inadequate, especially if we consider their effects on off-target organisms. However, further studies are recommended to elucidate the internalization mechanisms as well as the rate of internalization of PC and bare VAuNPs. Also, besides the present

dose-dependent study, time- and shape-dependent toxicological investigations of gold salt, VAuNPs and PC-VAuNPs, as well as analysis of their interaction with other biomolecules is warranted.

DATA AVAILABILITY STATEMENT

The original contributions presented in the study are included in the article/**Supplementary Material**, further inquiries can be directed to the corresponding author.

AUTHOR CONTRIBUTIONS

SA and SL conceptualized the experiments. SA took part in the investigation, methodology, and analysis. SA wrote the manuscript. SL, JR, and DC helped in the critical review and the editing of the manuscript.

ACKNOWLEDGMENTS

SA acknowledges Deakin University, Australia for the provision of a post-graduate fellowship.

SUPPLEMENTARY MATERIAL

The Supplementary Material for this article can be found online at: https://www.frontiersin.org/articles/10.3389/fbioe.2022.849464/full#supplementary-material

REFERENCES

Aarabi, A., Mizani, M., and Honarvar, M. (2017). The Use of Sugar Beet Pulp Lignin for the Production of Vanillin. *Int. J. Biol. macromolecules* 94, 345–354. doi:10.1016/j.ijbiomac.2016.10.004

Adair, B. M., and Cobb, G. P. (1999). Improved Preparation of Small Biological Samples for Mercury Analysis Using Cold Vapor Atomic Absorption Spectroscopy. *Chemosphere* 38, 2951–2958. doi:10.1016/s0045-6535(98)00493-7

Ansari, S., Bari, A., Ullah, R., Mathanmohun, M., Veeraraghavan, V. P., and Sun, Z. (2019). Gold Nanoparticles Synthesized with Smilax Glabra Rhizome Modulates the Anti-obesity Parameters in High-Fat Diet and Streptozotocin Induced Obese Diabetes Rat Model. *J. Photochem. Photobiol. B: Biol.* 201, 111643. doi:10.1016/j.jphotobiol.2019.111643

Arya, S. S., Mahto, B. K., Sengar, M. S., Rookes, J. E., Cahill, D. M., and Lenka, S. K. (2022). Metabolic Engineering of Rice Cells with Vanillin Synthase Gene (VpVAN) to Produce Vanillin. *Mol. Biotechnol.*, 1–12. doi:10.1007/s12033-022-00470-8

Arya, S. S., Rookes, J. E., Cahill, D. M., and Lenka, S. K. (2021a). Vanillin: a Review on the Therapeutic Prospects of a Popular Flavouring Molecule. *Adv. Tradit Med. (Adtm)* 21, 1–17. doi:10.1007/s13596-020-00531-w

Arya, S. S., Sharma, M. M., Das, R. K., Rookes, J., Cahill, D., and Lenka, S. K. (2019). Vanillin Mediated green Synthesis and Application of Gold Nanoparticles for Reversal of Antimicrobial Resistance in *Pseudomonas aeruginosa* Clinical Isolates. *Heliyon* 5, e02021. doi:10.1016/j.heliyon.2019.e02021

Arya, S. S., Sharma, M. M., Rookes, J. E., Cahill, D. M., and Lenka, S. K. (2021b). Vanilla Modulates the Activity of Antibiotics and Inhibits Efflux Pumps in Drug-Resistant *Pseudomonas aeruginosa*. *Biologia* 76, 781–791. doi:10.2478/s11756-020-00617-5

Balalakshmi, C., Gopinath, K., Govindarajan, M., Lokesh, R., Arumugam, A., Alharbi, N. S., et al. (2017). Green Synthesis of Gold Nanoparticles Using a Cheap *Sphaeranthus indicus* Extract: Impact on Plant Cells and the Aquatic Crustacean Artemia Nauplii. *J. Photochem. Photobiol. B: Biol.* 173, 598–605. doi:10.1016/j.jphotobiol.2017.06.040

Boldeiu, A., Simion, M., Mihalache, I., Radoi, A., Banu, M., Varasteanu, P., et al. (2019). Comparative Analysis of Honey and Citrate Stabilized Gold Nanoparticles: *In Vitro* Interaction with Proteins and Toxicity Studies. *J. Photochem. Photobiol. B: Biol.* 197, 111519. doi:10.1016/j.jphotobiol.2019.111519

Bonciu, E., Firbas, P., Fontanetti, C. S., Wusheng, J., Karaismailoğlu, M. C., Liu, D., et al. (2018). An Evaluation for the Standardization of theAllium Cepatest as Cytotoxicity and Genotoxicity Assay. *Caryologia* 71, 191–209. doi:10.1080/00087114.2018.1503496

Cao, M., Li, J., Tang, J., Chen, C., and Zhao, Y. (2016). Gold Nanomaterials in Consumer Cosmetics Nanoproducts: Analyses, Characterization, and Dermal Safety Assessment. *Small* 12, 5488–5496. doi:10.1002/smll.201601574

Cao, Y., Xie, Y., Liu, L., Xiao, A., Li, Y., Zhang, C., et al. (2017). Influence of Phytochemicals on the Biocompatibility of Inorganic Nanoparticles: a State-Of-The-Art Review. *Phytochem. Rev.* 16, 555–563. doi:10.1007/s11101-017-9490-8

Charbgoo, F., Nejabat, M., Abnous, K., Soltani, F., Taghdisi, S. M., Alibolandi, M., et al. (2018). Gold Nanoparticle Should Understand Protein corona for Being a Clinical Nanomaterial. *J. controlled release* 272, 39–53. doi:10.1016/j.jconrel.2018.01.002

Cheng, X., Tian, X., Wu, A., Li, J., Tian, J., Chong, Y., et al. (2015). Protein corona Influences Cellular Uptake of Gold Nanoparticles by Phagocytic and Nonphagocytic Cells in a Size-dependent Manner. *ACS Appl. Mater. Inter.* 7, 20568–20575. doi:10.1021/acsami.5b04290

Cvjetko, P., Milošić, A., Domijan, A.-M., Vinković Vrček, I., Tolić, S., Peharec Štefanić, P., et al. (2017). Toxicity of Silver Ions and Differently Coated Silver Nanoparticles in Allium cepa Roots. *Ecotoxicology Environ. Saf.* 137, 18–28. doi:10.1016/j.ecoenv.2016.11.009

Das, S., Debnath, N., Pradhan, S., and Goswami, A. (2017). Enhancement of Photon Absorption in the Light-Harvesting Complex of Isolated Chloroplast in the Presence of Plasmonic Gold Nanosol-A Nanobionic Approach towards Photosynthesis and Plant Primary Growth Augmentation. *Gold Bull.* 50, 247–257. doi:10.1007/s13404-017-0214-z

Debnath, P., Mondal, A., Hajra, A., Das, C., and Mondal, N. K. (2018). Cytogenetic Effects of Silver and Gold Nanoparticles on Allium cepa Roots. *J. Genet. Eng. Biotechnol.* 16, 519–526. doi:10.1016/j.jgeb.2018.07.007

Deng, F., Wang, S., and Xin, H. (2016). Toxicity of CuO Nanoparticles to Structure and Metabolic Activity of Allium cepa Root Tips. *Bull. Environ. Contam. Toxicol.* 97, 702–708. doi:10.1007/s00128-016-1934-0

Ding, Y., Bai, X., Ye, Z., Gong, D., Cao, J., and Hua, Z. (2019). Humic Acid Regulation of the Environmental Behavior and Phytotoxicity of Silver Nanoparticles to Lemna Minor. *Environ. Sci. Nano* 6, 3712–3722. doi:10.1039/c9en00980a

Ekvall, M. T., Hedberg, J., Odnevall Wallinder, I., Malmendal, A., Hansson, L. A., and Cedervall, T. (2021). Adsorption of Bio-Organic Eco-corona Molecules Reduces the Toxic Response to Metallic Nanoparticles in Daphnia magna. *Sci. Rep.* 11, 10784–10811. doi:10.1038/s41598-021-90053-5

Fadoju, O. M., Osinowo, O. A., Ogunsuyi, O. I., Oyeyemi, I. T., Alabi, O. A., Alimba, C. G., et al. (2020). Interaction of Titanium Dioxide and Zinc Oxide Nanoparticles Induced Cytogenotoxicity in Allium cepa. *The Nucleus*, 1–8. doi:10.1007/s13237-020-00308-1

Falahati, M., Attar, F., Sharifi, M., Haertlé, T., Berret, J.-F., Khan, R. H., et al. (2019). A Health Concern Regarding the Protein corona, Aggregation and Disaggregation. *Biochim. Biophys. Acta (Bba) - Gen. Subjects* 1863, 971–991. doi:10.1016/j.bbagen.2019.02.012

Fatoni, A., Hariani, P. L., Hermansyah, H., and Lesbani, A. (2018). Synthesis and Characterization of Chitosan Linked by Methylene Bridge and Schiff Base of 4,4-Diaminodiphenyl Ether-Vanillin. *Indones. J. Chem.* 18, 92–101. doi:10.22146/ijc.25866

Fytianos, G., Rahdar, A., and Kyzas, G. Z. (2020). Nanomaterials in Cosmetics: Recent Updates. *Nanomaterials* 10, 979. doi:10.3390/nano10050979

Gechev, T. S., Van Breusegem, F., Stone, J. M., Denev, I., and Laloi, C. (2006). Reactive Oxygen Species as Signals that Modulate Plant Stress Responses and Programmed Cell Death. *Bioessays* 28, 1091–1101. doi:10.1002/bies.20493

Gomez, V., Irusta, S., Balas, F., Navascues, N., and Santamaria, J. (2014). Unintended Emission of Nanoparticle Aerosols during Common Laboratory Handling Operations. *J. Hazard. Mater.* 279, 75–84. doi:10.1016/j.jhazmat.2014.06.064

Gopinath, K., Venkatesh, K. S., Ilangovan, R., Sankaranarayanan, K., and Arumugam, A. (2013). Green Synthesis of Gold Nanoparticles from Leaf Extract of Terminalia Arjuna, for the Enhanced Mitotic Cell Division and Pollen Germination Activity. *Ind. crops Prod.* 50, 737–742. doi:10.1016/j.indcrop.2013.08.060

Govindaraju, S., Rengaraj, A., Arivazhagan, R., Huh, Y.-S., and Yun, K. (2018). Curcumin-conjugated Gold Clusters for Bioimaging and Anticancer Applications. *Bioconjug. Chem.* 29, 363–370. doi:10.1021/acs.bioconjchem.7b00683

Grandviewresearch (2019). *Gold Nanoparticles Market Worth $6.33*. Billion By 2025. *Grand View Research* Accessed (15/03/2021), Available at: https://www.grandviewresearch.com/press-release/global-gold-nanoparticles-market.

Grant, W. F. (1982). Chromosome Aberration Assays in Allium. *Mutat. Research/Reviews Genet. Toxicol.* 99, 273–291. doi:10.1016/0165-1110(82)90046-x

He, X., Pan, Y., Zhang, J., Li, Y., Ma, Y., Zhang, P., et al. (2015). Quantifying the Total Ionic Release from Nanoparticles after Particle-Cell Contact. *Environ. Pollut.* 196, 194–200. doi:10.1016/j.envpol.2014.09.021

Janani, B., Raju, L. L., Thomas, A. M., Alyemeni, M. N., Dudin, G. A., Wijaya, L., et al. (2021). Impact of Bovine Serum Albumin - A Protein corona on Toxicity of ZnO NPs in Environmental Model Systems of Plant, Bacteria, Algae and Crustaceans. *Chemosphere* 270, 128629. doi:10.1016/j.chemosphere.2020.128629

Katsnelson, B., Privalova, L., Gurvich, V., Makeyev, O., Shur, V., Beikin, Y., et al. (2013). Comparative *In Vivo* Assessment of Some Adverse Bioeffects of Equidimensional Gold and Silver Nanoparticles and the Attenuation of Nanosilver's Effects with a Complex of Innocuous Bioprotectors. *Ijms* 14, 2449–2483. doi:10.3390/ijms14022449

Kumar, D., Rajeshwari, A., Jadon, P. S., Chaudhuri, G., Mukherjee, A., Chandrasekaran, N., et al. (2015). Cytogenetic Studies of Chromium (III) Oxide Nanoparticles on Allium cepa Root Tip Cells. *J. Environ. Sci.* 38, 150–157. doi:10.1016/j.jes.2015.03.038

Kumari, M., Khan, S. S., Pakrashi, S., Mukherjee, A., and Chandrasekaran, N. (2011). Cytogenetic and Genotoxic Effects of Zinc Oxide Nanoparticles on Root Cells of Allium cepa. *J. Hazard. Mater.* 190, 613–621. doi:10.1016/j.jhazmat.2011.03.095

Kumawat, M., Madhyastha, H., Umapathi, A., Singh, M., Revaprasadu, N., and Daima, H. K. (2022). Surface Engineered Peroxidase-Mimicking Gold Nanoparticles to Subside Cell Inflammation. *Langmuir* 38, 1877–1887. doi:10.1021/acs.langmuir.1c03088

Kyriazi, M.-E., Giust, D., El-Sagheer, A. H., Lackie, P. M., Muskens, O. L., Brown, T., et al. (2018). Multiplexed mRNA Sensing and Combinatorial-Targeted Drug Delivery Using DNA-Gold Nanoparticle Dimers. *Acs Nano* 12, 3333–3340. doi:10.1021/acsnano.7b08620

Li, H., Ye, X., Guo, X., Geng, Z., and Wang, G. (2016). Effects of Surface Ligands on the Uptake and Transport of Gold Nanoparticles in rice and Tomato. *J. Hazard. Mater.* 314, 188–196. doi:10.1016/j.jhazmat.2016.04.043

Li, S., Wang, S., Yan, B., and Yue, T. (2021). Surface Properties of Nanoparticles Dictate Their Toxicity by Regulating Adsorption of Humic Acid Molecules. *ACS Sustain. Chem. Eng.* 9, 13705–13716. doi:10.1021/acssuschemeng.1c02795

Li, Z., Xu, Y., Fu, J., Zhu, H., and Qian, Y. (2018). Monitoring of Au(iii) Species in Plants Using a Selective Fluorescent Probe. *Chem. Commun.* 54, 888–891. doi:10.1039/c7cc08333e

Liman, R., Başbuğ, B., Ali, M. M., Acikbas, Y., and Ciğerci, İ. H. (2021). Cytotoxic and Genotoxic Assessment of Tungsten Oxide Nanoparticles in Allium cepa Cells by Allium Ana-Telophase and Comet Assays. *J. Appl. Genet.* 62, 85–92. doi:10.1007/s13353-020-00608-x

Liman, R. (2013). Genotoxic Effects of Bismuth (III) Oxide Nanoparticles by Allium and Comet Assay. *Chemosphere* 93, 269–273. doi:10.1016/j.chemosphere.2013.04.076

Liu, N., Tang, M., and Ding, J. (2020). The Interaction between Nanoparticles-Protein corona Complex and Cells and its Toxic Effect on Cells. *Chemosphere* 245, 125624. doi:10.1016/j.chemosphere.2019.125624

Lopez-Chaves, C., Soto-Alvaredo, J., Montes-Bayon, M., Bettmer, J., Llopis, J., and Sanchez-Gonzalez, C. (2018). Gold Nanoparticles: Distribution, Bioaccumulation and Toxicity. *In Vitro* and *In Vivo* Studies. *Nanomedicine: Nanotechnology, Biol. Med.* 14, 1–12. doi:10.1016/j.nano.2017.08.011

Lovecká, P., Macůrková, A., Záruba, K., Hubáček, T., Siegel, J., and Valentová, O. (2021). Genomic Damage Induced in Nicotiana Tabacum L. Plants by Colloidal Solution with Silver and Gold Nanoparticles. *Plants* 10, 1260.

Maity, S., Chatterjee, A., Guchhait, R., De, S., and Pramanick, K. (2020). Cytogenotoxic Potential of a Hazardous Material, Polystyrene Microparticles on Allium cepa L. *J. Hazard. Mater.* 385, 121560. doi:10.1016/j.jhazmat.2019.121560

Mangalampalli, B., Dumala, N., and Grover, P. (2018). Allium cepa Root Tip Assay in Assessment of Toxicity of Magnesium Oxide Nanoparticles and Microparticles. *J. Environ. Sci.* 66, 125–137. doi:10.1016/j.jes.2017.05.012

Mosquera, J., García, I., Henriksen-Lacey, M., Martínez-Calvo, M., Dhanjani, M., Mascareñas, J. L., et al. (2020). Reversible Control of Protein Corona Formation on Gold Nanoparticles Using Host-Guest Interactions. *ACS nano* 14, 5382–5391. doi:10.1021/acsnano.9b08752

Mukherjee, S., Nethi, S. K., and Patra, C. R. (2017). "Green Synthesized Gold Nanoparticles for Future Biomedical Applications," in *Particulate Technology for Delivery of Therapeutics* (Springer), 359–393. doi:10.1007/978-981-10-3647-7_11

Naraginti, S., Kumari, P. L., Das, R. K., Sivakumar, A., Patil, S. H., and Andhalkar, V. V. (2016). Amelioration of Excision Wounds by Topical Application of green Synthesized, Formulated Silver and Gold Nanoparticles in Albino Wistar Rats. *Mater. Sci. Eng. C* 62, 293–300. doi:10.1016/j.msec.2016.01.069

Ovais, M., Ahmad, I., Khalil, A. T., Mukherjee, S., Javed, R., Ayaz, M., et al. (2018). Wound Healing Applications of Biogenic Colloidal Silver and Gold Nanoparticles: Recent Trends and Future Prospects. *Appl. Microbiol. Biotechnol.* 102, 4305–4318. doi:10.1007/s00253-018-8939-z

Pesnya, D. S. (2013). Cytogenetic Effects of Chitosan-Capped Silver Nanoparticles in theAllium Cepatest. *Caryologia* 66, 275–281. doi:10.1080/00087114.2013.852342

Piella, J., Bastús, N. G., and Puntes, V. (2017). Size-Dependent Protein-Nanoparticle Interactions in Citrate-Stabilized Gold Nanoparticles: The Emergence of the Protein Corona. *Bioconjug. Chem.* 28, 88–97. doi:10.1021/acs.bioconjchem.6b00575

Qin, L., Zeng, G., Lai, C., Huang, D., Xu, P., Zhang, C., et al. (2018). "Gold rush" in Modern Science: Fabrication Strategies and Typical Advanced Applications of Gold Nanoparticles in Sensing. *Coord. Chem. Rev.* 359, 1–31. doi:10.1016/j.ccr.2018.01.006

Rajeshwari, A., Kavitha, S., Alex, S. A., Kumar, D., Mukherjee, A., Chandrasekaran, N., et al. (2015). Cytotoxicity of Aluminum Oxide Nanoparticles on Allium cepa Root Tip-Effects of Oxidative Stress Generation and Biouptake. *Environ. Sci. Pollut. Res.* 22, 11057–11066. doi:10.1007/s11356-015-4355-4

Rajeshwari, A., Roy, B., Chandrasekaran, N., and Mukherjee, A. (2016a). Cytogenetic Evaluation of Gold Nanorods Using Allium cepa Test. *Plant Physiol. Biochem.* 109, 209–219. doi:10.1016/j.plaphy.2016.10.003

Rajeshwari, A., Suresh, S., Chandrasekaran, N., and Mukherjee, A. (2016b). Toxicity Evaluation of Gold Nanoparticles Using an Allium cepa Bioassay. *RSC Adv.* 6, 24000–24009. doi:10.1039/c6ra04712b

Sabo-Attwood, T., Unrine, J. M., Stone, J. W., Murphy, C. J., Ghoshroy, S., Blom, D., et al. (2012). Uptake, Distribution and Toxicity of Gold Nanoparticles in Tobacco (Nicotiana Xanthi) Seedlings. *Nanotoxicology* 6, 353–360. doi:10.3109/17435390.2011.579631

Saha, N., and Dutta Gupta, S. (2017). Low-dose Toxicity of Biogenic Silver Nanoparticles Fabricated by Swertia Chirata on Root Tips and Flower Buds of Allium cepa. *J. Hazard. Mater.* 330, 18–28. doi:10.1016/j.jhazmat.2017.01.021

Sani, A., Cao, C., and Cui, D. (2021). Toxicity of Gold Nanoparticles (AuNPs): A Review. *Biochem. Biophys. Rep.* 26, 100991. doi:10.1016/j.bbrep.2021.100991

Scherer, M. D., Sposito, J. C. V., Falco, W. F., Grisolia, A. B., Andrade, L. H. C., Lima, S. M., et al. (2019). Cytotoxic and Genotoxic Effects of Silver Nanoparticles on Meristematic Cells of Allium cepa Roots: A Close Analysis of Particle Size Dependence. *Sci. Total Environ.* 660, 459–467. doi:10.1016/j.scitotenv.2018.12.444

Siegel, J., Záruba, K., Švorčík, V., Kroumanová, K., Burketová, L., and Martinec, J. (2018). Round-shape Gold Nanoparticles: Effect of Particle Size and Concentration on *Arabidopsis thaliana* Root Growth. *Nanoscale Res. Lett.* 13, 95. doi:10.1186/s11671-018-2510-9

Smaka-Kincl, V., Stegnar, P., Lovka, M., and Toman, M. J. (1996). The Evaluation of Waste, Surface and Ground Water Quality Using the Allium Test Procedure. *Mutat. Research/Genetic Toxicol.* 368, 171–179. doi:10.1016/s0165-1218(96)90059-2

Soltys, D., Rudzińska-Langwald, A., Kurek, W., Gniazdowska, A., Sliwinska, E., and Bogatek, R. (2011). Cyanamide Mode of Action during Inhibition of Onion (Allium cepa L.) Root Growth Involves Disturbances in Cell Division and Cytoskeleton Formation. *Planta* 234, 609–621. doi:10.1007/s00425-011-1429-5

Song, C., Li, X., Wang, S., and Meng, Q. (2016). Enhanced Conversion and Stability of Biosynthetic Selenium Nanoparticles Using Fetal Bovine Serum. *RSC Adv.* 6, 103948–103954. doi:10.1039/c6ra22747c

Souza, I. R., Silva, L. R., Fernandes, L. S. P., Salgado, L. D., Silva de Assis, H. C., Firak, D. S., et al. (2020). Visible-light Reduced Silver Nanoparticles' Toxicity in Allium cepa Test System. *Environ. Pollut.* 257, 113551. doi:10.1016/j.envpol.2019.113551

Sztandera, K., Gorzkiewicz, M., and Klajnert-Maculewicz, B. (2018). Gold Nanoparticles in Cancer Treatment. *Mol. Pharmaceutics* 16, 1–23. doi:10.1021/acs.molpharmaceut.8b00810

Taylor, A. F., Rylott, E. L., Anderson, C. W. N., and Bruce, N. C. (2014). Investigating the Toxicity, Uptake, Nanoparticle Formation and Genetic Response of Plants to Gold. *PLOS one* 9, e93793. doi:10.1371/journal.pone.0093793

Tedesco, S., and Laughinghouse Iv, H. (2012). *Bioindicator of Genotoxicity: The Allium cepa Test*. Environmental contamination, 137–156.

Tefera, W., Liu, T., Lu, L., Ge, J., Webb, S. M., Seifu, W., et al. (2020). Micro-XRF Mapping and Quantitative Assessment of Cd in rice (Oryza Sativa L.) Roots. *Ecotoxicology Environ. Saf.* 193, 110245. doi:10.1016/j.ecoenv.2020.110245

Tsi Ndeh, N., Maensiri, S., and Maensiri, D. (2017). The Effect of green Synthesized Gold Nanoparticles on rice Germination and Roots. *Adv. Nat. Sci. Nanosci. Nanotechnol.* 8, 035008. doi:10.1088/2043-6254/aa724a

Umapathi, A., Pn, N., Madhyastha, H., Singh, M., Madhyastha, R., Maruyama, M., et al. (2020). Curcumin and Isonicotinic Acid Hydrazide Functionalized Gold Nanoparticles for Selective Anticancer Action. *Colloids Surf. A: Physicochemical Eng. Aspects* 607, 125484. doi:10.1016/j.colsurfa.2020.125484

Venzhik, Y. V., Moshkov, I. E., and Dykman, L. A. (2021). Gold Nanoparticles in Plant Physiology: Principal Effects and Prospects of Application. *Russ. J. Plant Physiol.* 68, 401–412. doi:10.1134/s1021443721020205

Wheeler, K. E., Chetwynd, A. J., Fahy, K. M., Hong, B. S., Tochihuitl, J. A., Foster, L. A., et al. (2021). Environmental Dimensions of the Protein corona. *Nat. Nanotechnol.* 16, 617–629. doi:10.1038/s41565-021-00924-1

Who (1985). *Guide to Short-Term Tests for Detecting Mutagenic and Carcinogenic Chemicals*. Geneva, Switzerland: World Health Organization.

Ye, X., Li, H., Wang, Q., Chai, R., Ma, C., Gao, H., et al. (2018). Influence of Aspartic Acid and Lysine on the Uptake of Gold Nanoparticles in rice. *Ecotoxicology Environ. Saf.* 148, 418–425. doi:10.1016/j.ecoenv.2017.10.056

Zhang, H., Goh, N. S., Wang, J. W., Pinals, R. L., González-Grandío, E., Demirer, G. S., et al. (2022). Nanoparticle Cellular Internalization is Not Required for RNA Delivery to Mature Plant Leaves. *Nat. Nanotechnol.* 17 (2), 197–205.

Zhu, Z.-J., Wang, H., Yan, B., Zheng, H., Jiang, Y., Miranda, O. R., et al. (2012). Effect of Surface Charge on the Uptake and Distribution of Gold Nanoparticles in Four Plant Species. *Environ. Sci. Technol.* 46, 12391–12398. doi:10.1021/es301977w

Zong, J., Cobb, S. L., and Cameron, N. R. (2017). Peptide-functionalized Gold Nanoparticles: Versatile Biomaterials for Diagnostic and Therapeutic Applications. *Biomater. Sci.* 5, 872–886. doi:10.1039/c7bm00006e

Conflict of Interest: The authors declare that the research was conducted in the absence of any commercial or financial relationships that could be construed as a potential conflict of interest.

Publisher's Note: All claims expressed in this article are solely those of the authors and do not necessarily represent those of their affiliated organizations or those of the publisher, the editors, and the reviewers. Any product that may be evaluated in this article, or claim that may be made by its manufacturer, is not guaranteed or endorsed by the publisher.

frontiers | Frontiers in Bioengineering and Biotechnology

REVIEW
published: 06 July 2022
doi: 10.3389/fbioe.2022.855195

The Emerging Applications of Nanotechnology in Neuroimaging: A Comprehensive Review

Khunza Faiz[1†], Fred C. Lam[2,3†], Jay Chen[1], Ekkehard M. Kasper[3*] and Fateme Salehi[1*]*

[1]Department of Radiology, McMaster University Faculty of Health Sciences, Hamilton, ON, Canada, [2]Koch Institute for Integrative Cancer Research at MIT, Cambridge, MA, United States, [3]Division of Neurosurgery, Saint Elizabeth Medical Center, Brighton, MA, United States

Neuroimaging modalities such as computer tomography and magnetic resonance imaging have greatly improved in their ability to achieve higher spatial resolution of neurovascular and soft tissue neuroanatomy, allowing for increased accuracy in the diagnosis of neurological conditions. However, the use of conventional contrast agents that have short tissue retention time and associated renal toxicities, or expensive radioisotope tracers that are not widely available, continue to limit the sensitivity of these imaging modalities. Nanoparticles can potentially address these shortcomings by enhancing tissue retention and improving signal intensity in the brain and neural axis. In this review, we discuss the use of different types of nanotechnology to improve the detection, diagnosis, and treatment of a wide range of neurological diseases.

Keywords: nanotechnology, neurooncology, neuroimaging, neurodegenerative diseases, cerebrovascular disease

OPEN ACCESS

Edited by:
Qingxin Mu,
University of Washington,
United States

Reviewed by:
Leopoldo Sitia,
University of Milan, Italy
Jacopo Annese,
The Institute for Brain and Society,
United States

***Correspondence:**
Fred C. Lam
fredlam@mit.edu
Ekkehard M. Kasper
kaspere@mcmaster.ca
Fateme Salehi
sfateme@gmail.com

[†]These authors have contributed equally to this work

Specialty section:
This article was submitted to Nanobiotechnology, a section of the journal Frontiers in Bioengineering and Biotechnology

Received: *14 January 2022*
Accepted: *06 June 2022*
Published: *06 July 2022*

Citation:
Faiz K, Lam FC, Chen J, Kasper EM and Salehi F (2022) The Emerging Applications of Nanotechnology in Neuroimaging: A Comprehensive Review. Front. Bioeng. Biotechnol. 10:855195. doi: 10.3389/fbioe.2022.855195

INTRODUCTION

Current non-invasive modalities used in neuroimaging and diagnosis of diseases of the central nervous system (CNS) include: computed tomography (CT), magnetic resonance imaging (MRI), functional MRI (fMRI), functional near-infrared spectroscopy, functional photoacoustic imaging, and molecular imaging including positron emission tomography (PET), single photon emission CT (SPECT), and molecular MRI (George et al., 2018). While conventional CT and MRI are by far the workhorses in neuroradiology, limitations of these techniques exist, including: the relative low sensitivity and tissue resolution of CT, the long acquisition time required for MRI, and the high cost of radioisotopes and low resolution of PET (George et al., 2018). Furthermore, common gadolinium-based (Gd) contrast agents such as gadopentetate dimeglumine (Magnevist®, Bayer), administered intravenously to allow for enhancement and better visualization of both intra- and extra-axial brain tumors, have a short half-life in the bloodstream, low retention time in the tumor microenvironment, and increased risk of nephrotic systemic fibrosis in patients with renal insufficiency (Bayer, 2017). To overcome these limitations, researchers have began incorporating the use of nanotechnology to enhance the ability of these agents to achieve longer retention time in the CNS, better spatial resolution on imaging, and delivery of therapies to the cells of interest in the brain (Ngowi et al., 2021).

The diverse biophysical and chemical properties of nanoparticles (NPs) are distinct advantages for their use in CNS applications. Their small size (usually 1–100 nm in largest diameter), modularity, diverse chemical compositions, and ability to be functionalized with surface moieties to allow for targeting across the blood-brain barrier (BBB) to a specific cell type of interest, makes NPs an attractive carrier for the delivery of cargo into the CNS for use in downstream biomedical

applications (Sim and Wong, 2021). In this review, we will discuss the emerging use of nanotechnology to assist in the imaging of neurological conditions including: 1) Primary and secondary brain tumors; 2) Cerebrovascular disorders; 3) Neurodegenerative disorders; and 4) Functional neurological disorders.

NANOTECHNOLOGY FOR THE IMAGING OF BRAIN TUMORS

MRI with and without the use of Gd contrast allows for the delineation of higher grade primary brains tumors such as glioblastoma, secondary brain metastases, and extra-axial tumors such as meningiomas, due to the nature of these tumors to secrete vascular endothelial growth factor which causes the formation a tortuous and leaky BBB around the tumor which allows for the extravasation of contrast agent, leading to visualization of the tumor mass on subsequent T1-weighted MRI sequences (Jain et al., 2007; George et al., 2018). However, conventional contrast-enhanced MRI sequences are limited in being able to differentiate the phenomenon of pseudoprogression (caused by radiation changes to surrounding tumor vasculature increasing leakiness and subsequent enhancement on post-treatment MRI scans) from true tumor progression.

To increase the spatial resolution of tumors on MRI, magnetic NPs such as iron oxide nanoparticles (IONPs) or manganese oxide nanoparticles (MnO NPs) have demonstrated increased relaxivity on T1-and T2-weighted MRI sequences (Vallabani et al., 2019). Functionalization of IONPs and MnO NPs with folate or albumin have enabled specific targeting of glioma cells in orthotopic mouse models of glioma, enabling longer periods of signal enhancement on MRI and could possibly aid in differentiating between true tumor signal versus pseudoprogression (Chen et al., 2014; Zhou et al., 2019). Other researchers have synthesized Gd-chelated-IONPs functionalized with interleukin-13 (Li et al., 2015), antibodies against the mutant epidermal growth factor receptor (EGFRvIII) (Hadjipanayis et al., 2010), or cyclic arginine-glycine-aspartic acid (cRGD) peptides (Booth et al., 2017), to enhance glioma targeting for enhanced imaging in preclinical animal models of glioma. A recent clinical trial demonstrated the ability of the FDA-approved IONP ferumoxytol conjugated to gadolinium contrast to define glioma pseudoprogression on MRI (Barajas et al., 2019), while another pilot study demonstrated the ability of feromoxytol to detect tumor-associated macrophages on enhanced MRI (Iv et al., 2019), showing the potential for IONP enhanced MRIs to improve cellular resolution of brain tumors.

Current clinical trials investigating the use of IONPs for molecular imaging of brain tumors include: 1) A phase I safety trial of intravenous ferumoxytol for dynamic MR imaging of recurrent high-grade gliomas patients on chemotherapy (NCT00769093) (Institute, 2017a); 2) A phase I study of ferumoxytol to assess early treatment response using perfusion MRI in patients with glioblastoma (NCT00660543) (Institute, 2017b); 3) A phase 0 safety and effectiveness exploratory trial of ferumoxytol in assessing vascular properties of pediatric brain tumors in a single imaging session (NCT00978562) (Institute, 2018); 4) A phase 2 study comparing ferumoxytol in characterizing tumor vasculature compared to Gd-contrast MRI in 3 and 7 T MRI machines in patients with malignant brain tumors (NCT00659126) (Institute, 2021); 5) A phase 2 study of ferumoxytol in characterizing tumor-associated vasculature in patients with primary brain tumors or lung or breast brain metastases using MRI (NCT00103038) (Institute, 2017c); and 6) A phase 2 study of the safety of ferumoxytol in causing CNS inflammation (NCT00659776) (OHSU, 2022).

NANOTECHNOLOGY FOR THE DIAGNOSIS OF NEURODEGENERATIVE DISORDERS

Neurodegenerative disorders encompass a wide variety of neurological conditions, from Alzheimer's Disease (AD), Parkinson's Disease (PD), Huntington's Disease (HD), to Multiple Sclerosis (MS) and motor neuron diseases. As a full discussion of all these disorders goes beyond the scope of this review, we will focus on AD and PD—the two neurodegenerative disorders for which there have been the most prolific application of NPs as a neuroimaging tool to aid in diagnosis and management.

i) Alzheimer's Disease

The two pathognomonic features of AD include extracellular beta-amyloid (Aβ) plaques and neurofibrillary tangles of hyperphosphorylated tau protein in dystrophic neurites (Alzheimer's Association, 2014). Current imaging modalities for the diagnosis of Aβ plaques and tau tangles include radioactive PET tracers such as fluorodeoxyglucose, [^{18}F] flutemetamol, and [^{18}F]flortaucipir (Mason et al., 2010). However, these radioisotopes are costly and not readily available worldwide. To help overcome these limitations, researchers have developed various IONP nanoprobes that can detect Aβ plaques in the brain via a conjugated Aβ antibody on MRI in transgenic AD mice (Sillerud et al., 2013; Viola et al., 2015; Li et al., 2016). Nanotechnology-based PET has also been used in preclinical models to detect Aβ plaques *in vivo* (Sharma et al., 2017), demonstrating the potential for use in diagnostic imaging of human AD patients.

ii) Parkinson's Disease

Progressive degeneration of dopaminergic neurons in the basal ganglia substantia nigra with abnormal deposition of α-synuclein protein is thought to cause the bradykinesia, and dystonia seen in PD patients (Obeso et al., 2017). Aggregates of α-synuclein seen in other nuclei in the brain are thought to further contribute to the non-motor symptoms seen in PD patients such as hyposmia and dysautonomia, making α-synuclein an attractive biomarker for tracking disease

progression (Surmeier et al., 2017). ^{123}I-ioflupane labelled dopamine SPECT can be used to monitor olfactory nerve dysfunction and serial MRI of basal ganglia are current tools for diagnosis and tracking of PD (Booij et al., 2001; Morbelli et al., 2020). Novel non-invasive preclinical imaging tools to detect fibrillary α-synuclein currently lack adequate sensitivity and specificity. A recent study using a dLight1 fluorescence sensor to detect dopaminergic signals in the brains of transgenic PD mice yielded promising preliminary results in being able to detect fluorescent signals in dopaminergic neurons (Patriarchi et al., 2018), while a dopamine-responsive nanoprobe that reacts in the near-infrared spectrum detected dopamine signals in preclinical models of drug abuse and PD (Feng et al., 2018), suggesting that these experimental imaging modalities and targeted nanoprobes could have potential applications in human diagnosis of PD.

NANOTECHNOLOGY FOR THE IMAGING OF CEREBRAL ISCHEMIA

Acute blockage of blood vessels in the brain leads to cerebral ischemia or stroke, which requires prompt diagnosis and treatment to prevent permanent ischemic injury to the areas of the brain supplied by the affected blood vessels to prevent motor or sensory deficits (Moskowitz et al., 2010). Ischemic stroke is the second most common cause of death worldwide after cardiovascular disease, with approximately 87% mortality if left untreated (Association, 2015). The ability to detect and locate the blockage and visualize the affected region of the brain with high sensitivity and spatial resolution can allow for accurate diagnosis, treatment, and serial monitoring of the treatment outcomes.

MRI and MR perfusion scans to assess cerebral blood flow are the current gold standard non-invasive modalities for stroke imaging (Marks, 2016). Similar to the use of NPs to augment contrast enhancement for the detection of brain tumor vasculature, researchers have used NPs to increase the sensitivity and cellular resolution of areas of the brain affected by ischemia. IONPs conjugated with RGD peptide targeting the αvβ3 integrin receptors on endothelium have been used to enhance imaging of collateral vessels that form in the surrounding area of ischemia (Wang et al., 2018). Another study comparing carbohydrate wrapped ferumoxytol to a Gd-based contrast agent found that ferumoxytol was able to detect cerebral blood volume at higher resolution at steady state than dynamic susceptibility contrast MR perfusion imaging using Gd (Varallyay et al., 2013). By leveraging the relative acidic environment in the ischemic penumbra, pH-responsive IONPs encapsulated in poly(β-amino ester)-poly(aminodoamine)-poly(ethylene glycol) block copolymer were released and accumulated in the ischemic region of the brain in a rat model of cerebral ischemia, enabling detection on MRI (Gao et al., 2011). A safety study of IONPs in canines and macaque monkeys demonstrated sensitive detection of ischemia on T1-weighted MR sequences in cerebral ischemia-induced animals, providing further preclinical evidence supporting their safety for use in human stroke patients (Lu et al., 2017).

CT angiography (CTA) using iodinated contrast agent provides 3-dimensional reconstructed images of large vessel occlusion. Encapsulation of CT contrast agents may facilitate enhanced delivery of imaging agents to the affected region of the brain. Polyethylene glycol (PEG) wrapped or PEGylated $BaHoF_5$ nanoprobes with an average diameter of 7 nm exhibited superior enhancement properties compared to the clinical contrast agent iohexol® in CTA and CT perfusion imaging of a rat model of left middle cerebral artery occlusion (Wang et al., 2015). Gold NPs have also been used due to their biocompatibility and ability to incorporate targeting, therapeutic, and imaging moieties for multimodal imaging and theranostics. Chitosan-coated gold NPs with the ability to target fibrin were used to quantitate the amount of thrombolysis in a cerebral thromboembolic model of stroke in mice following treatment with intravenous tissue plasminogen activator (tPA). Serial CT imaging detected rapid thrombolysis following tPA treatment (Kim et al., 2017).

Ultrasonography can be used to detect and image flow through blood vessels. Ultrasound contrast enhancers such as gas-filled microbubbles increase the "echogenicity" of the vessels, thereby increasing their chances to be detected using ultrasound (Sirsi and Borden, 2009). These microbubbles are composed of albumin, lipids, or polymers and can be filled with air, perfluorocarbons, or nitrogen, and can be functionalized with surface ligands for targeting (Paefgen et al., 2015). Perfluorocarbon emulsions conjugated with anti-fibrin antibodies have demonstrated the ability to visualize thrombus in a model of cerebral ischemia on ultrasound (Chen et al., 2013a).

IONPs have also been used to visualize areas of relative signal attenuation using microwave imaging in a rabbit model of cerebral ischemia as well as in a human volunteer (Hudson et al., 2019). Applying a PEG coating to the surface of IONPs can greatly increase the circulation time of these NPs in the bloodstream (Khandhar et al., 2017), enabling three-dimensional angiography following a single injection of PEGylated IONPs to allow for real-time imaging of cerebral vasculature in mouse models to assess cerebral hemorrhage in a mouse model of traumatic brain injury over a period of hours (Goodwill et al., 2012; Orendorff et al., 2017). Taken together, these emerging uses of NPs to enhance multimodal imaging and assessment of cerebral ischemia may hopefully translate into the clinic to improve patient outcomes. Please refer to an excellent review on the emerging uses of nanotechnology in the imaging of stroke by Kaviarasi and colleagues for further information on this topic (Kaviarasi et al., 2019) and for ease of reference for our readers, we have compiled a list of NPs that are in human clinical trials or have been approved for neurological disorders (**Table 1**).

DISCUSSION

Implementation of nanoscale materials for neuroimaging is still in the early stages of preclinical development. Several limitations exist that currently prevent the widespread application of nanomaterials for use in the CNS space. The

TABLE 1 | Nanoparticles approved or currently in clinical trials for neurological diseases. List of nanoparticles that are in human clinical trials or have been approved for the treatment of neuro-oncologic, neurodegenerative, and cerebovascular disorders.

Neuro-oncology		
Trade name	**Product formulation**	**Level of clinical development and treatment applications**
SGT-53 (Anselmo and Mitragotri, 2016)	Transferrin-functionalized liposomal plasmid wild-type p53 DNA	NCT02340156—Phase II open label, single-arm, multicenter study of IV SGT-53 and oral temozolomide in patients with confirmed recurrent glioblastoma or progression.
DepoCyt (Zhang et al., 2008; Khanbabaie and Jahanshahi, 2012)	Liposomal cytarabine	Approved for treatment of malignant lymphomatous meningitis.
DaunoXome (Zhang et al., 2008; Khanbabaie and Jahanshahi, 2012)	Liposomal daunorubicin	Approved for HIV-related Kaposi's sarcoma.
Neulasta (Gabizon et al., 2006; Kumar et al., 2013)	PEGylated granulocyte colony-stimulating factor	Approved for treatment of chemotherapy-associated neutropenia.
Cornell Dots (Anselmo and Mitragotri, 2016)	PEGylated silica NPs of ^{124}I-cRGDY NIR fluorophore	Phase 0 safety trial of imaging of melanoma and malignant brain tumors.
Neurodegenerative Disorders		
Trade Name	**Product Formulation**	**Level of Clinical Development and Treatment Applications**
Visudyne (Zhang et al., 2008; Khanbabaie and Jahanshahi, 2012)	Liposomal verteporfin	Approved for treatment of age-related mascular degeneration, pathologic myopia, and ocular histoplasmosis.
Macugen (Gabizon et al., 2006; Kumar et al., 2013)	PEGylated anti-VEGF aptimer	Approved for age-related macular degeneration.
Partisiran (Anselmo and Mitragotri, 2016)	Liposomal transthyretin siRNA	Phase I-III study for the treatment of hereditary transthyretin-mediated amyloidosis. Characterized by peripheral sensorimotor and autonomic neuropathy. RNA interference that reduces production of both wild-type and mutant transthyretin protein. Phase III APOLLO study showed significant improvement in polyneuropathy.
Copaxone (Gabizon et al., 2006; Kumar et al., 2013)	Copolymer of L-Glutamic acid, L-alanine, and L-tyrosine	Approved for the treatment of Multiple Sclerosis.
Cerebrovascular Disorders		
Trade Name	**Product Formulation**	**Level of Clinical Development and Treatment Applications**
Definity (Anselmo and Mitragotri, 2016)	Perflutren lipid microspheres	Approved ultrasound contrast agent for imaging of cerebral ischemia and transcranial brain injuries.

presence of the intact BBB with endothelial tight junctions that limit passage of most materials greater than 100 nm in diameter restricts the bulkiness of nanomaterials that can be delivered systemically into the brain (Sarin et al., 2009). The cellular complexity of the CNS makes it difficult to target NPs to specific cells of interest (i.e. neurons and not glia) and avoid unintended off-target effects to different types of nearby cells. Finally, the brain is bathed in cerebrospinal fluid (CSF), which pulses with each heartbeat, creating a natural washout effect that actively prevents accumulation of cargo at the desired site of delivery (Hendricks et al., 2015). Furthermore, even with targeted delivery approaches using functionalized NPs that preferentially recognize protein receptors on cell surfaces (i.e., transferrin receptors on the surfaces of glioma cells), the percent injected dose of NPs that ultimately cross the BBB via the bloodstream is meager and would require dosing human subjects with hundreds of milliliters of NPs intravenously to achieve a detectable phenotypic effect (Wilhelm et al., 2016). More invasive mechanisms of bypassing the BBB such as direct administration of NPs into the brain using stereotactic implantable catheters or use of convection enhanced delivery or local ultrasonic disruption of the BBB can improve the uptake of NPs, but these tools are limited to specialized hospital centers, require collaborative efforts from a neurosurgical team, and are generally not recommended for use in day-to-day neuroimaging procedures (McDannold et al., 2012; Hendricks et al., 2015; Magill et al., 2020).

Metallic NPs are currently the most researched nanomaterials for emerging neuroimaging technologies. Due to their physicochemical compositions, metal oxide NPs have been incorporated in a broad range of biomedical applications, from imaging contrast agents to scaffolding materials for tissue regeneration. Their small size (~50 nm) also makes them ideal for trafficking across the BBB into the CNS space to enhance neuroimaging modalities and deliver various types of cargo for the treatment of neurological disorders (Stark et al., 1988; Jung and Jacobs, 1995; Barajas et al., 2019). The iron oxide contrast agent ferumoxytol (Feraheme®, AMAG) has seen increasing usage in MR imaging in North America, while the IONP formulation ferumoxtran-10 (Sinerem/Combidex) has been gaining interest in human clinical trials in Europe (Harisinghani et al., 2003; Heesakkers et al., 2008; Triantafyllou et al., 2013; Smits et al., 2016). With decades of longitudinal data regarding the biodistribution, pharmacokinetics, and pharmacodynamics of IONPs, we now have a deeper understanding of how IONPs behave in the CNS and its associated neurotoxicities, which may limit their

translational potential. *In vitro* studies have demonstrated uptake of IONPs into neurons, glia, and astrocytes via micropinocytosis and clathrin-mediated endocytosis with trafficking into lysosomal compartments (Luther et al., 2013; Huerta-García et al., 2015; Pongrac et al., 2018). Exposure to silver NPs in a BBB co-culture model led to shrinkage of mitochondria, expansion of the endoplasmic reticulum, and vacuolation in astrocytes with altered gene expression across 23 genes associated with metabolic, biosynthetic, and cell death processes (Xu et al., 2013). Astrocytes increased production of reactive oxygen species and decreased viability when exposed to copper oxide NPs (Bulcke et al., 2014). Interestingly, studies have shown that the toxicity of IONPs depended on the surface coating. Polydimethyloamine coating caused cell membrane disruption and cell death in cultured cortical neurons, while aminosilane coating left the cell membrane intact but affected cellular metabolism, but dextran remained inert to cultured neurons (Rivet et al., 2012). *In vivo* toxicity experiments have demonstrated accumulation of aluminum NPs in mouse brain endothelial cells causing neurovascular damage and increased BBB permeability (Chen et al., 2013b), while acute exposure of gold NPs to male Wistar rats led to catabolic and energy metabolic suppression in the hippocampus, striatum, and cerebral cortex but long-term exposure only resulted in inhibition of catalase and energy metabolism in the cortex (Ferreira et al., 2017). Taken together, these data indicate that neurotoxicity studies need to be done in higher order organisms such as non-human primates to better understand the mechanisms of neurotoxicity associated with NPs that are applied for CNS applications in humans.

We recently reviewed emerging applications of nanotechnology in the fields of neurosurgery, neuro-oncology, and neuroradiology from the perspective of clinician-scientists (Lam et al., 2022). One emerging area is the ability to imbue NPs with theranostic capabilities—functionalizing NPs with the dual ability to detect cells of interest and deliver therapeutic cargo. A recent first-in-human trial using the EGFR antibody cetuximab conjugated to the near-infrared (NIR) fluorescent dye IRDye800 (cetuximab-IRDye800) during neurosurgical resection of gliomas demonstrated the specificity of the antibody-dye conjugate to specifically attach to EGFR-expressing glioma cells in the brain, enhancing the detection of tumor cells during surgery and potentially assisting the neurosurgeon in achieving a more extensive surgical resection, which could improve patient survival (Miller et al., 2018). Conjugation of a CD133 monoclonal antibody to a phototoxic phthalocyanine NIR dye IR700 allowed for specific targeting and imaging of CD133+ glioma stem cells and treatment using NIR photoimmunotherapy to cause tumor shrinkage and cell death in a murine intracranial orthotopic model of glioma (Jing et al., 2016). Multi-walled carbon nanotubes have been used to replace conventional silver-silver chloride electrodes used in electroencephalography to eliminate the metal-associated artifacts seen in CT and x-ray images of the brain, to allow for better visualization of the brain during image-guided neurosurgical procedures (Awara et al., 2014). Nanoknives made from silicon nitride with 20 nm tips can make minute and precise incisions to reduce the amount of cerebral tissue damage associated with using conventional neurosurgical tools (Chang et al., 2007). Finally, dextran-coated IONPs covalently linked to tPA in an agarose gel can enhance the fibrinolytic activity of tPA for days, prolonging thrombolysis and potentially improving outcomes for stroke victims (Heid et al., 2017). With further development of these exciting preclinical discoveries, there is hope that researchers will be able to bridge the gap from benchtop to bedside.

CONCLUSION

The application of nanotechnology for use in neuroimaging has gained steady progress. Although this platform is still in its early stages of technology development, the ability to harness NPs as a theranostic will further enhance the function of NPs in the CNS to treat a wide variety of neurological disorders. The ability to decrease the neurotoxic nature of NPs will improve their safety profile and improve the translational potential for use in patients.

AUTHOR CONTRIBUTIONS

All authors listed have made a substantial, direct, and intellectual contribution to the work and approved it for publication.

REFERENCES

Alzheimer's Association (2014). 2014 Alzheimer's Disease Facts and Figures. *Alzheimers Dement.* 10, e47–92. doi:10.1016/j.jalz.2014.02.001

Anselmo, A. C., and Mitragotri, S. (2016). Nanoparticles in the Clinic. *Bioeng. Transl. Med.* 1, 10–29. doi:10.1002/btm2.10003

Association, T. A. H. (2015). Ischemic Strokes (Clots). Available at: http://www.strokeassociation.org/STROKEORG/AboutStroke/TypeofStroke/IschemicClots/Ischemic-Strokes-Clots_UCM_310939_Article.jsp#.WdzLmY-OPIU%0.

Awara, K., Kitai, R., Isozaki, M., Neishi, H., Kikuta, K., Fushisato, N., et al. (2014). Thin-film Electroencephalographic Electrodes Using Multi-Walled Carbon Nanotubes Are Effective for Neurosurgery. *Biomed. Eng. Online* 13, 166. doi:10.1186/1475-925X-13-166

Barajas, R. F., Hamilton, B. E., Schwartz, D., McConnell, H. L., Pettersson, D. R., Horvath, A., et al. (2019). Combined Iron Oxide Nanoparticle Ferumoxytol and Gadolinium Contrast Enhanced MRI Define Glioblastoma Pseudoprogression. *Neuro Oncol.* 21, 517–526. doi:10.1093/neuonc/noy160

Bayer (2017). Magnevist Product Monograph. Available at: http://www.bayer.com/sites/default/files/2020-11/magnevist-pm-en.pdf.

Booij, J., Speelman, J. D., Horstink, M. W. I. M., and Wolters, E. C. (2001). The Clinical Benefit of Imaging Striatal Dopamine Transporters with [123I]FP-CIT SPET in Differentiating Patients with Presynaptic Parkinsonism from Those with Other Forms of Parkinsonism. *Eur. J. Nucl. Med.* 28, 266–272. doi:10.1007/s002590000460

Booth, H. D. E., Hirst, W. D., and Wade-Martins, R. (2017). The Role of Astrocyte Dysfunction in Parkinson's Disease Pathogenesis. *Trends Neurosci.* 40, 358–370. doi:10.1016/j.tins.2017.04.001

Bulcke, F., Thiel, K., and Dringen, R. (2014). Uptake and Toxicity of Copper Oxide Nanoparticles in Cultured Primary Brain Astrocytes. *Nanotoxicology* 8, 1–11. doi:10.3109/17435390.2013.829591

Chang, W. C., Hawkes, E. A., Kliot, M., and Sretavan, D. W. (2007). *In Vivo* use of a Nanoknife for Axon Microsurgery. *Neurosurgery* 61, 683–692. discussion 691-682. doi:10.1227/01.NEU.0000298896.31355.80

Chen, J., Pan, H., Lanza, G. M., and Wickline, S. A. (2013). Perfluorocarbon Nanoparticles for Physiological and Molecular Imaging and Therapy. *Adv. Chronic Kidney Dis.* 20, 466–478. doi:10.1053/j.ackd.2013.08.004

Chen, L., Zhang, B., and Toborek, M. (2013). Autophagy Is Involved in Nanoalumina-Induced Cerebrovascular Toxicity. *Nanomedicine Nanotechnol. Biol. Med.* 9, 212–221. doi:10.1016/j.nano.2012.05.017

Chen, N., Shao, C., Qu, Y., Li, S., Gu, W., Zheng, T., et al. (2014). Folic Acid-Conjugated MnO Nanoparticles as a T1 Contrast Agent for Magnetic Resonance Imaging of Tiny Brain Gliomas. *ACS Appl. Mat. Interfaces* 6, 19850–19857. doi:10.1021/am505223t

Feng, P., Chen, Y., Zhang, L., Qian, C.-G., Xiao, X., Han, X., et al. (2018). Near-Infrared Fluorescent Nanoprobes for Revealing the Role of Dopamine in Drug Addiction. *ACS Appl. Mat. Interfaces* 10, 4359–4368. doi:10.1021/acsami.7b12005

Ferreira, G. K., Cardoso, E., Vuolo, F. S., Galant, L. S., Michels, M., Gonçalves, C. L., et al. (2017). Effect of Acute and Long-Term Administration of Gold Nanoparticles on Biochemical Parameters in Rat Brain. *Mater. Sci. Eng. C* 79, 748–755. doi:10.1016/j.msec.2017.05.110

Gabizon, A. A., Shmeeda, H., and Zalipsky, S. (2006). Pros and Cons of the Liposome Platform in Cancer Drug Targeting. *J. Liposome Res.* 16, 175–183. doi:10.1080/08982100600848769

Gao, G. H., Lee, J. W., Nguyen, M. K., Im, G. H., Yang, J., Heo, H., et al. (2011). pH-Responsive Polymeric Micelle Based on PEG-Poly(β-Amino Ester)/(amido Amine) as Intelligent Vehicle for Magnetic Resonance Imaging in Detection of Cerebral Ischemic Area. *J. Control. Release* 155, 11–17. doi:10.1016/j.jconrel.2010.09.012

George, E., Guenette, J. P., and Lee, T. C. (2018). Introduction to Neuroimaging. *Am. J. Med.* 131, 346–356. doi:10.1016/j.amjmed.2017.11.014

Goodwill, P. W., Saritas, E. U., Croft, L. R., Kim, T. N., Krishnan, K. M., Schaffer, D. V., et al. (2012). X-space MPI: Magnetic Nanoparticles for Safe Medical Imaging. *Adv. Mat.* 24, 3870–3877. doi:10.1002/adma.201200221

Hadjipanayis, C. G., Machaidze, R., Kaluzova, M., Wang, L., Schuette, A. J., Chen, H., et al. (2010). EGFRvIII Antibody-Conjugated Iron Oxide Nanoparticles for Magnetic Resonance Imaging-Guided Convection-Enhanced Delivery and Targeted Therapy of Glioblastoma. *Cancer Res.* 70, 6303–6312. doi:10.1158/0008-5472.CAN-10-1022

Harisinghani, M. G., Barentsz, J., Hahn, P. F., Deserno, W. M., Tabatabaei, S., van de Kaa, C. H., et al. (2003). Noninvasive Detection of Clinically Occult Lymph-Node Metastases in Prostate Cancer. *N. Engl. J. Med.* 348, 2491–2499. doi:10.1056/NEJMoa022749

Heesakkers, R. A., Hövels, A. M., Jager, G. J., van den Bosch, H. C., Witjes, J. A., Raat, H. P., et al. (2008). MRI with a Lymph-node-specific Contrast Agent as an Alternative to CT Scan and Lymph-Node Dissection in Patients with Prostate Cancer: a Prospective Multicohort Study. *Lancet Oncol.* 9, 850–856. doi:10.1016/S1470-2045(08)70203-1

Heid, S., Unterweger, H., Tietze, R., Friedrich, R. P., Weigel, B., Cicha, I., et al. (2017). Synthesis and Characterization of Tissue Plasminogen Activator-Functionalized Superparamagnetic Iron Oxide Nanoparticles for Targeted Fibrin Clot Dissolution. *Int. J. Mol. Sci.* 18, E1837. [pii]10.3390/ijms18091837. doi:10.3390/ijms18091837

Hendricks, B. K., Cohen-Gadol, A. A., and Miller, J. C. (2015). Novel Delivery Methods Bypassing the Blood-Brain and Blood-Tumor Barriers. *Foc* 38, E10. doi:10.3171/2015.1.FOCUS14767

Hudson, J. S., Chung, T. K., Prout, B. S., Nagahama, Y., Raghavan, M. L., and Hasan, D. M. (2019). Iron Nanoparticle Contrast Enhanced Microwave Imaging for Emergent Stroke: A Pilot Study. *J. Clin. Neurosci.* 59, 284–290. doi:10.1016/j.jocn.2018.10.100

Huerta-García, E., Márquez-Ramírez, S. G., Ramos-Godinez, M. d. P., López-Saavedra, A., Herrera, L. A., Parra, A., et al. (2015). Internalization of Titanium Dioxide Nanoparticles by Glial Cells Is Given at Short Times and Is Mainly Mediated by Actin Reorganization-dependent Endocytosis. *Neurotoxicology* 51, 27–37. doi:10.1016/j.neuro.2015.08.013

Institute, O. K. C. (2017). Assessing Dynamic Magnetic Resonance (MR) Imaging in Patients with Recurrent High Grade Glioma Receiving Chemotherapy (Code 7228). Available at: http://clinicaltrials.gov/ct2/show/NCT00769093.

Institute, O. K. C. (2021). Ferumoxytol and Gadolinium Magnetic Resonance Imaging (MRI) at 3T and 7T in Patients with Malignant Brain Tumors. Available at: http://clinicaltrials.gov/ct2/show/NCT00659126.

Institute, O. K. C. (2018). Imaging Vascular Properties of Pediatric Brain Tumors Using Ferumoxytol and Gadolinium in a Single Imaging Session. Available at: http://www.clinicaltrials.gov/ct2/show/NCT00978562.

Institute, O. K. C. (2017). Magnetic Resonance (MR) Imaging Study Using Ferumoxytol to Assess Early Tumor Response in Patients with Glioblastoma Multiforme. Available at: http://clinicaltrials.gov/show/NCT00660543.

Institute, O. K. C. (2017). MRI Using Ferumoxytol in Patients with Primary Brain Cancer or Brain Metastases from Lung or Breast Cancer. Available at: http://clinicaltrials.gov/ct2/show/NCT00103038.

Iv, M., Samghabadi, P., Holdsworth, S., Gentles, A., Rezaii, P., Harsh, G., et al. (2019). Quantification of Macrophages in High-Grade Gliomas by Using Ferumoxytol-Enhanced MRI: A Pilot Study. *Radiology* 290, 198–206. doi:10.1148/radiol.2018181204

Jain, R. K., di Tomaso, E., Duda, D. G., Loeffler, J. S., Sorensen, A. G., and Batchelor, T. T. (2007). Angiogenesis in Brain Tumours. *Nat. Rev. Neurosci.* 8, 610–622. doi:10.1038/nrn2175

Jing, H., Weidensteiner, C., Reichardt, W., Gaedicke, S., Zhu, X., Grosu, A.-L., et al. (2016). Imaging and Selective Elimination of Glioblastoma Stem Cells with Theranostic Near-Infrared-Labeled CD133-specific Antibodies. *Theranostics* 6, 862–874. doi:10.7150/thno.12890

Jung, C. W., and Jacobs, P. (1995). Physical and Chemical Properties of Superparamagnetic Iron Oxide MR Contrast Agents: Ferumoxides, Ferumoxtran, Ferumoxsil. *Magn. Reson. Imaging* 13, 661–674. doi:10.1016/0730-725x(95)00024-b

Kaviarasi, S., Yuba, E., Harada, A., and Krishnan, U. M. (2019). Emerging Paradigms in Nanotechnology for Imaging and Treatment of Cerebral Ischemia. *J. Control. Release* 300, 22–45. doi:10.1016/j.jconrel.2019.02.031

Khanbabaie, R., and Jahanshahi, M. (2012). Revolutionary Impact of Nanodrug Delivery on Neuroscience. *Curr. Neuropharmacol.* 10, 370–392. CN-10-370 [pii] (2012). doi:10.2174/157015912804143513

Khandhar, A. P., Keselman, P., Kemp, S. J., Ferguson, R. M., Goodwill, P. W., Conolly, S. M., et al. (2017). Evaluation of PEG-Coated Iron Oxide Nanoparticles as Blood Pool Tracers for Preclinical Magnetic Particle Imaging. *Nanoscale* 9, 1299–1306. doi:10.1039/c6nr08468k

Kim, D.-E., Kim, J.-Y., Schellingerhout, D., Ryu, J. H., Lee, S.-K., Jeon, S., et al. (2017). Quantitative Imaging of Cerebral Thromboemboli *In Vivo*. *Stroke* 48, 1376–1385. doi:10.1161/STROKEAHA.117.016511

Kumar, A., Chen, F., Mozhi, A., Zhang, X., Zhao, Y., Xue, X., et al. (2013). Innovative Pharmaceutical Development Based on Unique Properties of Nanoscale Delivery Formulation. *Nanoscale* 5, 8307–8325. doi:10.1039/c3nr01525d

Lam, F. C., Salehi, F., and Kasper, E. M. (2022). Integrating Nanotechnology in Neurosurgery, Neuroradiology, and Neuro-Oncology Practice-The Clinicians' Perspective. *Front. Bioeng. Biotechnol.* 10, 801822. doi:10.3389/fbioe.2022.801822

Li, S.-S., Lin, C.-W., Wei, K.-C., Huang, C.-Y., Hsu, P.-H., Liu, H.-L., et al. (2016). Non-invasive Screening for Early Alzheimer's Disease Diagnosis by a Sensitively Immunomagnetic Biosensor. *Sci. Rep.* 6, 25155. doi:10.1038/srep25155

Li, T., Murphy, S., Kiselev, B., Bakshi, K. S., Zhang, J., Eltahir, A., et al. (2015). A New Interleukin-13 Amino-Coated Gadolinium Metallofullerene Nanoparticle for Targeted MRI Detection of Glioblastoma Tumor Cells. *J. Am. Chem. Soc.* 137, 7881–7888. doi:10.1021/jacs.5b03991

Lu, Y., Xu, Y.-J., Zhang, G.-b., Ling, D., Wang, M.-q., Zhou, Y., et al. (2017). Iron Oxide Nanoclusters for T 1 Magnetic Resonance Imaging of Non-human Primates. *Nat. Biomed. Eng.* 1, 637–643. doi:10.1038/s41551-017-0116-7

Luther, E. M., Petters, C., Bulcke, F., Kaltz, A., Thiel, K., Bickmeyer, U., et al. (2013). Endocytotic Uptake of Iron Oxide Nanoparticles by Cultured Brain Microglial Cells. *Acta Biomater.* 9, 8454–8465. doi:10.1016/j.actbio.2013.05.022

Magill, S. T., Choy, W., Nguyen, M. P., and McDermott, M. W. (2020). Ommaya Reservoir Insertion: A Technical Note. *Cureus* 12, e7731. doi:10.7759/cureus.7731

Marks, M. P. (2016). *Magnetic Resonance of the Brain and Spine Vol. 2*. Editor W. Atlas. (Wolters Kluwer Health).

Mason, S. E., McShane, R., and Ritchie, C. W. (2010). Diagnostic Tests for Alzheimer's Disease: Rationale, Methodology, and Challenges. *Int. J. Alzheimer's Dis.* 2010, 1–6. doi:10.4061/2010/972685

McDannold, N., Arvanitis, C. D., Vykhodtseva, N., and Livingstone, M. S. (2012). Temporary Disruption of the Blood-Brain Barrier by Use of Ultrasound and Microbubbles: Safety and Efficacy Evaluation in Rhesus Macaques. *Cancer Res.* 72, 3652–3663. doi:10.1158/0008-5472.CAN-12-0128

Miller, S. E., Tummers, W. S., Teraphongphom, N., van den Berg, N. S., Hasan, A., Ertsey, R. D., et al. (2018). First-in-human Intraoperative Near-Infrared Fluorescence Imaging of Glioblastoma Using Cetuximab-IRDye800. *J. Neurooncol* 139, 135–143. doi:10.1007/s11060-018-2854-0

Morbelli, S., Esposito, G., Arbizu, J., Barthel, H., Boellaard, R., Bohnen, N. I., et al. (2020). EANM Practice Guideline/SNMMI Procedure Standard for Dopaminergic Imaging in Parkinsonian Syndromes 1.0. *Eur. J. Nucl. Med. Mol. Imaging* 47, 1885–1912. doi:10.1007/s00259-020-04817-8

Moskowitz, M. A., Lo, E. H., and Iadecola, C. (2010). The Science of Stroke: Mechanisms in Search of Treatments. *Neuron* 67, 181–198. doi:10.1016/j.neuron.2010.07.002

Ngowi, E. E., Wang, Y.-Z., Qian, L., Helmy, Y. A. S. H., Anyomi, B., Li, T., et al. (2021). The Application of Nanotechnology for the Diagnosis and Treatment of Brain Diseases and Disorders. *Front. Bioeng. Biotechnol.* 9, 629832. doi:10.3389/fbioe.2021.629832

Obeso, J. A., Stamelou, M., Goetz, C. G., Poewe, W., Lang, A. E., Weintraub, D., et al. (2017). Past, Present, and Future of Parkinson's Disease: A Special Essay on the 200th Anniversary of the Shaking Palsy. *Mov. Disord.* 32, 1264–1310. doi:10.1002/mds.27115

OHSU (2022). MR, Histologic and EM Imaging of Intravenous Ferumoxytol in Central Nervous System (CNS) Inflammation.

Orendorff, R., Peck, A. J., Zheng, B., Shirazi, S. N., Matthew Ferguson, R., Khandhar, A. P., et al. (2017). Firstin Vivotraumatic Brain Injury Imaging via Magnetic Particle Imaging. *Phys. Med. Biol.* 62, 3501–3509. doi:10.1088/1361-6560/aa52ad

Paefgen, V., Doleschel, D., and Kiessling, F. (2015). Evolution of Contrast Agents for Ultrasound Imaging and Ultrasound-Mediated Drug Delivery. *Front. Pharmacol.* 6, 197. doi:10.3389/fphar.2015.00197

Patriarchi, T., Cho, J. R., Merten, K., Howe, M. W., Marley, A., Xiong, W.-H., et al. (2018). Ultrafast Neuronal Imaging of Dopamine Dynamics with Designed Genetically Encoded Sensors. *Science* 360. doi:10.1126/science.aat4422

Pongrac, I. M., Ahmed, L. B., Mlinarić, H., Jurašin, D. D., Pavičić, I., Marjanović Čermak, A. M., et al. (2018). Surface Coating Affects Uptake of Silver Nanoparticles in Neural Stem Cells. *J. Trace Elem. Med. Biol.* 50, 684–692. doi:10.1016/j.jtemb.2017.12.003

Rivet, C. J., Yuan, Y., Borca-Tasciuc, D.-A., and Gilbert, R. J. (2012). Altering Iron Oxide Nanoparticle Surface Properties Induce Cortical Neuron Cytotoxicity. *Chem. Res. Toxicol.* 25, 153–161. doi:10.1021/tx200369s

Sarin, H., Kanevsky, A. S., Wu, H., Sousa, A. A., Wilson, C. M., Aronova, M. A., et al. (2009). Physiologic Upper Limit of Pore Size in the Blood-Tumor Barrier of Malignant Solid Tumors. *J. Transl. Med.* 7, 51. doi:10.1186/1479-5876-7-51

Sharma, A. K., Schultz, J. W., Prior, J. T., Rath, N. P., and Mirica, L. M. (2017). Coordination Chemistry of Bifunctional Chemical Agents Designed for Applications in 64Cu PET Imaging for Alzheimer's Disease. *Inorg. Chem.* 56, 13801–13814. doi:10.1021/acs.inorgchem.7b01883

Sillerud, L. O., Solberg, N. O., Chamberlain, R., Orlando, R. A., Heidrich, J. E., Brown, D. C., et al. (2013). SPION-enhanced Magnetic Resonance Imaging of Alzheimer's Disease Plaques in AβPP/PS-1 Transgenic Mouse Brain. *Jad* 34, 349–365. doi:10.3233/JAD-121171

Sim, S., and Wong, N. (2021). Nanotechnology and its Use in Imaging and Drug Delivery (Review). *Biomed. Rep.* 14, 1–9. doi:10.3892/br.2021.1418

Sirsi, S. R., and Borden, M. A. (2009). Microbubble Compositions, Properties and Biomedical Applications. *Bubble Sci. Eng. Technol.* 1, 3–17. doi:10.1179/175889709X446507

Smits, L. P., Coolen, B. F., Panno, M. D., Runge, J. H., Nijhof, W. H., Verheij, J., et al. (2016). Noninvasive Differentiation between Hepatic Steatosis and Steatohepatitis with MR Imaging Enhanced with USPIOs in Patients with Nonalcoholic Fatty Liver Disease: A Proof-Of-Concept Study. *Radiology* 278, 782–791. doi:10.1148/radiol.2015150952

Stark, D. D., Weissleder, R., Elizondo, G., Hahn, P. F., Saini, S., Todd, L. E., et al. (1988). Superparamagnetic Iron Oxide: Clinical Application as a Contrast Agent for MR Imaging of the Liver. *Radiology* 168, 297–301. doi:10.1148/radiology.168.2.3393649

Surmeier, D. J., Obeso, J. A., and Halliday, G. M. (2017). Selective Neuronal Vulnerability in Parkinson Disease. *Nat. Rev. Neurosci.* 18, 101–113. doi:10.1038/nrn.2016.178

Triantafyllou, M., Studer, U. E., Birkhäuser, F. D., Fleischmann, A., Bains, L. J., Petralia, G., et al. (2013). Ultrasmall Superparamagnetic Particles of Iron Oxide Allow for the Detection of Metastases in Normal Sized Pelvic Lymph Nodes of Patients with Bladder And/or Prostate Cancer. *Eur. J. Cancer* 49, 616–624. doi:10.1016/j.ejca.2012.09.034

Vallabani, N. V. S., Singh, S., and Karakoti, A. S. (2019). Magnetic Nanoparticles: Current Trends and Future Aspects in Diagnostics and Nanomedicine. *Cdm* 20, 457–472. doi:10.2174/1389200220666181122124458

Varallyay, C. G., Nesbit, E., Fu, R., Gahramanov, S., Moloney, B., Earl, E., et al. (2013). High-resolution Steady-State Cerebral Blood Volume Maps in Patients with Central Nervous System Neoplasms Using Ferumoxytol, a Superparamagnetic Iron Oxide Nanoparticle. *J. Cereb. Blood Flow. Metab.* 33, 780–786. doi:10.1038/jcbfm.2013.36

Viola, K. L., Sbarboro, J., Sureka, R., De, M., Bicca, M. A., Wang, J., et al. (2015). Towards Non-invasive Diagnostic Imaging of Early-Stage Alzheimer's Disease. *Nat. Nanotech* 10, 91–98. doi:10.1038/nnano.2014.254

Wang, J., Ni, D., Bu, W., Zhou, Q., Fan, W., Wu, Y., et al. (2015). BaHoF 5 Nanoprobes as High-Performance Contrast Agents for Multi-Modal CT Imaging of Ischemic Stroke. *Biomaterials* 71, 110–118. doi:10.1016/j.biomaterials.2015.08.038

Wang, T., Hou, Y., Bu, B., Wang, W., Ma, T., Liu, C., et al. (2018). Timely Visualization of the Collaterals Formed during Acute Ischemic Stroke with Fe3 O4 Nanoparticle-Based MR Imaging Probe. *Small* 14, 1800573. doi:10.1002/smll.201800573

Wilhelm, S., Anthony, J. T., Qin, D., Seiichi, O., Julie, A., Harold, F. D., et al. (2016). Analysis of Nanoparticle Delivery to Tumours. *Nat. Rev. Mat.* 1, 1–12. doi:10.1038/natrevmats.2016.14

Xu, F., Piett, C., Farkas, S., Qazzaz, M., and Syed, N. I. (2013). Silver Nanoparticles (AgNPs) Cause Degeneration of Cytoskeleton and Disrupt Synaptic Machinery of Cultured Cortical Neurons. *Mol. Brain* 6, 29. doi:10.1186/1756-6606-6-29

Zhang, L., Gu, F., Chan, J., Wang, A., Langer, R., and Farokhzad, O. (2008). Nanoparticles in Medicine: Therapeutic Applications and Developments. *Clin. Pharmacol. Ther.* 83, 761–769. doi:10.1038/sj.clpt.6100400

Zhou, Z., Bai, R., Wang, Z., Bryant, H., Lang, L., Merkle, H., et al. (2019). An Albumin-Binding T1-T2 Dual-Modal MRI Contrast Agents for Improved Sensitivity and Accuracy in Tumor Imaging. *Bioconjugate Chem.* 30, 1821–1829. doi:10.1021/acs.bioconjchem.9b00349

Conflict of Interest: The authors declare that the research was conducted in the absence of any commercial or financial relationships that could be construed as a potential conflict of interest.

Publisher's Note: All claims expressed in this article are solely those of the authors and do not necessarily represent those of their affiliated organizations, or those of the publisher, the editors and the reviewers. Any product that may be evaluated in this article, or claim that may be made by its manufacturer, is not guaranteed or endorsed by the publisher.

frontiers | Frontiers in Bioengineering and Biotechnology

TYPE Review
PUBLISHED 05 August 2022
DOI 10.3389/fbioe.2022.944518

OPEN ACCESS

EDITED BY
Rosaria Rinaldi,
University of Salento, Italy

REVIEWED BY
Thamil Selvee Ramasamy,
University of Malaya, Malaysia
Ennio Tasciotti,
Università telematica San Raffaele, Italy

*CORRESPONDENCE
Size Wu,
wsz074@aliyun.com

SPECIALTY SECTION
This article was submitted to Nanobiotechnology, a section of the journal Frontiers in Bioengineering and Biotechnology

RECEIVED 16 May 2022
ACCEPTED 06 July 2022
PUBLISHED 05 August 2022

CITATION
Wang C and Wu S (2022), Research update on cell membrane camouflaged nanoparticles for cancer therapy. *Front. Bioeng. Biotechnol.* 10:944518. doi: 10.3389/fbioe.2022.944518

Research update on cell membrane camouflaged nanoparticles for cancer therapy

Chengfang Wang and Size Wu*

Department of Ultrasound, The First Affiliated Hospital of Hainan Medical University, Haikou, China

Cell membrane-camouflaged biomimetic functionalization of nanoparticles has emerged as a promising strategy for cancer theranostics. These cell membranes used for camouflaging are generally isolated from natural or engineered erythrocytes, neutrophils, macrophages, T lymphatic cells, stem cells, and cancer cells. The camouflaging strategy of coating nanoparticles with cell membranes allows for tumor homotypic targeting through self-recognition as source cells, immune evasion, and a prolonged blood circulation time, thereby improving the effective payload delivery and tumor therapy. More so, some engineered cell membranes with functionalized peptides, proteins and moieties on membrane surface can be transferred for therapy in the same time. In this review, we summarize the latest research on various types of cell membrane-camouflaged nanoparticles aimed at anti-cancer therapy, focusing on the biological advantages of different cell membranes, constitutions of nanoparticles, fabrication processes, key findings, potential therapies, and discuss the major challenges and future opportunities.

KEYWORDS

tumor therapy, biomimetic, cell membrane-coated nanoparticle, immune evasion, homotypic targeting

1 Introduction

Cancer has become one of the leading causes of disease-related death in the world with the growth of the aging population (Schilsky et al., 2020; Sung et al., 2021). The treatment of cancer has been changing and patients' options now include surgical treatment, chemotherapy, radiotherapy, interventional treatment, and immune checkpoint inhibitor-based immunotherapy, among others (Schilsky et al., 2020; Seligson et al.,

Abbreviations: CTL: cytotoxic T-lymphocyte; CXCR4, C-X-C motif chemokine receptor 4; DOX, doxorubicin; EPR, enhanced permeability and retention; ICG, indocyanine green; MHC, major histocompatibility complex; MSC, mesenchymal stem cell; NK, natural killer; NIR, near-infrared; NP, nanoparticle; $^1O_2$, single oxygen; PDGF, platelet-derived growth factor; PDGFR, platelet-derived growth factor receptor; PTX, paclitaxel; PDT, photodynamic therapy; PEG, polyethylene glycol; PLGA, poly(Lactic-co-glycolic acid); PPy, polypyrrole; PTT, photothermal therapy; RBC, red blood cell; ROS, reactive oxygen species; SDF, stromal cell-derived factor-1; SDT, sonodynamic therapy; TAN, tumor-associated neutrophil; UCNP, upconversion nanoparticle; VEGF, vascular endothelial growth factor; VEGFR, vascular endothelial growth factor receptor.

2021). Despite the continued progress that has been made, challenges remain to a certain extent as the therapeutic effects show only marginal increases, and adverse effects have not been eliminated or substantially decreased, thus often resulting in poor therapeutic outcomes (Bonsignore et al., 2021; Seligson et al., 2021).

To solve these issues, several measures have been adopted, such as using optimization of drugs' size, shape, and surface charge, controlled release, targeted delivery, and a biomimetic nanoarchitecture to improve cancer treatment (Wu et al., 2021a; Castro et al., 2021; Jha et al., 2021). Targeted delivery comprises active and passive delivery. To reach its target in the tumor, the drug must overcome several difficulties after systematic administration, such as immune clearance, the barrier of the capillary endothelium, and the impediment of the extracellular matrix (Attia et al., 2019; Castro et al., 2021). In active targeting, a cell-specific ligand with the ability to bind to specific receptors overexpressed on tumors is conjugated to the therapeutic cargo; and in passive targeting, the therapeutic payload reaches the desire site by enhanced permeability and retention (EPR) effect (Attia et al., 2019; Dash et al., 2020). The ligand works when it nears or arrives at the target site, taking advantage of its increased affinity for the target.

Biomimetics was introduced to overcome associated challenges, and biomimetic nanoparticles (NPs) were thus fabricated. Biomimetic NPs consist of either material-based core NPs coated the biomimetic membrane or biomimetic membrane itself acting as a therapeutic cargo carrier (Attia et al., 2019; Dash et al., 2020; Jha et al., 2021). Biomimetic NPs camouflaged with cell membrane can exhibit cell-like behaviors, potentially affording them a prolonged circulation time (Hu et al., 2011; Liu et al., 2018; Xuan et al., 2018; Bidkar et al., 2019; Huang et al., 2019; Lee et al., 2019; Wang et al., 2020a; Wang et al., 2020b; Wang et al., 2020c; Dash et al., 2020; Li and Zhang, 2020; Peng et al., 2020; Wu et al., 2021b), immune escape (Pitchaimani et al., 2018; Cao et al., 2020; Wang et al., 2021a; Liu et al., 2021; Zhang et al., 2021), and/or increased targeting abilities (Parodi et al., 2013; Gao et al., 2016; Zhang et al., 2017; Pitchaimani et al., 2018; Yang et al., 2018; Bidkar et al., 2019; Cao et al., 2020; Wang et al., 2020c; Gong et al., 2020; Li et al., 2020; Poudel et al., 2020; Wu et al., 2020; Chen et al., 2021a; Li et al., 2021a; Wang et al., 2021a; Zhao et al., 2021a; Wu et al., 2021c; Fan et al., 2021; Liu et al., 2021; Shen et al., 2021; Zhang et al., 2021) on their intravenous administration.

Cell membrane-camouflaged NPs normally comprise a "core–shell" structure, in which the therapeutic payload loaded NP is the core, and a thin layer of cellular plasma membrane coating over the core NP is the shell. The core NP carries the payload that needs to be delivered to the desired site. Membranes obtained from different source cells are isolated and formed membrane vesicles through a combination of procedures. The obtained membrane vesicles are then coated onto the core NPs by co-extruding the membrane vesicles with the core NPs or a combination of sonication and extrusion (Attia et al., 2019; Dash et al., 2020; Castro et al., 2021; Jha et al., 2021). There are also other techniques such a microfluidic electroporation to form the shell (Jha et al., 2021).

The shell derived from the source cell shares the same innate properties of self-recognition. Cell membranes provide innate transmembrane proteins and moieties with little loss in functionality during therapeutic agents' formulation for delivery, such as membrane-bound antigens that are essential for immune evasion and targeting (Attia et al., 2019; Dash et al., 2020; Castro et al., 2021; Jha et al., 2021). The cell membrane coating acts as a medium to functionalize synthetic NPs, making for a suitable delivery vehicle in various biomedical applications (Dash et al., 2020; Jha et al., 2021). The choice of cell membrane depends on the target site and desired therapeutic aims. The preferential delivery and retention of membrane-coated NPs deep in the tumor improve the therapeutic efficacy of antitumor and reduce systemic toxicity (Attia et al., 2019; Dash et al., 2020; Castro et al., 2021; Jha et al., 2021). Figure 1A illustrates the fabrication processes of cell membrane-camouflaged therapeutic payload loaded NPs; and Figure 1B illustrates the potential anticancer therapies of biomimetic NPs.

The first to be developed biomimetic NPs were red blood cell (RBC) membrane-camouflaged NPs (Hu et al., 2011; Huang et al., 2019; Castro et al., 2021). Since the successful proof-of-concept study that using cloaking NPs with cellular membranes isolated from freshly harvested erythrocytes and transferring bioactive cellular components to the surface of synthetic materials in order to confer unique functions not otherwise attainable through other bioconjugation techniques a decade ago, many source cells have been used for the fabrication of cellular membrane-camouflaged NPs (Table 1), including erythrocytes (Hu et al., 2011; Liu et al., 2018; Xuan et al., 2018; Huang et al., 2019; Lee et al., 2019; Wang et al., 2020a; Li and Zhang, 2020; Peng et al., 2020; Wu et al., 2021b), neutrophils (Wang et al., 2021a; Zhang et al., 2021), macrophages (Parodi et al., 2013; Cao et al., 2020; Poudel et al., 2020), natural killer (NK) cells (Pitchaimani et al., 2018), cytotoxic T cells (Zhang et al., 2017), stem cells (Gao et al., 2016; Yang et al., 2018), platelets (Wu et al., 2020; Li et al., 2021a), and cancer cells (Li et al., 2020; Chen et al., 2021a; Zhao et al., 2021a; Fan et al., 2021; Shen et al., 2021).

During the past decade, great advances have been made, membranes used for camouflaging from cell membranes derived from single source cell to hybrid cell membranes derived from several source cells, from the use of the innate properties of cell membranes to the combination use of both the innate and acquired properties of cell membranes from engineered source cells, or with modification of cell membrane surface charge; with different methods for isolation of cell membranes and coating (Zhang et al., 2017; Yang et al., 2018; Wang et al., 2020b; Li et al., 2020; Wang et al., 2021a). Customizable exosome-like lipid

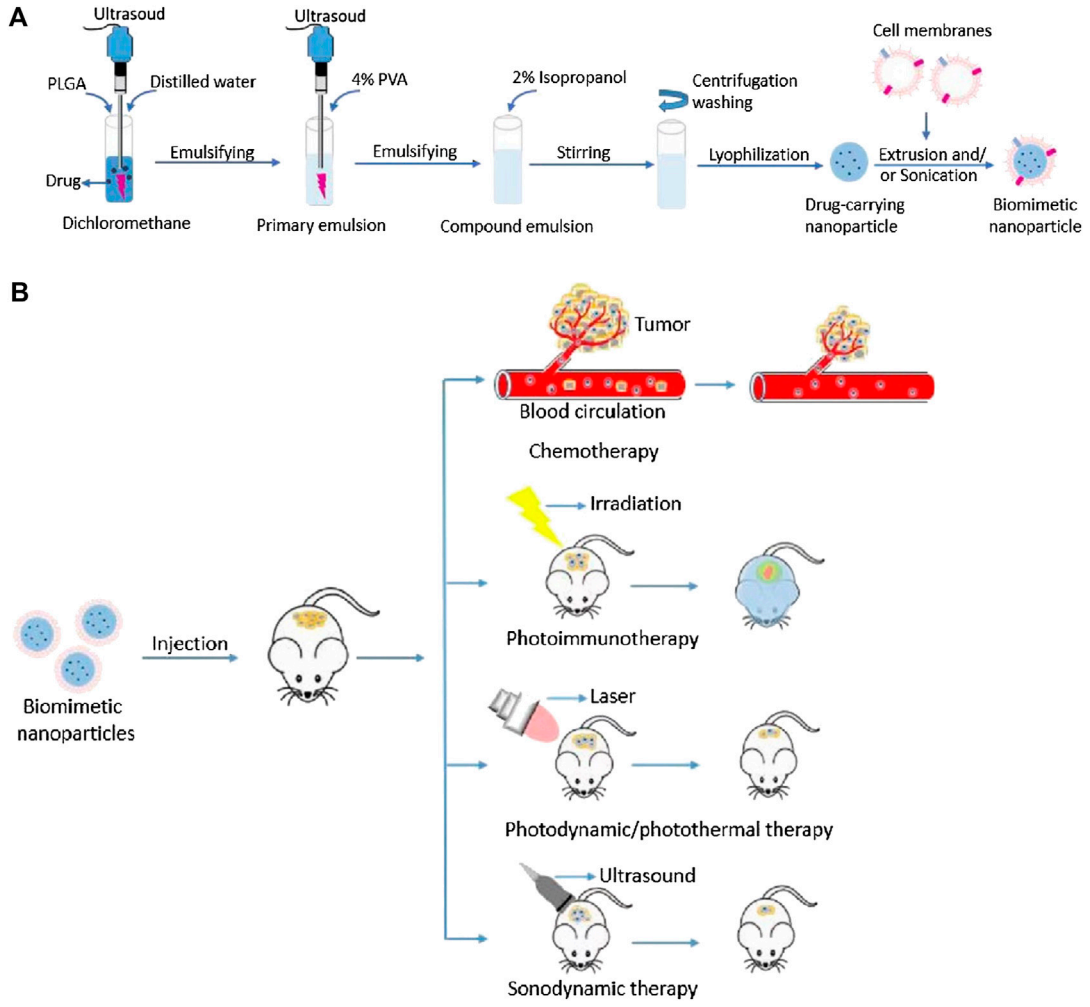

FIGURE 1
(A) Schematic illustration of fabrication processes of cell membrane-camouflaged drug loaded PLGA nanoparticles; **(B)** Schematic illustration of the potential anticancer therapies of cell membrane-camouflaged biomimetic nanoparticles. PLGA: Poly (lactic-co-glycolic acid).

nanovesicles have been engineered by integrating membrane proteins that are unbiasedly sourced from human pluripotent stem-cell-derived neurons for next-generation functionalized theranostics; in the process both endogenous and genetically engineered cell-derived proteins can be transferred effectively without disruption of physicochemical properties (Zinger et al., 2021). Genetically engineered chimeric antigen receptors (CARs) T lymphatic cell and natural T lymphatic cell that extracted from human T cells enriched from peripheral blood mononuclear cells have been obtained, the CAR-T cells could recognize GPC3 expressed on the surface of hepatocellular carcinoma cells, enhancing targeting ability, and the CAR T cells could eliminate cancer cells by single-chain variable region (ScFv) on the cell membranes of CAR-T cells, in a non-major histocompatibility complex-restricted way (Ma et al., 2020). Wild-type cancer cells (wild-type B16-F10 murine melanoma cells) can be genetically engineered to express a co-stimulatory marker that enables them to directly present their own antigens to the immune system under an immunostimulatory context. NPs cloaked with cell membranes from these engineering modified cancer cells are able to elicit anticancer immunity *in vivo* while sparing the need for conventional cell-mediated antigen presentation (Jiang et al., 2020a). These present a great promising for the development and antitumor application of cell membrane-camouflaged NPs. Meanwhile, various potential side effects that can be caused by cell membranes for NPs have been studied. The response of the complement and to the cascade of reactions that occurs on the surfaces of injected NPs and that generates active components with various effector functions has been investigated. Cell membranes coated NPs and biological systems are crucial to predict and interpret their biodistribution, targeting, and efficacy,

TABLE 1 Summary of different source cells for membrane camouflaged nanoparticles.

Source cell	References	Author
Red blood cell	(Hu et al., 2011; Pei et al., 2018; Wan et al., 2018; Xuan et al., 2018; Bidkar et al., 2019; Huang et al., 2019; Lee et al., 2019; Wang et al., 2020a; Wang et al., 2020c; Li and Zhang, 2020; Peng et al., 2020; Zhai et al., 2020; Wu et al., 2021b; Gao et al., 2021)	Hu et al., Wang et al., Li et al., Lee et al., Wu et al., Huang et al., Xuan et al., Peng et al., Bidkar et al., Wang et al., Wan et al., Zhai et al., Pei et al., Gao et al
Platelet	(Xu et al., 2018; Chen et al., 2019; Wang et al., 2019; Jiang et al., 2020b; Wu et al., 2020; Li et al., 2021a; Lyu et al., 2021)	Wu et al., Li et al., Chen et al., Wang et al., Jiang et al., Lyu et al., Xu et al
Neutrophil	(Wang et al., 2021a; Zhao et al., 2021b; Zhang et al., 2021)	Zhang et al., Wang et al., Zhao et al
Cancer cell	(Jiang et al., 2020a; Wang et al., 2020b; Wang et al., 2020d; Li et al., 2020; Chen et al., 2021a; Zhao et al., 2021a; Fan et al., 2021; Jin et al., 2021; Liu et al., 2021; Shen et al., 2021; Xu et al., 2021)	Wang et al., Liu et al., Li et al., Chen et al., Zhao et al., Shen et al., Fan et al., Jiang et al., Wang et al., Jin et al., Xu et al
Nature killer cell	Pitchaimani et al. (2018)	Pitchaimani et al
Macrophage	(Parodi et al., 2013; Evangelopoulos et al., 2016; Palomba et al., 2016; Molinaro et al., 2018; Bhattacharyya and Ghosh, 2020; Cao et al., 2020; Gong et al., 2020; Ji et al., 2020; Poudel et al., 2020; Xia et al., 2020; Chen et al., 2021b)	Parodi et al., Cao et al., Poudel et al., Gong et al., Evangelopoulos et al., Bhattacharyya et al., Chen et al., Xia et al., Molinaro et al., Palomba et al., Ji et al
Stem cell	(Gao et al., 2016; Yang et al., 2018; Li et al., 2021b; Mu et al., 2021; Zinger et al., 2021)	Gao et al., Yang et al., Zinger et al., Mu et al., Li et al
T-lymphocyte	(Evangelopoulos et al., 2016; Palomba et al., 2016; Zhang et al., 2017; Molinaro et al., 2018; Ma et al., 2020)	Zhang et al., Ma et al., Evangelopoulos et al., Molinaro et al., Palomba et al
Erythrocyte-platelet	Liu et al. (2018)	Liu et al
Platelet-Tumor cell	Wu et al. (2021c)	Wu et al
Macrophage-cancer cell	(Gong et al., 2020; Ji et al., 2020)	Gong et al., Ji et al
Erythrocyte-cancer cell	(Jiang et al., 2019; Xiong et al., 2021)	Xiong et al., Jiang et al
143B epithelioid cell-RAW264.7 cell	Cai et al. (2022)	Cai et al

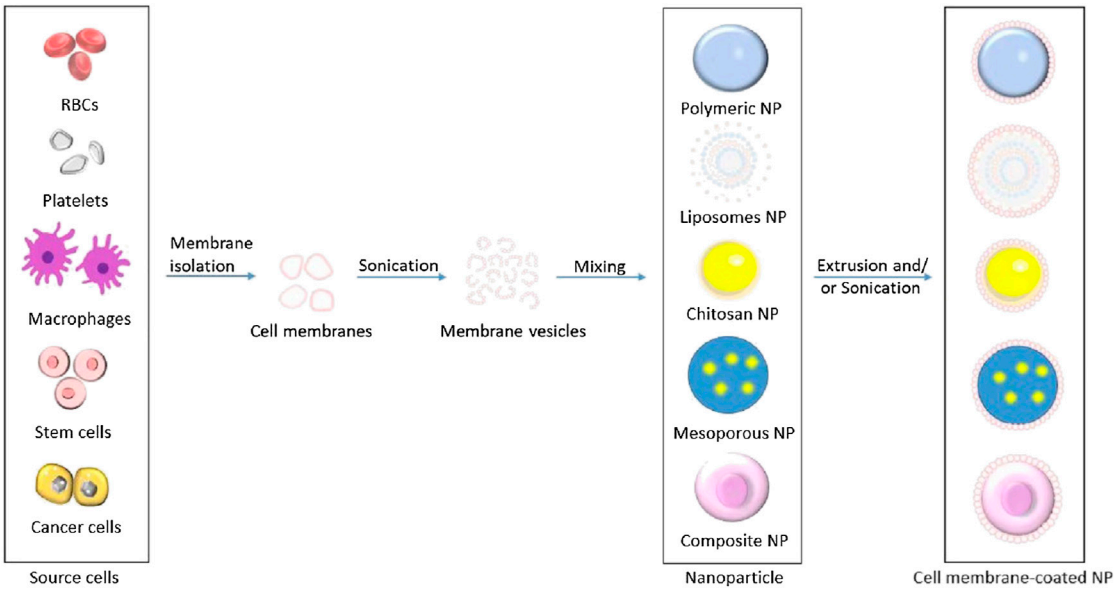

FIGURE 2
Schematic illustration of processes of isolating cell membranes and making cell membrane vesicles from different source cells for camouflaging different core nanoparticles.

and thus need to design more effective therapeutic payload delivery systems. NPs are coated by a protein corona after intravenous injection. This confers a new biological identity on the NPs that largely determines their biological fate. In this context, the formation of a protein corona and of its effect on NPs' function have also been studied, which provides reference for the design of more effective therapeutic carriers (Corbo et al., 2016; Liu et al., 2021). To probe potential side effects that can be caused by syngeneic and xenogeneic membranes (i.e., murine and human) applied to synthetic NPs, a comprehensive study was conducted. The results showed that the source of membrane is critical in inhibiting cellular internalization and rapid clearance of the NPs, although less so in triggering an acute inflammatory response (Evangelopoulos et al., 2016). This implies that to design new therapeutics, attention should be paid to not elicit an immune activation. Meanwhile, inspired by the popularity of cell membrane-camouflaging, diverse novel core NPs were fabricated using top-down or bottom-up fabrication approaches for diverse aims of PTT, PDT, SDT, immunological therapy, starvation therapy, imaging, diagnosis, etc (Zhang et al., 2017; Chen et al., 2019; Lee et al., 2019; Bhattacharyya and Ghosh, 2020; Wang et al., 2020b; Li et al., 2020; Poudel et al., 2020; Liu et al., 2021; Mu et al., 2021; Xiong et al., 2021; Zhang et al., 2021; Zinger et al., 2021).

Figure 2 illustrates the processes of isolating cell membranes from different source cells for NPs camouflaging. This review summarizes the recent cutting-edge research on different types of cell membrane-camouflaged NPs, related source cell properties, formulation processes, important findings, and potential applications in cancer therapy.

2 Components and development of cell membrane-camouflaged NPs

A cell membrane-camouflaged NP typically consists of an NP loaded with a therapeutic payload in the center (core) and a thin layer of cellular plasma membrane on the outside (shell), forming a core–shell structure (Dash et al., 2020; Jha et al., 2021). The development of cell membrane-camouflaged NPs comprises three processes: isolating cell membranes from the source cells, designing the core NP, and fusing cell membranes with the core NP to form a core–shell structure (Figure 1). All preparation processes are important in the development of cell membrane-cloaked NPs, including derivation of the lipid bilayer of the plasma membrane from source cells. Cell membranes that separate the cell cytoplasm from the outer environment are phospholipid bilayer semi-permeable structures with embedded and bound proteins and other motifs. The isolation of plasma membranes from source cells mainly involves a combination of hypotonic lysis, mechanical membrane fragmentation, and emptying the intracellular contents through differential centrifugation (Parodi et al., 2013; Gao et al., 2016; Zhang et al., 2017; Pitchaimani et al., 2018; Yang et al., 2018; Cao et al., 2020; Gong et al., 2020; Li et al., 2020; Poudel et al., 2020; Wu et al., 2020; Chen et al., 2021a; Li et al., 2021a; Wang et al., 2021a; Zhao et al., 2021a; Wu et al., 2021c; Fan et al., 2021; Liu et al., 2021; Shen et al., 2021; Zhang et al., 2021). Generally, cell membrane vesicles used for core NPs coating are obtained using a combination of hypotonic lysis buffer to lyse cells or the freeze–thaw method to obtain cell membranes; mechanical disruption of cell membranes using a dounce homogenizer, sonication, and/or extrusion, and finally, differential ultracentrifugation to obtain membrane vesicles (Parodi et al., 2013; Gao et al., 2016; Zhang et al., 2017; Liu et al., 2018; Pitchaimani et al., 2018; Xuan et al., 2018; Yang et al., 2018; Bidkar et al., 2019; Huang et al., 2019; Lee et al., 2019; Wang et al., 2020b; Cao et al., 2020; Wang et al., 2020c; Li et al., 2020; Peng et al., 2020; Poudel et al., 2020; Wu et al., 2020; Chen et al., 2021a; Li et al., 2021a; Wang et al., 2021a; Zhao et al., 2021a; Wu et al., 2021b; Fan et al., 2021; Liu et al., 2021; Shen et al., 2021; Zhang et al., 2021). The pellet of cell membrane vesicles obtained is suspended in adequate phosphate-buffered saline and lyophilized for subsequent use. Microfluidic electroporation is another approach to make cell plasm membrane as shell (Molinaro et al., 2018; Castro et al., 2021). Different synthetic cores and source cells for membrane camouflaged NPs are summarized in Table 2.

2.1 Cores of cell membrane-camouflaged NPs

In living beings, the core part of life is covered by a coating structure, along with the cell and some organelles. A functional artificial entity may be fabricated as a complex biomimetic entity consisting of a core and outer shell, with versatile functions that interact and fit with the environment and circumstances, thus enabling it to perform its core function (Attia et al., 2019; Dash et al., 2020; Wu et al., 2021a; Castro et al., 2021; Jha et al., 2021). The core constituents of cell membrane-camouflaged NPs can be organic, inorganic, or organic–inorganic hybrid nanosystems (Attia et al., 2019; Dash et al., 2020; Wu et al., 2021a; Castro et al., 2021; Jha et al., 2021). Typically, the core of the NP, which must be delivered and released at the target site, consists of its therapeutic agent and framework, which are shielded by cell membranes isolated from source cells (Gao et al., 2016; Zhang et al., 2017; Pitchaimani et al., 2018; Yang et al., 2018; Cao et al., 2020; Gong et al., 2020; Li et al., 2020; Poudel et al., 2020; Wu et al., 2020; Chen et al., 2021a; Li et al., 2021a; Wang et al., 2021a; Zhao et al., 2021a; Wu et al., 2021c; Fan et al., 2021; Shen et al., 2021).

2.1.1 Organic NPs

Organic NPs are fabricated using organic compounds, such as polymers, liposomes, gelatin, chitosan, and human serum albumin (Lai et al., 2014; Gao et al., 2016; Liu et al., 2018;

TABLE 2 Different synthetic cores and source cells for membrane camouflaged nanoparticles and potential application.

Core material	Therapeutic agents	Source cell	Methods for coating	Potential utility	References
PLGA NPs	-	RBC	Extrusion	Drug loading	(Hu et al., 2011) Hu et al. (2011)
MNCs	-	RBC	Sonication	PTT	(Wang et al., 2020a) Wang et al. (2020)
Au NRs; TiO2 NPs	-	RBC	Sonication and extrusion	PTT	(Li and Zhang, 2020) Li et al. (2020)
Polypyrrole NPs	-	Erythrocyte-platelet	Extrusion	PTT	(Liu et al., 2018) Liu et al. (2018)
^{89}Zr-HMSNs	-	RBC	Extrusion	Tumor diagnosis and treatment	(Lee et al., 2019) Lee et al. (2019)
Lipids	-	RBC	Sonication and extrusion	PTT	(Wu et al., 2021b) Wu et al. (2021)
BPQDs	DOX; Kirenol	RBC	Sonication; extrusion	Chemotherapy; anti-inflammatory therapy	(Huang et al., 2019) Huang et al. (2019)
MMSNs	-	RBC	Sonication	PDT	(Xuan et al., 2018) Xuan et al. (2018)
MSNs	-	RBC	Sonication	PTT	(Peng et al., 2020) Peng et al. (2020)
PAAO-UCNPs	Glucose oxidase	Cancer cell	Sonication	Starvation therapy; phototherapy	(Wang et al., 2020b) Wang et al. (2020)
PLGA NPs	Curcumin; Tirapazamine	RBC	Extrusion	Chemotherapy	(Bidkar et al., 2019) Bidkar et al. (2019)
PLGA NPs	DOX	RBC	Sonication	PTT; Chemotherapy	(Wang et al., 2020c) Wang et al. (2020)
NanoPorous Silicon particles	DOX	Macrophage; THP-1 phagocytic cell	-	Chemotherapy	(Parodi et al., 2013) Parodi et al. (2013)
PLGA NPs	-	Neutrophil	Extrusion	PDT	(Zhang et al., 2021) Zhang et al. (2021)
Liposomes	Ac4GalNAz/ Ac4ManNAz	Cancer cell	Extrusion	Personalized diagnosis and treatment	(Liu et al., 2021) Liu et al (2021)
Liposomes	DOX	NK cell	Extrusion	Chemotherapy	(Pitchaimani et al., 2018) Pitchaimani et al. (2018)
PLGA NPs	PTX	Neutrophil	Sonication; extrusion	Chemotherapy	(Wang et al., 2021a) Wang et al. (2021)
Albumin NPs	PTX	Macrophage	Extrusion	Chemotherapy	(Cao et al., 2020) Cao et al (2020)
CuSNPs	PTX	Macrophage	Extrusion	PTT; PDT; Chemotherapy	(Poudel et al., 2020) Poudel et al. (2020)
Gelatin nanogels	DOX	Stem cell	Extrusion	Chemotherapy	(Gao et al., 2016) Gao et al. (2016)
PLGA NPs	DOX	Stem cell	Sonication	Chemotherapy	(Yang et al., 2018)Yang et al. (2018)
PLGA NPs	PTX	T-lymphocyte	Extrusion	Chemotherapy; radiotherapy	(Zhang et al., 2017) Zhang et al. (2017)
Polypyrrole NPs	DOX	Platelet	Extrusion	PTT; Chemotherapy	(Wu et al., 2020) Wu et al. (2020)
MSNs	Combretastatin A4; Apatinib	Platelet	Sonication	Chemotherapy	(Li et al., 2021a) Li et al. (2021)
PFCE-PLGA NPs	-	Cancer cell	Extrusion	PTT; tri-modal imaging	(Li et al., 2020) Li et al. (2020)
Catalase-HMSN	-	Cancer cell	Sonication; extrusion	PTT; PDT	(Chen et al., 2021a) Chen et al. (2021)
MSNs	ISOIM	Cancer cell	Sonication; extrusion	Chemotherapy	(Zhao et al., 2021a) Zhao et al. (2021)
Ir-B-TiO2 NPs	-	Cancer cell	Extrusion	PTT; SDT	(Shen et al., 2021) Shen et al. (2021)
HCPT-NS	-	Cancer cell	Sonication	Chemotherapy	(Fan et al., 2021) Fan et al. (2021)
PLGA NPs	β-mangostin	Platelet-Tumor cell	Extrusion	Chemotherapy	(Wu et al., 2021c) Wu et al. (2021)
PLGA NPs	DOX	Macrophage-cancer cell	Sonication	Chemotherapy	(Gong et al., 2020) Gong et al. (2020)
Liposomes	Proteins	Stem cell; neuron	Microfluidic	Neuron targeting	(Zinger et al., 2021) Zinger et al. (2021)

(Continued on following page)

TABLE 2 (*Continued*) Different synthetic cores and source cells for membrane camouflaged nanoparticles and potential application.

Core material	Therapeutic agents	Source cell	Methods for coating	Potential utility	References
MSNs	-	T-lymphocyte	Sonication; extrusion	PTT	(Ma et al., 2020) Ma et al. (2020)
PLGA NPs	-	Cancer cell	Sonication	Immunotherapy	(Jiang et al., 2020a) Jiang et al. (2020)
MSV	-	Macrophage; T lymphocyte	-	-	(Evangelopoulos et al., 2016) Evangelopoulos et al. (2016)
PDA NPs	DOX; PD-L1 siRNA	Stem cell	Extrusion	Chemotherapy; Immunotherapy	(Mu et al., 2021) Mu et al. (2021)
Chitosan NPs	TNFα	Macrophage	Extrusion	Immunotherapy	(Bhattacharyya and Ghosh, 2020) Bhattacharyya et al. (2020)
Fe_3O_4 NPs	-	Erythrocyte-cancer cell	Sonication	PTT; immunotherapy	(Xiong et al., 2021) Xiong et al. (2021)
BMSNRs	-	Platelet	Sonication	PTT; radiotherapy	(Chen et al., 2019) Chen et al. (2019)
Liposomes	-	Macrophage; T-lymphocyte	Microfluidic	-	(Molinaro et al., 2018) Molinaro et al. (2018)
CS-pPLGA NPs	Bufalin	Platelet	Sonication; extrusion	Chemotherapy	(Wang et al., 2019) Wang et al. (2019)
PLGA NPs	PTX	143B epithelioid cell-RAW264.7 cell	Sonication; extrusion	Chemotherapy	(Cai et al., 2022) Cai et al. (2022)
MSN	DOX	Stem cell	Sonication	Chemotherapy	(Li et al., 2021b) Li et al. (2021)
Fe_3O_4 NPs	Sulfasalazine	Platelet	Extrusion	Immunotherapy	(Jiang et al., 2020b) Jiang et al. (2020)
UCNPs; AuNPs	-	Cancer cell	Extrusion	PTT	(Wang et al., 2020d) Wang et al. (2020)
UCNPs	-	Macrophage	Extrusion	PDT; immunotherapy	(Chen et al., 2021b) Chen et al. (2021)
UCNPs	PTD	Cancer cell	Extrusion	PDT; chemotherapy	(Jin et al., 2021) Jin et al. (2021)
CANS	-	Platelet	Extrusion	Brachytherapy	(Lyu et al., 2021) Lyu et al. (2021)
MSNs	DOX; SM	Neutrophil	Sonication; extrusion	Chemotherapy; anti-inflammatory therapy	(Zhao et al., 2021b) Zhao et al. (2021)
Nanoporous silicon particles	-	T-lymphocyte; Macrophage	-	-	(Palomba et al., 2016) Palomba et al. (2016)
MUNs	DOX	Cancer cell	Extrusion	PTT; PDT; Chemotherapy	(Xu et al., 2021) Xu et al. (2021)
ICG/DOX nanocomplexes	DOX	RBC	Extrusion	PTT; PDT; Chemotherapy	(Wan et al., 2018) Wan et al. (2018)
Melanin NPs	-	Erythrocyte-cancer cell	Sonication; extrusion	PTT	(Jiang et al., 2019) Jiang et al. (2019)
PNs	-	RBC	Sonication	Chemotherapy	(Zhai et al., 2020) Zhai et al. (2020)
PEG-b-PDLLA	PTX dimer	RBC	Extrusion	PDT; Chemotherapy	(Pei et al., 2018) Pei et al. (2018)
PLGA NPs	-	Platelet	Sonication	PDT	(Xu et al., 2018) Xu et al. (2018)
miR155-nanogel	miR155	RBC	Extrusion	Immunotherapy	(Gao et al., 2021) Gao et al. (2021)
CuS NPs	Sorafenib; Anti-VEGFR antibody	Macrophage-cancer cell	Sonication	PTT; chemotherapy	(Ji et al., 2020) Ji et al. (2020)

BPQDs: black phosphorus nanoparticle quantum dots; DOX: doxorubicin; EM: enaminitrile molecule; HCPT:10-hydroxycamptothecin; hollow mesoporous silica nanospheres; ICG: indocyanine green; HMSNs: MMSNs: Magnetic mesoporous silica nanoparticles; MSNs: mesoporous silica nanoparticles; MSV: multistage nanovector; NK: natural killer; NIR: near-infrared; NP: nanoparticle; NS: nanosuspension PDT: photodynamic therapy; PFCE: Perflfluoro-15-crown-5-ether; PAAO: polyacrylic acid-n -octylamine; PNs: PTX nanoparticles; PTD: polyethylene glycol-thioketal-doxorubicin; PTX: Paclitaxel; PTT: photothermal therapy; PLGA: poly (Lactic-co-glycolic acid); RBC: red blood cell; RT: brachytherapy; SDT: sonodynamic therapy; SM: shanzhiside methylester; TNFα: tumor necrosis factor-α; UCNP: upconversion nanoparticle; VEGFR: vascular endothelial growth factor receptor.

Pitchaimani et al., 2018; Bidkar et al., 2019; Wang et al., 2019; Cao et al., 2020; Poudel et al., 2020; Wu et al., 2020; Wang et al., 2021a; Liu et al., 2021; Ma et al., 2021; Zhang et al., 2021; Cai et al., 2022). Poly (lactic-co-glycolic acid) (PLGA) is an organic biodegradable and biocompatible compound and can be used for preparing polymeric core NPs as the skeleton of the core (Lai et al., 2014; Bidkar et al., 2019; Wang et al., 2020c; Zhang et al., 2021). These polymeric NPs, when loaded with anticancer drugs, near-infrared (NIR) dye, and/or other materials, can be used in comprehensive antitumor therapy or a combination of imaging and therapy (Lai et al., 2014; Bidkar et al., 2019; Wang et al., 2020c; Zhang et al., 2021).

Using PLGA to prepare drug loading NPs has been popular in recent decades. Bidkar et al. (Bidkar et al., 2019) developed RBC membrane-coated PLGA NPs for the co-delivery of chemotherapeutic drugs. In their work, curcumin (Cur), and the hypoxia-activated molecule tirapazamine (TPZ) (Cur + TPZ@RB) by an extrusion process. Compared with free drugs, Cur + TPZ@RB NPs had a stronger antiproliferative effect by generating reactive oxygen species (ROS) and thus DNA damage, thereby including apoptosis; accordingly, reduced cell migration and downregulations of mesenchymal markers were observed after Cur + TPZ@RB NP treatment. At 105 nm in size, the NPs were smaller than RBCs. The NPs exhibited prolonged circulation stability, superb biocompatibility, and efficient cellular internalization, and they could diffuse out of capillaries and into solid tumors, thereby significantly increasing their numbers in tumors, reducing hypoxic conditions, and supporting cancer therapy.

Zhang et al. (Zhang et al., 2021), meanwhile, developed neutrophil membrane-camouflaged PLGA NPs (NM-HB NPs) for synchronous near-infrared fluorescence (NIR FL) imaging and photodynamic therapy (PDT) against hepatocellular carcinoma using a broad-spectrum anti-inflammatory strategy. The NM-HB NPs were targeted effectively to the tumor site and could overcome the drawbacks of a short blood circulation time and high immune clearance *in vivo* and *in vitro*, and they showed significant PDT efficacy and suppression of tumor growth.

Polypyrrole (PPy) is a conductive polymer, the chemical structure comprises repeating units of the py monomer, a nitrogen-containing aromatic ring. It can be conjugated with biomolecules by chemical modification. PPy has high stability and superior biocompatibility. In tissue engineering, it can be used to fabricate biocompatible stimulus-responsive scaffolds. PPy can efficiently convert absorbed NIR light into heat, and can be used as photothermal therapy (PTT) agent for cancer therapy (Liu et al., 2018; Wu et al., 2020). Wu et al. (Wu et al., 2020) constructed PLT-PPy–DOX NPs for PTT and chemotherapy of hepatocellular carcinoma. The core NPs were PPy loaded with DOX, and membrane vesicles isolated from platelet were coated onto core NPs as shell. Further study showed that these NPs had good immune evasiveness and tumor targeting abilities *in vivo*; when under 808 nm laser irradiation, PPy in the NPs generated high heat to ablate tumors while DOX was released to kill cancer cells, which effectively suppressed the growth of primary tumor and inhibited tumor metastases.

Chitosan

Chitosan is a polycationic macromolecules derived from the alkaline deacetylation of chitin, and it is composed of randomly distributed β-(1-4)-linked D-glucosamine and *N*-acetyl-D-glucosamine (Bhattacharyya and Ghosh, 2020; Ma et al., 2021). It is a porous material with a high surface areas and interconnected pore channels, and it is a good candidate to be used as an adsorbent. In that vein, Ma et al. (Ma et al., 2021) employed a one-pot method to fabricate gold-embedded chitosan NPs (Au@CS NPs), which were modified by applying benzaldehyde-terminated poly [(2-methacryloyloxy) ethyl phosphorylcholine] (PMPC). The obtained Au@CS-PMPC NPs had a diameter of 135 nm and showed features of elevated colloidal stability, high loading capacity of drugs, pH-responsive drug release, superior biocompatibility, and marked fluorescence emission. Bhattacharyya et al. (Bhattacharyya and Ghosh, 2020), meanwhile, developed TNFα-expressed macrophage membrane-coated chitosan NPs. The chitosan core NPs were synthesized using the ionic gelation method, and macrophage membranes were coated on the core NPs by serially extruding the membranes through 0.8 and 0.4 μm-pore membranes, followed by coextrusion of the cell membranes and NPs, with a 0.2 μm-pore membrane in the extruder.

Gelatin

Gelatin is another type of organic material used for cell membranes cloaked NPs, and it is a mixture of peptides and proteins. Gao et al. fabricated bone marrow-derived stem cell membranes camouflaged gelatin nanogels by preparing gelatin nanogels, loading with DOX, and then coating them with mesenchymal stem cells (MSCs) membranes (SCMGs-DOX) using a top-down protocol (Gao et al., 2016). The SCMGs-DOX had the innate functions of natural MSCs membranes and demonstrated a strong ability to evade immune system clearance, along with having an improved tumor-targeting capability and enhanced antitumor efficacy.

Liposomes

Liposomes possess hydrophilic and hydrophobic properties that can be used as the core material for loading both hydrophilic and hydrophobic therapeutic cargos (Pitchaimani et al., 2018; Liu et al., 2021). Liu et al. (Liu et al., 2021) constructed cancer cell membrane–camouflaged azido sugar liposomes with a feature of cell-selective glycan imaging. In this work, the core NPs were azido sugar liposomes, and cell membranes of cervical and breast cancer were coated onto the core NPs through sonication and extrusion. These liposomes can image different cancer cells and subtype cells of triple-negative breast cancer, as well as to label metastatic tumors, with features of pH-responsive, preventing protein corona formation, immune evasion, extension of blood circulation time, facilitating metabolic glycan labeling, and increased prominent cell selectivity to homotypic cancer cells. In another study, Pitchaimani et al. (Pitchaimani et al., 2018) also successfully developed biomimetic NPs with liposomes for anticancer. They developed DOX-loaded biomimetic liposomes using thin-film hydration and membrane extrusion techniques, with NK cell membranes for camouflaging.

2.1.2 Inorganic NPs

Inorganic NPs are synthetic nanoscale materials that are used as cores, and which can be cloaked with different cellular membranes for various aims of application. Inorganic NPs with tunable and diverse properties hold great potential in the field of nanomedicine, but their non-negligible toxicity for healthy tissues and organs has restricted their clinical use (Wang et al., 2021b). There are many inorganic materials available for biomedical applications, and the most commonly used inorganics are silicon, Fe_3O_4 and upconverted materials.

Silica

Compared with other porous silica nanocarriers, mesoporous silica NPs, with a pore size ranging from 2 to 50 nm, high capability of therapeutic cargo loading and a highly biocompatible nature, make excellent candidates for drug delivery and biomedical applications (Wu et al., 2021a; Wang et al., 2021b). Accordingly, biomedical silica NPs are developed for cargo delivery, disease treatment, and bioimaging. To develop imaging-guided tumor PTT, Peng et al. (Peng et al., 2020) prepared MSN-ICG@RBC NPs by forming mesoporous silica NPs (MSNs), modifying their surface functionalization in various ways (-COOH, -SH, $-NH_2$), conjugating them with ICG, and coating RBC membrane ghosts. The MSN-ICG@RBC NPs with an optimized particle size of 60 nm showed prolonged blood circulation, higher accumulation at target sites, and efficient imaging-guided PTT. Li et al. (Li et al., 2021b), meanwhile, developed a DOX-loaded MSN@M for antitumor treatment. The membranes of MSCs were coated onto DOX-loaded mesoporous silica NPs (MSN@M). Subsequent study showed the NPs had good self-positioning drug delivery ability, immune evasion, stronger tumor targeting and penetration, effective tumor inhibition, and minimal side effects.

Magnetic NPs

Magnetic NPs can be magnetized under an external magnetic field; accordingly, they can be used for alternate magnetic field-mediated hyperthermia and magnetic resonance imaging. In a study by Wang et al. (Wang et al., 2020a), biomimetic Cyp-MNC@RBCs were established for bimodal NIR fluorescence and magnetic resonance imaging-guided cancer PTT. The superparamagnetic nanoclusters (MNCs) had an average diameter of 90 nm and were fabricated using iron (iii) chloride hexahydrate ($FeCl_3.6H_2O$) as the precursor by a modified solvothermal reaction method. A NIR with a peak at 785 nm, containing carboxyl groups with cypate, was loaded into the MNCs through coordinated chemical interactions between the Fe atoms and carboxyl groups and, then, RBC membranes were coated on MNCs to form Cyp-MNC@RBCs. The Cyp-MNC@RBCs demonstrated excellent biocompatibility, prolonged blood circulation, superior tumor-homing capacity, and improved photothermal conversion ability when compared with their MNCs counterparts. Treated with a Cyp-MNC@RBC injection and 808 nm laser irradiation, the growth of tumors was effectively suppressed.

In further work, Wang et al. (Wang et al., 2020c) fabricated magnetically targeted RBC membrane-camouflaged NPs of DOX@IRP@RBC for PTT and chemotherapy of cancers. DOX, IR-780 iodide, and Fe_3O_4 was loaded into the PLGA core NPs, then coated with RBC membranes by sonication. The DOX@IRP@RBC NPs exhibited good immune evasion, a prolonged blood circulation, good biocompatibility, high tumor accumulation, minimal systemic side effects; more so, an external magnetic field can be used for magnetic-guided targeted drug delivery and therapy.

Beyond this, to combat ovarian cancer, Xiong et al. (Xiong et al., 2021) fabricated biomimetic Fe_3O_4-ICG@IRM NPs for synergistic PTT and immunotherapy. ICG was loaded into magnetic NPs (Fe_3O_4) and then camouflaged with murine-derived ID8 ovarian cancer cell membranes and RBC membranes (IRM). The resulting Fe_3O_4-ICG@IRM NPs demonstrated highly specific self-recognition of ID8 cells, had a prolonged blood circulation, activated specific immunity in a tumor-bearing model, and supported synergistic PTT and antitumor immunotherapy for primary ovarian cancer and metastatic tumors.

NPs with Fe_3O_4 can trigger ferroptotic cell death, induce a tumor-specific immune response, and promote macrophages polarizing to an antitumor M1 phenotype, as reported by Jiang et al. (Jiang et al., 2020b). In their work, sulfasalazine (SAS) was loaded into the mesoporous magnetic NPs (Fe_3O_4), and then coated with platelet (PLT) membranes via extrusion. The prepared Fe_3O_4-SAS@PLT NPs exhibited high efficacy of cancer immunotherapy.

Upconverted NPs

Upconverted NPs are a group of inorganic fluorophores that utilize the anti-Stokes mechanism and can convert NIR wavelengths to visible or ultraviolet wavelengths under the assistance of dopant activators or emitter elements in the nanocrystal core (Corbo et al., 2016; Evangelopoulos et al., 2016; Bhattacharyya and Ghosh, 2020; Wang et al., 2020b; Ma et al., 2021). These NPs have some strengths, such as narrow emission peaks, low toxicity, exceptional photostability, a remarkable light-penetration depth, and negligible background fluorescence (Wang et al., 2020d; Chen et al., 2021b; Jin et al., 2021; Rostami, 2021). They can be used in tumor imaging or imaging-guided therapy. In a study, Wang et al. (Wang et al., 2020b) made use of upconverted materials to fabricate cancer cell membrane-coated $NaYF_4$: Yb, Tm UCNPs for homotypic

targeting cancer multimodal therapy, and which exhibited good performance *in vitro* and vivo.

In further work, Wang et al. (Wang et al., 2020d) fabricated cancer cell membrane-camouflaged UCNP/AuNPs for multimodal imaging-guided NIR PTT. The researchers produced cancer cell membrane-cloaked upconverted NPs (CC-UCNPs) and gold NPs (CC-AuNPs). These NPs allowed simultaneous dual-modal imaging on a dual-modal imaging system with a special designed detector that can simultaneously detect both high-energy X-ray and low-energy visible light. Further *in vitro* and *in vivo* studies showed these NPs had highly specific upconverted luminescence imaging and PTT-based anti-tumor efficacy, with abilities of superior immune evasion, a long blood circulation time, and high tumor-targeting specificity. Beyond this, Chen et al. (Chen et al., 2021b) developed NPR@TAMM NPs by synthesizing NaYF4: Yb, Er upconverted NPs, which were then loaded with PS, to yield NPR as the core NP, and coated with tumor-associated macrophage membranes (TAMM) as the shell. Further study showed that these NPs had good tumor-homing ability and immune evasion, and exhibited high performance of PDT and immunotherapy in antitumor.

2.2 Source cells used for camouflaging, membrane properties and their mechanisms

The source cells used for camouflaging core NPs mainly include RBCs, platelets, macrophages, NK cells, T lymphocytes (TLs), neutrophils, stem cells, and cancer cells, as listed in Table 1.

RBCs are the essential blood cells, with an exclusive function of carrying oxygen to the tissues and cells of the body. On RBCs membranes present surface proteins, such as CD47 that can bind receptors on the leukocyte membrane (i.e., SIRPα), inhibiting their clearance; and other "self-markers" on their surfaces that prevent clean by the reticuloendothelial system and prevent immune attack (Hu et al., 2011; Liu et al., 2018; Xuan et al., 2018; Bidkar et al., 2019; Huang et al., 2019; Lee et al., 2019; Wang et al., 2020a; Wang et al., 2020b; Li and Zhang, 2020; Peng et al., 2020; Wu et al., 2021b). Combined with the above properties, NPs coated with RBC membranes provide much longer plasmatic half-life, which making them suitable for use as long-circulating carriers.

Platelets contain unique surface moieties and have innate functions of binding injured blood vasculature, facilitating subendothelial adhesion, working with the immune system, and adhering to and interacting with pathogens (Chen et al., 2019; Wang et al., 2019; Jiang et al., 2020b; Wu et al., 2020; Li et al., 2021a; Lyu et al., 2021) Platelet membrane-camouflaged NPs can escape immune attack and bind to injured blood vessels and some pathogens, which allows the core NPs to deliver their payload.

Neutrophils are granulocytes in the white blood cells that abundantly present in the blood. Neutrophils are not confined in the blood circulation and can move through capillary walls to tissues to instantly attack antigens (Jaillon et al., 2020; Wang et al., 2021a; Zhao et al., 2021b; Zhang et al., 2021). Neutrophils are a key component of the body immune system and are functioned in protecting the body from contagious diseases and foreign invaders; they also play a crucial role in tumor progression. Tumors recruit neutrophils by secreting a chemoattractant (Jaillon et al., 2020). Neutrophile membranes have properties of immune evasion and target tissue localization, the latter of which functions via cell–cell interactions (Wang et al., 2021a; Zhao et al., 2021b; Zhang et al., 2021). As for the former, NPs camouflaged with neutrophil membranes can escape immune system processes of opsonization and uptake (Wang et al., 2021a; Zhao et al., 2021b; Zhang et al., 2021).

Macrophages develop from monocytes in the bone marrow and many forms of mononuclear phagocytes can be found in tissues; and these phagocytes can replenish themselves in peripheral tissues directly from local precursors (Xia et al., 2020). Macrophages have functions in identifying, intaking, and digesting cellular debris and other foreign substances (Cao et al., 2020; Poudel et al., 2020; Xia et al., 2020). In addition, macrophages can present antigens to T cells and release cytokines that initiate inflammation and activate other cells. Macrophages in the tumor microenvironment are often associated with tumor progression and metastasis (Parodi et al., 2013; Evangelopoulos et al., 2016; Molinaro et al., 2018; Bhattacharyya and Ghosh, 2020; Cao et al., 2020; Gong et al., 2020; Poudel et al., 2020; Chen et al., 2021b). Macrophage membrane-camouflaged NPs show excellent biocompatibility, prolonged blood circulation, selective tumor site accumulation, and strong cellular internalization and antitumor efficacy (Parodi et al., 2013; Evangelopoulos et al., 2016; Molinaro et al., 2018; Bhattacharyya and Ghosh, 2020; Cao et al., 2020; Gong et al., 2020; Poudel et al., 2020; Chen et al., 2021b).

A previous study indicated that NPs camouflaged with purified leukocyte (human T-cell and murine macrophage) membranes presented cell-like behaviour in the blood circulation in the orthotopic 4T1 tumor models, which could molecularly interact with the surface of the cell through triggering and activating the clustering of intercellular adhesion molecule one on endothelial cells, increasing the targeting properties, promoting firm adhesion to the tumor vasculature, resulting in an increase in intracellular calcium and ROS concentrations, resulting in an independent activation of PKCα. PKCα increases lead to the phosphorylation of vascular endothelial-cadherin (VE-cadherin, also known as cadherin-5 and CD144) that resulting in the disassembly of VE-cadherin and protein displacement,

leading to enlarged gaps between endothelial cells and an increase in tumor vascular permeability (Palomba et al., 2016).

NK cells are lymphocytes in the same family as T and B cells, which all originate from a common progenitor (Pitchaimani et al., 2018). NK cells belong to group I innate lymphocytes and respond quickly to many pathological challenges, such as killing cells infected by virus and detecting and controlling cancer in early stage. NK cells can attack cancer cells directly through inhibitory and activating receptors on their cell surfaces and can also cause cell killing without prior sensitization (in contrast to cytotoxic T cells, which require priming by antigen-presenting cells) (Pitchaimani et al., 2018). Coated with NK cell membranes, a biomimetic system of DOX-loaded NPs exhibited high affinity toward cancer, excellent tumor-homing efficacy and antitumor activity, while these depended exclusively upon the membrane features of NK-92 cell membrane receptors (Pitchaimani et al., 2018).

Cytotoxic T lymphocytes (CTLs) are another type of immune cells. They can kill cancer cells and other infected cells (Evangelopoulos et al., 2016; Palomba et al., 2016; Zhang et al., 2017; Ma et al., 2020), and facilitate chosen target cell death via granule and receptor-mediated mechanisms. CTL-mediated immunity relies on granzymes, and gasdermin-mediated pyroptosis has been identified as a CTL-killing mechanism (Zhou et al., 2020). CTLs have innate properties that recognize T cell receptors on target cells and antigen-derived peptide fragments on the cells' surfaces with specificity for antigens, which locate in the grooves of class 1 MHC (Raskov et al., 2021). Except for as mediators of antitumor immunity, CTLs are good candidates for the treatment of some systemic diseases, for CTLs can circulate throughout the body repeatedly and can find out antigens. One of the mechanisms of MHC class 1 in immune response is to activate cytolysis by recognizing a single peptide. To the end, CTLs may work by employing non-effector mechanisms along with the production of a cytokine of interferon-gamma composing of several antitumor properties (Zhou et al., 2020; Raskov et al., 2021). CTL membrane-camouflaged cargo-loaded NPs can avoid opsonization thanks to their prolonged circulation time and can localize and accumulate at the tumor site, thus bearing enhanced targeting ability (Zhang et al., 2017).

Cancer cells have a natural property that one adheres to one another, thus allowing tumor to continuous growing, known as homotypic binding. A study indicated that interactions of surface adhesion molecules like galectin-3 and Thomsen-Friedenreich antigen (T antigen) are involved in carbohydrate-mediated metastatic cell heterotypic (between carcinoma cells and endothelium) and homotypic (between carcinoma cells) adhesion (Zou et al., 2005); and similar phenomena was found in another study with different cancer cells (Khaldoyanidi et al., 2003). Making use of the homotypic binding property of membranes of different cancer cells during the contact of the tumor cell membrane, individualized cancer cell membrane-coated biomimetic NPs can be developed to aid homotypic targeting and facilitate internalization by source cells thanks to their self-recognition properties (Li et al., 2020; Chen et al., 2021a; Zhao et al., 2021a; Fan et al., 2021; Shen et al., 2021). Homotypic cell membranes increase the chances of NP-to-cell adhesion and may target different sites with cancer metastasis potential. Cancer cell membranes coated NPs have similar cell adhesion molecules to those of their source cells. The ability of cancer cell membranes coated NPs to initiate homologous targeting with innate self-adhesive properties allows for augmented delivery of different anticancer payloads to the tumor. The preferential accumulation of cancer cell membrane NPs in the tumor improves the therapeutic efficacy as well as reduces the systemic toxicity. These made the cancer cell membranes coated NPs have a variety of applications, including drug delivery, and image-guided PTT and sonodynamic therapy (SDT), anticancer vaccination, targeted oxygen interference for chemoresistance to increase the therapeutic effect (Li et al., 2020; Chen et al., 2021a; Zhao et al., 2021a; Fan et al., 2021; Jin et al., 2021; Liu et al., 2021; Shen et al., 2021; Xu et al., 2021). NPs coated with cancer cell membranes can effectively deliver tumor-associated membrane-bound antigens with immunological adjuvants to antigen-presenting cells by inducing the anticancer immune response (Li et al., 2020; Chen et al., 2021a; Zhao et al., 2021a; Fan et al., 2021; Jin et al., 2021; Shen et al., 2021).

Stem cells can self-renew with high replicative potential in multilineage differentiation (Gao et al., 2016; Yang et al., 2018; Li et al., 2021b; Mu et al., 2021; Zinger et al., 2021). Embryonic stem cells are generally used for therapeutic purposes because of their superb totipotency and long lifespan. MSCs have the unique ability to home and engraft in tumor stroma. MSCs homing is a process that endogenous or exogenous MSCs migrate to the targeted tissue and colonize under the action of relevant factors. Different signaling molecules generated from different microenvironments and attract MSCs to these sites. Bone marrow, various organs and even tumor are the eventual sites of MSCs homing. Studies showed that some ligands and corresponding receptors involve in MSCs migration, such as SDF-1/CXCR4, PDGF/PDGFR, and VEGF/VEGFR (Yang et al., 2018). These specific signaling molecules secreted by tumor cells can bind to corresponding proteins on the surface MSCs and result in the homing behavior of MSCs. The vascular endothelial growth factors formed at the tumors allowing the recruitment of MSCs for the formation of tumoral stroma and pericytes aimed at angiogenesis (Gao et al., 2016; Yang et al., 2018; Li et al., 2021b). It is believed that MSCs homing is similar to the chemotaxis of immune cells to the damaged or stimulated site. The exact mechanism of MSCs homing to tumor remains unclear (Gao et al., 2016; Yang et al., 2018; Mu et al., 2021). Because MSCs hardly express MHC molecules that may trigger immune response, so tumor targeting of MSCs has no species-specific property, this allows the alternative for clinical application of

MSCs derived from other species (Wang et al., 2019; Zinger et al., 2021). These features render them potentially a very useful tool as MSC have been used for treatment in several fields, from the treatment of graft-versus-host-disease to tissue engineering and design of targeted delivery vehicles which can deliver antitumor therapeutic cargos to the tumor, with the aim of enhancing drugs selective accumulation at the tumor sites (Yang et al., 2018; Li et al., 2021b; Mu et al., 2021; Zinger et al., 2021).

In general, the membranes obtained from source cells have innate properties; NPs camouflaged with such cell membranes can avoid immune clearance and benefit from a prolonged systemic circulation time. Stem cell membrane-coated NPs can thus help target cancer, and cancer cell membrane-coated NPs exhibit homologous tumor-targeting because of their homotypic binding.

3 Process of fabricating cell membrane camouflaged NPs

Generally, cell membrane-camouflaged NPs are fabricated in three steps: the preparation of core NPs, isolation of cell membranes and formation of membrane vesicles, and fusion of core NPs with those vesicles by extrusion, sonication, a combination of sonication and extrusion, or microfluidic electroporation (Parodi et al., 2013; Gao et al., 2016; Zhang et al., 2017; Pei et al., 2018; Pitchaimani et al., 2018; Wan et al., 2018; Xu et al., 2018; Xuan et al., 2018; Yang et al., 2018; Bidkar et al., 2019; Huang et al., 2019; Jiang et al., 2019; Lee et al., 2019; Li et al., 2019; Wang et al., 2019; Wang et al., 2020b; Cao et al., 2020; Wang et al., 2020c; Gong et al., 2020; Li et al., 2020; Peng et al., 2020; Poudel et al., 2020; Wu et al., 2020; Zhai et al., 2020; Chen et al., 2021a; Li et al., 2021a; Wang et al., 2021a; Zhao et al., 2021a; Wu et al., 2021b; Wu et al., 2021c; Fan et al., 2021; Gao et al., 2021; Jha et al., 2021; Liu et al., 2021; Mu et al., 2021; Shen et al., 2021; Zhang et al., 2021), as listed in Table 2. In the process of extrusion, both the membrane vesicles and core NPs are coextruded many times through a porous membrane with the same or different pore size (polycarbonate, polyester) (Pitchaimani et al., 2018; Huang et al., 2019; Li and Zhang, 2020; Wu et al., 2021b). Ultrasound sonication is a procedure that putting the core NPs and membrane vesicles in the same container, using ultrasonic waves with a certain power to form membrane-coated NPs. A drawback of the sonication method is that the membrane-coating formed might be uniformity and the NPs may be polydisperse (Huang et al., 2019; Wang et al., 2020c; Jha et al., 2021; Liu et al., 2021). Electroporation, meanwhile, refers to the application of strong external electric-field pulses to cells and tissues to structurally rearrange cell membranes, causing multiple pores to form in these membranes (Balantič et al., 2021; Jha et al., 2021), through which the core NPs diffuse into cells. Though the purposes of transferring biological features from cell membranes to synthetic NPs for therapeutic cargos delivery have been achieved, a standardizable, batch-to-batch consistent, scalable, and high-throughput assembly method has not been well developed. Microfluidics may be a promising tool for the controlled synthesis of NPs in a versatile and reproducible approach (Molinaro et al., 2018; Zinger et al., 2021).

4 Fabrication and biomedical presentation of different cell membrane- camouflaged NPs

Coating core NPs with cell membranes reserves the physicochemical properties of NPs while adds the cellular membrane functions of the source cells. These source cell membrane-camouflaged NPs have improved biocompatibility, enhanced immune evasion, increased tumor-targeting ability, and implemented engineered membrane peptides and motifs transferring. As a result, deriving cellular membranes from source cells, to use for anticancer NP camouflaging, has become a common practice (Table 1).

4.1 Erythrocyte membrane-camouflaged NPs

Many studies have been conducted on NPs camouflaged with membranes derived from RBCs (Khaldoyanidi et al., 2003; Hu et al., 2011; Liu et al., 2018; Wan et al., 2018; Xuan et al., 2018; Bidkar et al., 2019; Huang et al., 2019; Jiang et al., 2019; Lee et al., 2019; Wang et al., 2020a; Wang et al., 2020c; Li and Zhang, 2020; Peng et al., 2020; Zhai et al., 2020; Wu et al., 2021b). RBCs were used in the first-reported membrane-camouflaged NPs (Hu et al., 2011), whereby Li et al. (Li and Zhang, 2020) constructed Au/TiO_2@RBC NPs for tumor PDT by isolating RBC membranes and coating them on Au/TiO_2 NPs via sonication and extrusion. Peng et al. (Peng et al., 2020) later enveloped ICG conjugated mesoporous silica NPs (MSNs) with RBC membranes using repeated extrusion to develop MSN-ICG@RBC NPs for cancer PTT, which demonstrated longer blood circulation and good target site accumulation.

Following on from this, Wu et al. (Wu et al., 2021b) formulated IR780@rRBC NPs for PTT anti-tumor, with recombinant RBC membranes as camouflage [Figure 3]. The RBC membranes were isolated using a hypotonic lysis method and then treated with a compound organic solvent to separate the lipids and proteins, after which the lipids were used to load IR780 iodide with the film dispersion method. IR780@rRBC NPs showed low toxicity, high stability, and optimized pharmacokinetics and pharmacodynamics.

In further work, RBC membrane-camouflaged NPs were also used for synergistic anticancer of PTT and chemotherapy

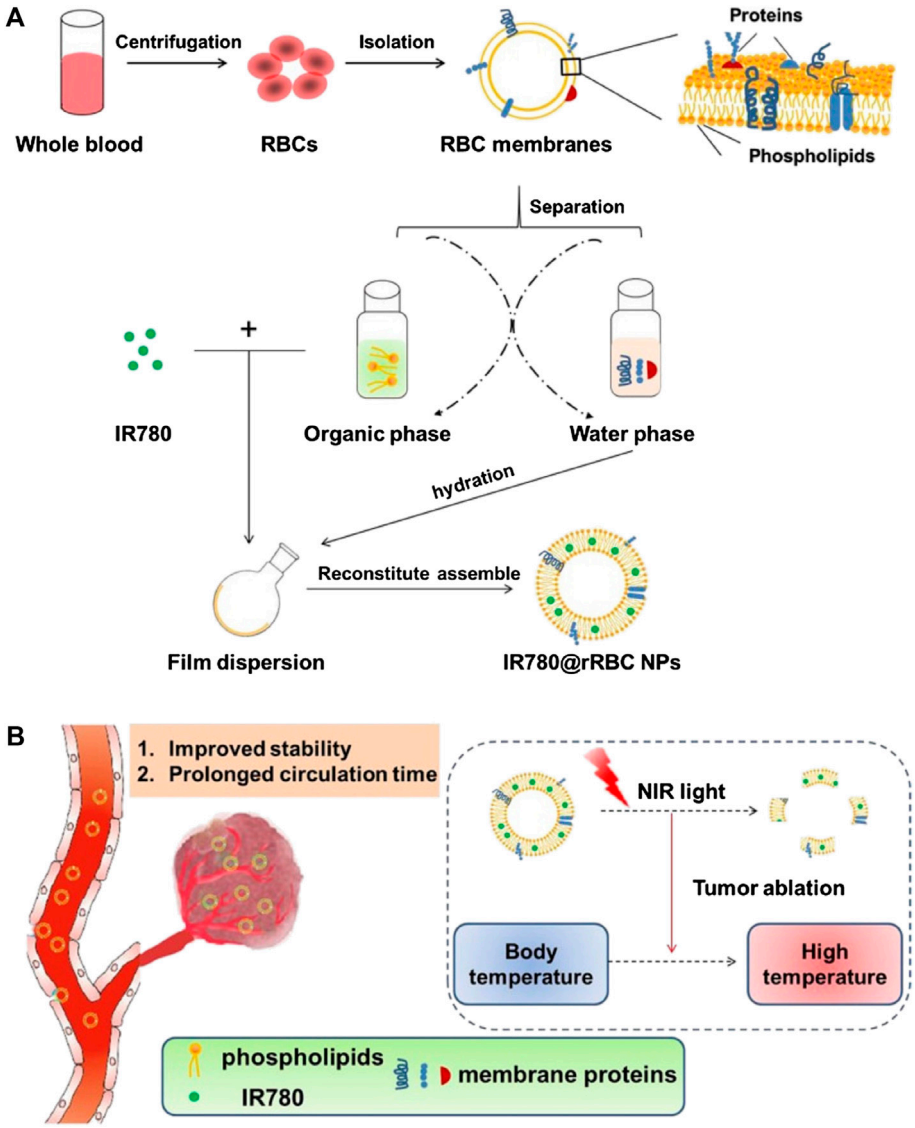

FIGURE 3
Schematic illustration of procedures for the preparation of IR780 loaded reconstitute RBC membrane nanoparticles (IR780@rRBC NPs) **(A)** RBC membrane was prepared by a hypotonic lysis method. Then RBC membranes were treated by mixed organic solvent, to separate the lipids and proteins. Lipid part was used to load IR780 by film dispersion method. At last, IR780@rRBC NPs were formed by adding proteins with the film, following further extrusion **(B)** IR780@rRBC NPs increased stability *in vitro*, and prolonged circulation capacity and enhanced PTT efficacy *in vivo*. IR780: IR780 iodide; PTT: photothermal therapy; RBC: red blood cell; rRBC: reconstitute RBC. Reproduced with permission from reference (Wu et al., 2021b). Copyrights © Springer Nature. 2022 BioMed Central.

(Khaldoyanidi et al., 2003; Jiang et al., 2019). Zhai et al. (Zhai et al., 2020) formulated a biomimetic PTX-NP-EM (PNM) system for anticancer therapy. Paclitaxel (PTX)-loaded polyethylene glycol (PEG) was used for the core NPs, and the erythrocyte membrane (EM) was isolated and utilized for cloaking via sonication and extrusion. The resulting system presented superior tumor cell uptake, stronger tumor cell killing, greater accumulation in tumors, and was markedly effective against tumor growth.

Nevertheless, RBC membrane coating of NPs should base on other important considerations in their design, including their shape or size, which influence significantly their fate *in vivo*. Such an example was seen in a work by Li et al. (Li et al., 2019) indicated that smaller, spherical RBCs membrane coated PLGA NPs (80 nm) had a longer blood serum half-life (30 h) and reduced liver accumulation compared to bigger NPs (100 and 200 nm, with an half-life around 10 h). The reason is that bigger NPs in liver filtration via sinusoid capillaries reduced. Thus,

smaller particles appeared to be more suitable to enable long circulation time.

4.2 Platelet membrane-camouflaged NPs

Platelets are important for the maintenance of homeostasis. Platelet membranes contain the proteins, surface moieties and antigens present on the source platelets. Platelet membrane-camouflaged NPs have various biomedical applications, including drug delivery and anticancer therapy (Xu et al., 2018; Chen et al., 2019; Wang et al., 2019; Jiang et al., 2020b; Wu et al., 2020; Li et al., 2021a; Lyu et al., 2021). Platelet membranes can be used for camouflage with different aims of drug delivery and therapy. Li et al. (Li et al., 2021a) constructed MSN@PM-C-A NPs for antitumor treatment; mesoporous silica NPs (MSNs) loaded with CA4 antibodies and apatinib were the core NPs, and platelet membranes (PMs) were used as the shell. A further study in animal models showed that MSN@PM-C-A NPs accumulated in the tumor and targeted adhesion of the PM surface to the sites of damaged blood vessels in the tumor, resulting in significant vascular disruption and efficient anti-angiogenesis.

The similar merits of platelet membranes coating were exhibited in another study by Xu et al. (Xu et al., 2018). In their work, a biomimetic system of NP-Ver@P was developed for antitumor PDT. The core NPs were prepared using PLGA, with verteporfin NPs loaded, and sonication technique was used for platelet membranes camouflaging. Subsequent study showed that NP-Ver@P had an active targeting capacity, able to ablate tumors without causing skin damage. Platelet membranes camouflaging for NPs for synergistic of radiotherapy and PTT also indicated good performance. In another study by Chen et al. (Chen et al., 2019), BMSNR@PM NPs for tumor radiotherapy enhancement were formulated using solvothermal and ultrasonic methods. In their work, the core NPs were mesoporous silica-coated bismuth nanorods (BMSNR), and platelet membranes were used for coating. As a result, BMSNR@PM NPs showed a synergistic effect of radiotherapy *in vivo* with the photothermal effect induced by 808 nm NIR irradiation.

4.3 Neutrophile membrane-camouflaged NPs

Neutrophils play important roles in the protection of body from infection and in the activation and regulation of inherent and adaptive immunity. Neutrophils have properties of diversity and plasticity, these underlie the dual potential of tumor-associated neutrophils (TANs) in the tumor microenvironment (Jaillon et al., 2020). In the context of cancer, TANs have been an important component of the tumor microenvironment (Jaillon et al., 2020). TANs can contribute to tumor-promoting processes by promoting angiogenesis, extracellular matrix remodeling, metastasis, and immunosuppression. Conversely, neutrophils can also boost antitumor responses by directly killing tumor cells and incorporating into cellular networks that mediate antitumor resistance.

Using neutrophil membranes as NPs camouflaging were popular. Zhao et al. (Zhao et al., 2021b) developed Nm@MSNs-DOX/SM NPs for antitumor chemotherapy and anti-inflammatory therapy. They loaded mesoporous silica NPs (MSNs) with DOX, using the anti-inflammatory drug shanzhiside methylester (SM) for the preparation of core NPs and neutrophil membranes (Nm) as the shells. Subsequent study demonstrated that Nm@MSNs-DOX/SM NPs escaped the recognition of macrophages, reduced the phagocytosis of macrophages, exhibited excellent biocompatibility, increased the EPR effect and active tumor targeting, remodeled the tumor microenvironment, and amplified the antitumor effect of DOX. In another study by Zhang et al. (Zhang et al., 2021), the merits of neutrophil membranes camouflaging were validated too. In their work, PLGA NPs loaded with hypocrellin B were constructed as core NPs, and neutrophil membranes were used as the shell, with the aim for hepatocellular carcinoma PDT. Subsequent study showed that the fabricated NM-HB NPs adequately targeted the tumor and mitigated removal from the blood circulation and immune elimination.

4.4 Macrophage membrane-camouflaged NPs

A macrophage membrane-camouflaged NP contains associated membrane proteins of source macrophages, thus making it adequate for tumor targeting (Parodi et al., 2013; Evangelopoulos et al., 2016; Molinaro et al., 2018; Bhattacharyya and Ghosh, 2020; Cao et al., 2020; Gong et al., 2020; Poudel et al., 2020; Chen et al., 2021b). Macrophages have α-4 integrins on membranes, which have ability to actively bind to vascular adhesion molecule on cancer cells. In a study by Cao et al. (Cao et al., 2020), PTX-loaded RANPs were fabricated for targeted therapy against malignant melanoma. In their work, core NPs loaded with PTX were formulated via nanoprecipitation technique using human serum albumin; RAW 264.7 macrophage membranes and membrane vesicles were obtained using a combination of hypotonic lysis, mechanical membrane fragmentation, and differential centrifugation; and finally, the PTX-loaded RANPs were built via coextrusion of the membrane vesicles and the core NPs. A further study showed that the PTX-loaded RANPs had a prolonged blood circulation time, selective accumulation at the tumor, and markedly improved antitumor efficacy in tumor-bearing mouse xenografts.

In a further study by Bhattacharyya et al. (Bhattacharyya and Ghosh, 2020), a novel TNFα-expressed macrophage membrane was engineered as camouflaging shell for the fabrication of NPs for antitumor therapy. Transmembrane TNFα is a crucial signaling cytokine with anticell proliferative potential. In their work, bacterial lipopolysaccharide was used to induce the expression of membrane-bound TNFα through challenging phorbol 12-myristate 13-acetate-differentiated THP-1 cells, and the TNFα-expressed macrophage membranes were isolated and saved. Meanwhile, a well-established ionic gelation method was used to synthesize chitosan core NPs, and finally the core NPs were coated with the TNFα-expressed macrophage membranes through coextrusion. Subsequent study indicated that both the innate and acquired biological properties had been transferred to the fabricated NPs, which showed significant innate anti-cell proliferative potential, inherent capacity of immune escaping, excellent biocompatibility, and dose-dependent cell death in tumor spheroids.

4.5 Natural killing cell membrane-camouflaged NPs

NK cells are lymphocytes of the innate immune system that function between the innate and adaptive immunity. They play important roles for the defense against viral infections, tumor surveillance, autoimmune and inflammatory disorders, and atopic diseases (Pitchaimani et al., 2018; Dash et al., 2020; Jha et al., 2021). Biomimetic NPs camouflaged with NK membranes have high tumor-homing ability, excellent biocompatibility, can prevent immune evasion, as were proved in a study by Pitchaimani et al. (Pitchaimani et al., 2018). In their work, a biomimetic system of DOX@NKsome NPs was developed for targeted tumor therapy. In the process, cationic fusogenic liposome was prepared using thin-film hydration and extrusion techniques, anticancer drug DOX was loaded into the liposomes as the core NPs, and finally the isolated NK membranes were used for shell of camouflage.

4.6 T cell membrane-camouflaged NPs

Cytotoxic T cells have CD8 receptors that recognize antigens on the surfaces of virus-infected cells; once infected cells are detected, the cytotoxic T cells bind to and kill them. Cytotoxic T cell membrane-camouflaged NPs could thus be used as tumor-targeting NPs.

Using T cell membranes as NPs camouflaging was not copious in the present literature, but from the available studies, its merits have presented. In a study by Zhang et al. (Zhang et al., 2017), human cytotoxic T lymphocyte membranes were used for fabricating TPNPs for the therapy of gastric cancer. In the process, the membrane vesicles were obtained by a combination techniques of hypotonic lysis, homogenizer disruption, centrifugation, and sonication, and finally the membrane vesicles were coated onto the core PTX-loaded PLGA NPs via coextrusion. Subsequent study showed that the TPNPs exhibited longer circulation time, good tumor site accumulation, and strong inhibition of the growth of human gastric cancer in mice after local low-dose irradiation.

Recently, some newly emerged biological techniques have been used for the modification of cell membranes for anticancer agents loaded NPs camouflaging and/or therapy, which can not only camouflage the core NPs but be able to transfer engineered functionalized proteins, peptides and/or motifs to the tumor sites for treatment, and improve therapeutic efficacy (Jiang et al., 2020a; Bhattacharyya and Ghosh, 2020; Ma et al., 2020; Zinger et al., 2021). Ma et al. (Ma et al., 2020) fabricated a novel kind of NPs for hepatocellular carcinoma PTT (Figure 4). Mesoporous silica NPs loaded with IR780 were constructed as the core NPs, the cell membranes used for coating were derived from genetically engineered chimeric antigen receptors (CARs) T lymphatic cell and natural T lymphatic cell that extracted from human T cells enriched from peripheral blood mononuclear cells. Further studies *in vitro* and *in vivo* showed the CAR-T cells could recognize GPC3 expressed on the surface of hepatocellular carcinoma cells, which enhanced targeting abilities of the NPs; and the CAR T cells could eliminate cancer cells by single-chain variable region (ScFv) on the cell membranes of CAR-T cells, in a non-major histocompatibility complex-restricted way. These NPs showed superior biocompatibility, outstanding targeting ability and excellent photothermal response.

4.7 Cancer cell membrane-camouflaged NPs

NPs coated with cancer cell membranes effectively deliver tumor-associated membrane-bound antigens with immunological adjuvants to antigen-presenting cells by inducing the anticancer immune response (Jiang et al., 2019; Li et al., 2020; Chen et al., 2021a; Zhao et al., 2021a; Fan et al., 2021; Shen et al., 2021). NPs functionalized with cancer cell membranes aid homotypic targeting, which, in turn, facilitates internalization by source cells through self-recognition; these NPs strongly resist the immune system thanks to their capacity to replicate surface antigenic diversity (Chen et al., 2021a; Zhao et al., 2021a; Fan et al., 2021; Shen et al., 2021).

There were copious studies of cancer cell membrane-camouflaging in literature. Among them, in a work by Li et al. (Li et al., 2020), a biomimetic system of AM-PP@ICG NPs for targeted 19 F magnetic resonance/photoacoustic/fluorescence imaging-guided PTT was fabricated. The core was AM-PP@ICGNPs, and A549 lung cancer cell membranes

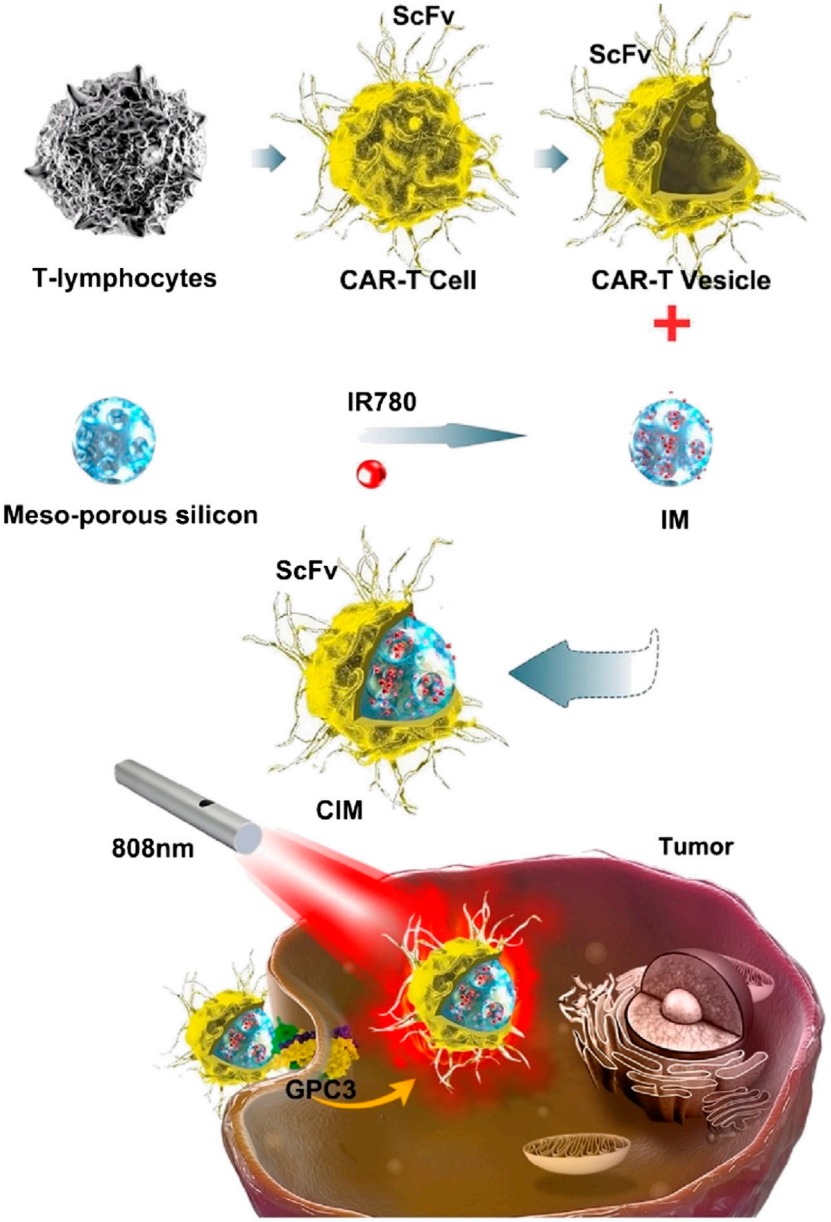

FIGURE 4
Schematic illustration of chimeric antigen receptor-T (CAR-T) membrane coated nanoparticles for tumor photothermal therapy. CAR-T: chimeric antigen receptor-T; CIM: CAR-T cell membrane-coated nanoparticle; GPC3: Glypican-3; IR780: IR780 iodide; IM: IR780-loaded MSN; MSN: mesoporous silica nanoparticle; ScFv: single-chain variable region (derived from monoclonal antibody heavy and light chains and expressed on the cell membrane of CAR-T cells). Reproduced with permission from reference (Ma et al., 2020). Copyright © The author(s).

were used as camouflage. Subsequent study indicated that the NPs had biocompatibility, time-dependent tumor homing with high sensitivity, a prominent photothermal effect for tumors under NIR laser irradiation, and a strong antitumor response *in vivo*. In another study by Zhao et al. (Zhao et al., 2021a), for the therapy of non-Hodgkin's lymphoma, CCM@MSNs-ISOIM NPs were fabricated. In the process, mesoporous silica was used to load an herb-derived traditional Chinese medicine to form core NPs, and OCI-LY10 tumor cell membranes were used for camouflaging. The NPs exhibited good effects on blocking the lymphoma cell cycle and promoting mitochondrial-mediated apoptosis, with features of low pH sensitivity, high immune evasion, good biocompatibility, and active tumor targeting.

In previous research, the accumulation of payload delivered by cancer cell membrane-coated NPs in the tumor increased, and

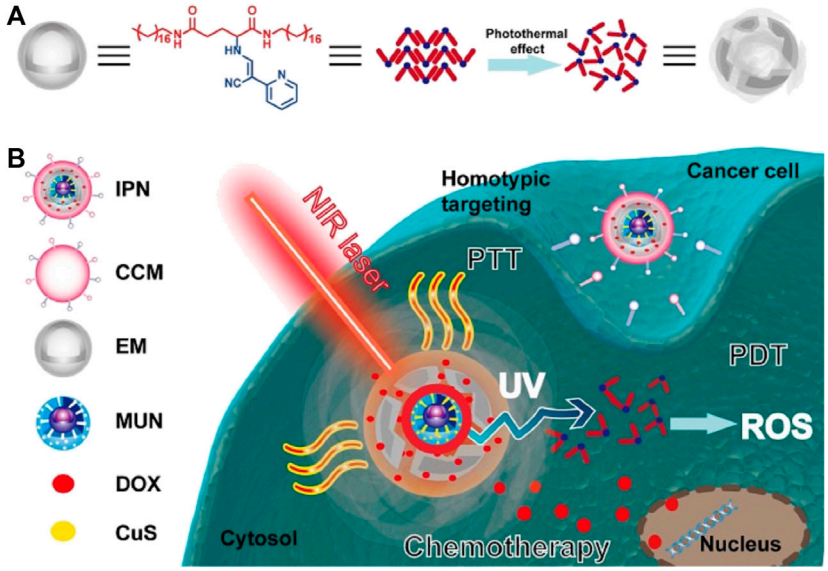

FIGURE 5
Schematic illustration of the intelligent phototriggered nanoparticles. **(A)** Chemical structure of EM gel and illustration of its photothermally induced phase transition; **(B)** Main components of IPNs and a schematic illustration of the domino effect induced by IPNs for multimodal tumor therapy. CCM: cancer cell membrane; CuS: copper sulfide; DOX: doxorubicin; EM: enaminitrile molecular; IPN: intelligent phototriggered nanoparticle; MUN: mesoporous silica-coated UCNP; NIR: near-infrared; PDT: photodynamic therapy; PTT: photothermal therapy; ROS: reactive oxygen species; UV: ultraviolet (UV); UCNP: upconversion nanoparticle. Reproduced with permission from reference (Xu et al., 2021). Copyright © The author(s).

the mechanisms were that specific homotypic targeting and passive targeting via the EPR effect facilitated the delivery (Li et al., 2020). The core NPs were ICG loaded PLGA NPs, cancer cell membranes camouflaging facilitated effective targeting delivery, and these NPs demonstrated well in dual-modal (fluorescence/photoacoustic) image-guided PTT (Li et al., 2020). Yet, treatment resistance of the tumors to PDT owing to oxygen deficiency largely compromised the therapeutic efficacy; looking ahead, if oxygen levels in tumors can be increased, the therapeutic efficacy may be improved.

To solve the above issues, in further work, Chen et al. (Chen et al., 2021a) fabricated N/P@MCC NPs for PTT and PDT of tumor. Nitrogen-doped graphene quantum dots (N-GQDs) and protoporphyrin IX (PpIX) were constructed, with a hydrophobic mesoporous silica NP (HMSN) coating and loaded with catalase to obtain core NPs, and cancer cell membranes (CCMs) were used to coat core NPs via coextrusion. In the process of therapy, the N/P@MCC NPs generated $^1O_2$, and yielded local low-temperature hyperthermia for thermally ablating cancer cells and infrared imaging. These NPs effectively scavenged excess H_2O_2 to sustainably maintain oxygen for synchronous O_2 self-supply and hypoxia alleviation by augmenting the intrinsic catalytic features of catalase. Synergistically, the increased O_2 reacted with N-GQDs and PpIX to enable a maximally increased $^1O_2$ output for augmented PDT, thus facilitating hypoxic tumor elimination.

With the same consideration as above mentioned, Shen et al. (Shen et al., 2021) developed Ir–B–TiO_2@CCM NPs for targeted cancer imaging and synergistic anticancer of PTT and SDT. In the process, B–TiO_2 was prepared using chemical methods and functionalized with Ir to obtain Ir–B–TiO_2 core NPs, cancer cell membranes were isolated from source cells of human cervical carcinoma (HeLa), and finally the cell membrane vesicles (CCMs) were camouflaged onto the core NPs through extrusion. The Ir–B–TiO_2@CCM NPs generated heat efficiently under irradiation, catalytically formed ROS under ultrasound radiation, demonstrated selective localization in the mitochondria, and preferentially accumulated in cancerous rather than non-cancerous cells, thereby exhibiting targeting. Under synergistic irradiation at 1,064 nm and ultrasound radiation, the Ir–B–TiO_2@CCM NPs showed imaging effect and the tumor was identified with a high spatial resolution, meanwhile, these NPs completely eradicated tumors in a mouse model.

To further improve therapeutic efficacy of biomimetic NPs, some new attempts were conducted. Xu et al. (Xu et al., 2021) developed intelligent phototriggered NPs (IPNs) for multimodal antitumor therapy of the breast cancer (Figure 5). They loaded mesoporous silica-coated upconversion ($NaYF_4$: Yb/Tm) NPs (UCNPs) with copper sulfide to form core NPs, synthesized thermosensitive and photosensitive enaminitrile molecule (EM) organogel and loaded with antitumor drug DOX, encapsulated

the core NPs with the antitumor drug DOX loaded EM organogel, and camouflaged them with cancer cell membranes isolated from breast cancer cells of MCF-7 and 4T1 cells for shell. The combined EM gel with UCNPs enabled PDT with NIR excitation, EM switched displaying H^+-induced aggregate emission in tumor acidic microenvironments to generate ROS with ultraviolet irradiation, and was used as the second domino to control drug release. Subsequent studies showed that a domino effect was activated when irradiated the IPNs with an NIR laser, initiating photothermal effect by copper sulfide for PTT that also resulted in phase transformation of the anticancer DOX loaded EM gel to release DOX. In the process, the upconversion core converted the NIR light energy into ultraviolet light by exciting the EM, which generated ROS for PDT. The IPNs exhibited outstanding anticancer effects with little systemic toxicity.

4.8 Stem cell membrane-camouflaged NPs

Stem cell membrane-camouflaged NPs can evade immune system clearance, and thanks to their intrinsic tumor tropic property, are suitable for tumor therapy (Gao et al., 2016; Li et al., 2021b; Mu et al., 2021). Mu et al. (Mu et al., 2021) developed PDA-DOX/siPD-L1@SCM NPs to target prostate cancer (PCa) bone metastases. In their work, core NPs of PDA–DOX/siRNA were formulated using dopamine hydrochloride (polydopamine (PDA)), DOX, and siPD-L1 or $siRNA^{FAM}$, and MSC membranes were camouflaged via coextrusion. Subsequent studies demonstrated that PDA-DOX/siPD-L1@SCM NPs effectively enhanced the blood circulation time and improved penetration ability and accumulation at tumor sites, and they exhibited excellent performance in the synergistic chemoimmunotherapy for PCa bone metastases.

In another study, Li et al. (Li et al., 2021b) fabricated DOX-loaded MSN@M NPs for antitumor treatment. In their work, core NPs were constructed by loading DOX with mesoporous silica (MSN), and sonication technique was used to camouflage the MSC derived membranes onto the core NPs. Ensuing study showed that DOX-loaded MSN@M NPs had high capacity for drug loading and sustained drug release, a reduced clearance rate, stronger tumor targeting and penetration abilities, more effective inhibition of tumor growth, and decreased side effects.

4.9 Hybrid cell membrane-camouflaged NPs

In hybrid cell membranes cloaked NPs, multiple functionalities can be integrated into a single platform by fusing cell membranes isolated different cell sources, which can enhance the flexibility control of NP functionality and offer new opportunities for biomedical applications. For the effective treatment of breast cancer metastasis, Gong et al. (Gong et al., 2020) formulated DPLGA@[RAW-4T1] NPs. In their work, DOX-loaded PLGA (DPLGA) NPs were formulated as core NPs, cell membranes isolated from RAW264.7 macrophage cells (RAW) and 4T1 breast cancer cells (4T1) were combining used for fusion, and the sonication technique was used to coat the fused RAW-4T1 hybrid membranes onto the core DPLGA NPs. The hybrid membrane-coated DPLGA NPs exhibited excellent biocompatibility, targeted specific metastases, and displayed homogenous tumor-targeting ability *in vitro*. Beyond this, these NPs demonstrated a markedly enhanced multi-target ability in an animal model with lung metastases, and exhibited excellent anti-metastasis efficacy for the breast cancer-derived lung metastases.

In a further study, Jiang et al. (Jiang et al., 2019) constructed Melanin@RBC-M to enhance the PTT efficacy. In their work, melanin core NPs were extracted and formed from the ink sac of fresh cuttlefish and centrifuged. Hybrid membranes were created from RBC-derived and human breast cancer MCF-7 cell-derived membranes by cell membrane fusion. The hybrid membranes were coated onto melanin core NPs using an extrusion method. Ensuing study showed that the fused RBC-M hybrid membranes preserved cell membrane proteins of RBC and MCF-7 cell, and the resultant Melanin@RBC-M exhibited a prolonged blood circulation time, enhanced homotypic targeting ability, reduced cellular uptake by macrophages, and significantly increased tumor accumulation and PTT efficacy.

Beyond this, Xiong et al. (Xiong et al., 2021) fabricated Fe_3O_4-ICG@IRM for ovarian cancer therapy. In their work, ICG loaded magnetic NPs (Fe_3O_4) were the core NPs, ID8 ovarian cancer cell-derived and RBC-derived membrane vesicles were fused to yield hybrids through membrane fusion, and coextrusion technique was used to coat the hybrid membranes onto Fe_3O_4-ICG core NPs. Ensuing study showed that the Fe_3O_4-ICG@IRM preserved cell membrane proteins of both ID8 and RBC cell and exhibited highly specific self-recognition of ID8 cells, prolonged circulation time, and activated specific immunity. The NPs demonstrated good efficacy of synergistic PTT and immunotherapy. The immunotherapy was resulted from the release of whole-cell tumor antigens by photothermal-induced tumor necrosis.

For synergistic PTT and chemotherapy against hepatocellular carcinoma, Ji et al. (Ji et al., 2020) fabricated sorafenib (SF) loaded cancer cell-macrophage hybrid membrane-coated NIR-responsive hollow copper sulfide (CuS) NPs with a surface modified with anti-VEGFR (CuS-SF@CMV NPs). These CuS-SF@CMV NPs expressed the characteristic membrane proteins of both cancer cells and macrophages, exhibited good tumor cell targeting, high capacity of drug loading, increased immune evasion, and selectively accumulated in cancer cells *in vitro* and tumors *in vivo*. The

CuS-SF@CMV NPs exhibited synergistic PTT and chemotherapy in cancer cells under NIR irradiation, and with 94.3% inhibition of tumor growth in a tumor-bearing mouse model. After the tumor cells were killed by the initial PTT, sorafenib and the anti-VEGFR antibody sustained the anticancer effect through inhibiting tumor cell proliferation and angiogenesis.

5 Conclusions and future perspectives

In this review, we have discussed the progress of using nanotechnology towards the design, formulation, characterization, function, effect and potential application of cell membrane-coated NPs, and some problems have been analyzed. Development of cell membrane-modified biomimetic NPs has progressed greatly in recent years. Their key value lies in how they are recognized as their respective source cells, which can support their prolonged circulation time, immune evasion, exceptional biocompatibility, and homotypic targeting. More so, some engineered cell membranes have extra therapeutic functions. Thanks to these advantages, NPs are strong candidates for use in cancer therapies; researchers aim to apply them to improve the therapeutic outcomes and reduce the side effects of existing therapies, to make advances in targeted drug delivery, chemotherapy, PTT, PDT, SDT and (photo) immunotherapy.

Nevertheless, NPs have several limitations: lack of precision understanding of the molecular mechanisms; denaturation of cellular membrane proteins may trigger potential immune responses to endogenous antigens, and profound study is insufficient; biomimetic nanoparticle-based PTT/PDT have lower light penetration, oxygen dependence, and limited therapeutic efficacy; tumor-targeting, payload-loaded NPs have low utilization efficiency as the delivery and distribution of tumor-targeting NPs work through the EPR effect; the EPR effect can become saturated, and an aberrant EPR effect causes NPs to lose access to the target cells in deep tissues of the tumor, thus lowering the sustainability of their accumulation in tumor.

Previous studies focus mainly on short-term effects of NPs stability, positive therapeutic response and side effects, and deficiency in longer systemic study and heterogeneity-related study. To achieve clinical translation of biomimetic NPs and a delivery system, NPs long-term toxicity, overall stability, the eventual potential to scale-up should be studied, and a system showing adequate *in vivo* promise must be considered too. In the future, further modifying the isolated cell membranes—such as to eliminate denatured cell membrane proteins, add a double-membrane coating, modify cell membranes via biological engineering and incorporate novel fabrication techniques and therapeutics; and use of modeling and computational simulations to justify design of NPs—will better optimize the outcomes we can currently achieve and support the development of new strategies for cell membrane-camouflaging anticancer therapy.

Author contributions

Conceptualization, SW; methodology, SW, CW; software, CW; validation, SW, CW; formal analysis, SW; investigation, SW, CW; resources, SW; data curation, SW, CW; original draft preparation, CW; writing review and editing, SW; supervision, SW; funding acquisition, SW. All authors have read and agreed to the published version of the manuscript.

Funding

This research was funded by National Natural Science Foundation of China(Grant No. 81860308; 81560290).

Conflict of interest

The authors declare that the research was conducted in the absence of any commercial or financial relationships that could be construed as a potential conflict of interest.

Publisher's note

All claims expressed in this article are solely those of the authors and do not necessarily represent those of their affiliated organizations, or those of the publisher, the editors and the reviewers. Any product that may be evaluated in this article, or claim that may be made by its manufacturer, is not guaranteed or endorsed by the publisher.

References

Attia, M. F., Anton, N., Wallyn, J., Omran, Z., and Vandamme, T. F. (2019). An overview of active and passive targeting strategies to improve the nanocarriers efficiency to tumour sites. *J. Pharm. Pharmacol.* 71, 1185–1198. doi:10.1111/jphp.13098

Balantič, K., Miklavčič, D., Križaj, I., and Kramar, P. (2021). The good and the bad of cell membrane electroporation. *Acta Chim. Slov.* 68, 753–764. doi:10.17344/acsi.2021.7198

Bhattacharyya, S., and Ghosh, S. S. (2020). Transmembrane tnfα-expressed macrophage membrane-coated chitosan nanoparticles as cancer therapeutics. *ACS Omega* 5, 1572–1580. doi:10.1021/acsomega.9b03531

Bidkar, A. P., Sanpui, P., and Ghosh, S. S. (2019). Red blood cell-membrane-coated poly(lactic-co-glycolic acid) nanoparticles for enhanced chemo- and hypoxia-activated therapy. *ACS Appl. Bio Mat.* 2, 4077–4086. doi:10.1021/acsabm.9b00584

Bonsignore, G., Patrone, M., Grosso, F., Martinotti, S., and Ranzato, E. (2021). Cancer therapy challenge: It is time to look in the "st. Patrick's well" of the nature. *Int. J. Mol. Sci.* 22, 10380. doi:10.3390/ijms221910380

Cai, J. X., Liu, J. H., Wu, J. Y., Li, Y. J., Qiu, X. H., Xu, W. J., et al. (2022). Hybrid cell membrane-functionalized biomimetic nanoparticles for targeted therapy of osteosarcoma. *Int. J. Nanomedicine* 17, 837–854. doi:10.2147/ijn.s346685

Cao, X., Tan, T., Zhu, D., Yu, H., Liu, Y., Zhou, H., et al. (2020). Paclitaxel-loaded macrophage membrane camouflaged albumin nanoparticles for targeted cancer therapy. *Int. J. Nanomedicine* 15, 1915–1928. doi:10.2147/ijn.s244849

Castro, F., Martins, C., Silveira, M. J., Moura, R. P., Pereira, C. L., Sarmento, B., et al. (2021). Advances on erythrocyte-mimicking nanovehicles to overcome barriers in biological microenvironments. *Adv. Drug Deliv. Rev.* 170, 312–339. doi:10.1016/j.addr.2020.09.001

Chen, C., Song, M., Du, Y., Yu, Y., Li, C., Han, Y., et al. (2021). Tumor-associated-macrophage-membrane-coated nanoparticles for improved photodynamic immunotherapy. *Nano Lett.* 21, 5522–5531. doi:10.1021/acs.nanolett.1c00818

Chen, H., Zheng, D., Pan, W., Li, X., Lv, B., Gu, W., et al. (2021). Biomimetic nanotheranostics camouflaged with cancer cell membranes integrating persistent oxygen supply and homotypic targeting for hypoxic tumor elimination. *ACS Appl. Mat. Interfaces* 13, 19710–19725. doi:10.1021/acsami.1c03010

Chen, Y., Zhao, G., Wang, S., He, Y., Han, S., Du, C., et al. (2019). Platelet-membrane-camouflaged bismuth sulfide nanorods for synergistic radio-photothermal therapy against cancer. *Biomater. Sci.* 7, 3450–3459. doi:10.1039/c9bm00599d

Corbo, C., Molinaro, R., Taraballi, F., Toledano Furman, N. E., Sherman, M. B., Parodi, A., et al. (2016). Effects of the protein corona on liposome-liposome and liposome-cell interactions. *Int. J. Nanomedicine* 11, 3049–3063. doi:10.2147/IJN.S109059

Dash, P., Piras, A. M., and Dash, M. (2020). Cell membrane coated nanocarriers - an efficient biomimetic platform for targeted therapy. *J. Control. Release* 327, 546–570. doi:10.1016/j.jconrel.2020.09.012

Evangelopoulos, M., Parodi, A., Martinez, J. O., Yazdi, I. K., Cevenini, A., van de Ven, A. L., et al. (2016). Cell source determines the immunological impact of biomimetic nanoparticles. *Biomaterials* 82, 168–177. doi:10.1016/j.biomaterials.2015.11.054

Fan, Y., Hao, W., Cui, Y., Chen, M., Chu, X., Yang, Y., et al. (2021). Cancer cell membrane-coated nanosuspensions for enhanced chemotherapeutic treatment of glioma. *Molecules* 26, 5103. doi:10.3390/molecules26165103

Gao, C., Lin, Z., Jurado-Sánchez, B., Lin, X., Wu, Z., He, Q., et al. (2016). Stem cell membrane-coated nanogels for highly efficient *in vivo* tumor targeted drug delivery. *Small* 12, 4056–4062. doi:10.1002/smll.201600624

Gao, X., Li, S., Ding, F., Liu, X., Wu, Y., Li, J., et al. (2021). A virus-mimicking nucleic acid nanogel reprograms microglia and macrophages for glioblastoma therapy. *Adv. Mat.* 33, e2006116. doi:10.1002/adma.202006116

Gong, C., Yu, X., You, B., Wu, Y., Wang, R., Han, L., et al. (2020). Macrophage-cancer hybrid membrane-coated nanoparticles for targeting lung metastasis in breast cancer therapy. *J. Nanobiotechnology* 18, 92. doi:10.1186/s12951-020-00649-8

Hu, C. M., Zhang, L., Aryal, S., Cheung, C., Fang, R. H., Zhang, L., et al. (2011). Erythrocyte membrane-camouflaged polymeric nanoparticles as a biomimetic delivery platform. *Proc. Natl. Acad. Sci. U. S. A.* 108 (27), 10980–10985. doi:10.1073/pnas.1106634108

Huang, X., Wu, B., Li, J., Shang, Y., Chen, W., Nie, X., et al. (2019). Anti-tumour effects of red blood cell membrane-camouflaged black phosphorous quantum dots combined with chemotherapy and anti-inflammatory therapy. *Artif. Cells Nanomed. Biotechnol.* 47, 968–979. doi:10.1080/21691401.2019.1584110

Jaillon, S., Ponzetta, A., Di Mitri, D., Santoni, A., Bonecchi, R., Mantovani, A., et al. (2020). Neutrophil diversity and plasticity in tumour progression and therapy. *Nat. Rev. Cancer* 20, 485–503. doi:10.1038/s41568-020-0281-y

Jha, A., Nikam, A. N., Kulkarni, S., Mutalik, S. P., Pandey, A., Hegde, M., et al. (2021). Biomimetic nanoarchitecturing: A disguised attack on cancer cells. *J. Control. Release* 329, 413–433. doi:10.1016/j.jconrel.2020.12.005

Ji, B., Cai, H., Yang, Y., Peng, F., Song, M., Sun, K., et al. (2020). Hybrid membrane camouflaged copper sulfide nanoparticles for photothermal-chemotherapy of hepatocellular carcinoma. *Acta Biomater.* 111, 363–372. doi:10.1016/j.actbio.2020.04.046

Jiang, Q., Liu, Y., Guo, R., Yao, X., Sung, S., Pang, Z., et al. (2019). Erythrocyte-cancer hybrid membrane-camouflaged melanin nanoparticles for enhancing photothermal therapy efficacy in tumors. *Biomaterials* 192, 292–308. doi:10.1016/j.biomaterials.2018.11.021

Jiang, Q., Wang, K., Zhang, X., Ouyang, B., Liu, H., Pang, Z., et al. (2020). Cancer immunotherapy: Platelet membrane-camouflaged magnetic nanoparticles for ferroptosis-enhanced cancer immunotherapy (small 22/2020). *Small* 16, 2070119. doi:10.1002/smll.202070119

Jiang, Y., Krishnan, N., Zhou, J., Chekuri, S., Wei, X., Kroll, A. V., et al. (2020). Engineered cell-membrane-coated nanoparticles directly present tumor antigens to promote anticancer immunity. *Adv. Mat.* 32 (30), e2001808. doi:10.1002/adma.202001808

Jin, F., Qi, J., Liu, D., You, Y., Shu, G., Du, Y., et al. (2021). Cancer-cell-biomimetic Upconversion nanoparticles combining chemo-photodynamic therapy and CD73 blockade for metastatic triple-negative breast cancer. *J. Control. Release* 337, 90–104. doi:10.1016/j.jconrel.2021.07.021

Khaldoyanidi, S. K., Glinsky, V. V., Sikora, L., Glinskii, A. B., Mossine, V. V., Quinn, T. P., et al. (2003). MDA-MB-435 human breast carcinoma cell homo- and heterotypic adhesion under flow conditions is mediated in part by Thomsen-Friedenreich antigen-galectin-3 interactions. *J. Biol. Chem.* 278 (6), 4127–4134. doi:10.1074/jbc.m209590200

Lai, P., Daear, W., Löbenberg, R., and Prenner, E. J. (2014). Overview of the preparation of organic polymeric nanoparticles for drug delivery based on gelatine, chitosan, poly(d, l-lactide-co-glycolic acid) and polyalkylcyanoacrylate. *Colloids Surfaces B Biointerfaces* 118, 154–163. doi:10.1016/j.colsurfb.2014.03.017

Lee, J. Y., Vyas, C. K., Kim, G. G., Choi, P. S., Hur, M. G., Yang, S. D., et al. (2019). Red blood cell membrane bioengineered Zr-89 labelled hollow mesoporous silica nanosphere for overcoming phagocytosis. *Sci. Rep.* 9, 7419. doi:10.1038/s41598-019-43969-y

Li, B., Chu, T., Wei, J., Zhang, Y., Qi, F., Lu, Z., et al. (2021). Platelet-membrane-coated nanoparticles enable vascular disrupting agent combining anti-angiogenic drug for improved tumor vessel impairment. *Nano Lett.* 21, 2588–2595. doi:10.1021/acs.nanolett.1c00168

Li, H., Jin, K., Luo, M., Wang, X., Zhu, X., Liu, X., et al. (2019). Size dependency of circulation and biodistribution of biomimetic nanoparticles: Red blood cell membrane-coated nanoparticles. *Cells* 8 (8), 881. doi:10.3390/cells8080881

Li, S., Jiang, W., Yuan, Y., Sui, M., Yang, Y., Huang, L., et al. (2020). Delicately designed cancer cell membrane-camouflaged nanoparticles for targeted 19F MR/PA/FL imaging-guided photothermal therapy. *ACS Appl. Mat. Interfaces* 12, 57290–57301. doi:10.1021/acsami.0c13865

Li, S., and Zhang, L. (2020). Erythrocyte membrane nano-capsules: Biomimetic delivery and controlled release of photothermal-photochemical coupling agents for cancer cell therapy. *Dalton Trans.* 49, 2645–2651. doi:10.1039/c9dt04335g

Li, Y. S., Wu, H. H., Jiang, X. C., Zhang, T. Y., Zhou, Y., Huang, L. L., et al. (2021). Active stealth and self-positioning biomimetic vehicles achieved effective antitumor therapy. *J. Control. Release* 335, 515–526. doi:10.1016/j.jconrel.2021.05.031

Liu, Y., Wang, X., Ouyang, B., Liu, X., Du, Y., Cai, X., et al. (2018). Erythrocyte-platelet hybrid membranes coating polypyrrol nanoparticles for enhanced delivery and photothermal therapy. *J. Mat. Chem. B* 6, 7033–7041. doi:10.1039/c8tb02143k

Liu, Z., Wang, F., Liu, X., Sang, Y., Zhang, L., Ren, J., et al. (2021). Cell membrane-camouflaged liposomes for tumor cell-selective glycans engineering and imaging *in vivo*. *Proc. Natl. Acad. Sci. U. S. A.* 118, e2022769118. doi:10.1073/pnas.2022769118

Lyu, M., Chen, M., Liu, L., Zhu, D., Wu, X., Li, Y., et al. (2021). A platelet-mimicking theranostic platform for cancer interstitial brachytherapy. *Theranostics* 11, 7589–7599. doi:10.7150/thno.61259

Ma, K., Cheng, Y., Wei, X., Chen, D., Zhao, X., Jia, P., et al. (2021). Gold embedded chitosan nanoparticles with cell membrane mimetic polymer coating for pH-sensitive controlled drug release and cellular fluorescence imaging. *J. Biomater. Appl.* 35, 857–868. doi:10.1177/0885328220952594

Ma, W., Zhu, D., Li, J., Chen, X., Xie, W., Jiang, X., et al. (2020). Coating biomimetic nanoparticles with chimeric antigen receptor T cell-membrane provides high specificity for hepatocellular carcinoma photothermal therapy treatment. *Theranostics* 10, 1281–1295. doi:10.7150/thno.40291

Molinaro, R., Evangelopoulos, M., Hoffman, J. R., Corbo, C., Taraballi, F., Martinez, J. O., et al. (2018). Design and development of biomimetic nanovesicles using a microfluidic approach. *Adv. Mat.* 30 (15), e1702749. doi:10.1002/adma.201702749

Mu, X., Zhang, M., Wei, A., Yin, F., Wang, Y., Hu, K., et al. (2021). Doxorubicin and PD-L1 siRNA co-delivery with stem cell membrane-coated polydopamine nanoparticles for the targeted chemoimmunotherapy of PCa bone metastases. *Nanoscale* 13, 8998–9008. doi:10.1039/d0nr08024a

Palomba, R., Parodi, A., Evangelopoulos, M., Acciardo, S., Corbo, C., de Rosa, E., et al. (2016). Biomimetic carriers mimicking leukocyte plasma membrane to increase tumor vasculature permeability. *Sci. Rep.* 6, 34422. doi:10.1038/srep34422

Parodi, A., Quattrocchi, N., van de Ven, A. L., Chiappini, C., Evangelopoulos, M., Martinez, J. O., et al. (2013). Synthetic nanoparticles functionalized with biomimetic leukocyte membranes possess cell-like functions. *Nat. Nanotechnol.* 8 (1), 61–68. doi:10.1038/nnano.2012.212

Pei, Q., Hu, X., Zheng, X., Liu, S., Li, Y., Jing, X., et al. (2018). Light-activatable red blood cell membrane-camouflaged dimeric prodrug nanoparticles for synergistic photodynamic/chemotherapy. *ACS Nano* 12, 1630–1641. doi:10.1021/acsnano.7b08219

Peng, H., Xu, Z., Wang, Y., Feng, N., Yang, W., Tang, J., et al. (2020). Biomimetic mesoporous silica nanoparticles for enhanced blood circulation and cancer therapy. *ACS Appl. Bio Mat.* 3, 7849–7857. doi:10.1021/acsabm.0c01014

Pitchaimani, A., Nguyen, T. D. T., and Aryal, S. (2018). Natural killer cell membrane infused biomimetic liposomes for targeted tumor therapy. *Biomaterials* 160, 124–137. doi:10.1016/j.biomaterials.2018.01.018

Poudel, K., Banstola, A., Gautam, M., Soe, Z., Phung, C. D., Pham, L. M., et al. (2020). Macrophage-membrane-camouflaged disintegrable and excretable nanoconstruct for deep tumor penetration. *ACS Appl. Mat. Interfaces* 12, 56767–56781. doi:10.1021/acsami.0c17235

Raskov, H., Orhan, A., Christensen, J. P., and Gögenur, I. (2021). Cytotoxic CD8+ T cells in cancer and cancer immunotherapy. *Br. J. Cancer* 124, 359–367. doi:10.1038/s41416-020-01048-4

Rostami, I. (2021). Empowering the emission of upconversion nanoparticles for precise subcellular imaging. *Nanomater. (Basel)* 11, 1541. doi:10.3390/nano11061541

Schilsky, R. L., Nass, S., Le Beau, M. M., and Benz, E. J., Jr (2020). Progress in cancer research, prevention, and care. *N. Engl. J. Med. Overseas. Ed.* 383, 897–900. doi:10.1056/nejmp2007839

Seligson, N. D., Knepper, T. C., Ragg, S., and Walko, C. M. (2021). Developing drugs for tissue-agnostic indications: A paradigm shift in leveraging cancer biology for precision medicine. *Clin. Pharmacol. Ther.* 109, 334–342. doi:10.1002/cpt.1946

Shen, J., Karges, J., Xiong, K., Chen, Y., Ji, L., Chao, H., et al. (2021). Cancer cell membrane camouflaged iridium complexes functionalized black-titanium nanoparticles for hierarchical-targeted synergistic NIR-II photothermal and sonodynamic therapy. *Biomaterials* 275, 120979. doi:10.1016/j.biomaterials.2021.120979

Sung, H., Ferlay, J., Siegel, R. L., Laversanne, M., Soerjomataram, I., Jemal, A., et al. (2021). Global cancer statistics 2020: GLOBOCAN estimates of incidence and mortality worldwide for 36 cancers in 185 countries. *Ca. A Cancer J. Clin.* 71, 209–249. doi:10.3322/caac.21660

Wan, G., Chen, B., Li, L., Wang, D., Shi, S., Zhang, T., et al. (2018). Nanoscaled red blood cells facilitate breast cancer treatment by combining photothermal/photodynamic therapy and chemotherapy. *Biomaterials* 155, 25–40. doi:10.1016/j.biomaterials.2017.11.002

Wang, H., Wang, Z., Tu, Y., Li, Y., Xu, T., Yang, M., et al. (2020). Homotypic targeting upconversion nano-reactor for cascade cancer starvation and deep-tissue phototherapy. *Biomaterials* 235, 119765. doi:10.1016/j.biomaterials.2020.119765

Wang, H., Wu, J., Williams, G. R., Fan, Q., Niu, S., Wu, J., et al. (2019). Platelet-membrane-biomimetic nanoparticles for targeted antitumor drug delivery. *J. Nanobiotechnology* 17 (1), 60. doi:10.1186/s12951-019-0494-y

Wang, J., Gu, X., Ouyang, Y., Chu, L., Xu, M., Wang, K., et al. (2021). Engineering of neutrophil membrane camouflaging nanoparticles realizes targeted drug delivery for amplified antitumor therapy. *Int. J. Nanomedicine* 16, 1175–1187. doi:10.2147/ijn.s288636

Wang, L., Chen, S., Pei, W., Huang, B., and Niu, C. (2020). Magnetically targeted erythrocyte membrane coated nanosystem for synergistic photothermal/chemotherapy of cancer. *J. Mat. Chem. B* 8, 4132–4142. doi:10.1039/d0tb00364f

Wang, R., Yang, H., Fu, R., Su, Y., Lin, X., Jin, X., et al. (2020). Biomimetic upconversion nanoparticles and gold nanoparticles for novel simultaneous dual-modal imaging-guided photothermal therapy of cancer. *Cancers (Basel)* 12, 3136. doi:10.3390/cancers12113136

Wang, S., Yin, Y., Song, W., Zhang, Q., Yang, Z., Dong, Z., et al. (2020). Red-blood-cell-membrane-enveloped magnetic nanoclusters as a biomimetic theranostic nanoplatform for bimodal imaging-guided cancer photothermal therapy. *J. Mat. Chem. B* 8, 803–812. doi:10.1039/c9tb01829h

Wang, X., Zhong, X., Li, J., Liu, Z., and Cheng, L. (2021). Inorganic nanomaterials with rapid clearance for biomedical applications. *Chem. Soc. Rev.* 50, 8669–8742. doi:10.1039/d0cs00461h

Wu, H., Xu, X. F., Zhu, J. Q., Wang, M. D., Li, C., Liang, L., et al. (2021). Mesoporous silica nanoparticles for potential immunotherapy of hepatocellular carcinoma. *Front. Bioeng. Biotechnol.* 9, 695635. doi:10.3389/fbioe.2021.695635

Wu, L., Li, Q., Deng, J., Shen, J., Xu, W., Yang, W., et al. (2021). Platelet-tumor cell hybrid membrane-camouflaged nanoparticles for enhancing therapy efficacy in glioma. *Int. J. Nanomedicine* 16, 8433–8446. doi:10.2147/ijn.s333279

Wu, L., Xie, W., Zan, H. M., Liu, Z., Wang, G., Wang, Y., et al. (2020). Platelet membrane-coated nanoparticles for targeted drug delivery and local chemo-photothermal therapy of orthotopic hepatocellular carcinoma. *J. Mat. Chem. B* 8 (21), 4648–4659. doi:10.1039/d0tb00735h

Wu, P., Jiang, X., Yin, S., Yang, Y., Liu, T., Wang, K., et al. (2021). Biomimetic recombinant of red blood cell membranes for improved photothermal therapy. *J. Nanobiotechnology* 19, 213. doi:10.1186/s12951-021-00949-7

Xia, Y., Rao, L., Yao, H., Wang, Z., Ning, P., Chen, X., et al. (2020). Engineering macrophages for cancer immunotherapy and drug delivery. *Adv. Mat.* 32, e2002054. doi:10.1002/adma.202002054

Xiong, J., Wu, M., Chen, J., Liu, Y., Chen, Y., Fan, G., et al. (2021). Cancer-erythrocyte hybrid membrane-camouflaged magnetic nanoparticles with enhanced photothermal-immunotherapy for ovarian cancer. *ACS Nano* 15, 19756–19770. doi:10.1021/acsnano.1c07180

Xu, L., Gao, F., Fan, F., and Yang, L. (2018). Platelet membrane coating coupled with solar irradiation endows a photodynamic nanosystem with both improved antitumor efficacy and undetectable skin damage. *Biomaterials* 159, 59–67. doi:10.1016/j.biomaterials.2017.12.028

Xu, X., Han, C., Zhang, C., Yan, D., Ren, C., Kong, L., et al. (2021). Intelligent phototriggered nanoparticles induce a domino effect for multimodal tumor therapy. *Theranostics* 11, 6477–6490. doi:10.7150/thno.55708

Xuan, M., Shao, J., Zhao, J., Li, Q., Dai, L., Li, J., et al. (2018). Magnetic mesoporous silica nanoparticles cloaked by red blood cell membranes: Applications in cancer therapy. *Angew. Chem. Int. Ed. Engl.* 57, 6157–6161. doi:10.1002/ange.201712996

Yang, N., Ding, Y., Zhang, Y., Wang, B., Zhao, X., Cheng, K., et al. (2018). Surface functionalization of polymeric nanoparticles with umbilical cord-derived mesenchymal stem cell membrane for tumor-targeted therapy. *ACS Appl. Mat. Interfaces* 10 (27), 22963–22973. doi:10.1021/acsami.8b05363

Zhai, Z., Xu, P., Yao, J., Li, R., Gong, L., Yin, Y., et al. (2020). Erythrocyte-mimicking paclitaxel nanoparticles for improving biodistributions of hydrophobic drugs to enhance antitumor efficacy. *Drug Deliv. (Lond).* 27, 387–399. doi:10.1080/10717544.2020.1731862

Zhang, L., Li, R., Chen, H., Wei, J., Qian, H., Su, S., et al. (2017). Human cytotoxic T-lymphocyte membrane-camouflaged nanoparticles combined with low-dose irradiation: A new approach to enhance drug targeting in gastric cancer. *Int. J. Nanomedicine* 12, 2129–2142. doi:10.2147/ijn.s126016

Zhang, Z., Li, D., Cao, Y., Wang, Y., Wang, F., Zhang, F., et al. (2021). Biodegradable Hypocrellin B nanoparticles coated with neutrophil membranes for hepatocellular carcinoma photodynamics therapy effectively via JUNB/ROS signaling. *Int. Immunopharmacol.* 99, 107624. doi:10.1016/j.intimp.2021.107624

Zhao, Q., Jiang, D., Sun, X., Mo, Q., Chen, S., Chen, W., et al. (2021). Biomimetic nanotherapy: Core-shell structured nanocomplexes based on the neutrophil membrane for targeted therapy of lymphoma. *J. Nanobiotechnology* 19, 179. doi:10.1186/s12951-021-00922-4

Zhao, Q., Sun, X., Wu, B., Shang, Y., Huang, X., Dong, H., et al. (2021). Construction of homologous cancer cell membrane camouflage in a nano-drug delivery system for the treatment of lymphoma. *J. Nanobiotechnology* 19, 8. doi:10.1186/s12951-020-00738-8

Zhou, Z., He, H., Wang, K., Shi, X., Wang, Y., Su, Y., et al. (2020). Granzyme A from cytotoxic lymphocytes cleaves GSDMB to trigger pyroptosis in target cells. *Science* 368, eaaz7548. doi:10.1126/science.aaz7548

Zinger, A., Cvetkovic, C., Sushnitha, M., Naoi, T., Baudo, G., Anderson, M., et al. (2021). Humanized biomimetic nanovesicles for neuron targeting. *Adv. Sci. (Weinh).* 8 (19), e2101437. doi:10.1002/advs.202101437

Zou, J., Glinsky, V. V., Landon, L. A., Matthews, L., and Deutscher, S. L. (2005). Peptides specific to the galectin-3 carbohydrate recognition domain inhibit metastasis-associated cancer cell adhesion. *Carcinogenesis* 26 (2), 309–318. doi:10.1093/carcin/bgh329

frontiers | Frontiers in Molecular Biosciences

TYPE Original Research
PUBLISHED 11 October 2022
DOI 10.3389/fmolb.2022.997471

OPEN ACCESS

EDITED BY
Abolfazl Heydari,
Polymer Institute (SAS), Slovakia

REVIEWED BY
Fereshteh Kazemi-Aghdam,
Slovak Academy of Sciences (SAS), Slovakia
Elham Ahmadian,
Tabriz University of Medical Sciences, Iran
Ziba Gharehnazifam,
University of Tehran, Iran

*CORRESPONDENCE
Kamyar Shameli,
kamyarshameli@gmail.com
Hassan Moeini,
hassan.moeini@tum.de

SPECIALTY SECTION
This article was submitted to Nanobiotechnology, a section of the journal Frontiers in Molecular Biosciences

RECEIVED 18 July 2022
ACCEPTED 12 September 2022
PUBLISHED 11 October 2022

CITATION
Lee KX, Shameli K, Nagao Y, Yew YP, Teow S-Y and Moeini H (2022), Potential use of gold-silver core-shell nanoparticles derived from Garcinia mangostana peel for anticancer compound, protocatechuic acid delivery.
Front. Mol. Biosci. 9:997471.
doi: 10.3389/fmolb.2022.997471

Potential use of gold-silver core-shell nanoparticles derived from *Garcinia mangostana* peel for anticancer compound, protocatechuic acid delivery

Kar Xin Lee[1], Kamyar Shameli[1]*, Yuki Nagao[2], Yen Pin Yew[1], Sin-Yeang Teow[3] and Hassan Moeini[4]*

[1]Malaysia-Japan International Institute of Technology (MJIIT), Universiti Teknologi Malaysia, Kuala Lumpur, Malaysia, [2]School of Materials Science, Japan Advanced Institute of Science and Technology (JAIST), Nomi, Japan, [3]Department of Medical Sciences, School of Medical and Life Sciences (SMLS), Sunway University, Jalan Universiti, Bandar Sunway, Selangor Darul Ehsan, Malaysia, [4]School of Medicine, Institute of Virology, Technical University of Munich, Munich, Germany

Colorectal cancer is one of the most killing cancers and this has become a global problem. Current treatment and anticancer drugs cannot specifically target the cancerous cells, thus causing toxicity towards surrounding non-cancer cells. Hence, there is an urgent need to discover a more target-specific therapeutic agent to overcome this problem. Core-shell nanoparticles have emerged as good candidate for anticancer treatment. This study aimed to synthesize core-shell nanoparticles *via* green method which utilised crude peels extract of *Garcinia mangostana* as reducing and stabilising agents for drug delivery. Gold-silver core-shell nanoparticles (Au-AgNPs) were synthesized through seed germination process in which gold nanoparticles acted as the seed. A complete coating was observed through transmission electron microscopy (TEM) when the ratio of AuNPs and AgNPs was 1:9. The size of Au-AgNPs was 38.22 ± 8.41 nm and was mostly spherical in shape. Plant-based drug, protocatechuic acid (PCA) was loaded on the Au-AgNPs to investigate their anticancer activity. In HCT116 colon cancer cells, PCA-loaded Au-AgNPs (IC_{50} = 10.78 μg/ml) showed higher inhibitory action than the free PCA (IC_{50}= 148.09 μg/ml) and Au-AgNPs alone (IC_{50}= 24.36 μg/ml). Up to 80% inhibition of HCT116 cells was observed after the treatment of PCA-loaded Au-AgNPs at 15.63 μg/ml. The PCA-loaded Au-AgNPs also showed a better selectivity towards HCT116 compared to CCD112 colon normal cells when tested at the same concentrations. These findings suggest that Au-AgNPs system can be used as a potent nanocarrier to combat cancerous cells by offering additional anticancer properties to the loaded drug.

KEYWORDS

colorectal cancer, green synthesis, core-shell nanoparticles, gold-silver, protocatechuic acid, drug delivery, HCT116, CCD112

Highlights

- Through the green bio-synthesis method the gold-silver core-shell nanoparticles (Au-Ag NPs) synthesised by Garcinia mangostana crude peels extract as a reducing and stabilising agents.
- Structural, morphological, and compositional properties were investigated by the physicochemical characterization method.
- Protocatechuic acid (PCA) as a plant-based drug has been loaded on Au-Ag NPs to investigate their anticancer activity against colon cancer cells.
- The nanodrug showed a better selectivity towards colon cancer cell (HCT116) compared to colon normal cells (CCD112) when tested at the same concentrations.

Introduction

According to the Malaysia statistics (year 2012–2016), breast, colorectal, and lung cancers are among the most common human cancers across all ethnicity (Azizah et al., 2016). Colorectal cancer (CRC) emerges as a deadly cancer among others (Xu et al., 2019). Patients diagnosed with CRC often have to undergo surgery, chemo- and/or radio-therapy. Chemotherapy is frequently used to treat CRC especially at the late stages (Shen et al., 2019), other newer therapies are monoclonal antibody and immunotherapy. However, these treatments often accompany with undesired toxicities and side effects to human body (Nyst et al., 2009). Healthy tissues surrounding the tumours tend to take up the chemotherapeutic drugs as well due to the poor drug selectivity and specificity (Benoist and Bernard 2009). Therefore, the focus of researches nowadays is to improve the efficiency as well as the specificity of these drugs. One of the approaches is to use a novel and non-toxic nanoparticles (NPs)-based drug delivery system which is superior in improving drug bio-distribution, selectivity, dosage efficiency, and therapeutic indices (Cho et al., 2008).

Nanotechnology has been an exciting field by introducing a novel drug delivery system. Nanoparticles can act as a highly versatile platform for the combination of therapeutic agents and tracking agents. When specific features are developed such as size, shape, hydrophobicity, surface properties, and other physicochemical characteristics, NPs of interest could specifically target diseased cells rather than offering non-target-specific delivery (Bendale, Bendale, and Paul 2017; Sargazi et al., 2022). Core-shell NPs is one of the examples that can act as a nanocarrier for therapeutic agents. Core-shell NPs consist of a core and a shell that is coated on top of the core which can be constructed by both organic and inorganic materials to achieve the desired effects and properties (Ghosh Chaudhuri and Paria 2011). Core-shell NPs exhibit unique and superior properties as compared to the individual NPs counterparts due to the bifunctional effects (Liu and Priestley 2016). These unique properties such as biocompatibility, easy surface modifications, and tunable surface plasmonic resonance properties arise from the large surface area of their nano sizes (1–100 nm) and the synergy of the core with the shell material (Matlou and Abrahamse 2022). These characteristics have numerous advantages for therapeutic applications such as the increasing of residence time, bioavailability, dispersity, stability, and the reduction of active dosage (Chatterjee et al., 2014). Fabrication of gold-silver core-shell NPs (Au-AgNPs) is of great interest because they are useful not only as a drug carriers but have also shown distinct optical properties that are beneficial in cancer marker studies and imaging (Gheorghe et al., 2011).

The synthesis of NPs can be achieved through conventional method such as chemical and physical method, but these methods are relatively toxic (Alam et al., 2014). In contrast, the environmental-friendly biosynthesis focuses more on reduction and elimination of the use of hazardous chemical substances (Jahangirian et al., 2017). This method is less toxic and more suitable for biomedical applications. In this study, we synthesized the Au-AgNPs from *Garcinia mangostana* (GM) (mangosteen) crude extract. The ratio of gold nanoparticles (AuNPs) and silver nanoparticles (AgNPs) was then optimised to obtain the optimal size and shape. The Au-AgNPs was loaded with protocatechuic acid (PCA) which is a natural-occurring phenolic acid present in most of the edible medicinal plants (Cai et al., 2004). PCA was chosen as it has been previously reported to kill cancer cells by inducing apoptosis (Barahuie et al., 2013). PCA served as a preventive action towards cancers by its antioxidant properties. Generation of free radicals is inhibited by PCA. They also scavenge and increase the catalytic activity of endogenous enzymes involved in the neutralization of free radicals (Tanaka, Tanaka, and Tanaka 2011). However, its anticancer activity is greatly limited by the target selectivity, thermal stability, dosage and timing between administration (Barahuie et al., 2015; Usman et al., 2018a), which can be potentially solved by introducing a nanocarrier. The novelty of this study is the synthesis of core-shell NPs using GM extract as a targeted drug carrier for plant based PCA that highly dependent on the dose used and the timing between administration of the acid. To the best of our knowledge, this is the first report showing the synthesis of core-shell NPs using GM extract that can be used as a drug nanocarrier against human colon cancer cells.

Materials and methods

Materials and reagents

GM fruit were collected from an orchard located at Terengganu, Malaysia. Tetrachloroauric (III) acid ($HAuCl_4$) (≥99.9%) and silver nitrate ($AgNO_3$) (>99.8%) which act as precursors were purchased from Sigma-Aldrich and Acros Organics, respectively. Phosphate

buffer saline (PBS) solution was purchased from R&M Chemicals. Protocatechuic acid (PCA) (≥97%) was purchased from Sigma-Aldrich. All reagents used were of analytical grade.

Preparation of *G. mangostana* fruit peels extract

GM peels were collected and washed thoroughly with tap water to remove dirt. The peels were washed again with distilled water before drying in an oven at 40°C. All the peels were ground into fine powder using an electrical blender and stored in an air-tight bottle at room temperature for future use. When needed, fruit peels extract was prepared using fine powder of GM (0.5 g) added into 20 ml of deionised water and stirred at 60°C for 30 min. Crude peels extract was filtered and used for the synthesis of NPs.

Synthesis of gold nanoparticles

AuNPs was synthesized based on our previous work with slight modification in which the synthesis parameters were optimised to obtain AuNPs so that the size and shape is suitable to act as the core of Au-AgNPs (Lee et al., 2016; Lee et al., 2017). AuNPs were used as the core NPs for the formation of Au-AgNPs which is described below. 2 ml of 10 mM $HAuCl_4$ was mixed with 20 ml of GM crude peels extract that was heated at 45°C with pH 4. Colour change of the reaction was observed and recorded. AuNPs was characterised as shown in Supplementary Data A.

Synthesis of gold-silver core-shell nanoparticles

Au-AgNPs were synthesized through seed-mediated method adapted by Wang et al. (2016) with slight modification. A series of mixture (10 ml) was prepared by mixing different ratio of the AuNPs seeds solution with 7.5 mM $AgNO_3$ aqueous solution. After that, 10 ml of 25 mg/ml GM crude extract was added immediately into the mixture. The reaction system was stirred continuously with 500 rpm for 5 h. Temperature of the reaction system was kept constant at 45°C in a water bath. The colour change of solution was observed and UV-vis analysis was carried out instantly after the reaction.

Loading of protocatechuic acid into gold nanoparticles and gold-silver core-shell nanoparticles

10 ml of Au-AgNPs and AuNPs suspensions were added into 50 ml of 5 mg/ml PCA aqueous solution. The reaction was mixed under ultra-sonication (30 amplitudes) for 1 h with 1 s on and off to improve the interaction between PCA and NPs. The obtained drug-loaded NPs (AuPCA and Au-AgPCA) were centrifuged and washed repeatedly three times before drying in an oven for further characterization.

Characterisation of gold nanoparticles and gold-silver core-shell nanoparticles

The formation of AuNPs and Au-AgNPs were determined by UV-visible Spectrometer (Shimadzu UV-2600) in the range of 300–800 nm. Morphology, size and distribution of the samples were captured by high-resolution transmission electron microscope (HR-TEM, JEM-2100F). Surface morphology of the NPs was observed using field emission scanning microscope (JEOL-FESEM, model JEM-2100F) at accelerating voltage of 15 kV and working distance of 21–22 nm. EDX system (OXFORD) with XMAX 50 detector was used to obtain the EDX result. Elemental composition of the samples was measured using AXIS-ULTRA (Kratos Analytical). Functional groups present in the synthesized NPs were determined using Fourier transform infrared spectroscope (Shimadzu IRTracer-100). NETZSCH STA 449F3 STA449F3A-1108-M was used to conduct thermogravimetric analysis (TGA) to determine the loading of drug on the NPs. Zeta potential and hydrodynamic radius of the samples were recorded using Anton Paar Litesizer 500. 10 drops of all the samples were diluted with 3 ml of PBS (pH 7.4) before running the zeta potential test.

Drug release

5 mg PCA-loaded NPs were suspended in 5 ml PBS adjusted to pH 5.0 (mimicking the intratumoural acidic pH) placed into dialysis bags with the two ends tied) (Walker and Walker 1992; Jain 2017). The dialysis bags were immersed fully into 40 ml of PBS with constant stirring of 100 rpm. The whole system was incubated at 37°C. 1 ml aliquot was sampled from the system at chosen time intervals (0, 15, 30, 45 min, 1, 2, 3, 4, 6, 8, 10, 24, and 26 h) for analysis. After the removal of aliquot, an equal volume of fresh medium was immediately replenished to keep the volume constant. The collected samples were then analysed using UV-visible spectrometer at 250 nm. All of the experiments were repeated in triplicate.

Cell culture

HCT116 (ATCC CCL-247) colorectal carcinoma and CCD112 (ATCC CRL-1541) colon normal cell lines were purchased from American Type Culture Collection (ATCC, United States). Both cell lines were maintained in Dulbecco's Modified Eagle's medium (DMEM) supplemented with 10% fetal

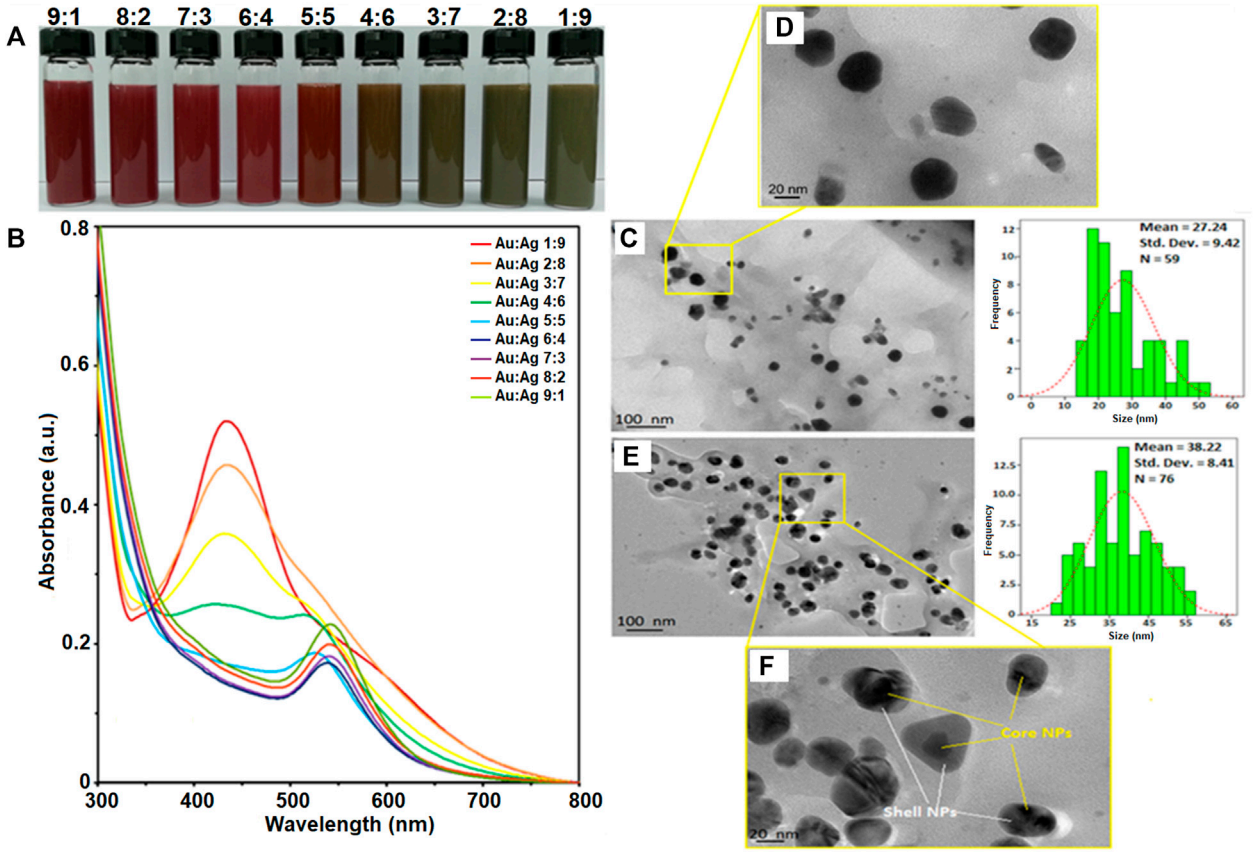

FIGURE 1
Characterisation of gold-silver core-shell nanoparticles (Au-AgNPs). **(A)** Colour changes of reaction, **(B)** UV-vis spectra of the sample at different ratios of Au:Ag, **(C)** Size and shape of sample Au:Ag 9:1 by TEM image, **(D)** Zoomed in TEM image of sample Au:Ag 9:1, **(E)** Size and shape of sample Au:Ag 1:9 by TEM image and **(F)** Zoomed in TEM image of sample Au:Ag 1:9.

bovine serum (FBS) (Gibco) and 1% penicillin/streptomycin (Gibco). CellTiter 96 Aqueous One Solution or MTS reagent (#G3582, Promega) was purchased to evaluate the cytotoxicity of AuNPs, Au-AgNPs and Au-AgPCA NPs on the cell lines as described below.

Cytotoxicity assay

To determine the cellular killing effect of AuNPs, Au-AgNPs, and Au-AgPCA NPs, MTS assay (Promega) was performed according to the manufacturer's instruction with slight modification as previously described by our group (Sukri et al., 2019). Briefly, 5,000 HCT116 and CCD112 cells per well (100 µl/well) were seeded onto a 96-well plate and incubated overnight at 37°C in a 5% CO_2 incubator. The next day, 2-fold serially diluted NPs (250, 125, 62.5, 31.3, 15.6, 7.8, 3.9, 0 µg/ml) (100 µl/well) were added into the wells and the plate was incubated for 72 h at 37°C in the 5% CO_2 incubator. Then 20 µl MTS reagent per well was added into the plate and incubated for additional 3 h at 37°C in the 5% CO_2 incubator. The optical density (OD) was then measured at 490 nm using a multimode microplate reader (Tecan). The dose-response graph was plotted by calculating the percent cell viability using the formula below:

$$\%\,\text{Cell viability} = \frac{\text{mean}\,(\text{OD}_{\text{sample}} - \text{OD}_{\text{blank}})}{\text{mean}\,(\text{OD}_{\text{control}} - \text{OD}_{\text{blank}})} \times 100 \qquad (1)$$

In addition, the inhibitory concentration causing 50% growth inhibition (IC_{50} value) was also determined using an online calculator (https://www.aatbio.com/tools/ic50-calculator).

Live/dead cell staining

Live/dead cell staining assay was performed as described previously with some modifications (Yusefi et al., 2021).

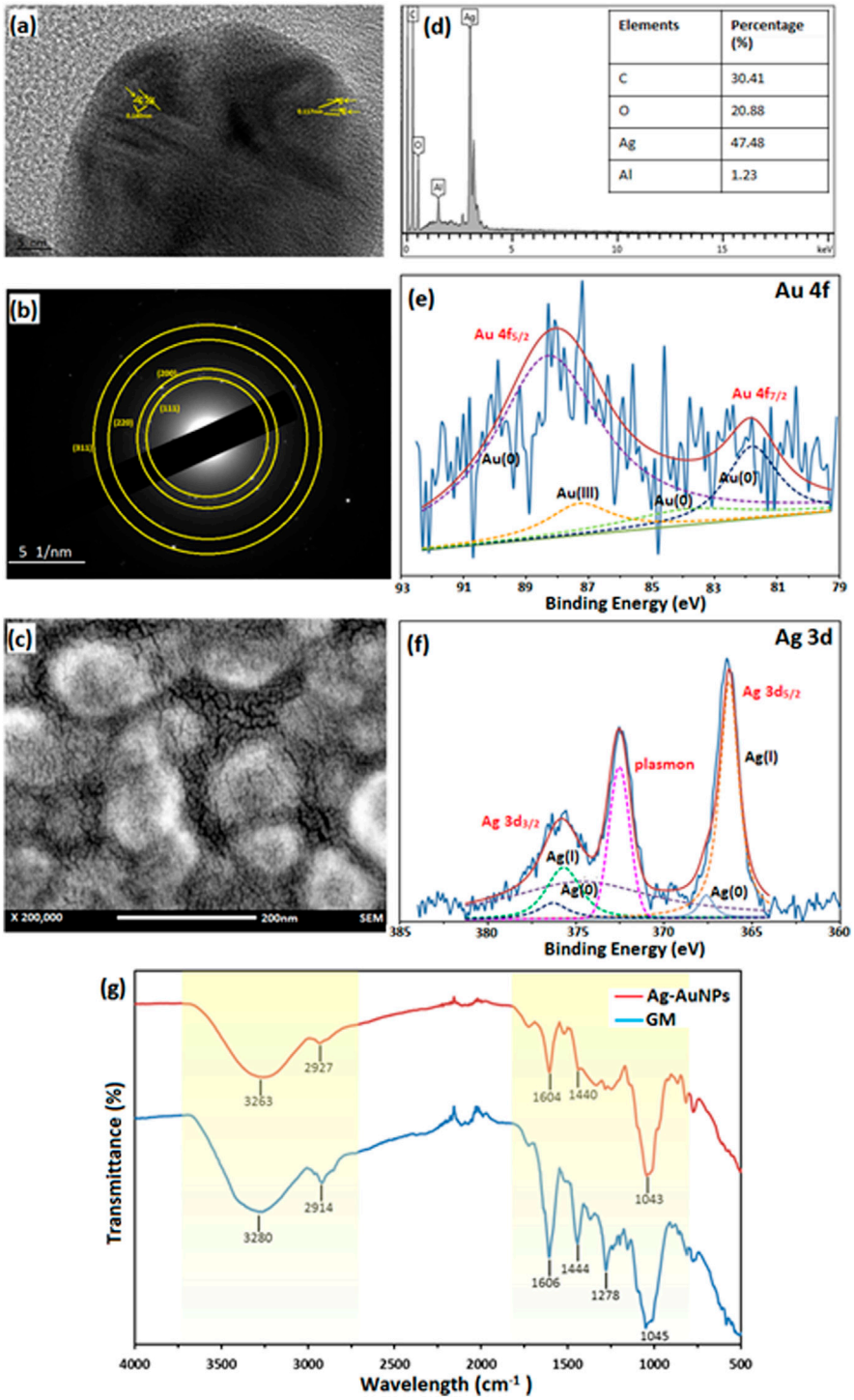

FIGURE 2
Characterisation of sample Au:Ag 1:9. **(A)** Lattice spacing of TEM image, **(B)** SAED of Au-AgNPs, **(C)** FESEM image of Au-AgNPs, **(D)** EDX spectra, **(E)** XPS spectra of Au-AgNPs (Au 4f band), **(F)** XPS spectra of Au-AgNPs (Ag 3d band), and **(G)** FTIR spectrum of Au-AgNPs and GM extract.

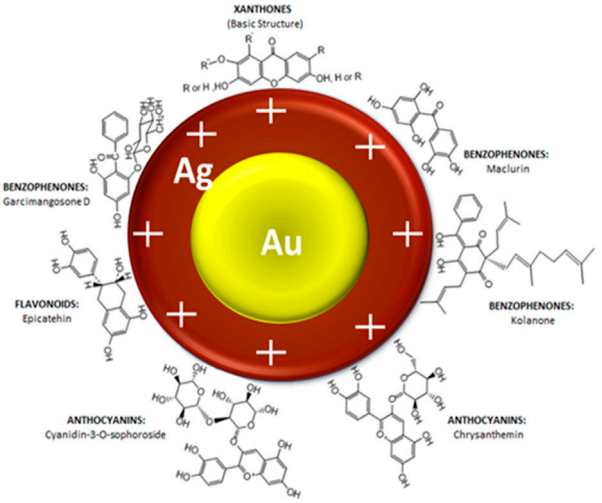

FIGURE 3
Schematic illustration of interaction between Au-AgNPs and the active functional groups present in GM peels extract.

HCT116 and CCD112 cells were seeded and treated with 15 μg/ml PCA, Au-AgNPs, and Au-AgPCA, respectively as described above. After 72 h, the live/dead cell status of treated cells were stained with 0.5 μM Calcein AM (#C1430, Invitrogen) and 50 μg/ml propidium iodide (PI) (#556463, BD Pharmingen) for 1 h at 37°C before viewing under the inverted fluorescence microscope (Nikon Eclipse Ti-S, Japan). Calcein staining was observed using green fluorescence filter (excitation maximum 388 nm, emission maximum 530 nm) while PI staining was observed using red fluorescence filter (excitation maximum 535 nm, emission maximum 617 nm). Images were captured at different magnification and overlaid using the Nikon NIS-Elements (Japan) microscope imaging software.

Statistical analysis

Independent experiments were repeated at least three times, and the data were expressed as mean ± standard deviation for all triplicates within an individual experiment. Data were analysed using a Student's *t*-test. $p < 0.05$ was considered significant.

Results and discussion

Synthesis and characterisation of gold-silver core-shell nanoparticles

Gold-silver core-shell nanoparticles (Au-AgNPs) was synthesized *via* seed germination method. AuNPs seed synthesised was discuss in our first paper where AuNPs was synthesized using GM peel extract through bottom up synthesis. In this study, different concentration of GM peel extract was reacted with $HAuCl_4$ to form circular NPs (Lee et al., 2017; Lee et al., 2019). The synthesis method was optimised to produce AuNPs nano-seed as shown in Supplementary Data A (Baran et al., 2021a). Au nanoseed was synthesized firstly and mixed with silver nitrate ($AgNO_3$) to form core-shell NPs. Figure 1 shows the colour changes in the reaction, UV-vis spectra of Au-AgNPs at different ratios, and TEM images of Au:Ag 1:9 and Au:Ag 9:1 samples. Colour changes were observed when different ratios of AuNPs and $AgNO_3$ reacted as shown in Figure 1A. The colour changes depended on the amount of $AgNO_3$ solution, wherein the colour changed from wine red to brown, and then to greyish brown following the increased amount of $AgNO_3$. Ag^+ ions dissociated and reacted with AuNPs, fresh GM extract was then added to reduce the Ag^+ into Ag^0. A layer of Ag shell was absorbed onto the Au seeds and grew epitaxially (Wang et al., 2016).

Au-AgNPs solution was generated and analysed by UV-visible spectroscopy to confirm the formation of core-shell NPs. Figure 1B shows the UV-vis spectra of Au-AgNPs synthesized at different ratios of Au:Ag. At the ratio of 9:1 (Au:Ag), a sharp peak at 544 nm was observed. This peak corresponds to AuNPs peak which is in accordance with the AuNPs previously synthesized by our group (Lee et al., 2017). The complete characterization data of AuNPs is shown in Supplementary Data A. At the ratio of 6:4 (Au:Ag), the intensity of peak dropped and the absorption band broadened. The increased peak intensity suggested the increase of particle size or possible aggregation (Wang et al., 2016). At ratio 4:6, 3:7, and 2:8, the UV-vis spectra showed two plasmon bands: one broader plasmon band at 430 nm and another weak shoulder band at 519 nm, indicated the initiation of Au_{core}/Ag_{shell} NPs formation which is consistent with previous finding (Zhang et al., 2013). A peak at 430 nm is corresponded with AgNPs while 519 nm is corresponded with AuNPs (Lee et al., 2017; Baran et al., 2021b), and started to form as shown for sample 3:7 and 2:8 (Figure 1B). The difference between UV profile of 4:6 and 3:7 suggested that pure silver critical shell thickness was exceeded and hence, a peak started to form at 400–500 nm (Zhang, Okuni, and Toshima 2011). As the ratio of Ag increased to 1:9, a sharp plasmon band at 434 nm was recorded and the Au plasmon at 544 nm disappeared. When AgNPs was successfully coated around AuNPs seed, the surface plasmon resonance (SPR) band of AuNPs was sealed by the AgNPs. Hence, UV-vis spectrophotometer could only detect the SPR signal of AgNPs (Zhang et al., 2013). Therefore, this result of sample 1:9 suggested that Ag was successfully coated around Au seed, assuming that the coating was continuous and uniform. The increased peak intensity of Ag for sample 1:9 suggested that the particles were well-dispersed through the shell deposition process and the NPs formed corresponded to the Ag characteristics (Lu et al., 2013; Berahim et al., 2018).

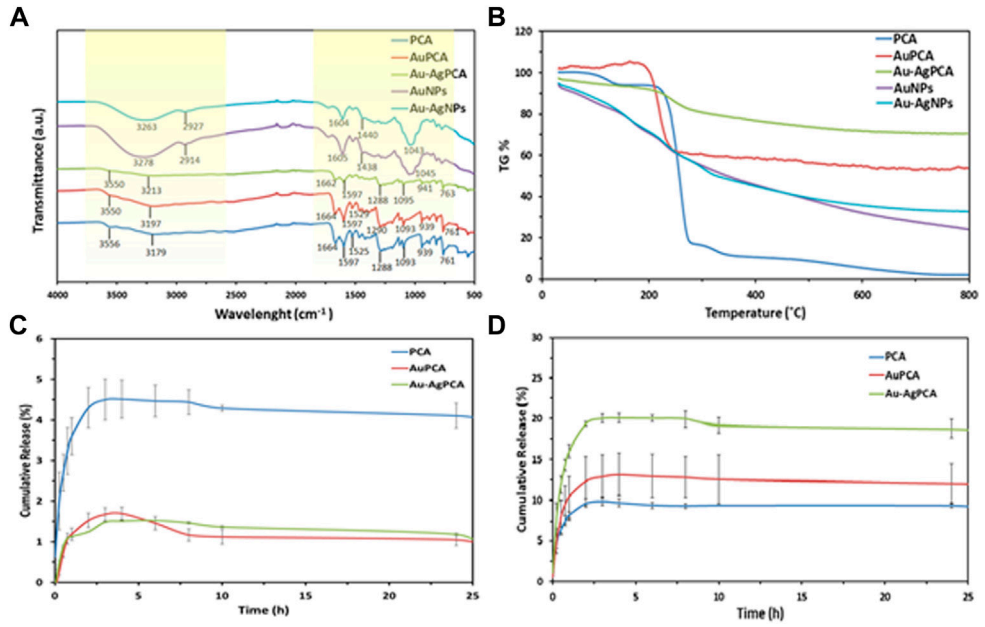

FIGURE 4
Drug loading of AuPCA and Au-AgPCA based on **(A)** FTIR, **(B)** TGA and **(C)** drug release of AuPCA and Au-AgPCA at pH 7 and **(D)** pH 5.

Therefore, sample Au:Ag 1:9 was chosen for further analysis of the purity, shape and size.

Figure 1C shows the sample of Au:Ag 9:1 where most of the NPs were spherical in shape with some irregular and rod shape. The average size of the Au-AgNPs was 27.24 nm, which was bigger than the AuNPs (17.95 nm in size after optimisation). Even smaller NPs (10–15 nm) were also observed which could consist of the AgNPs that were not fully coated on the surface of Au seed. When the ratio of Ag increased to 9, the size of Au-AgNPs increased to 38.22 nm as shown in Figure 1E. The distribution and size of the NPs was more uniform for sample Au:Ag 1:9 as compared to 9:1. This result was in line with the previous report which demonstrated that Au-AgNPs formed spontaneously *via* self-organisation (Zhang et al., 2013; Prabhawathi et al., 2019). Well-separated core-shell NPs were observed in Figure 1F. NPs were properly capped in which a darker spot was observed in the centre while a lighter shell was observed surrounding the darker spot. The observation on Au:Ag 1:9 was similar to a previous study showing the formation of core-shell NPs (Karthika et al., 2017). These findings showed that GM extract can act as a reducing agent for the synthesis of core-shell Au-AgNPs with desired particle size as compared to previous studies in which chemical method were adopted (Gheorghe et al., 2011; Lu et al., 2013; Tripathy et al., 2017).

The sample Au:Ag 1:9 was further analysed to determine the physicochemical properties of core-shell NPs as shown in Figure 2. Lattice spacing of the sample Au:Ag 1:9 resulted in the measurement of 1.40 Å and 1.17 Å, respectively as shown in Figure 2A. The measurement corresponded to plane (220) and (222) of fcc structure, respectively. The metallic property of Au-AgNPs was further supported by SAED result in Figure 2B. Ring patterns that can be indexed to (111), (200), (220), and (311) were obtained and the result was in line with the database on JCPS file no. 00-004-0783 and 00-004-0784 (Saikia et al., 2018). Using XRD peak values, a crystal size of 24.55 nm were calculated according to the Debye-Scherrer equations with the formulation of $[D = K\lambda/(\beta\cos\theta)]$ where D is the particle size, K is the constant (0.9), λ is the X-ray wavelength value (1.5418 Å), β is the value of peak at maximum height and θ is the Bragg angle of the highest peak (Baran et al., 2021a). The slightly smaller in size is due to the presence of some smaller NPs of Ag that is not filly coated on the AuNPs surface. Since AuNPs and AgNPs are crystallite fcc structure in nature, therefore they have a similar lattice spacing and planes (Sapkota and Han 2017).

From the field emission scanning electron microscopy (FESEM) image in Figure 2C, core-shell NPs were spherical in shape and well-dispersed without agglomeration. EDX analysis recorded 47.48% of Ag on the surface of the NPs which suggested that AgNPs was coated uniformly around the core (Figure 2D). Traces of carbon and oxygen that were recorded on the surface of the Au-AgNPs also suggested that GM matrix acts as the stabilising agent in the reduction process.

In Figures 2E,F, the deconvolution of X-ray photoelectron spectroscopy (XPS) confirmed the presence of Au and Ag

TABLE 1 Mass loss and drug loading capacity of PCA, AuPCA and Au-AgPCA.

Sample	Mass loss at 348.7°C (%)	Drug loading capacity (%)
PCA	88.28	—
AuPCA NPs	40.67	40.67
Au-AgPCA NPs	21.26	21.26

PCA, protocatechuic acid; NPs, nanoparticles; AuPCA, Gold NPs loaded with protocatechuic acid; Au-AgPCA, Gold-silver NPs loaded with protocatechuic acid.

TABLE 2 Zeta potential and hydrodynamic radius of NPs.

Sample	Zeta potential (mV)	Hydrodynamic radius (nm)
Au NPs	−23.7	219.8
Ag NPs	−21.4	249.5
Au-Ag NPs	−25.8	275.4
Au-AgPCA NPs	−21.3	249.5

through a doublet representing Au $4f_{5/2}$ and Au $4f_{7/2}$ in the metallic 4f band of Au with binding energy of 88.1 and 83.74 eV (Sylvestre et al., 2004; Sapkota and Han 2017). Deconvoluted Au 4f spectra consisted of four peaks which corresponds to Au^{3+} (87.3 eV) and Au^0 (88.3, 83.9, and 81.8 eV) (Sylvestre et al., 2004; Bhandari et al., 2011). Other than that, two peaks that represented Ag 3d band were observed with binding energy of 375.9 eV (Ag $3d_{3/2}$) and 366.3 eV (Ag $3d_{5/2}$). Two peaks were attributed to Ag $3d_{3/2}$ that were Ag+ and Ag^0 with the binding energy of 375.7 and 374.7 eV respectively (Zhang et al., 2014; Kumar-Krishnan et al., 2015). Another two peaks that attributed to Ag $3d_{5/2}$ were 366.3 eV for Ag+ and 367.6 eV for Ag^0 (Shen et al., 2015). This result suggests that most of the Ag exist in ionic state and part of them had been reduced to metallic AgNPs (Kumar-Krishnan et al., 2015). Plasmon was observed at 372.5 eV, it is related to the energy loss when the photoelectron interacted with other electrons.

Lastly, FTIR results in Figure 2G further supported that GM matrix reacts closely in the stabilising process. The major stretching appeared at the region of 3,000–3,500 cm^{-1} and 1,000–1,600 cm^{-1} for both GM peels and Au-AgNPs. Stretching at 3,263 cm^{-1} (Au-AgNPs) and 3,280 cm^{-1} (GM) are related to O-H functional group. A shifting was observed at this region for Au-AgNPs suggested that this group involved in the reduction and capping of the core-shell NPs (Sapkota and Han 2017). At 2,914 cm^{-1} (GM) and 2,927 cm^{-1} (Au-AgNPs) presence of C-H bond in xanthone and other compounds in the peels extract (El-Naggar et al., 2016) were detected. On the other hand, peaks around area 1,606 and 1,444 cm^{-1} for both GM and Au-AgNPs were associated with C=C aromatic ring structure (Wang et al., 2016). Finally, C-O-C stretch can be found in the range of 1,000–1,300 cm^{-1} where the peak at 1,278 cm^{-1} for GM disappeared after the reaction with Au-AgNPs (Sathiyanarayanan et al., 2014). All of the above analysis suggested that GM peel extract reacted closely to form and stabilise the NPs (Shankar et al., 2004).

A schematic illustration of the stabilised Au-AgNPs is shown in Figure 3 based on the known organic compounds present in GM peels extract. FTIR analysis suggested that hydroxyl groups are involved closely in the stabilisation of Au-AgNPs. Surface of the core-shell NPs is speculated to be positively charged in order for hydroxyl groups to stabilise the NPs as supported by the finding from FTIR. Since the surface of Au-AgNPs is speculated to be positively charged, the loading of PCA could took place at the–COOH groups (Barahuie et al., 2015) (Effective cancer treatment by targeted pH sensitive–gold nanoparticles without using laser irradiation).

Drug loading and drug release study

Protocatechuic acid (PCA) was loaded into the synthesized AuNPs and Au-AgNPs through sonication method to improve the interaction between PCA and surface of the NPs. The successful loading of PCA was shown by UV-vis spectroscopy where two peaks corresponding to PCA were observed at 251 and 288 nm as shown in Supplementary Data B. Peaks at the range of 225–325 nm were highlighted and enlarged because the samples were diluted so that the loading peaks could be recorded. The PCA-loaded NPs were then analysed by FTIR and thermogravimetric analysis (TGA). FTIR spectra of PCA, PCA-loaded AuNPs (AuPCA) and PCA-loaded Au-AgNPs (Au-AgPCA) were studied as shown in Figure 4A to

TABLE 3 Kinetic study assessment of AuPCA and Ag-AuPCA based on various kinetic mathematical models.

Sample	Correlation coefficient of model (R^2)				
	Zero order	First order	Hixon-Crowell	Higuchi	Korsmever-Peppas
AuPCA NPs	0.7507	0.7662	0.7603	0.9628	0.9448
Au-AgPCA NPs	0.7338	0.7791	0.7638	0.9606	0.9714

NPs, nanoparticles; AuPCA, Gold NPs loaded with protocatechuic acid; Au-AgPCA, Gold-silver NPs loaded with protocatechuic acid.

TABLE 4 IC_{50} values of mangosteen extract, protocatechuic acid, and nanoparticles against two cell lines.

Cell line	IC_{50} (μg/ml)					
	GM extract	PCA	Au NPs	Au PCA NPs	Au-AgNPs	Au-AgPCA NPs
HCT116 (cancer)	35.74	148.09	82.99	>250	24.36	10.78
CCD112 (normal)	49.58	224.39	>250	>250	27.48	43.48

GM, *Garcinia mangostana*; IC, inhibitory concentration; PCA, protocatechuic acid; NPs, nanoparticles; AuNPs, Gold NPs; AuPCA NPs, Gold NPs loaded with protocatechuic acid; Au-AgNPs, Gold-silver NPs; Au-AgPCA NPs, Gold-silver NPs loaded with protocatechuic acid.

understand the interactions between the functional groups of PCA and the NPs that occurred during the loading process. Clear differences were observed between the spectra of bare NPs and PCA-loaded NPs. The spectrum of PCA-loaded NPs was comparable to PCA spectrum suggesting that the reaction occurred between PCA and NPs. O-H stretch was observed around the region of 3,200 and 3,550 cm^{-1} for all of the three samples. Shifting from 3,179 to 3,213 cm^{-1} occurred for sample Au-AgPCA and the reduced intensity of 3,213 cm^{-1} stretch suggested that hydrogen bonding occurred between the drug and Au-AgNPs nanocarrier (Usman et al., 2018b). The peaks at 1,288 and 1,664 cm^{-1} were attributed to C=O stretching of carboxylic group for all three tested samples (Barahuie et al., 2013). Slight shifting and decrease in intensity also occurred to the 1,288 cm^{-1} band after loading with different NPs. This is due to the occurrence of hydrogen bonding between PCA and the NPs (Usman et al., 2018a). Peaks at the region of 1,525 and 1,597 cm^{-1} for all three samples were attributed to aromatic C=C bands (Xu et al., 2018). 1,093–1,095 cm^{-1} for C=O bond was observed in the FTIR spectra of all samples (Usman et al., 2018b). Similarly, reduced intensity was observed at 941 cm^{-1} for Au-AgPCA. The reduced intensity and shifting at 939 cm^{-1} suggests that the reaction took place between the–COOH groups of PCA and NPs (Barahuie et al., 2015). Finally, peaks at 761–763 cm^{-1} corresponded to C-H bonding of all samples (Saifullah et al., 2018).

Figure 4B demonstrates the thermal analysis of the bare NPs, PCA, and PCA-loaded NPs. Bare NPs showed gradual weight loss due to the gradual combustion of metallic NPs. PCA showed three main weight loss stages. The first weight loss stage (4.64%) corresponded to the loss of absorbed water at 138°C based on a previous study (Barahuie et al., 2015). Second stage of weight loss (77.64%) occurred at 200°C–299°C. This was related to the decomposition combustion of PCA (Barahuie et al., 2013). The last stage of weight loss (6%) occurred at the region of 299°C–350°C which was due to the decomposition of PCA residue (Usman et al., 2018a). The weight loss of PCA ended at 348.7°C. Drug-loaded NPs only showed a single stage of weight loss at the region of 240°C–299°C which was due to the combustion of PCA. The drug-loaded NPs appeared to be more thermally stable as compared to PCA. The TGA result suggested that the stability of PCA increased after being loaded on the nanocarriers.

From the TGA findings, encapsulation efficiency and drug loading efficiency were calculated as shown in Table 1. Mass loss of each of the samples was determined at 348.7°C. AuNPs have a higher loading with PCA (40.67%) mainly due to its multisurface functionality (Ovais et al., 2017). The drug loading capacity of Au-AgNPs was lower (21.26%), this is because AuNPs were fully coated by AgNPs, hence reducing the loading property of the Au-AgNPs.

As shown in Figures 4C,D, the release of PCA was observed under neutral condition (pH7.4) and a slightly acidic condition (pH 5.0), which mimics the tumour microenvironment with actively proliferating tumour cells. Based on Figure 4C, the released was completed in about 5 h. For PCA the maximum released was 4.5%, while for AuPCA and Au-AgPCA was 1.7% and 1.5% respectively. Based on Figure 4D, the cumulative release percent of AuPCA at pH 5 was 13%. The release rate of Au-AgPCA was faster as compared to the AuNPs with a cumulative release of 20% in

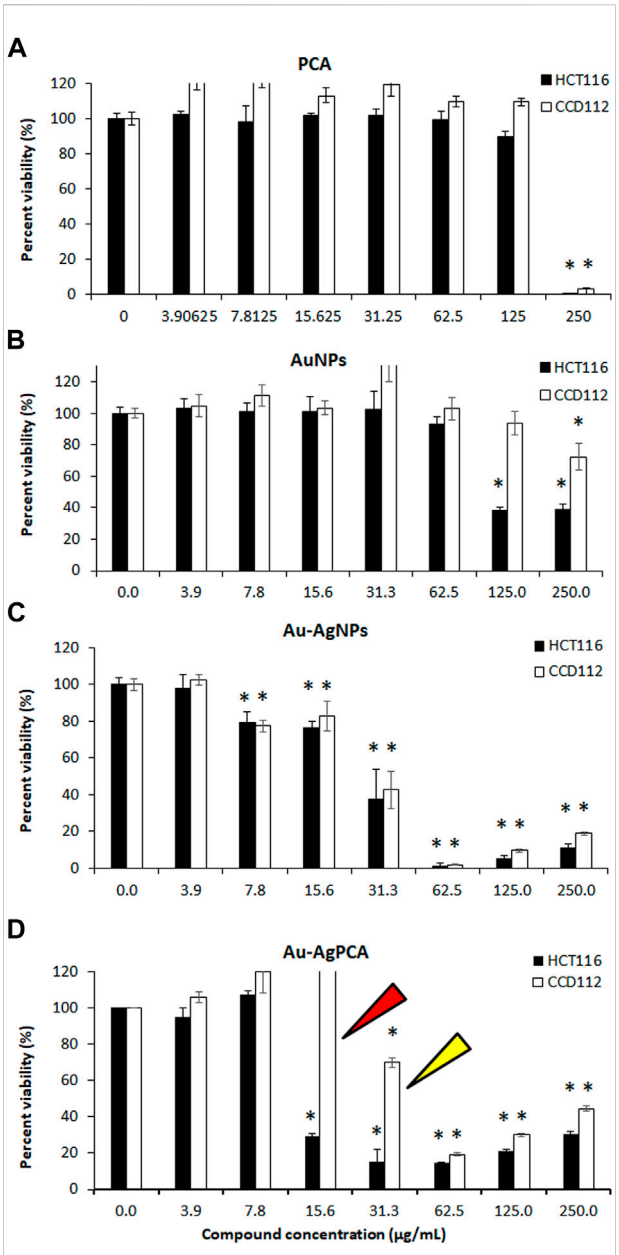

FIGURE 5
Cytotoxic effects of nanoparticles against colorectal cancer (HCT116) and colon normal (CCD112) cell lines. **(A)** protocatechuic acid (PCA); **(B)** AuNPs; **(C)** Au-AgNPs and **(D)** Au-AgPCA. Arrows show specific cytotoxicity of Au-AgPCA on cancer cells but not in normal cells. Data are expressed as mean ± standard deviation for triplicates within an individual experiment. Statistical significance was performed using Student's *t*-test. (*$p < 0.05$).

6 h at pH 5 while AuNPs cumulative release in 6 h is around 13% only. The release of all samples achieved equilibrium after 12 h and no further changes up to 25 h. Sustain release of medication throughout the day (24 h) will reduce the dosage of drug taken. Hence, for nanoparticles drug delivery system, the timing of release is crucial to enable its release at target side continuously instead of dissociate at non-desirable areas (Patra et al., 2018). The cumulative release of the samples at pH 7 is much lower than pH 5, suggesting that the samples could target cancerous cells at specific pH environment (Yew et al., 2019). Ag-AuPCA suggest a passive targeting pathway by direct chemical conjugation where the drug carrier complex circulates in bloodstream and driven to target side by the influence of pH (Lu et al., 2016) Burst release was observed in all samples at the first 15 min as shown in Figure 4D. This phenomena indicates that PCA was weakly bound or adsorbed on the large surface area of the NPs (Villaverde 2011; Barahuie et al., 2015). After that, the remaining PCA were released in a gradual and sustained manner for about 6 h before reaching plateau. The continual release of PCA in Au-AgNPs was due to drug diffusion and surface erosion of the NPs (Duzgunes 2012). This could be explained by the hydrogen bonding between PCA and Au-AgNPs as shown by FTIR earlier (Usman et al., 2018a; Usman et al., 2018b). PCA solution that acts as a control had a rapid release and completed the process in about 3 h with a cumulative release of 9.7% as shown in Figure 4D. Rapid release of PCA occurred because the PCA was dispersed freely in the system.

Table 2 shows the zeta potential and hydrodynamic radius of various NPs. All NPs possessed negatively charged surface which is consistent with the FTIR data that suggested hydroxyl groups took part in the stabilisation of the NPs, forming an anions layer on the NPs surface (AL-Jawad et al., 2019). All of the NPs are considered stable as for a suspension system, zeta potential value of ±20 mV is enough because of the present of combined electrostatic and steric stabilization among the NPs in the system (Jacobs et al., 2002). The zeta potential of AuNPs (−23.7 mV) and AgNPs (−21.4 mV) decreased to −25.8 mV after the formation of Au-AgNPs, suggesting that electrostatic interactions occurred between the two NPs (Zhang et al., 2020). After the loading of PCA, zeta potential of Au-AgPCA NPs increased to −21.3 mV which suggests the successful coating of PCA on Au-AgNPs following the interaction with–COOH groups as shown by the FTIR data (Jiang et al., 2019). The hydrodynamic radius data showed the increased size of Au-AgNPs (275.4 nm) which supports the formation of core-shell. The reduced hydrodynamic radius of PCA-loaded Au-AgNPs (249.5 nm) indicated that aggregation was unlikely to occur after the drug loading (George et al., 2020). The hydrodynamic radius value is higher than the particles size calculated by TEM because of nanoparticles surface hydration (Martínez et al., 2020). TEM image only gave information about the diameter of the core of the nanoparticles (George et al., 2020). In this case, the NPs are not suitable to measure using particle size analyser because the NPs are in solid form that does not disperse well in solvent. The very high value of hydrodynamic radius suggest that the NPs particles dynamically aggregate and de-aggregate, given the large value result (Eaton et al., 2017).

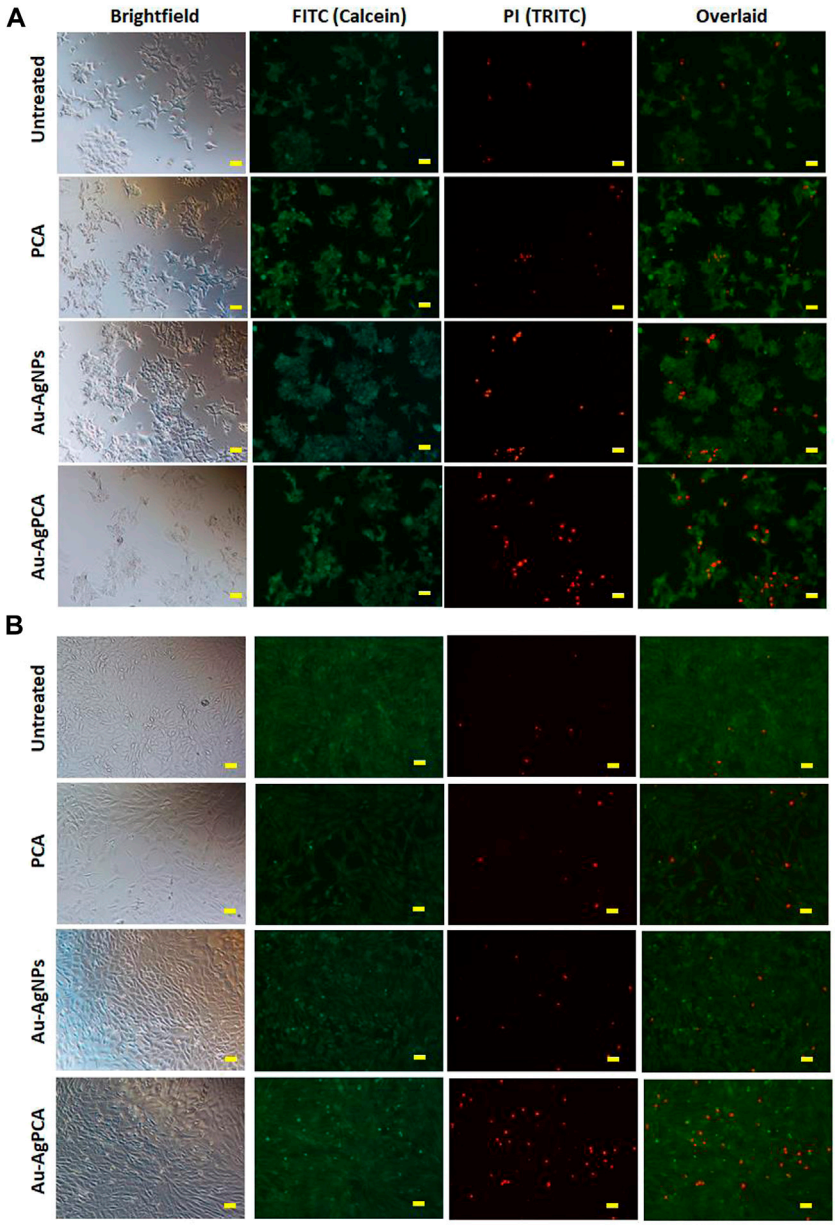

FIGURE 6
Live/dead cells staining. Calcein AM (green: live cells) and propidium iodide (red: dead cells) staining of **(A)** HCT116 and **(B)** CCD112 cells treated with 15 μg/ml PCA, Au-AgNPs, and Au-AgPCA, respectively. Images were captured at ×10 magnification. Scale bar represents 50 μm.

To understand the mechanism and kinetics in the drug delivery, the drug release data was fitted into five mathematical models (zero order, first order, Hixon-Crowell, Higuchi and Korsmeyer-Peppas). Table 3 shows the correlation coefficient of AuPCA and Au-AgPCA fitted into the different models. It was found that the release of AuPCA was well-fitted into the Higuchi method with R^2 of 0.9628. Au-AgPCA also fitted well to this model with R^2 of 0.9606. This model suggested that the release of PCA occurred *via* diffusion based on the Fick's Law (Nivethaa et al., 2015). The release data were then fitted into Korsmeyer-Peppas model to understand more about the dissolution mechanism. The R^2 for all tested samples were in the range of $0.5< n < 1$ indicating that the drug were released through both diffusion and erosion controlled (non-fickian) method (Safwat et al., 2018). Dissolution-filling approach occurred as PCA gradually released and diffused from the NPs that carried them (Farooq et al., 2018).

In vitro anticancer study

Cytotoxic effect of GM peels extract, PCA and other NPs was determined against colon-derived HCT116 (cancer) and CCD112 (normal) cells up to 250 μg/ml. Table 4 shows the determined IC_{50} values for all tested compounds. AuNPs and Au-AgNPs showed cytotoxic effects against HCT116 cells with IC_{50} of 82.99 and 24.36 μg/ml, respectively. When combined with PCA, the IC_{50} values were further reduced except for AuNPs. This result suggested that combining AgNPs and Au-AgNPs with PCA was beneficial in killing the HCT116 cells. AuPCA below 250 μg/ml did not show any cytotoxic effects against both colon cell lines.

To examine the selectivity, those NPs which showed lower IC_{50} values in HCT116 compared to CCD112 cells (AuNPs, Au-AgNPs and Au-AgPCA) were selected and replotted as depicted in Figure 5. Overall, dose-dependent inhibitions were observed in the three NPs. However, the level of cytotoxic effect in HCT116 and CCD112 did not show any difference in Au-AgNPs in most of the tested concentrations. As seen in Table 4, AuNPs alone did not kill CCD112 cells up to 250 μg/ml. However the core-shell Au-AgNPs killed both HCT116 and CCD112 cells almost equally. This killing effect might have attributed to the AgNPs as previously described by our group which showed IC_{50} of 40.2 and 47 μg/ml against HCT116 and CCD112 cells, respectively (Lee et al., 2019). Another possible explanation might be the free Ag^{+} ions which have caused such non-specific toxicities. In contrast, AuNPs and Au-AgPCA in some of the tested concentrations showed higher cytotoxic effect in HCT116 compared to CCD112. This result suggests the selectivity of the NPs which is consistent with previous findings (Dykman and Khlebtsov 2012). Interestingly, 15.6 μg/ml Au-AgPCA could kill almost 70% of HCT116 while did not affect the CCD112 cells (shown by a red triangle in Figure 5C). At 31.3 μg/ml, Au-AgPCA showed lower inhibition (30%) towards CCD112 as shown by a yellow triangle. At 15.6 and 31.3 μg/ml, the PCA drug alone did not affect the cell viability of both HCT116 and CCD112 cells. This suggests that Au-AgPCA exibit a better drug specificity against normal cells even at higher dosage and highlights that core-shell NPs has high potential in cancer teatment compared to monometallic NPs (Ghosh Chaudhuri and Paria 2011). Consistent with Figure 5D, live/dead staining of HCT116 (Figure 6A) showed that 15 μg/ml Au-AgPCA killed larger portion of cells (indicated by PI staining and low density of cells in brighfield), but most of the treated CCD112 normal cells remained unharmed as shown in Figure 6B (high density of cells in brightfield). As expected, 15 μg/ml PCA did not affect cell viability of both HCT116 and CCD112 cells which showed similar staining pattern with untreated cells. Meanwhile, 15 μg/ml Au-AgNPs exhibited relatively higher killing in HCT116 cells compared to PCA and untreated, but this was not observed in CCD112 cells.

In short, Au-AgPCA performs better as an anticancer agent against colon cancer cells and meanwhile, it is more specific towards cancerous cells than normal cells. This could be partly attributed to the selectivity of both PCA and AuNPs which showed higher cytoxicity effects against the cancer cells than the normal cells (Table 4). The fact that Au-AgNPs has very similar IC_{50} in both cell lines suggested that the combination of Au and AgNPs was not responsible for the selectivity of Au-AgPCA. Our finding is consistent with a previous study in which doxorubicin-loaded Au-AgNPs was shown to delivered to the HeLa cervical cancer cells and 50% inhibition was observed after 24 h incubation (Chen et al., 2016). As previously reported, doxorubicin-loaded Au-AgNPs could also exhibit a better biocompatiblity and enhanced intracellular binding ability towards the cancerous cells compared to monometallic NPs, hence improving their *in vitro* anticancer action compared to free drug (Jiang et al., 2019). Previous studies have reported that Ag/Au bimetallic NPs could kill HCT116 cells by inducing apoptosis (Katifelis et al., 2022). The triggered apoptosis in HCT116 cells may also be contributed by Ag and Au ions from Ag NPs (Satapathy et al., 2013; Sufyani et al., 2019) and Au NPs (Maddah et al., 2022), respectively. Similarly, apoptosis induction of Ag-NPs was also seen in another colorectal cancer cell line, HT-29 cells (Bao et al., 2022). Besides that, the apoptosis may be also caused by the loaded PCA as previous reports have shown that PCA could trigger apoptosis in another colon cancer cells, CaCo-2 cells (Acquaviva et al., 2021) as well as other cells including breast, lung, liver, cervix and prostate cancer cells (Yin et al., 2009). Other possible pathways that might lead to the cancer cell killing include lactate dehydrogenase leakage (LDH), reactive oxygen species (ROS) generation, impairment of mitochondrial function and DNA damage (Gurunathan et al., 2018).

Conclusion

This study highlights the green synthesis of Au-AgNPs using *G. mangostana* fruit peel extract and its potential use as a non-toxic nanocarrier for drug delivery. Uniformly distributed spherical shaped Au-AgNPs that is 38 nm was formed when the ratio of Au:Ag was 1:9. The success loading of PCA on the nanoparticles was due to the interaction between–COOH groups of PCA and the nanoparticles. Then, PCA was released from the nanoparticles through both diffusion and erosion controlled based on mathematical models. 15.6 μg/ml Au-AgPCA showed potent inhibition (70%) against colon cancer cell line, HCT116 and remained non-toxic to colon normal cells, CCD112. This highlights the high cancer cell selectivity of Au-AgPCA. At same concentration, both HCT116 and CCD112 did not respond to PCA. Therefore, core-shell Au-AgNPs appear to be an ideal nanocarrier compared to AuNPs and PCA alone in terms of anticancer activity and toxicity.

Data availability statement

The original contributions presented in the study are included in the article/Supplementary Material, further inquiries can be directed to the corresponding authors.

Author contributions

KL: Formal analysis, conceptualization, writing—review and editing. KS: resources, supervision, funding acquisition, review and editing. YN: instrumental analysis, interpretation of results. YY: writing—review and editing. ST: resources, supervision, writing—review and editing and HM: review and editing and financial sponsor. All authors have given approval to the final version of the manuscript.

Funding

This research was funded by a Takasago Thermal Engineering Co. Ltd. grant (R.K130000.7343.4B422) of Universiti Teknologi Malaysia and Malaysia-Japan International Institute of Technology. This work was also partly supported by Sunway University Individual Grant 2022 (GRTIN-IGS-DMS(S)-04-2022).

Acknowledgments

The authors wish to express gratitude to the research management centre of Universiti Teknologi Malaysia and Malaysia-Japan International Institute of Technology for providing an excellent research environment and facilities. Special thanks to the School of Medical and Life Sciences, Sunway University for providing cell culture facilities for measuring anticancer assays.

Conflict of interest

The authors declare that the research was conducted in the absence of any commercial or financial relationships that could be construed as a potential conflict of interest.

Publisher's note

All claims expressed in this article are solely those of the authors and do not necessarily represent those of their affiliated organizations, or those of the publisher, the editors and the reviewers. Any product that may be evaluated in this article, or claim that may be made by its manufacturer, is not guaranteed or endorsed by the publisher.

Supplementary Material

The Supplementary Material for this article can be found online at: https://www.frontiersin.org/articles/10.3389/fmolb.2022.997471/full#supplementary-material

References

Acquaviva, R., Tomasello, B., Di Giacomo, C., Santangelo, S., La Mantia, A., Naletova, I., et al. (2021). Protocatechuic acid, a simple plant secondary metabolite, induced apoptosis by promoting oxidative stress through HO-1 downregulation and p21 upregulation in colon cancer cells. *Biomolecules* 11, 1485. doi:10.3390/biom11101485

Al-Jawad, S. M. H., Taha, M. H., Al-Barram, A. A., and Al-Barram, L. F. (2019). Effective cancer treatment by targeted pH sensitive-gold nanoparticles without using laser irradiation. *J. Sol-Gel Sci. Technol.* 89, 473–485. doi:10.1007/s10971-018-4832-6

Alam, M. N., Das, S., Batuta, S., Roy, N., Chatterjee, A., Mandal, D., et al. (2014). Murraya koenegii spreng. Leaf extract: An efficient green multifunctional agent for the controlled synthesis of Au nanoparticles. *ACS Sustain. Chem. Eng.* 2, 652–664. doi:10.1021/sc400562w

Azizah, A. M., Nor Saleha, I. T., Noor Hashimah, A., Asmah, Z. A., and Mastulu, W. (2016). *Malaysian national cancer registry report*. Malaysia: National Cancer Institute.

Bao, J., Jiang, Z., Ding, W., Cao, Y., Yang, Y., and Liu, J. (2022). Silver nanoparticles induce mitochondria-dependent apoptosis and late non-canonical autophagy in HT-29 colon cancer cells. *Nanotechnol. Rev.* 11, 1911–1926. doi:10.1515/ntrev-2022-0114

Barahuie, F., Hussein, M. Z., Gani, S. A., Fakurazi, S., and Zainal, Z. (2015). Synthesis of protocatechuic acid-zinc/aluminium-layered double hydroxide nanocomposite as an anticancer nanodelivery system. *J. Solid State Chem.* 221, 21–31. doi:10.1016/j.jssc.2014.09.001

Barahuie, F., Hussein, M. Z., Hussein-Al-Ali, S., Arulselvan, P., Fakurazi, S., and Zainal, Z. (2013). Preparation and controlled-release studies of a protocatechuic acid-magnesium/aluminum-layered double hydroxide nanocomposite. *Ijn* 8, 1975. doi:10.2147/ijn.s42718

Baran, A., Baran, M. F., Keskin, C., Valiyeva, M., Mehraliyeva, S., Khalilov, R., et al. (2021a). 'Ecofriendly/rapid synthesis of silver nanoparticles using extract of waste parts of artichoke (*Cynara scolymus* L.) and evaluation of their cytotoxic and antibacterial activities. *J. Nanomater.* 2021, 2270472. doi:10.1155/2021/2270472

Baran, A., Keskin, C., Baran, M. F., Huseynova, I., Khalilov, R., Eftekhari, A., et al. (2021b). Ecofriendly synthesis of silver nanoparticles using ananas comosus fruit peels: Anticancer and antimicrobial activities. *Bioinorganic Chem. Appl.* 2021, 2058149. doi:10.1155/2021/2058149

Bendale, Y., Bendale, V., and Paul, S. (2017). Evaluation of cytotoxic activity of platinum nanoparticles against normal and cancer cells and its anticancer potential through induction of apoptosis. *Integr. Med. Res.* 6, 141–148. doi:10.1016/j.imr.2017.01.006

Benoist, St, and Nordlinger, Nr (2009). The role of preoperative chemotherapy in patients with resectable colorectal liver metastases. *Ann. Surg. Oncol.* 16, 2385–2390. doi:10.1245/s10434-009-0492-7

Berahim, N., Basirun, B., Leo, B., and Johan, M. (2018). Synthesis of bimetallic gold-silver (Au-Ag) nanoparticles for the catalytic reduction of 4-nitrophenol to 4-aminophenol. *Catalysts* 8, 412. doi:10.3390/catal8100412

Bhandari, S., Deepa, M., Joshi, A. G., Saxena, A. P., and Srivastava, A. K. (2011). Revelation of graphene-Au for direct write deposition and characterization. *Nanoscale Res. Lett.* 6, 424. doi:10.1186/1556-276x-6-424

Cai, Y., Luo, Q., Sun, M., and Corke, H. (2004). Antioxidant activity and phenolic compounds of 112 traditional Chinese medicinal plants associated with anticancer. *Life Sci.* 74, 2157–2184. doi:10.1016/j.lfs.2003.09.047

Chatterjee, K., Sarkar, S., Jagajjanani Rao, K. J., and Paria, S. (2014). Core/shell nanoparticles in biomedical applications. *Adv. colloid interface Sci.* 209, 8–39. doi:10.1016/j.cis.2013.12.008

Chen, P., Wang, Z., Zong, S., Zhu, D., Chen, H., Zhang, Y., et al. (2016). pH-sensitive nanocarrier based on gold/silver core-shell nanoparticles decorated multi-walled carbon manotubes for tracing drug release in living cells. *Biosens. Bioelectron.* 75, 446–451. doi:10.1016/j.bios.2015.09.002

Cho, K., Wang, X., Nie, S., Chen, M., and Shin, D. (2008). Therapeutic nanoparticles for drug delivery in cancer. *Clin. Cancer Res.* 14, 1310–1316. doi:10.1158/1078-0432.ccr-07-1441

Duzgunes, N. (2012). *Nanomedicine: Cancer, diabetes, and cardiovascular, central nervous system, pulmonary and inflammatory diseases*. United States: Academic Press.

Dykman, L., and Khlebtsov, N. (2012). Gold nanoparticles in biomedical applications: Recent advances and perspectives. *Chem. Soc. Rev.* 41, 2256–2282. doi:10.1039/c1cs15166e

Eaton, P., Quaresma, P., Soares, C., Neves, C., de Almeida, M. P., Pereira, P., et al. (2017). A direct comparison of experimental methods to measure dimensions of synthetic nanoparticles. *Ultramicroscopy* 182, 179–190. doi:10.1016/j.ultramic.2017.07.001

El-Naggar, M. E., Shaheen, E., FoudaShaheen, I., Hebeish, M. M., and Hebeish, A. A. (2016). Eco-friendly microwave-assisted green and rapid synthesis of well-stabilized gold and core-shell silver-gold nanoparticles. *Carbohydr. Polym.* 136, 1128–1136. doi:10.1016/j.carbpol.2015.10.003

Farooq, A., Ali, S., Cai, A., Tosheva, L., Kelly, P., Whitehead, D., et al. (2018). 'Titania coating of mesoporous silica nanoparticles for improved biocompatibility and drug release within blood vessels. *Acta Biomater.* 76, 208–216. doi:10.1016/j.actbio.2018.06.024

George, J. M., Priyanka, Ra N., and Mathew, B. (2020). Bimetallic Ag-Au nanoparticles as pH dependent dual sensing probe for Mn(II) ion and ciprofloxacin. *Microchem. J.* 155, 104686. doi:10.1016/j.microc.2020.104686

Gheorghe, D. E., Cui, L., Karmonik, C., Brazdeikis, A., Penaloza, J. M., YoungYoung, K., et al. (2011). Gold-silver alloy nanoshells: A new candidate for nanotherapeutics and diagnostics. *Nanoscale Res. Lett.* 6, 554. doi:10.1186/1556-276X-6-554

Ghosh Chaudhuri, R., and Paria, S. (2011). Core/shell nanoparticles: Classes, properties, synthesis mechanisms, characterization, and applications. *Chem. Rev.* 112, 2373–2433. doi:10.1021/cr100449n

Gurunathan, S., Qasim, M., Park, C., Yoo, H., Kim, J., and Hong, K. (2018). Cytotoxic potential and molecular pathway analysis of silver nanoparticles in human colon cancer cells HCT116. *Ijms* 19, 2269. doi:10.3390/ijms19082269

Jacobs, C., Müller, R. H., and Helmut Müller, R. (2002). 'Production and characterization of a budesonide nanosuspension for pulmonary administration. *Pharm. Res.* 19, 189–194. doi:10.1023/a:1014276917363

Jahangirian, H., Ghasemian, T. J., Webster, R., Rafiee-Moghaddam, Y., and Abdollahi, Y. (2017). A review of drug delivery systems based on nanotechnology and green chemistry: Green nanomedicine. *Ijn* 12, 2957–2978. doi:10.2147/ijn.s127683

Jain, A. (2017). 'Colon targeting using pH sensitive materials. *Adv. Res. Gastroenterol. Hepatol.* 8, 1–3. doi:10.19080/ARGH.2018.08.555748

Jiang, P., Hu, Y., and Li, G. (2019). Biocompatible Au@Ag nanorod@ZIF-8 core-shell nanoparticles for surface-enhanced Raman scattering imaging and drug delivery. *Talanta* 200, 212–217. doi:10.1016/j.talanta.2019.03.057

Karthika, V., Arumugam, A., Gopinath, K., Kaleeswarran, P., Govindarajan, M., Alharbi, N. S., et al. (2017). Guazuma ulmifolia bark-synthesized Ag, Au and Ag/Au alloy nanoparticles: Photocatalytic potential, DNA/protein interactions, anticancer activity and toxicity against 14 species of microbial pathogens. *J. Photochem. Photobiol. B Biol.* 167, 189–199. doi:10.1016/j.jphotobiol.2017.01.008

Katifelis, H., Nikou, M-P., Mukha, I., Vityuk, N., Lagopati, N., Piperi, C., et al. (2022). Ag/Au bimetallic nanoparticles trigger different cell death pathways and affect damage associated molecular pattern release in human cell lines. *Cancers* 14, 1546. doi:10.3390/cancers14061546

Kumar-Krishnan, S., Prokhorov, E., Hernández-Iturriaga, M., Mota-MoralesMota-Morales, D., Vázquez-Lepe, M., Kovalenko, Y., et al. (2015). Chitosan/silver nanocomposites: Synergistic antibacterial action of silver nanoparticles and silver ions. *Eur. Polym. J.* 67, 242–251. doi:10.1016/j.eurpolymj.2015.03.066

Lee, K. X., Shameli, K., Miyake, M., Ahmad Khairudin, S. E., Mohamad, H., HaraYew, P., et al. (2017). Gold nanoparticles biosynthesis: A simple route for control size using waste peel extract. *IEEE Trans. Nanotechnol.* 16, 954–957. doi:10.1109/tnano.2017.2728600

Lee, K. X., Shameli, K., Miyake, M., Kuwano, N., Ahmad, B., and Yen, P. (2016). 'Green synthesis of gold nanoparticles using aqueous extract of *garcinia mangostana* fruit peels. *J. Nanomater.* 2016, 1–7. doi:10.1155/2016/8489094

Lee, K. X., Shameli, K., Mohamad, S. E., Yew, P., Isa, M., Yap, E., et al. (2019). Bio-Mediated synthesis and characterisation of silver nanocarrier, and its potent anticancer action. *Nanomaterials* 9, 1423. doi:10.3390/nano9101423

Liu, R., and Priestley, R. D. (2016). Rational design and fabrication of core-shell nanoparticles through a one-step/pot strategy. *J. Mat. Chem. A* 4, 6680–6692. doi:10.1039/c5ta09607c

Lu, H., Wang, J., Wang, T., Zhong, J., Bao, Y., and Hongxun, H. (2016). 'Recent progress on nanostructures for drug delivery applications. *J. Nanomater.* 2016, 1–12. doi:10.1155/2016/5762431

Lu, L., Burkey, G., Halaciuga, I., and Goia, D. V. (2013). Core-shell gold/silver nanoparticles: Synthesis and optical properties. *J. colloid interface Sci.* 392, 90–95. doi:10.1016/j.jcis.2012.09.057

Maddah, A., Ziamajidi, N., Khosravi, H., Danesh, H., and Abbasalipourkabir, R. (2022). Gold nanoparticles induce apoptosis in HCT-116 colon cancer cell line. *Mol. Biol. Rep.* 49, 7863–7871. doi:10.1007/s11033-022-07616-6

Martínez, R., Poupard, M. F. N., Álvarez, A., Soprano, E., Migliavacca, M., Carrillo-Carrión, C., et al. (2020). "'Nanoparticle behavior and stability in biological environments," in *Nanoparticles for biomedical applications* (Springer: Springer Singapore). doi:10.1016/b978-0-12-816662-8.00002-3

Matlou, G. G., and Abrahamse, H. (2022). "'Metallic core-shell nanoparticles as drug delivery vehicles in targeted photodynamic therapy of cancer," in *Handbook of oxidative stress in cancer: Therapeutic aspects* (Springer: Springer Singapore). doi:10.1007/978-981-16-1247-3_208-1

Nivethaa, E., Dhanavel, S., Narayanan, C. A., Vasu, A., and Stephen, A. (2015). An *in vitro* cytotoxicity study of 5-fluorouracil encapsulated chitosan/gold nanocomposites towards MCF-7 cells. *RSC Adv.* 5, 1024–1032. doi:10.1039/c4ra11615a

Nyst, H. J., Tan, I. B., Stewart, F. A., and Balm, J. M. (2009). Is photodynamic therapy a good alternative to surgery and radiotherapy in the treatment of head and neck cancer? *Photodiagnosis Photodyn. Ther.* 6, 3–11. doi:10.1016/j.pdpdt.2009.03.002

Ovais, M., Raza, A., Naz, S., Islam, N., Khalil, T., Ali, S., et al. (2017). Current state and prospects of the phytosynthesized colloidal gold nanoparticles and their applications in cancer theranostics. *Appl. Microbiol. Biotechnol.* 101, 3551–3565. doi:10.1007/s00253-017-8250-4

Patra, J. K., Das, G., Fraceto, L., Campos, L. S., Diaz-Torres, L. A., Rodriguez-Torres, R., et al. (2018). Nano based drug delivery systems: Recent developments and future prospects. *J. Nanobiotechnology* 16, 71–33. doi:10.1186/s12951-018-0392-8

Prabhawathi, V., Sivakumar, T., Boobalan, C., Manohar, M., and Doble, M. (2019). Design of antimicrobial polycaprolactam nanocomposite by immobilizing subtilisin conjugated Au/Ag core-shell nanoparticles for biomedical applications. *Mater. Sci. Eng. C* 94, 656–665. doi:10.1016/j.msec.2018.10.020

Safwat, M. A., Soliman, M. S., Sayed, D., and Attia, M. A. (2018). Fluorouracil-loaded gold nanoparticles for the treatment of skin cancer: Development, *in vitro* characterization, and *in vivo* evaluation in a mouse skin cancer xenograft model. *Mol. Pharm.* 15, 2194–2205. doi:10.1021/acs.molpharmaceut.8b00047

Saifullah, B., Buskaran, K., Shaikh, R., Barahuie, F., Fakurazi, S., Mohd Moklas, M., et al. (2018). Graphene oxide-PEG-protocatechuic acid nanocomposite formulation with improved anticancer properties. *Nanomaterials* 8, 820. doi:10.3390/nano8100820

Saikia, I., Hazarika, M., Yunus, S., Pal, M., Das, M. R., Borah, J., et al. (2018). Green synthesis of Au-Ag-In-rGO nanocomposites and its α-glucosidase inhibition and cytotoxicity effects. *Mater. Lett.* 211, 48–50. doi:10.1016/j.matlet.2017.09.084

Sapkota, K., and Han, S. (2017). A novel environmentally sustainable synthesis of Au-Ag@AgCl nanocomposites and their application as an efficient and recyclable catalyst for quinoline synthesis. *New J. Chem.* 41, 5395–5402. doi:10.1039/c7nj00764g

Sargazi, S., Laraib, U., Simge, E., Rahdar, A., Hassanisaadi, M., Zafar, M. N., et al. (2022). Application of green gold nanoparticles in cancer therapy and diagnosis. *Nanomaterials* 12, 1102. doi:10.3390/nano12071102

Satapathy, S., Mohapatra, P., Preet, R., Das, D., Sarkar, B., Choudhuri, T., et al. (2013). Silver-based nanoparticles induce apoptosis in human colon cancer cells mediated through p53. *Nanomedicine* 8, 1307–1322. doi:10.2217/nnm.12.176

Sathiyanarayanan, G., Vignesh, V., Saibaba, V., Vinothkanna, S., Dineshkumar, A., Viswanathan, K., et al. (2014). Synthesis of carbohydrate polymer encrusted gold nanoparticles using bacterial exopolysaccharide: A novel and greener approach. *RSC Adv.* 4, 22817–22827. doi:10.1039/c4ra01428f

Shankar, S. S., Rai, A., Ahmad, A., and Sastry, M. (2004). Rapid synthesis of Au, Ag, and bimetallic Au core-Ag shell nanoparticles using Neem (Azadirachta indica) leaf broth. *J. Colloid Interface Sci.* 275, 496–502. doi:10.1016/j.jcis.2004.03.003

Shen, C. C., Zhu, Q., Zhao, Z. W., Wen, T., Wang, X., and Xu, A. W. (2015). Plasmon enhanced visible light photocatalytic activity of ternary Ag2Mo2O7@ AgBr-Ag rod-like heterostructures. *J. Mat. Chem. A* 3, 14661–14668. doi:10.1039/c5ta02337h

Shen, M-Y., Liu, T., Yu, T-W., Kv, K., Chiang, W., Tsai, Y. C., et al. (2019). Hierarchically targetable polysaccharide-coated solid lipid nanoparticles as an oral chemo/thermotherapy delivery system for local treatment of colon cancer. *Biomaterials* 197, 86–100. doi:10.1016/j.biomaterials.2019.01.019

Sufyani, A., Moslah, N., and Ahmed Hussien, N. (2019). 'Characterization and anticancer potential of silver nanoparticles biosynthesized from Olea chrysophylla and Lavandula dentata leaf extracts on HCT116 colon cancer cells. *J. Nanomater.* 2019, 9. doi:10.1155/2019/7361695

Sukri, S., Shameli, K., Teow, S-Y., and Chew, J. (2019). 'Cytotoxicity and antibacterial activities of plant-mediated synthesized zinc oxide (ZnO) nanoparticles using Punica granatum (pomegranate) fruit peels extract. *J. Mol. Struct.* 1189, 57–65. doi:10.1016/j.molstruc.2019.04.026

Sylvestre, J-P., Poulin, S., Kabashin, V., Sacher, E., Meunier, M., and Luong, J. H. (2004). Surface chemistry of gold nanoparticles produced by laser ablation in aqueous media. *J. Phys. Chem. B* 108, 16864–16869. doi:10.1021/jp047134+

Tanaka, T., Tanaka, T., and Tanaka, M. (2011). Potential cancer chemopreventive activity of protocatechuic acid. *J. Exp. Clin. Med.* 3, 27–33. doi:10.1016/j.jecm.2010.12.005

Tripathy, T., Kolya, H., Jana, S., and Senapati, M. (2017). Green synthesis of Ag-Au bimetallic nanocomposites using a biodegradable synthetic graft copolymer; hydroxyethyl starch-g-poly (acrylamide-co-acrylic acid) and evaluation of their catalytic activities. *Eur. Polym. J.* 87, 113–123. doi:10.1016/j.eurpolymj.2016.12.019

Usman, M. S., Hussein, M. Z., Fakurazi, S., and Masarudin, M. J. (2018b). 'Synthesis and characterization of protocatechuic acid-loaded gadolinium-layered double hydroxide and gold nanocomposite for theranostic application. *Appl. Nanosci.* 1, 14. doi:10.1007/s13204-018-0752-6

Usman, M. S., Hussein, M. Z., Kura, S., Fakurazi, M. J., and Masarudin, M. (2018a). Graphene oxide as a nanocarrier for a theranostics delivery system of protocatechuic acid and gadolinium/gold nanoparticles. *Molecules* 23, 500. doi:10.3390/molecules23020500

Villaverde, A. (2011). *Nanoparticles in translational science and medicine*. United States: Academic Press.

Walker, A. R., and Walker, B. F. (1992). Faecal pH and colon cancer. *Gut* 33, 572. doi:10.1136/gut.33.4.572

Wang, R., Yao, Y., Shen, M., and Wang, X. (2016). Green synthesis of Au@Ag nanostructures through a seed-mediated method and their application in SERS. *Colloids Surfaces A Physicochem. Eng. Aspects* 492, 263–272. doi:10.1016/j.colsurfa.2015.11.076

Xu, C., Guan, S., Wang, B., Wang, S., Wang, Y., Sun, C., et al. (2018). Synthesis of protocatechuic acid grafted chitosan copolymer: Structure characterization and *in vitro* neuroprotective potential. *Int. J. Biol. Macromol.* 109, 1–11. doi:10.1016/j.ijbiomac.2017.12.019

Xu, J., Zhang, Y., Xu, J., Wang, M., Liu, G., Wang, J., et al. (2019). Reversing tumor stemness via orally targeted nanoparticles achieves efficient colon cancer treatment. *Biomaterials* 216, 119247. doi:10.1016/j.biomaterials.2019.119247

Yew, Y. P., Shameli, K., Mohamad, S. E., Nagao, Y., Teow, S-Y., Lee, K. X., et al. (2019). Potential anticancer activity of protocatechuic acid loaded in montmorillonite/Fe3O4 nanocomposites stabilized by seaweed Kappaphycus alvarezii. *Int. J. Pharm.* 572, 118743. doi:10.1016/j.ijpharm.2019.118743

Yin, M. C., Lin, C-C., Wu, H. C., Tsao, S-M., and Hsu, C-K. (2009). Apoptotic effects of protocatechuic acid in human breast, lung, liver, cervix, and prostate cancer cells: Potential mechanisms of action. *J. Agric. Food Chem.* 57, 6468–6473. doi:10.1021/jf9004466

Yusefi, M., Lee-Kiun, M. S., Shameli, K., Teow, S. Y., Ali, R. R., Siew, K. K., et al. (2021). 5-Fluorouracil loaded magnetic cellulose bionanocomposites for potential colorectal cancer treatment. *Carbohydr. Polym.* 273, 118523. doi:10.1016/j.carbpol.2021.118523

Zhang, C. X., Tanner, J. A., Li, H-W., and Wu, Y. (2020). A novel fluorescence probe of Plasmodium vivax lactate dehydrogenase based on adenosine monophosphate protected bimetallic nanoclusters. *Talanta* 213, 120850. doi:10.1016/j.talanta.2020.120850

Zhang, H., Haba, M., Okumura, M., Akita, T., Hashimoto, S., and Toshima, N. (2013). Novel formation of Ag/Au bimetallic nanoparticles by physical mixture of monometallic nanoparticles in dispersions and their application to catalysts for aerobic glucose oxidation. *Langmuir* 29, 10330–10339. doi:10.1021/la401878g

Zhang, H., Okuni, J., and Toshima, N. (2011). One-pot synthesis of Ag-Au bimetallic nanoparticles with Au shell and their high catalytic activity for aerobic glucose oxidation. *J. colloid interface Sci.* 354, 131–138. doi:10.1016/j.jcis.2010.10.036

Zhang, J., Yu, K., Yu, Y., Lou, L. L., Yang, Z., Yang, J., et al. (2014). Highly effective and stable Ag3PO4/WO3 photocatalysts for visible light degradation of organic dyes. *J. Mol. Catal. A Chem.* 391, 12–18. doi:10.1016/j.molcata.2014.04.010

Frontiers in
Bioengineering and Biotechnology

Accelerates the development of therapies, devices, and technologies to improve our lives

A multidisciplinary journal that accelerates the development of biological therapies, devices, processes and technologies to improve our lives by bridging the gap between discoveries and their application.

Discover the latest Research Topics

See more →

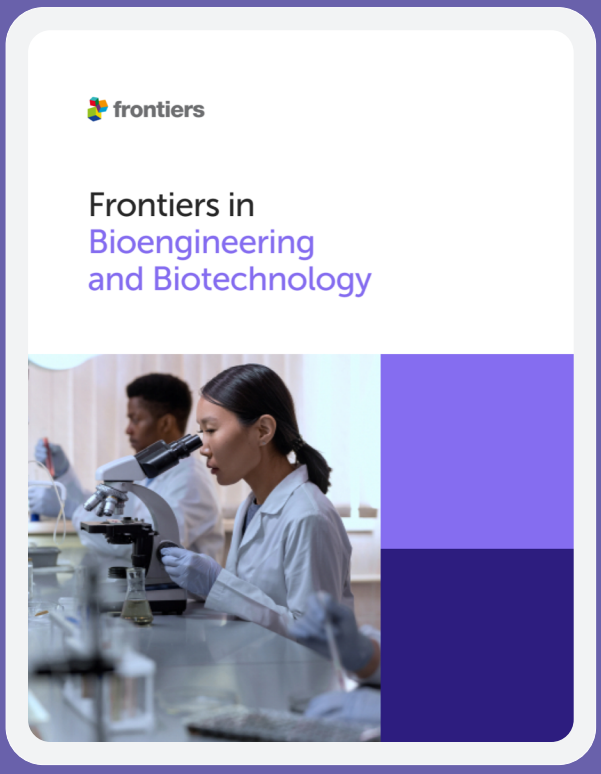

Frontiers

Avenue du Tribunal-Fédéral 34
1005 Lausanne, Switzerland
frontiersin.org

Contact us

+41 (0)21 510 17 00
frontiersin.org/about/contact